

Compact Antennas for Wireless Communications and Terminals

To my sons Tanguy and T rence

Compact Antennas for Wireless Communications and Terminals

Theory and Design

Edited by
Jean-Marc Laheurte

ISTE

 **WILEY**

First published 2011 in Great Britain and the United States by ISTE Ltd and John Wiley & Sons, Inc.

Apart from any fair dealing for the purposes of research or private study, or criticism or review, as permitted under the Copyright, Designs and Patents Act 1988, this publication may only be reproduced, stored or transmitted, in any form or by any means, with the prior permission in writing of the publishers, or in the case of reprographic reproduction in accordance with the terms and licenses issued by the CLA. Enquiries concerning reproduction outside these terms should be sent to the publishers at the undermentioned address:

ISTE Ltd
27-37 St George's Road
London SW19 4EU
UK

www.iste.co.uk

John Wiley & Sons, Inc.
111 River Street
Hoboken, NJ 07030
USA

www.wiley.com

© ISTE Ltd 2011

The rights of Jean-Marc Laheurte to be identified as the author of this work have been asserted by him in accordance with the Copyright, Designs and Patents Act 1988.

Library of Congress Cataloging-in-Publication Data

Compact antennas for wireless communications and terminals : theory and design / edited by Jean-Marc Laheurte.

p. cm.

Includes bibliographical references and index.

ISBN 978-1-84821-307-4

1. Antennas (Electronics)--Design and construction. 2. Wireless communication systems. I. Laheurte, Jean-Marc.

TK7871.6.C626 2011

621.384'135--dc23

2011021212

British Library Cataloguing-in-Publication Data

A CIP record for this book is available from the British Library

ISBN 978-1-84821-307-4

Printed and bound in Great Britain by CPI Antony Rowe, Chippenham and Eastbourne.



Table of Contents

Introduction	xi
Chapter 1. General Information About Printed Antennas	1
Jean-Marc LAHEURTE	
1.1. Physical characteristics	1
1.2. Properties, limitations, and applications	4
1.3. Printed rectangular antenna viewed as a wide microstrip line	7
1.4. Manufacturing processes	8
1.5. Microwave substrates	11
Chapter 2. Transmission Line Model	15
Jean-Marc LAHEURTE	
2.1. Introduction.	15
2.2. Equivalent circuit	16
2.2.1. Effective permittivity.	16
2.2.2. Equivalent line extension	16
2.2.3. End of line equivalent circuit	17
2.2.4. Process for design of a rectangular antenna	19
2.2.5. Example	20
2.3. Input impedance	20
Chapter 3. Cavity Model	25
Jean-Marc LAHEURTE	
3.1. Introduction.	25
3.2. Formulation of the electromagnetic problem	25
3.3. Calculation of expressions for fields and currents of a rectangular patch	29

3.4. Expressions for principal modes	31
3.5. Cartography of modal currents and associated radiation patterns	33
Chapter 4. Radiation of a Printed Antenna	39
Jean-Marc LAHEURTE	
4.1. Introduction.	39
4.2. Modelization using two equivalent radiating slots	40
4.3. Calculation of the field radiated by a horizontal radiating slot.	43
4.4. Calculation of the field radiated by the rectangular patch.	44
4.5. Determination of the radiation pattern in the principal planes	44
4.6. Influence of height.	46
4.7. Influence of the ground plane	47
4.8. Polarization.	48
4.9. Directivity.	49
4.10. Influence of the substrate on resonant frequency: parametric study based on antenna RCS	51
Chapter 5. Electrical Equivalent Circuit of a Printed Antenna	55
Jean-Marc LAHEURTE	
5.1. Energy considerations.	55
5.2. Equivalent circuit	57
5.3. Determination of W_E , W_M , and B for a rectangular patch.	58
5.4. Modeling using a tank circuit	60
5.5. Quality factor of an antenna	62
5.6. Calculation of radiation quality factor	63
5.7. Calculation of efficiency	64
5.7.1. Losses in conductive walls	64
5.7.2. Losses in the dielectric.	65
5.7.3. Radiated power	66
5.8. Influence of surface waves on bandwidth and efficiency	67
Chapter 6. Feeding Circuits for Microstrip Antennas	69
Jean-Marc LAHEURTE and Benoît POUSSOT	
6.1. Introduction.	69
6.2. Direct coupling by coaxial probe	71
6.3. Excitation by proximity coupling	73
6.4. Excitation by slot coupling.	74

Chapter 7. Circularly Polarized Antennas	89
Jean-Marc LAHEURTE, Marjorie GRZESKOWIAK and Stéphane PROTAT	
7.1. Principles of circular polarization	90
7.1.1. Elliptical and circular linear polarization	90
7.1.2. Right- or left-hand circular polarization.	91
7.1.3. Axial and cross-polarization ratios.	92
7.1.4. Measurement of circular polarization	93
7.2. Parasitic radiation – degradation of circular polarization	94
7.3. Patch fed by single or dual excitation	96
7.3.1. Single excitation	96
7.3.2. Dual excitation	98
7.4. Sequential array	99
7.4.1. Principle of sequential rotation: initial analysis	99
7.4.2. Sequential rotation applied to a radiating element fed by multiple feeds	106
7.5. Spiral and quadrifilar helix antennas	108
7.5.1. Spiral antennas	108
7.5.2. Quadrifilar helix antennas	113
7.6. Conclusion	119
Chapter 8. Wideband Antennas	121
Xavier BEGAUD	
8.1. Multiresonant antennas	122
8.1.1. Principle	122
8.1.2. Widening bandwidth through resonance coupling	122
8.2. Traveling wave antennas	125
8.2.1. Tapered slot antennas	125
8.3. Frequency independent antennas	126
8.3.1. Introduction	126
8.3.2. Equiangular antennas.	127
8.3.3. Log-periodic antennas	128
8.3.4. Sinuous antennas	129
8.4. Ultra-wideband antennas	132
8.4.1. Biconical and Bow-Tie antennas	134
8.4.2. Planar monopoles	137
8.5. Conclusion	140
Chapter 9. Miniature Antennas	143
Guillaume VILLEMAUD	
9.1. Introduction.	143
9.2. Which types of antennas should be used for integration?	144
9.2.1. Non-resonant antennas.	144

9.2.2. Resonant antennas	145
9.3. Integration limits in a finite volume	145
9.4. Resonant antennas in fundamental mode	146
9.4.1. General considerations	146
9.4.2. Wire antennas	148
9.4.3. Planar antennas	150
9.4.4. Comparison	152
9.4.5. 3D antennas	152
9.5. Bulk reduction techniques	152
9.5.1. Use of dielectrics with strong permittivity	153
9.5.2. Modification of wave path	153
9.5.3. Utilization of inductive, capacitive, and short-circuit effects	156
9.5.4. Control over radiation	160
9.6. Multiresonant antennas	164
9.7. Synthesis and discussion	166
Chapter 10. Reconfigurable Antennas	169
Jean-Marc LAHEURTE	
10.1. Introduction	169
10.2. Basic topologies and constraints	170
10.3. Switched components: available technologies	174
10.4. Frequency reconfigurable antennas (FRAs)	180
10.4.1. Introduction	180
10.4.2. Examples of radiating slot-based FRA	181
10.4.3. Examples of patch- or PIFA-based FRA integrating switchable slots	184
10.4.4. Examples of FRA using switched short circuits	184
10.4.5. FRA utilizing a loaded stub	185
10.5. Introduction to RAs in terms of polarization and radiation pattern	185
10.6. Polarized reconfigurable antennas (PRAs)	187
10.7. Radiation pattern reconfigurable antennas (RPRAs)	190
10.7.1. RPRA with rotational symmetry and switched parasitics	192
10.7.2. RPRA with parasitic elements loaded using switched reactance	193
10.7.3. Unit cell of reflective array based on a patch of slots [CAD 05]	202
Chapter 11. Introduction to Antenna Diversity	205
Lionel RUDANT	
11.1. Benefits of antenna diversity	205
11.1.1. Effects of multipath propagation	206

11.1.2. Principles of antenna diversity	207
11.1.3. Non-ideal antenna diversity	211
11.2. Performance of multiantenna systems	214
11.2.1. Antenna balance	214
11.2.2. Antenna independence	216
11.3. Multiantenna systems	222
11.3.1. Space diversity	222
11.3.2. Compact multiantenna system	224
11.4. Conclusion and looking toward MIMO	228
Bibliography	233
List of Authors	241
Index	243

Introduction

This publication covers microwave antennas and more specifically planar versions, which are the types of antenna preferred at microwave frequencies in modern integrated communication systems. We see variants of these in everyday life, hidden away in portable telephones, mobile phone base stations, electronic tags, or even portable computers. More generally, we see them in all applications requiring miniaturization and/or a fixed support structure, such as telephone casings. In terms of this publication, we are therefore not including reflector antennas, antenna arrays, or more generally directional antennas that occupy a surface or volume much greater than the wavelength.

Written by a collective of specialist engineers and research professors, this book is aimed at engineers and researchers who want to:

- understand the principles of planar and/or small volume antennas used in modern communication systems;
- comprehend the problems of design and manufacture;
- define the constraints and limitations presented by the antenna within the body of the communication system.

Chapter 1 deals with the physical characteristics of printed antennas (dielectric support, metallization), manufacturing techniques, and areas of application.

Chapters 2 and 3 describe the so-called transmission line and cavity models, respectively, of printed antennas. These two models provide complementary physical interpretations of the basic, usually rectangular geometry of antennas. These interpretations will apply to more complex yet short depth geometries. Also we will restrict ourselves to rectangular geometries, to limit the amount of analysis.

Chapter 4 deals with radiation from the rectangular planar antenna from the point of view of equivalent magnetic currents. We will examine in particular the influence on the characteristics of the radiation pattern, from fundamental parameters such as the thickness and dielectric permittivity of the substrate or the dimensions of the ground plane. We will also see that the calculation of the wave backscattered by an antenna illuminated by a plane wave enables the resonance frequency of the antenna to be determined.

Chapter 5 describes in depth the rationale leading to an electric RLC circuit model for this type of antenna. The concepts of bandwidth and efficiency are tackled from the quality factor of the equivalent resonant circuit. The influence of physical (permittivity of, and losses in the substrate) and geometrical parameters on these measurements is highlighted.

The different methods of powering antennas are described in Chapter 6 while emphasizing the concept of coupling between feeding circuit and radiating sections. Power by slot coupling is specifically examined, since it possesses a number of geometric parameters for adjusting the matching which are greater than excitation by direct coupling.

Chapter 7 examines in detail circular polarization, while defining primarily the base concepts before introducing several types of circular polarization antennas. On the one hand, we have simple, purely planar antennas with one or two ports, whose performance is improved with the principle of sequential rotation. On the other hand, we have spirals and quadri-helix antennas, whose performance in terms of bandwidth or purity of polarization over wide coverage areas, are much superior.

Chapter 8 deals with broadband and partially with multiband antennas. In the context where spread spectrum modulations are assuming increasing importance, the need to create antennas that are at the same time broadband and miniaturized has given rise to a great many studies in recent years. This chapter summarizes not only these, while attempting to describe the general design philosophy, but also the practical limitations of production, linked notably to the reduced size of the ground plane.

Chapter 9 is an introduction to the world of miniaturized antennas. This vast topic is the subject of specialist publications, where the problem of the antenna presenting an optimized efficiency and bandwidth over a given volume is handled both theoretically and experimentally. This chapter will instead attempt to reveal the base concepts that enable us, from resonant canonical patch or half-wave dipole antennas, to reduce the dimensions of antennas in line with the most common planar inverted-F antenna (PIFA), IFA, or wire-plate structures. The principle strategies in

miniaturization (addition of short circuits, introduction of slits) are extensively detailed.

Chapter 10 deals with the reconfigurability of antennas by active elements. This concerns antennas having the capacity to electronically reconfigure one or more of their characteristics (pattern, polarization, impedance). The object here is twofold. In the context of terminal miniaturization, it becomes possible to change the radiation characteristics and the working frequency of a structure through the switching or selection of feeding ports, in other words to produce the equivalent of several colocalized antennas. In the context of antenna diversity, we suggest some intelligent structures that are either opposing or adaptable to an evolving environment. Variations in the environment might result from signal fadings linked to multipaths in towns, disturbances due to the human body near to the terminal or quite simply changes in communication standards.

Chapter 11 is a didactic introduction to the diversity of antennas used more and more in modern communication systems. Using the base theory of multipath channels, the author emphasizes the advantages of multiantenna systems to combat fadings, while notably introducing the concept of diversity gain. The impact of the correlation and imbalance between the received signals on the link quality is underlined. We also state a fundamental relationship between the coefficient correlation and the coupling S-matrix between antennas. This chapter includes the study of produced and tested multiantenna systems.

Chapter 1

General Information About Printed Antennas

1.1. Physical characteristics

The basic printed antenna consists of a thin layer of metal (patch) positioned over a ground plane, both being etched on the two sides of a substrate of permittivity ϵ_r and thickness h (Figure 1.1). Typically, $h \ll \lambda_0$ and $0.003\lambda_0 < h < 0.05\lambda_0$. The length L of the patch is of the order of $L = \lambda_0/2 \sqrt{\epsilon_{\text{eff}}}$, where ϵ_{eff} is the relative permittivity of the patch.

The terms printed, plated, or patch antenna are used interchangeably to describe planar antennas produced using photolithographic techniques. Note that there are planar antennas that are not produced using these techniques. For example, this is the case with PIFA antennas or their variants in 1 GHz mobile telephony, the substrate here being made up of air with metallic parts produced using copper or aluminum foil that has been folded and machined (Figure 1.2).

Planar antennas can equally be produced under clean conditions over silicon (Figure 1.3) or glass substrates using microtechnological manufacturing processes. Because of the given antenna dimensions (of the order of 1 cm), the manufacturing costs and patterning tolerances, the applications planned are typically beyond the Ka band (about 20 GHz).

2 Compact Antennas for Wireless Communications & Terminals

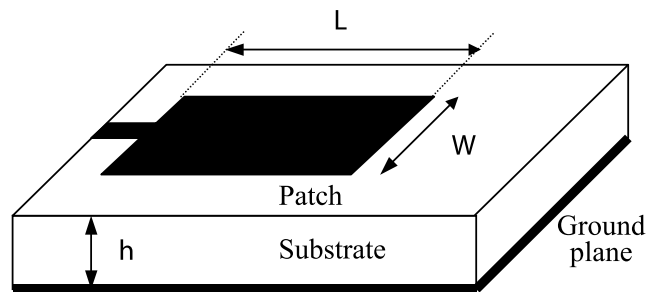


Figure 1.1. Geometry of a printed antenna excited by microstrip line

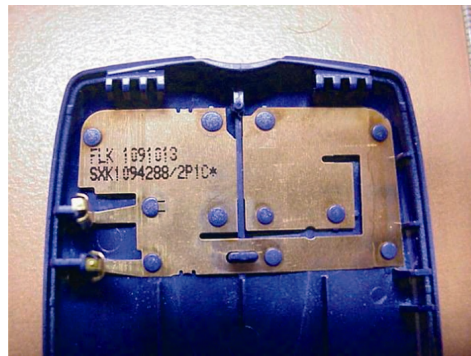


Figure 1.2. PIFA antenna modified for a portable telephone (Ericsson T65)

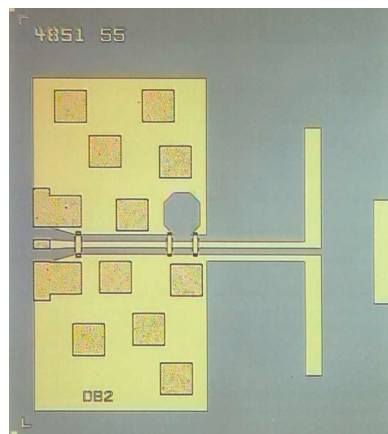


Figure 1.3. Dipole fed by a coplanar/coupled line. Antenna produced on silicon for millimetric applications

Finally, in very low-cost radio-frequency identification (RFID) applications in which electronic tags are manufactured in bulk, paper or plastic supports are used (Figure 1.4), a conductive ink thereby enabling the production of the radiating element.



Figure 1.4. Meander line dipole antenna for use in RFID applications

Typical permittivity values are in the range $2.2 < \epsilon_r < 12$. Low permittivity and increased substrate thickness lead to superior performance (better efficiency, greater bandwidth, higher directivity) at the cost of a more significant patch width, which can pose problems when antennas are put in an array structure. These dielectric substrate characteristics lead to less concentrated field lines around the patch, which is conducive to radiation.

Inversely, printed microwave circuits require increased permittivity and low substrate thickness to concentrate the field under the metallic sections, to limit the losses from radiation and to minimize the area occupied. There has to be a compromise, therefore, between antenna performance and integration of the feeding circuit, when we want to produce both in the same substrate.

The patch generally takes the form of a square, rectangle, disc, or a horizontal dipole, since these simple geometries lead to good purity of polarization and simple analysis. Printed dipoles possess a wide bandwidth and occupy a reduced space that makes them suitable for use in antenna arrays.

Linear or circular polarizations can easily be produced from all types of patches. Finally, while photolithography enables the simultaneous patterning of the patch array and its distribution circuit, we can easily obtain an increase in directivity, a pattern scanning, or an improvement in purity of polarization, depending on the technique used.

1.2. Properties, limitations, and applications

Printed antennas are of interest in all applications requiring one or more of the following properties:

- low cost;
- mass production, thanks to printed circuit technology;
- planarity;
- lightness;
- consistency on non-planar surfaces (cylinders, etc.);
- mechanical robustness;

properties that we find in wireless communications as well as in embedded systems (aircraft, missiles, etc.). Furthermore, the potential to integrate monolithic microwave integrated circuits (MMICs) or components onto the antenna substrate enables us to envisage:

- miniaturization of the RF front-end receiver;
- reduction in losses in transmission lines;
- reconfiguration capacities in pattern, directivity, polarization, or frequency.

Disadvantages of printed antennas that are often mentioned are:

- poor directivity (from about 6–8 dB);
- reduced efficiency and bandwidth (linked to an increased quality factor Q);
- limited input power;
- reduced purity of polarization;
- radiation interference in power circuits.

However, variants in design or geometry enable a sensible improvement in performance. For example, increasing the thickness of the substrate leads to efficiencies greater than 90% and bandwidths greater than 30%. Stacking patches also enables an increase in bandwidth.

For array applications, planar printed antennas have the following limitations:

- reduced scanning capacity, linked to the zero in the radiation pattern of the radiating element for end-fire directions;

- prohibitive losses in the distribution circuit for antenna arrays of a significant size (approximate directivity >30 dB);
- significant coupling through surface waves between radiating elements under certain conditions, notably for significant permittivities and substrates of non-negligible thickness, in comparison with the wavelength;
- low maximum power (of the order of 100 W).

Taken from [LUX 07], we summarize below the principle applications of printed antennas and corresponding systems in the area of communications and radar:

- satellites:
 - television, direct to homes or vehicles,
 - switched arrays for reconfigurable coverage,
 - detection of terrestrial resources (synthetic aperture radar imagery),
 - antennas for radio-based navigation systems via GPS, Galileo, Glonass (land vehicles or personal assistants and PCs);
- guidance telemetry:
 - monopulse systems,
 - arrays under radomes;
- adaptive networks:
 - multitarget acquisition,
 - semiconductor integrated array;
- portable radios or communication with land mobiles:
 - mobile telephony (GSM, DCS, PCS, UMTS, etc., portable terminals),
 - antennas on base stations,
 - FM radio antennas printed on car windscreens,
 - toll booths (antennas printed on RF badges);
- aeronautics (aircraft, rocket engines, missiles):
 - communication,
 - navigation,

6 Compact Antennas for Wireless Communications & Terminals

- altimeters,
- landing systems,
- antennas conformed onto the fuselage of aeronefs for navigation (radars, altimeters, automatic landing) and communication,
- plated antennas on missiles (telemetry);
- biomedical:
 - implants,
 - thermal applicators for microwave cancer treatment,
 - tomography;
- military applications:
 - surface-mounted antennas on vehicles,
 - antennas conformed onto missiles in telemetry,
 - embedded sensors,
 - monopulse or synchronous tracking radars,
 - electronic beam scanning of antenna arrays,
 - Doppler radars,
 - active antennas for detection and suppression of scrambling,
 - signal-processing active antennas for parasitic reflection cancellation;
- identification:
 - RFID tags (radio-frequency identification without contact with clothes, objects, people, etc.),
 - miniaturized sensors,
 - antennas stitched into clothing,
- WLAN wireless networks:
 - ultra-wideband and 60 GHz antennas for intrabuilding communications,
 - short distance radio technology (using Bluetooth and Wi-Fi standards) for electronic equipment (PCs, PDAs, etc.);
- security:
 - surveillance antennas (anti-intruder alarms).

1.3. Printed rectangular antenna viewed as a wide microstrip line

Different models of printed antennas (transmission line and cavity) will be introduced in detail in subsequent chapters. It is useful, however, as a first introduction, to explain the radiation mechanism of the printed antenna, based on a transmission line.

In a printed rectilinear line, the energy is only radiated to the level of the transitions. Let us assume that the horizontal components of the electric field “overflowing” the line constitute the secondary source of radiation (Huygens’ theorem, see Chapter 2).

Then, the contributions to the radiation from fields on both sides of the line balance each other out in all directions, since they are in phase opposition and since the width of the line is small. Conversely, the field at the transition level (an open circuit, as in the example in Figure 1.5) is not compensated for and contributes to the radiation.

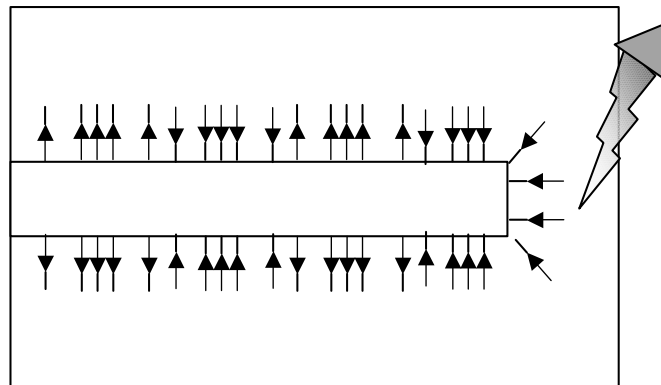


Figure 1.5. *Components of the tangential electric field at the surface of the substrate and “overflowing” an open circuit printed line*

This radiation is unwanted and interfering in the case of transmission lines or microwave circuits, but it does become useful if we wish to produce an antenna. A printed antenna can therefore be viewed as a very wide open circuit line presenting significant radiation at the level of rupture. The radiation will be all the more significant when the field lines are spread out, which will be the case over wide areas and for thick substrates presenting low permittivity.

If we now consider a section of line that is open at its two extremities, then the energy provided to this structure is susceptible to radiating from each extremity. If

the length of the section of line is $L = \lambda/2$, then the fields radiated by the two extremities will generate constructive interference *ad infinitum*.

The fact that the structure effectively acts as an antenna and not as a lossy resonant cavity can be visualized while we imagine a pulse of current or field spreading throughout the structure.

At the level of each extremity, one part of the pulse is radiated, the rest is reflected. During the propagation under the patch, the reflective part loses some of its intensity in the form of heat in the metals and leaking substrates that make up the structure.

After each round trip, a fraction of the pulse is reissued in phase with the preceding fraction, with the number of round trips necessary to mitigate completely the pulsation increasing based on the quality factor of the antenna. The reality of the radiation of the structure will depend on the link between the energy lost under the Joule effect and the energy radiated.

1.4. Manufacturing processes

There are several manufacturing processes partially linked to the substrate used and the level of integration chosen. We will describe briefly here screen printing techniques, the technology of printed circuits, mechanical patterning, as well as thin layer technologies and low-temperature co-fired ceramic (LTCC), which are used for circuits or antennas with strong levels of integration.

The thick-layer technique, or serigraphy, consists of applying a paste or ink onto the substrate, having masked the areas not requiring this deposit. A stage involving baking at high temperature (900°C) sets the ink and must be performed after each application. While it is flexible and reliable, this technique does, however, present some disadvantages, such as the poor conductivity of ink or an average pattern resolution.

The patterning of printed of circuits using photolithographic processes remains the most popular technique for producing microwave antennas. Although relatively low cost and easy to implement, it does have the disadvantage of producing an inadequate pattern quality when the width of the pattern is less than about 150 μm (“notched” edges).

This limitation reduces, for example, the maximum characteristic impedance allowable for a printed line. The principles of this technique are summarized in Figure 1.6.

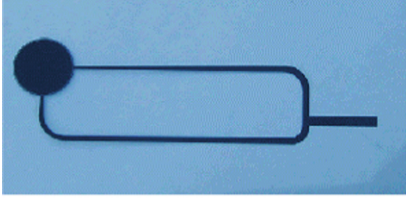
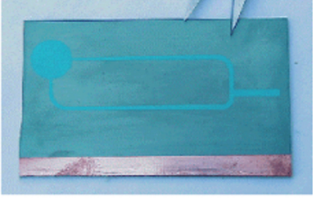
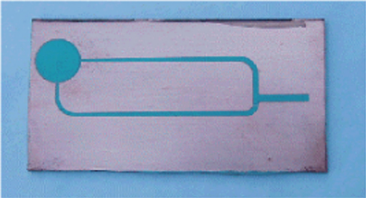
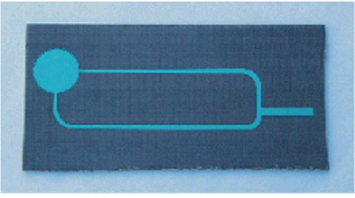
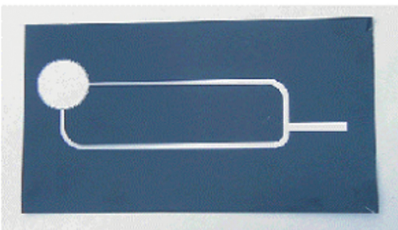
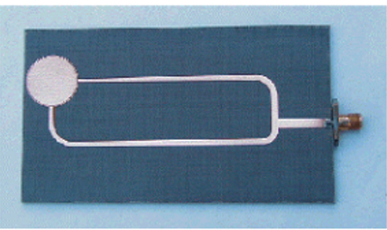
 <p>Stage 1. <i>Design of the flexible mask (CAD)</i></p>	 <p>Stage 2. <i>A thin film of photoresist has been placed by lamination on the pre-metallized substrate. Exposure to UV across the mask (the exposed sections are polymerized)</i></p>
 <p>Stage 3. <i>Development: the exposed photoresist is withdrawn using a basic solution</i></p>	 <p>Stage 4. <i>Patterning: the copper sections which are no longer protected by the photoresist are eliminated using an iron perchloride (acid) solution</i></p>
 <p>Stage 5. <i>Cleaning: the unexposed photoresist is withdrawn using acetone. The pattern has been transferred</i></p>	 <p>Stage 6. <i>The connector and the exterior components are soldered</i></p>

Figure 1.6. *The different stages of manufacture of a printed antenna using a photolithographic process*

The printed circuit technique can be replaced by mechanical patterning (Figure 1.7) when the aim is for a limited production (prototyping) or when wanting to avoid storing chemical products. It is a case of mechanically removing unwanted copper from the circuit using various tools, from a previously metallized substrate.

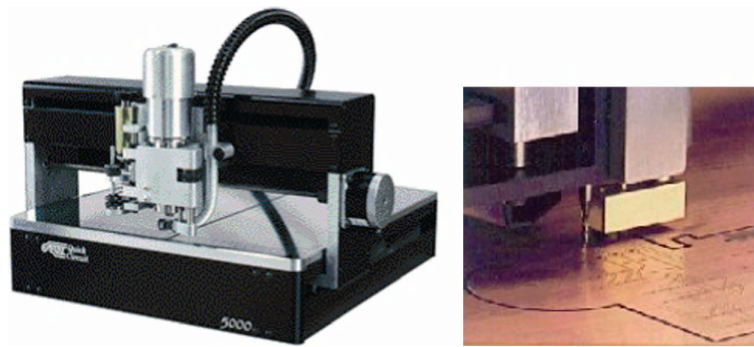


Figure 1.7. *T-Tech Quick Circuit micromilling machine and example of mechanical patterning*

Patterning precision is greater than in photolithographic processes, thanks to very small-sized drills (minimum width 100 μm) enabling a high cut definition. Masks are produced from standard CAD output files (Gerber, DXF, HPGL).

The contribution of thin layer technologies, which enable us a very high level of accuracy in patterning, is particularly significant in the manufacture of millimeter band antennas. This manufacturing process allows for:

- minimum dimensions of 10– to 15 μm , which are compatible with the production of detailed motifs (high impedance lines, Lange couplers, wideband self-spirals);
- a reduction in losses, thanks to the use of very pure gold and excellent definition of the line edges;
- the production of passive functions (capacities, inductances, lines) with precise characteristics, linked to the quality of the deposit and material patterning processes.

The LTCC or HTCC (high-temperature co-fired ceramic) processes have been developed in response to the demands of cost, performance, and complexity of millimeter band applications. They enable us the association of functions (filtering, amplification, etc.) with a planar surface made from several layers (ceramic, polyimide, Teflon, etc.) in which the conductive motifs and the passive elements are positioned using various processes (thin layer, serigraphy, or patterning). It is

possible to combine different uniplanar or microstrip technologies that, arranged over several levels, can be connected by metallized holes or coupled by an electromagnetic field. Several “ceramics” of different thicknesses and dielectric constants enable us to produce complex, small-sized circuits. Some circuits being able to reach more than 15 layers use this technique for applications up to 40 GHz. Some examples of LTCC constructions and structures are shown in Figure 1.8.

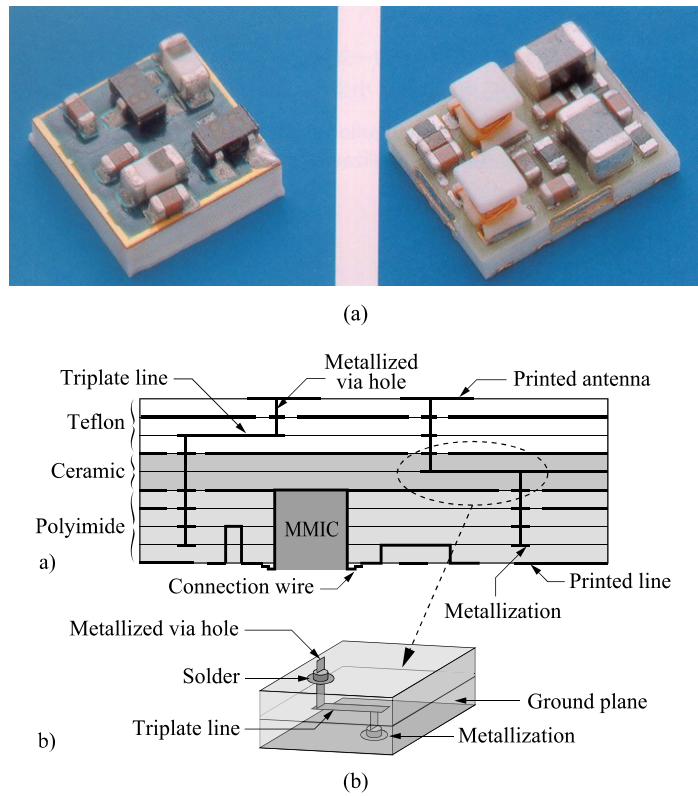


Figure 1.8. (a) Photos of SMCs (Surface Mount Components) mounted on an LTCC substrate; (b) example of an antenna powered by a 3D (horizontal/vertical) line and connected to an MMIC

1.5. Microwave substrates

The principle characteristics of a substrate are:

- dielectric constant (ϵ_r);
- dissipation factor or loss tangent ($\tan\delta$);

- thermal dilation coefficient (in ppm/°C);
- thermal conductivity (in W/m.K).

For microwave products, the performance of FR4 laminated epoxy glass FR4 does not meet requirements, and so we have to turn to “organic” laminated composite materials or otherwise to “ceramic” products.

A ceramic is an inorganic polycrystalline material with a complex structure. The most frequently used different varieties are monoxide ceramics, the best known of which is alumina, which is used as an electrical insulator.

Organic substrates consist of multiple layers of several materials, such as glass, quartz, quartz fiber, or carbon (hydrocarbon resin) fabrics, but the most widespread is polytetrafluoroethylene (PTFE), commonly known as Teflon. Loaded with ceramic, glass fiber, or woven glass, PTFE delivers a low dissipation factor and a level of control over the dielectric constant that the conventional laminates (FR4, Polyimide, etc.) are not able to attain. PTFE and glass fabric have a dielectric constants of 2.07 and 6, respectively. By combining the two materials, it becomes possible to vary the ϵ_r of the substrate.

In order to obtain increased levels of ϵ_r , amounts of ceramics are incorporated into the PTFE. By way of example, Table 1.1 gives the characteristics of some organic substrates.

RT/duroid 5880	$\epsilon_r = 2.20 \pm 0.02$	$\tan\delta = 4 \times 10^{-4}$	$\sigma = 3 \times 10^8$ mhos
RT/duroid 6010LM	$\epsilon_r = 10.2 \pm 0.025$	$\tan\delta = 2 \times 10^{-3}$	$\sigma = 3 \times 10^8$ mhos
TMM3	$\epsilon_r = 3.27 \pm 0.032$	$\tan\delta = 0.002 = 2 \times 10^{-3}$	$\sigma = 9 \times 10^9$ mhos
TMM4	$\epsilon_r = 4.5 \pm 0.045$	$\tan\delta = 0.002 = 2 \times 10^{-3}$	$\sigma = 1 \times 10^9$ mhos

RT/duroid 5880 (composite of PTFE reinforced with non-woven glass fibers), RT/duroid 6010LM (PTFE and ceramic composite), TMM3 and TMM4 (hydrocarbon resin and ceramic composite)

Table 1.1. *Electrical characteristics of some “organic” substrates*

Organic substrates are generally metallized on both sides (except in one particular instance). The two techniques commonly used to metallize these substrates (usually using copper) are the electrolytic deposit and lamination where the cost of manufacture is higher, but offset by excellent surface flatness. Standard

thicknesses are 8, 17, 35, and 70 μm , the most common metallization thickness being 35 μm .

For all types of substrate, commercial thicknesses are in whole multiples of mil (25.4 μm), typically 0.381, 0.508, 0.653, 0.762, 1.27, 1.524 mm, etc.

We recall that metallic losses increase with frequency and resistivity of metal (all the more significantly when the surface is rough).

We must also take into account the skin depth of the metal at the operating frequency, which must be much less than the metal thickness. With copper ($\sigma = 0.588106 \Omega^{-1}\text{cm}^{-1}$), the value of this thickness is about 2 μm at 1 GHz, which enables problem-free metallization of 35 μm or even 17 μm .

Dielectric losses increase with ϵ_r , $\text{tg}\delta$, and frequency. At low substrate thicknesses, metallic losses far exceed dielectric losses. The dielectric constant (ϵ_r) only varies between 0% and 0.05% at 100°C for basic PTFE substrates. Conversely, the loss tangent ($\text{tan}\delta$) varies enormously with humidity, up to 200% for a water absorption as low as 0.25% of the dielectric weight.

The choice of substrate also occurs through the study of mechanical and thermal constraints. Thermal conductivity is highly significant in cases of power devices. The thermal dilation coefficient determines the metal to be used for the substrate transfer (base plate or casing). The two dilation coefficients must effectively be of the same order to avoid complete deterioration of the mounting.

Chapter 2

Transmission Line Model

2.1. Introduction

The transmission line model is derived from the assimilation of a rectangular antenna with a section of very wide microstrip line. Owing to the fact that this line has a finite length and is open at both its extremities, a standing wave will be established as resonant in character if the line length L is roughly equal to half the guided wavelength λ_g .

We assume for this purpose that the transition formed by each of the open extremities is a source of radiation. When the two sources radiate at the same time, as is the case when $L \approx \lambda_g/2$, then this section of line can form an efficient antenna.

First, we will establish the equivalent circuit of the rectangular antenna, based on the transmission line model. Having declared the constituent elements of this circuit, we will then specify the value of the input impedance of the antenna as a function of the position of the feeding point.

2.2. Equivalent circuit

2.2.1. Effective permittivity

The open nature of the microstrip lines leads to a partial wave propagation in air and not solely in the substrate. As the propagation medium is not homogeneous, we cannot settle for ϵ_r to describe the medium and so we introduce effective permittivity ϵ_{eff} given by [BAL 89]:

$$\epsilon_{\text{eff}} = \frac{\epsilon_r + 1}{2} + \frac{\epsilon_r - 1}{2} \left[1 + 12 \frac{h}{W} \right]^{-1/2} \quad [2.1]$$

We observe that ϵ_{eff} becomes closer to ϵ_r when the substrate thickness h is low and the line width W is significant, since the bulk of the field is then concentrated under the line in the dielectric. The guided wavelength is given by:

$$\lambda_g = \frac{\lambda_0}{\sqrt{\epsilon_{\text{eff}}}} \quad [2.2]$$

2.2.2. Equivalent line extension

At the end of the microstrip line, the extension of field lines (Figure 2.1) changes the characteristics of propagation in the immediate vicinity. We can take this disturbance into account, at the same time retaining the effective wavelength (equation [2.2]) while adding a virtual extension ΔL to the physical length L of the antenna (Figure 2.1). The value of ΔL is given by [HAM 75]:

$$\frac{\Delta L}{h} = 0.412 \frac{(\epsilon_{\text{eff}} + 0.3) \left(\frac{W}{h} + 0.264 \right)}{(\epsilon_{\text{eff}} - 0.258) \left(\frac{W}{h} + 0.8 \right)} \quad [2.3]$$

The length $L_{\text{patch}} = L + 2\Delta L$ determines the physical length L of the resonant patch antenna.

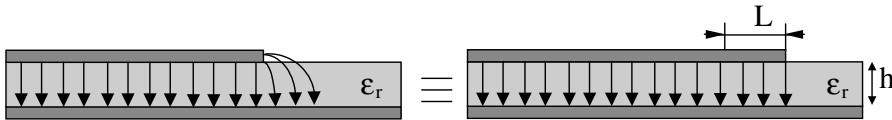


Figure 2.1. End-effect modeling using a virtual extension of the line length

In other words, the antenna will be resonant where:

$$L_{\text{patch}} = L + 2\Delta L = \frac{\lambda_{\text{eff}}}{2} \quad [2.4]$$

L is slightly less than $\lambda_{\text{eff}}/2$, typically of the order of $0.49\lambda_{\text{eff}}$ for classic substrate thicknesses.

2.2.3. End of line equivalent circuit

Each extremity of the line is comparable to a parallel equivalent circuit (Figure 2.2) of:

- susceptance $jB = jC\omega$, linked to the capacitive end effect between the ground plane and the line;
- conductance G , simulating the losses from radiation created as a result of discontinuity.

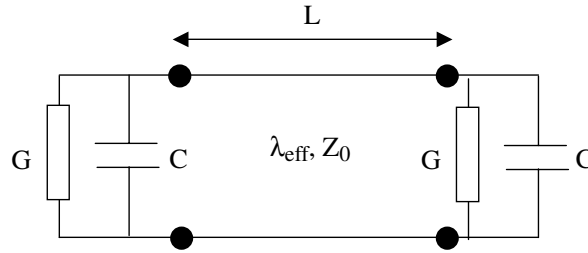


Figure 2.2. Equivalent schematic of a rectangular patch antenna.
End effect simulated by a capacity C in parallel with a conductance G

The capacitive effect can be linked to ΔL by identifying the susceptance jB with the admittance Y of an open-circuit *stub* characterized by its small length ΔL .

We have:

$$Y = \frac{j}{Z_0} \text{tg}(\beta\Delta L) \approx \frac{j\beta\Delta L}{Z_0} \quad [2.5]$$

from which, when $jB = Y$:

$$C \approx \frac{\Delta L \sqrt{\epsilon_{\text{eff}}}}{c_0 Z_0} \quad [2.6]$$

where:

$$Z_0 = \frac{120\pi}{\sqrt{\epsilon_{\text{eff}}}} \frac{h}{w} \quad \text{where} \quad \frac{h}{w} \ll 1 \quad [2.7]$$

and $c_0 = 3 \times 10^8$ m/s. We can therefore equally simulate the antenna using a section of line of length L , with an admittance of $G + jB$ at each extremity (Figure 2.2), or using a section of line of length $L + 2\Delta L$, with a conductance of G at each extremity (Figure 2.3).

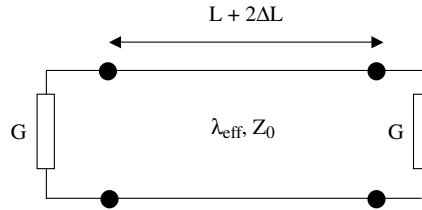


Figure 2.3. Equivalent schematic of a rectangular patch antenna.
End effect simulated by a virtual line extension of ΔL

Generally, the relationship between the conductance G of an antenna, the voltage V applied at its input point, and the power P_i , which is effectively provided to the antenna, is given by:

$$P_i = \frac{1}{2}GV^2 \quad [2.8]$$

In the absence of ohmic losses in the antenna, the whole of the power P_i is radiated ($P_i = P_r$ radiated power). The conductance is then interpreted as the radiation conductance given by:

$$G = \frac{2P_r}{V^2} \quad [2.9]$$

For a printed rectangular antenna, P_r corresponds to the power radiated by the extremity of an open microstrip line. We will refer to [BAL 05] for the details of the calculation based on the knowledge of radiated fields, which leads us to:

$$G = \frac{W}{120\lambda_0} \quad \text{for} \quad \frac{W}{\lambda_0} \gg 1 \quad [2.10]$$

and:

$$G = \frac{1}{90} \left(\frac{W}{\lambda_0} \right)^2 \quad \text{for} \quad \frac{W}{\lambda_0} \ll 1 \quad [2.11]$$

The validity range of these two formulae makes them of little practical use. It is noted that certain publications, such as [BAL 05, COM 97] also take coupling between the radiating edges into account via a mutual conductance G_{12} .

2.2.4. Process for design of a rectangular antenna

We need to determine the width W and length L of the antenna from the operating frequency f_r , along with the permittivity ϵ_r and thickness h of the substrate used. We use the following process:

1. Determination of the width W

The usual value of W is given by:

$$W = \frac{c_0}{2f_r} \sqrt{\frac{2}{\epsilon_r + 1}} \quad [2.12]$$

where f_r is the working frequency of the antenna. The choice of W is linked with the following compromise:

- if W is too high, interfering transverse modes will result (see Chapter 3);
- if W is too low, a printed dipole is obtained, for which an extremely poor radiation conductance does not enable direct feeding with a good match. For example, $G = 0.1$ m/s where $W/\lambda_0 = 1/10$, according to equation [2.12]. The printed dipole presents the characteristics of a high-quality factor resonator.

2. Determination of ΔL and ϵ_{eff} from equations [2.1] and [2.3]

3. Determination of the length L from equation [2.4]

$$L = \frac{\lambda_{\text{eff}}}{2\sqrt{\epsilon_{\text{eff}}}} - 2\Delta L = \frac{\lambda_0}{2\sqrt{\epsilon_{\text{eff}}}} - 2\Delta L \quad [2.13]$$

where:

$$\lambda_0 (\text{in cm}) \approx \frac{30}{f (\text{in GHz})} \quad [2.14]$$

2.2.5. Example

Assuming that $\epsilon_r = 2.2$, $h = 1.524$ mm, and $f_r = 3.0$ GHz, we obtain values $W = 39.53$ mm, $\epsilon_{\text{eff}} = 2.1$, $\Delta L = 0.80$ mm, $L = 32.93$ mm, and $Z_0 = 10 \Omega$. Moreover, we have $G = 1.74$ m/s and $B = 7.27$ m/s, which are essential to the calculation of the input impedance.

2.3. Input impedance

Let us assume a feeding point positioned on the bisecting line at a distance l from one of the radiating edge of width W , at a distance of l . This configuration is illustrated in Figure 2.4 with the associated equivalent circuit.

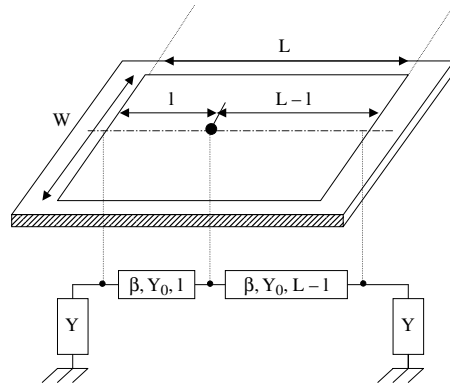


Figure 2.4. Patch powered at the bisecting line at a distance of l from the radiating edge. Equivalent circuit based on the parallel placement of two transmission lines loaded by the admittance of the radiating edges

The total input admittance Y_e is the sum of the admittances $Y(l)$ and $Y(L-l)$, derived at the feeding point for each radiating edge of admittance $Y = G + jB$. The value of Y_e is determined with the help of transmission lines theory:

$$Y_e = Y(l) + Y(L-l) = Y_0 \frac{(G + jB) + jY_0 \operatorname{tg}\beta l}{Y_0 + j(G + jB)\operatorname{tg}\beta l} + Y_0 \frac{(G + jB) + jY_0 \operatorname{tg}\beta(L-l)}{Y_0 + j(G + jB)\operatorname{tg}\beta(L-l)} \quad [2.15]$$

where $Y_0 = 1/Z_0$ is the patch characteristic admittance. We will demonstrate that Y_e is a purely real value, from reasoning based on a Smith chart (Figure 2.5). Note that a revolution of the chart corresponds to a distance $(\lambda_{\text{eff}}/2)$, which is $L + 2\Delta L$ at the patch resonance.

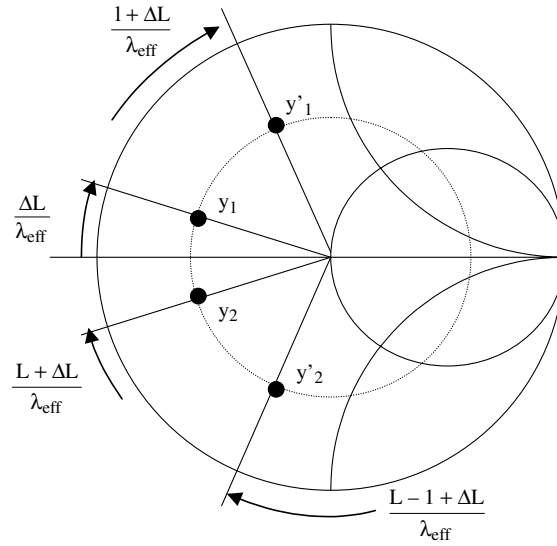


Figure 2.5. Representation of normalized admittances $y = Y/Y_0$ on a Smith chart

First, let us consider the case where the feeding point is at the edge of the patch ($l = 0$). We therefore have $Y_1 = Y(l = 0) = Y = G + jB$. We have seen that jB is the susceptance of a section of the line of length ΔL in open circuit. We can therefore obtain the imaginary part of the derived admittance $y_1 = Y_1/Y_0$ while calculating the normalized length $\Delta L/\lambda_{\text{eff}}$ from the chart, determined from the point of null admittance.

In order to graphically represent the admittance $Y_2 = Y(L)$ derived by the second radiating edge for a resonant patch length $L = (\lambda_{\text{eff}}/2) - 2\Delta L$, it is necessary to:

- start from point y_1 , which is the normalized admittance of a radiating edge;
- rotate a complete revolution in a positive direction, which corresponds to $\lambda_{\text{eff}}/2$;
- rotate a normalized length $2\Delta L/\lambda_{\text{eff}}$ in a negative direction.

We thus arrive at an admittance y_2 , symmetrical to y_1 and relative to the real axis, which is $Y_2 = Y_1^*$. We conclude that $Y_c = Y_1 + Y_2 = 2G$ when the feeding point is at one of the edges of the patch.

When $l \neq 0$, the admittance derived from the first edge $y_1' = Y(l)$ is determined by rotating positively from y_1 by a distance l/λ_{eff} on the chart. Conversely, the admittance derived from the second edge $y_2' = Y(L - l)$ is obtained by rotating negatively from y_2 by a distance l/λ_{eff} . Through symmetry we observe again that

$Y_2' = Y_1'^*$ and that the input admittance $Y_e = Y_1' + Y_2'$ is purely real, whatever the position of the feeding source.

If the power is positioned at the center of the bisecting line ($l = L/2$), a very high admittance Y_e , i.e. a short RF circuit, is obtained. The center of the patch can therefore be loaded at this point (e.g. by a biasing via-hole), without the antenna's characteristics being altered.

We can show [COM 97] that the expression for the input admittance of a resonant antenna eventually reduces to:

$$Y_e = 2G \left[\cos^2 \beta l + \frac{G^2 + B^2}{Y_0^2} \sin^2 \beta l - \frac{B}{Y_0} \sin 2\beta l \right]^{-1} \quad [2.16]$$

We observe that Y_e varies between $Y_e = 2G$ at the edge of the patch and $Y_e = \infty$ at the center. The evolution of the input resistance $R_e = 1/Y_e$ of the patch can be plotted as a function of the position l of the power source on the bisecting line (Figure 2.6).

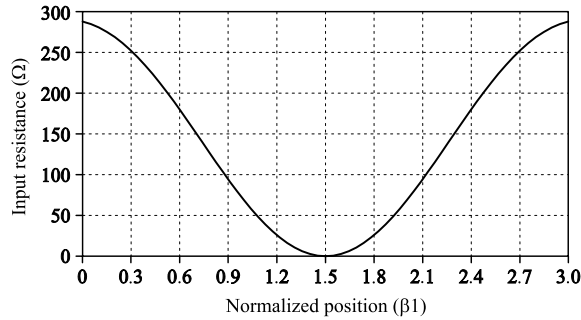


Figure 2.6. Evolution of the input resistance of a rectangular patch as a function of the normalized position βl of the power point on the bisecting line ($\epsilon_{\text{eff}} = 2.1$, $L = 32.93$ mm, $Z_0 = 10 \Omega$, $G = 1.74$ m/s, $B = 7.27$ m/s, $f_r = 3.0$ GHz)

With the admittance being low at the edge of the patch, and where G is typically of the order of 1 m/s, the value $R_e(l=0)$ is high. For the example given above in section 2.2.5, we see that $R_e = 287 \Omega$, when $G = 1.74$ m/s. From this we deduce that there is always a position between the edge of the patch and the center, which enables the antenna to be matched to the source, namely $1/Y_e = 50 \Omega$.

This position is usually around a third of the way along the length. We note that if the length L is not resonant, the input impedance must possess a non-null imaginary part.

If the feeding point is on an edge, it is necessary to add matching circuits that can be large and generate losses. Feeding using a coaxial connector enables easy connection between the inner conductor and the optimal point on the antenna (Figure 2.7). For feeding by microstrip line, the inside of the patch is penetrated with the line by cutting two fine slits, as shown in Figure 2.8 (notched line).

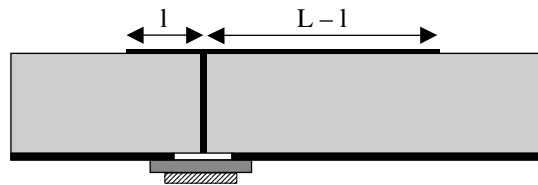


Figure 2.7. Feeding by coaxial connector

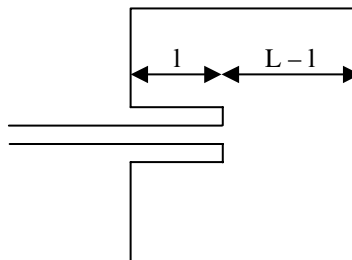


Figure 2.8. Feeding by notched line

Figure 2.9 shows the valid equivalent circuit for two types of excitation when a direct connection is created between the feeding line and the antenna.

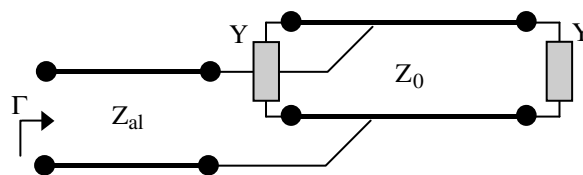


Figure 2.9. Equivalent circuit of a rectangular patch being fed directly.
 Z_{0l} is the characteristic impedance of the feed line

Chapter 3

Cavity Model

3.1. Introduction

The cavity model provides a formalism describing the fields in the antenna and the radiated fields. Contrary to the transmission line model which is limited to a rectangular patch, there is no *a priori* hypothesis regarding the shape of the radiating element. However, a didactic presentation is facilitated by the existence of analytical mode expressions, which can, for example, apply to either rectangular or circular patches. Here we will only examine the rectangular scenario and the reader should refer to existing literature [JAM 89] for other geometries.

The cavity model was developed at the end of the 1970s, at a time when the calculation power of computers did not allow for the possibilities offered by numerical resolution methods to be fully exploited. It is rich in a physical sense and will allow us to explain radiating fields analytically in Chapter 4. We have, however, used a purely numerical method in section 3.5 to trace the various modes of current and to highlight the influence of excitation.

3.2. Formulation of the electromagnetic problem

Let us consider the basic structure in Figure 3.1. The radiating element and the ground plane are assumed to be produced from a perfect metal and can therefore be

seen as electric walls. On the surface of a perfect metal, we know that the tangential component of the electrical field and the normal component of the magnetic field cancel out or according to the conventions in Figure 3.1:

$$\vec{n} \wedge \vec{E} = 0 \quad \text{and} \quad \vec{n} \cdot \vec{H} = 0 \quad [3.1]$$

on the ground plane and the patch, where \vec{n} is the normal outward direction for the two metallic surfaces.

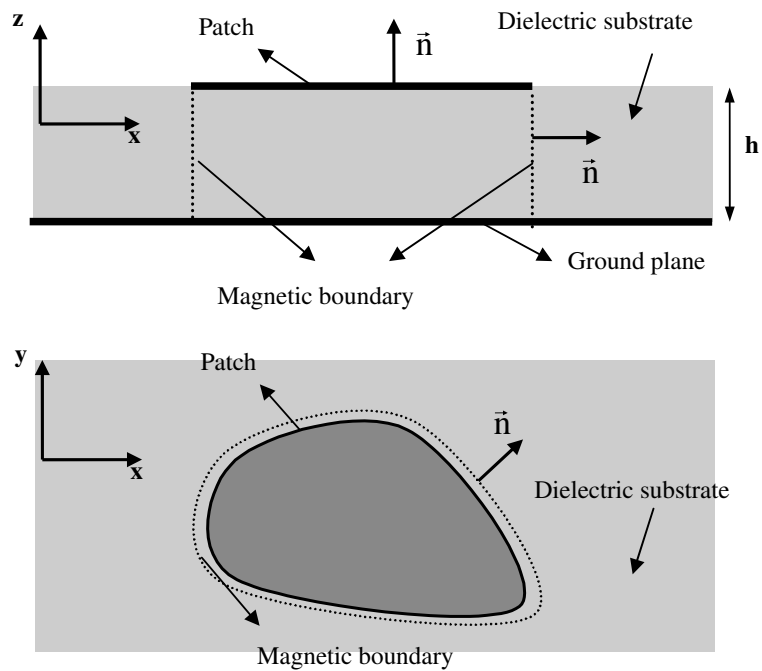


Figure 3.1. Basic structure of a patch with an ordinary geometry (viewed from the side and from above)

In the significant hypothesis where $h \ll \lambda$, the two metallic surfaces are so close to each other that there is insufficient space for either of the tangential components E or of the normal component H to exist. Moreover, the non-null components vary so little in the normal direction that this variation is negligible.

We will therefore include here the following valid simplifications between the patch and the ground plane:

- the electric field only flows in the direction z ;

- the magnetic field only possesses transverse components;
- the fields do not vary in the direction z .

When a conductor presents a rupture, the normal components of the electrical surface current \vec{J} cancel out at the level of this rupture (open circuit). From this we deduce that the tangential magnetic field cancels out along the boundaries of the patch according to the relationship:

$$\vec{n} \wedge \vec{H} = \vec{J}_S = 0 \quad [3.2]$$

This condition defines a perfectly vertical magnetic boundary that links the edges of the patch to the ground plane.

The area situated between the patch and the ground plane can therefore be treated as a quite thin cavity that is restricted by:

- lateral magnetic boundaries;
- electrical boundaries above and below.

However, unlike with purely metallic cavities, the electromagnetic energy is able to escape along the edges of the structure, which will form radiating apertures.

The boundary conditions above will be used to determine the structure of the fields below the patch. One of Maxwell's equations links \vec{E} and \vec{H} by:

$$\vec{\nabla} \wedge \vec{E} = -j\omega\mu\vec{H} \quad [3.3]$$

Since only the normal component E_z is non-null, we say:

$$\vec{E} = E_z \vec{u}_z \quad [3.4]$$

hence:

$$\vec{\nabla} \wedge \vec{E} = -\vec{u}_z \wedge \vec{\nabla} E_z \quad [3.5]$$

$$\vec{H} = \frac{1}{j\omega\mu} \vec{u}_z \wedge \vec{\nabla} E_z \quad [3.6]$$

Understanding the normal component E_z therefore enables us to calculate the other components of the field, with the result also found in the calculation of the TM mode in a metallic waveguide.

Moreover, manipulation of Maxwell's three other equations leads to the propagation equation:

$$\nabla^2 E_z + k^2 E_z = 0 \quad [3.7]$$

where k is the propagation constant of the wave in the medium. The z -variation in E_z , being null, equation [3.7] can be rewritten:

$$\frac{\partial^2 E_z}{\partial x^2} + \frac{\partial^2 E_z}{\partial y^2} + k^2 E_z = 0 \quad [3.8]$$

We can easily see that the general solution to this equation can take the form:

$$E_z(x, y) = A \cos(k_x x) \cos(k_y y) \quad [3.9]$$

where:

$$k_x^2 + k_y^2 = k^2 \quad [3.10]$$

The use of the boundary conditions on the magnetic and electrical walls will enable the analytical resolution of this equation.

The condition on the magnetic boundary is expressed:

$$\vec{n} \wedge \vec{H} = 0 \quad [3.11]$$

where \vec{n} is the outward direction normal to the magnetic wall. Using equation [3.6], we obtain:

$$\vec{n} \wedge (\vec{u}_z \wedge \vec{\nabla} E_z) = 0 \quad [3.12]$$

and then:

$$(\vec{n} \cdot \vec{\nabla} E_z) \vec{u}_z - (\vec{n} \cdot \vec{u}_z) \vec{\nabla} E_z = 0 \quad [3.13]$$

Since vectors \vec{n} and \vec{u}_z are orthogonal, we finally arrive at the relationship:

$$\vec{n} \cdot \vec{\nabla} E_z = \frac{\partial E_z}{\partial n} = 0 \quad [3.14]$$

The normal derivative of E_z to the surface of the magnetic wall is therefore null at the level of this wall.

3.3. Calculation of expressions for fields and currents of a rectangular patch

Let us now consider the rectangular patch shown in Figure 3.2 and apply the boundary conditions in equation [3.14] along each of its edges. Since the edges of the patch are set along axes Ox and Oy, the only angled derivatives $\partial/\partial n$ to be taken into account are $\partial/\partial x$ and $\partial/\partial y$. Therefore, we have:

$$\partial E_z/\partial x = 0 \quad \text{for } x = 0 \text{ and } x = L \quad [3.15]$$

$$\partial E_z/\partial y = 0 \quad \text{for } y = 0 \text{ and } y = W \quad [3.16]$$

and when applying these boundary conditions to equation [3.9], we find an infinite number of solutions (or modes) of the form:

$$E_z^{mn}(x, y) = A_{mn} \cos\left(\frac{m\pi x}{L}\right) \cos\left(\frac{n\pi y}{W}\right) \quad [3.17]$$

where m and n are positive whole numbers. Let us call TM_{mn} the mode corresponding to the pair (m, n) . By analogy with the metallic cavity case where we assume a dependence on z , sometimes we also come across the notation TM_{mn0} with the addition of a null third index. Each mode is characterized by its complex amplitude A_{mn} and a sinusoidal dependence with respect to x and y . We can therefore express the total field as an infinite sum of modes:

$$E_z(x, y) = \sum_{m,n} A_{mn} \cos\left(\frac{m\pi x}{L}\right) \cos\left(\frac{n\pi y}{W}\right) \quad [3.18]$$

The wavenumber for each mode is taken from equation [3.10]:

$$k_{mn} = \sqrt{\left(\frac{m\pi}{L}\right)^2 + \left(\frac{n\pi}{W}\right)^2} \quad [3.19]$$

and the associated resonance frequency is given by:

$$f_{mn} = \frac{k_{mn} c_0}{2\pi\sqrt{\epsilon_r}} \quad [3.20]$$

where ϵ_r is the permittivity of the substrate filling the cavity. Let us now take a look at coefficient A_{mn} . In the situation where the cavity excitation is applied through a vertical distribution of current J_z , [HAR 61] provides us with:

$$A_{mn} = \frac{j\omega\mu_0}{k^2 - k_{mn}^2} \frac{\iint J_z E_z^{mn*} ds}{\iint E_z^{mn} E_z^{mn*} ds} \quad [3.21]$$

An analogous relationship would be obtained for magnetic excitation. We observe that the amplitude of A_{mn} depends on two parameters:

– the level of coupling between the feed and the mode considered via the product $\iint J_z E_z^{m,n*} ds$. An optimal excitation of the mode will be obtained when the product is at its maximum value. Conversely, if the electric or magnetic feed is placed in a null position of the electric or magnetic field of the mode, then this will not be excited;

– the distance between the operating frequency f and the resonance frequency f_{mn} of the relevant mode. In the same way that the current is only intense in the capacitor or the inductance of a tank circuit at circuit resonance, a mode will only be susceptible to strong radiation if the frequency f is close to f_{mn} . This is especially true when the mode is strongly resonant. In practice, this means that the intrinsic gain of the antenna (apart from eventual mismatching) is at its maximum in the vicinity of the resonance of a mode, but when the antenna resonance is weak then this gain is relatively constant over a frequency band of several percent.

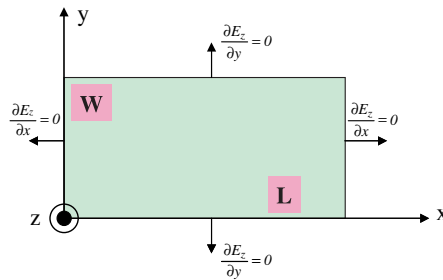


Figure 3.2. Boundary conditions for a rectangular patch

We note now two important points:

1. Every physical source (that is to say, anything with non-infinitesimal dimensions) might excite multiple modes, since the result of the surface integral can hardly be null at every point. The non-null values of A_{mn} correspond to unwanted

modes that are excited. Unwanted modes generate cross-polarization, alter the co-polarization radiation pattern, and modify the input impedance of the antenna.

In general, these unwanted modes are only very poorly stimulated (small A_{mn}) due to the distances between resonance frequencies and because the feeding point might not be properly located.

We will see that there are cases where two modes can be simultaneously excited, for example:

– TM_{10} and TM_{01} where the feeding point is shifted by comparison with the bisectors and $W = L$;

– TM_{10} and TM_{02} with feeding point on the bisector and $W = 2L$.

2. The denominator $k^2 - k_{mn}^2$ cannot be cancelled out and A_{mn} cannot diverge. Indeed, losses in the substrate and on the conductors, as well as radiation losses, lead in practice to a complex value of k .

We can easily deduce the transverse components of the magnetic field H beneath the cavity, and of the surface current J on the patch from equations [3.17], [3.2], and [3.6]:

$$H_x^{m,n}(x, y) = \frac{A_{mn}}{j\omega\mu} \frac{n\pi}{W} \cos\left(\frac{m\pi x}{L}\right) \sin\left(\frac{n\pi y}{W}\right) \quad [3.22]$$

$$H_y^{m,n}(x, y) = -\frac{A_{mn}}{j\omega\mu} \frac{m\pi}{L} \sin\left(\frac{m\pi x}{L}\right) \cos\left(\frac{n\pi y}{W}\right) \quad [3.23]$$

$$J_x^{m,n}(x, y) = -\frac{A_{mn}}{j\omega\mu} \frac{m\pi}{L} \sin\left(\frac{m\pi x}{L}\right) \cos\left(\frac{n\pi y}{W}\right) \quad [3.24]$$

$$J_y^{m,n}(x, y) = \frac{A_{mn}}{j\omega\mu} \frac{n\pi}{W} \cos\left(\frac{m\pi x}{L}\right) \sin\left(\frac{n\pi y}{W}\right) \quad [3.25]$$

3.4. Expressions for principal modes

In this section we take a number of integer pairs (m, n) utilized in practice and then trace the corresponding modes.

As an introduction, we note the specific case where $m = n = 0$, which forms the electrostatic limit at which the antenna is equivalent to the capacitor formed when the patch and the ground plane are placed opposite each other.

We will consider modes TM_{01} , TM_{10} , TM_{11} , and TM_{20} for which expressions of the currents and fields are given in Tables 3.1 and 3.2.

Mode	m=1, n=0	m=0, n=1
E-field	$E_z^{1,0} = A_{10} \cos\left(\frac{\pi x}{L}\right)$	$E_z^{0,1} = A_{01} \cos\left(\frac{\pi y}{W}\right)$
H-field	$H_x^{1,0} = 0 \quad H_y^{1,0} = -\frac{A_{10}}{j\omega\mu} \frac{\pi}{L} \sin\left(\frac{\pi x}{L}\right)$	$H_x^{0,1} = \frac{A_{01}}{j\omega\mu} \frac{\pi}{W} \sin\left(\frac{\pi y}{W}\right) \quad H_y^{0,1} = 0$
Current	$J_x^{1,0} = \frac{A_{10}}{j\omega\mu} \frac{\pi}{L} \sin\left(\frac{\pi x}{L}\right) \quad J_y^{1,0} = 0$	$J_x^{0,1} = 0 \quad J_y^{0,1} = -\frac{A_{01}}{j\omega\mu} \frac{\pi}{W} \sin\left(\frac{\pi y}{W}\right)$
Resonant frequency	$f_{1,0} = \left(\frac{c_0}{2L\sqrt{\epsilon_r}}\right)$	$f_{0,1} = \left(\frac{c_0}{2W\sqrt{\epsilon_r}}\right)$

Table 3.1. Expressions for fields, currents, and resonance frequencies for TM_{10} and TM_{01} modes

Mode	m=1, n=1	m=2, n=0
E-field	$E_z^{1,1} = A_{11} \cos\left(\frac{\pi x}{L}\right) \sin\left(\frac{\pi y}{W}\right)$	$E_z^{2,0} = A_{20} \cos\left(\frac{2\pi x}{L}\right)$
H-field	$H_x^{1,1} = \frac{A_{11}}{j\omega\mu} \frac{\pi}{L} \cos\left(\frac{\pi x}{L}\right) \sin\left(\frac{\pi y}{W}\right)$ $H_y^{1,1} = -\frac{A_{11}}{j\omega\mu} \frac{\pi}{L} \sin\left(\frac{\pi x}{L}\right) \cos\left(\frac{\pi y}{W}\right)$	$H_x^{2,0} = 0$ $H_y^{2,0} = -\frac{A_{20}}{j\omega\mu} \frac{2\pi}{L} \sin\left(\frac{2\pi x}{L}\right)$
Current	$J_x^{1,1} = \frac{A_{11}}{j\omega\mu} \frac{\pi}{L} \sin\left(\frac{\pi x}{L}\right) \cos\left(\frac{\pi y}{W}\right)$ $J_y^{1,1} = \frac{A_{11}}{j\omega\mu} \frac{\pi}{L} \cos\left(\frac{\pi x}{L}\right) \sin\left(\frac{\pi y}{W}\right)$	$J_x^{2,0} = \frac{A_{20}}{j\omega\mu} \frac{2\pi}{L} \sin\left(\frac{2\pi x}{L}\right)$ $J_y^{2,0} = 0$
Resonant frequency	$f_{1,1} = \frac{\sqrt{\left(\frac{\pi}{L}\right)^2 + \left(\frac{\pi}{W}\right)^2} c_0}{2\pi\sqrt{\epsilon_r}}$	$f_{2,0} = \frac{c_0}{L\sqrt{\epsilon_r}}$

Table 3.2. Expressions for fields, currents, and resonance frequencies for TM_{11} and TM_{20} modes

The distribution of the electric field in radiating apertures is shown in Figure 3.3.

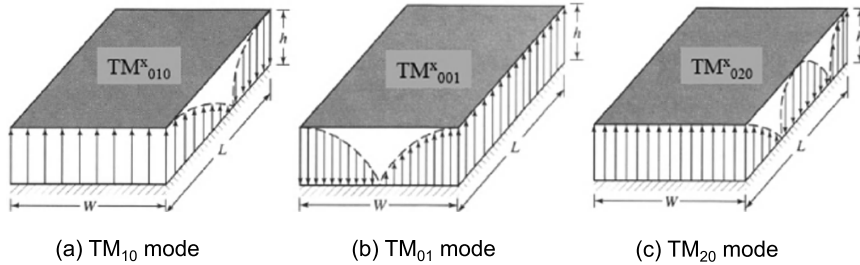


Figure 3.3. Distribution of electrical field over radiating apertures for TM_{10} , TM_{01} , and TM_{20} modes

3.5. Cartography of modal currents and associated radiation patterns

In the example, taken from [CHE 06], a rectangular patch ($L = 76$ mm, $W = 50$ mm, $h = 1.524$ mm, $\epsilon_r = 3.38$) is powered by a coaxial probe. The central core of the connector is soldered to the patch at $D_x = 29$ mm, $D_y = 15$ mm from the bottom left corner.

This position enables the four primary modes TM_{10} (1.075 GHz), TM_{01} (1.605 GHz), TM_{11} (1.955 GHz), and TM_{20} (2.145 GHz) to be excited with a correct matching (Figure 3.4).

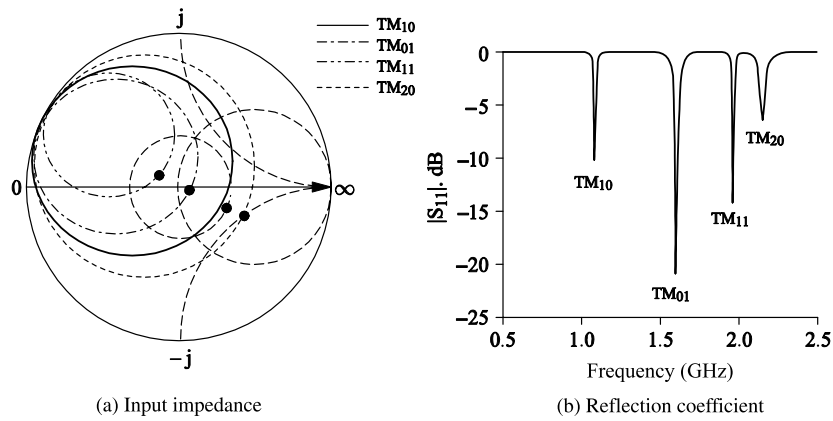


Figure 3.4. Input impedance and reflection coefficient S_{11}

The distributions of electric surface current and the radiation patterns are given for each of the four modes at the resonant frequency in Figures 3.5, 3.6, 3.7 and 3.8. We simultaneously trace the real (in phase with the source) and imaginary (in phase

quadrature) parts of the surface current in parts (a) and (b) of the figure respectively. The radiation patterns are given for both the xOz and yOz planes in parts (c) and (d) respectively.

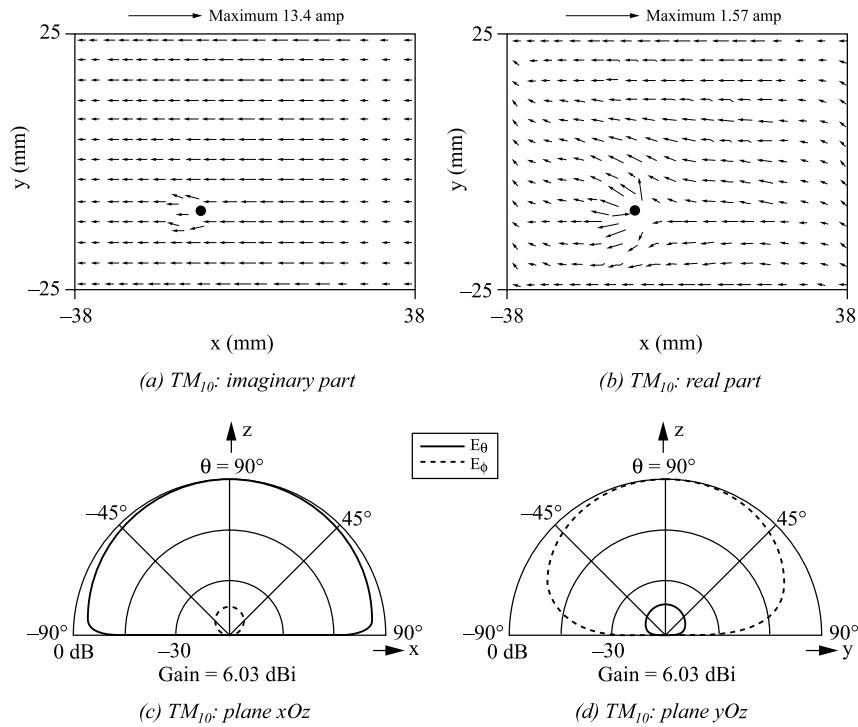


Figure 3.5. Distribution of current and radiation patterns for mode TM_{10}

On the one hand, we observe that the imaginary part is hardly affected by the probe feed, whereas the real part is locally disturbed around the feeding point.

On the other hand, the amplitude of the imaginary part is always far higher than that of the real part. This result is consistent with the purely imaginary nature of the current found in the ideal theoretical cavity model (see equations [3.24] and [3.25]).

Radiation patterns are shown in planes xOz and yOz. The power gain G_p in dB indicated for each cutting plane (P) is calculated using the following formula:

$$G_p = \frac{|E_{pmax}|^2 / 377}{P_i / 4\pi r^2} \quad [3.26]$$

where P_i is the power provided to the antenna, r is the distance over which the field is calculated, and E_{pmax} is the maximum field calculated in the plane under consideration.

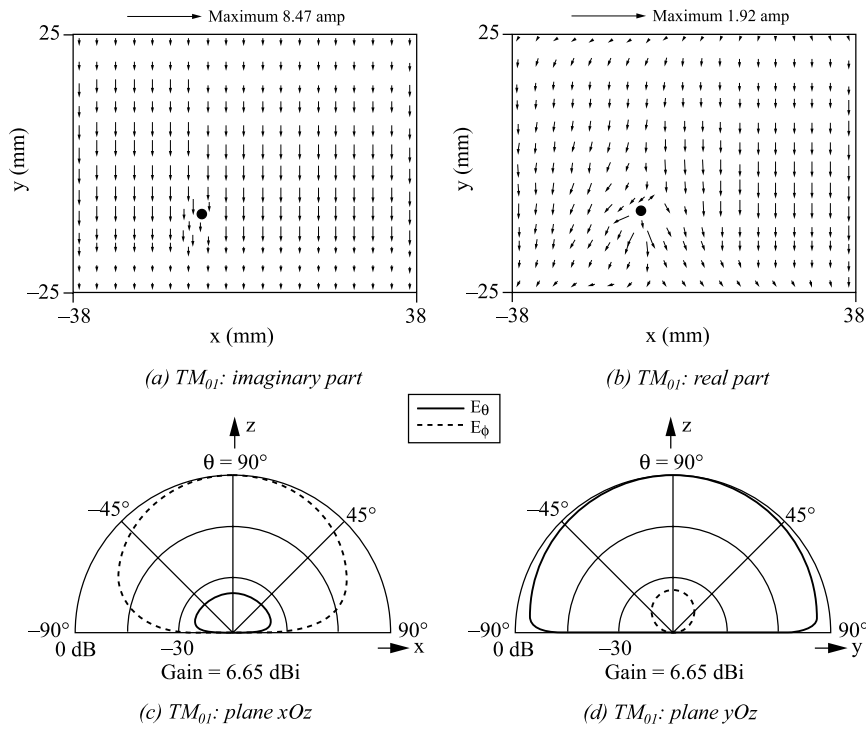


Figure 3.6. Distribution of current and radiation patterns for mode TM_{01}

Radiation patterns will be examined in more detail, based on the notion of radiating aperture, in Chapter 4.

We can, however, already make the following general statements:

- the radiating electrical field is oriented in the direction of the surface current;
- for mode TM_{10} : E_θ is the main component in plane xOz , with E_ϕ constituting the cross-polar component below -30 dB in all directions. Conversely, E_ϕ is the main component in plane yOz , with E_θ constituting the cross-polar component below -30 dB in all directions;
- for mode TM_{01} : E_θ is the main component in plane yOz , with E_ϕ constituting the cross-polar component below -30 dB in all directions. Conversely, E_ϕ is the

main component in plane xOz , with E_ϕ constituting the cross-polar component below -30 dB in all directions;

- for mode TM_{11} : we observe a radiation hollow in the axis, a maximum at 40° in plane xOz and a relative maximum at 42° in plane yOz . The cross-polar components are high in the two planes (about -10 dB in plane yOz);

- for mode TM_{20} , as a consequence of the antisymmetry of the currents relative to plane yOz , we observe a radiation hollow in the axis and a quasi-nullity of the field in plane yOz (gain = -20 dBi). The maximum radiation in plane xOz appears to be 62.5° .

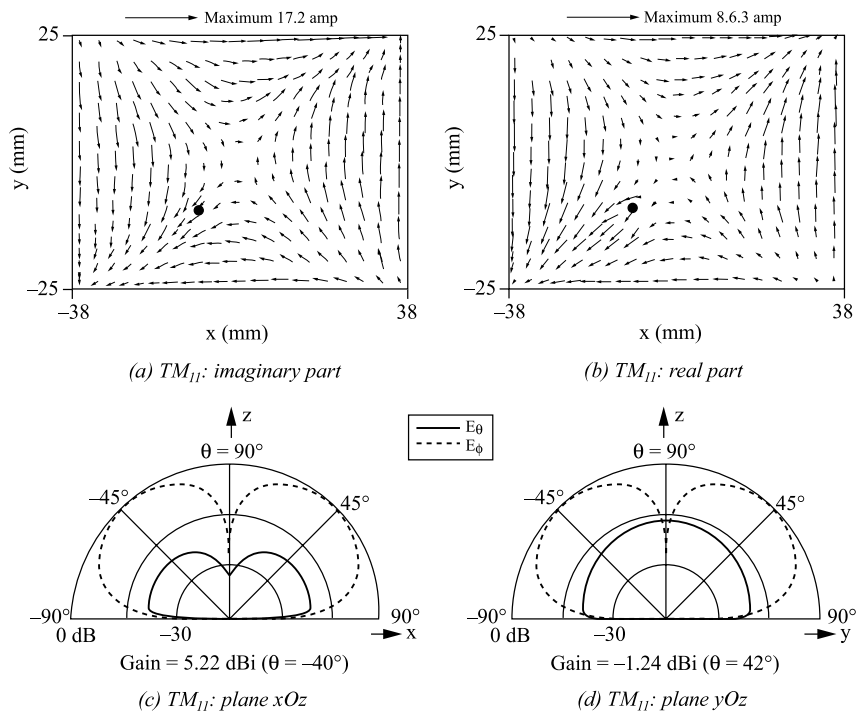


Figure 3.7. Distribution of current and radiation patterns for mode TM_{11}

Distributions of current and radiation patterns have been obtained using a numerical method, based on the resolution of integral equations using the method of moments.

Integral equations are derived from the cancellation condition of the tangential electric field over the metallic sections of the antenna, this electrical field being the

superposition of a known excitation field and a field created by distributions of electrical surface current over the metallic sections.

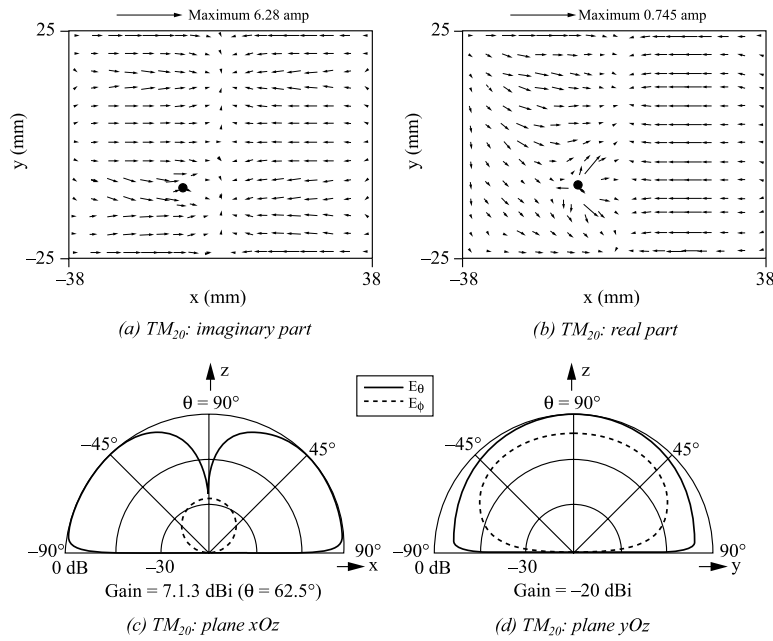


Figure 3.8. Distribution of current and radiation patterns for mode TM_{20}

The electrical current and the field that it creates are linked by Green’s functions, the analytical expression for which depends notably on the geometry and permittivity of the dielectric media.

In the method of moments, the current is broken down into N basic functions, which are spatially restricted to cells forming a mesh, which is, for instance, rectangular in [MOS 89]. This mesh can be observed in the vector representation of the current in Figures 3.5–3.8. The weighting of the basic functions, i.e. the amplitude and direction of the different vector currents, are the N unknowns of the problem.

They are obtained by transforming the integral equation into a system of N linear equations. These result from the calculation of the interaction between the basic functions and N so-called test functions [MOS 89], with the weightings being finally obtained by inversion of the system.

Chapter 4

Radiation of a Printed Antenna

4.1. Introduction

Our analysis of the radiation of a rectangular patch antenna will be based on the cavity model from Chapter 3. Using two equivalent radiating apertures, we will derive expressions for the radiated field and directivity. A parametric study of the influence of various characteristics (substrate height and permittivity, antenna width, and truncation of the ground plane) will also take place.

The equivalent sources of the problem are the virtual magnetic currents which result from Huygens' principle, with the associated concept of a radiating aperture. This approach is similar to that of the horn antennas, where knowing the electric field (or equivalent magnetic current) distribution in the aperture enables the radiation to be determined more easily than as a result of the distribution of the electric current on the metallic sides.

Note that the real sources are the electric currents and charges present in the metallic parts of the antenna. They constitute the unknown factors to be determined for a number of commercial software applications used in planar antenna design (such as IE3D or Ansoft Designer). This explains why nowadays engineers gain their understanding of the workings of an antenna from electrical current

cartographies rather than 3D electrical field distributions, i.e. from magnetic currents.

However, the physical approach to radiation through the radiating aperture concept is often more pertinent than that of the distribution of electrical sources which make up the patch. Indeed, the ground plane close to the patch fundamentally constitutes an electrical short circuit which, according to image theory, is little suited to the radiation of horizontal electrical currents. This obstacle is overcome by using the radiating aperture concept.

4.2. Modelization using two equivalent radiating slots

According to Huygens' principle, any closed surface which contains electromagnetic sources can be used in order to calculate the field that they radiate. The key is to determine the tangential E and H fields on this surface, or else the equivalent magnetic M and electrical J surface currents, which create the same radiated field as the sources. These fields or currents must satisfy the boundary conditions on the surface and become new sources of radiation, also called secondary sources. A judicious choice of surface can considerably simplify the calculation of the radiated field from secondary sources. In case of the rectangular patch antenna, the closed cavity formed from the lateral magnetic walls, the surface of the patch and the surface next to the ground plane will form the Huygens surface.

Let us apply image theory to replace the patch and the supposedly infinite ground plane with the patch and its image (Figure 4.1). On the one hand, the electrical surface current of the patch and the image of this current are running in opposite directions. On the other hand, the gap between these two currents is very small compared with the wavelength, as $h \ll \lambda$. The radiation of the two currents will therefore tend to cancel out, which justifies not taking the upper metallic surface of the cavity into account in the calculations. Note that this reasoning implicitly links the contributions of the currents which exist on the ground plane. In other words, the lower metallic surface of the equivalent cavity is also ignored in the calculation of the radiated field.

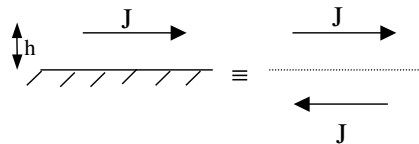


Figure 4.1. Image theory applied to horizontal electrical currents

In order to determine the E field on the vertical lateral surfaces, we will base our reasoning on the TM_{10} mode, the distribution for which is shown again in Figure 4.2. Along the so-called radiating edges with a width W , only the vertical component of the electrical field exists, uniformly distributed over the surface. Since the edges are a half guided wavelength apart, fields E_1 and E_2 on each aperture are of the same amplitude and in phase opposition. On the edges with a length L , which are said to be non-radiating, we observe a phase reversal of the purely vertical electrical field at the center of the surface.

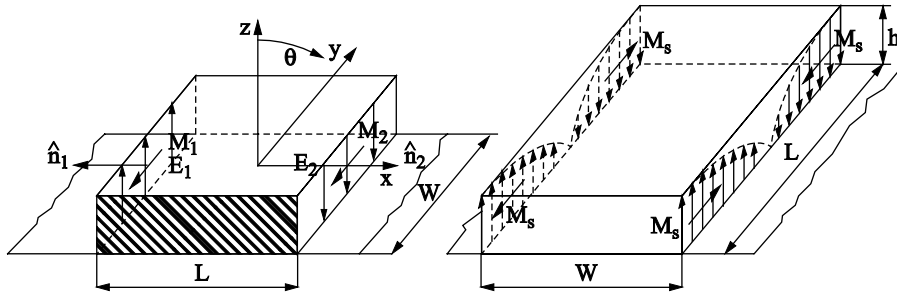


Figure 4.2. Distribution of magnetic current on radiating and non-radiating slots for the TM_{10} mode

The surfaces of the radiating edges can be seen as radiating apertures (or slots) and can be replaced by an equivalent distribution of surface current. This current does not contain any electrical component \vec{J}_S , the H field tangential component being null on the apertures. Let \vec{n}_1 and \vec{n}_2 be the normals to the apertures oriented toward the exterior of the cavity (Figure 4.2). The surface distributions of magnetic current \vec{M}_S over the two apertures are given by:

$$\vec{M}_{S1}(V/m) = -\vec{n}_1 \wedge \vec{E}_1 = -(-\vec{u}_x) \wedge E_0 \vec{u}_z = -E_0 \vec{u}_y \quad [4.1]$$

$$\vec{M}_{S2}(V/m) = -\vec{n}_2 \wedge \vec{E}_2 = -\vec{u}_x \wedge E_0 (-\vec{u}_z) = -E_0 \vec{u}_y \quad [4.2]$$

With the normals and fields being in opposite directions in each aperture, the magnetic currents M_{S1} and M_{S2} are oriented in the same direction. As $h \ll \lambda$ and E is constant over the aperture, we can assimilate the surface current M_S to a linear current M in each aperture, the intensity for which is given by:

$$\vec{M}(V) = \vec{M}_S \cdot h = -E_0 \cdot h \vec{u}_y = -V_0 \vec{u}_y \quad [4.3]$$

Applying the image principle, the ground plane is replaced by the image of the magnetic current, which is oriented in the same direction as the real current (Figure 4.3). Under the hypothesis $h \ll \lambda$, we can therefore combine the equivalent magnetic source of an aperture and its image into one single source of intensity $2V_0$.

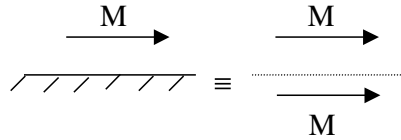


Figure 4.3. Image theory applied to horizontal magnetic currents

The linear currents in each aperture, M_1 and M_2 , are finally given by:

$$\vec{M}_1(V) = \vec{M}_2(V) = -2V_0 \vec{u}_y \quad [4.4]$$

It is convenient to replace these linear magnetic currents \vec{M}_1 and \vec{M}_2 with horizontal radiating apertures of the same dimensions as the vertical apertures described in Figure 4.4. Once again, this is only valid when $h \ll \lambda$ (in practice, $h < \lambda/50$).

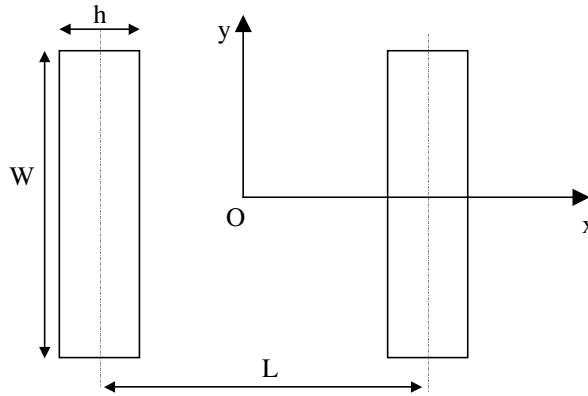


Figure 4.4. Modelization using two horizontal radiating slots

The idea is then to utilize the theory of radiating apertures in order to calculate the components of the field radiated by a slot, and then to combine the radiation of the two slots in order to obtain the radiation of the patch.

The same reasoning enables us to trace the linear magnetic currents over the non-radiating edges of the patch (Figure 4.2). We observe an inversion of the direction of magnetic current at each edge, as well as a phase opposition between the currents of opposing edges. These currents therefore lead to null radiation in the principal planes xOz and yOz .

Conversely, there is non-null radiation away from the axis in the other planes; however, the density of this is much weaker than that of the radiating edges.

In conclusion, it is possible to determine the field radiated by the rectangular patch by combining the radiation of two equivalent radiating slots which are positioned along the two edges with width W .

4.3. Calculation of the field radiated by a horizontal radiating slot

The field radiated by an aperture of length W and width h , in which a uniform field $\vec{E} = E_0 \vec{u}_x$ exists, is given by [BAL 05, CAR 81]:

$$E_\theta = -jk_0 V_0 W \frac{e^{-jk_0 r}}{2\pi r} \frac{\sin(k_0 W \sin \theta \sin \phi / 2)}{k_0 W \sin \theta \sin \phi / 2} \cos(k_0 h \cos \theta) \cos \phi \quad [4.5]$$

$$E_\phi = jk_0 V_0 W \frac{e^{-jk_0 r}}{2\pi r} \frac{\sin(k_0 W \sin \theta \sin \phi / 2)}{k_0 W \sin \theta \sin \phi / 2} \cos(k_0 h \cos \theta) \cos \theta \sin \phi \quad [4.6]$$

$$H_\theta = -E_\phi / \eta \quad [4.7]$$

$$H_\phi = +E_\theta / \eta \quad [4.8]$$

$$H_r = E_r = 0 \quad [4.9]$$

We note that when $h \ll \lambda$, then:

$$E_\theta \approx -jk_0 V_0 W \frac{e^{-jk_0 r}}{2\pi r} \frac{\sin(k_0 W \sin \theta \sin \phi / 2)}{k_0 W \sin \theta \sin \phi / 2} \cos \phi \quad [4.10]$$

$$E_\phi \approx jk_0 V_0 W \frac{e^{-jk_0 r}}{2\pi r} \frac{\sin(k_0 W \sin \theta \sin \phi / 2)}{k_0 W \sin \theta \sin \phi / 2} \cos \theta \sin \phi \quad [4.11]$$

4.4. Calculation of the field radiated by the rectangular patch

Let us now consider the mini-array comprising two slots, a distance of L apart, aligned along axis Ox , and let us take the center of the patch as the origin. Under these conditions, we know that the array factor AF of the two elements which are a distance of L apart is given by:

$$AF = 2 \cos(k_0 L \sin \theta \cos \phi / 2) \quad [4.12]$$

Using array theory, the total field is calculated by multiplying the field of an elementary source of the array by AF . The field radiated by the two equivalent slots is therefore given by:

$$E_\theta = -jk_0 V_0 W \frac{e^{-jk_0 r}}{\pi r} \frac{\sin(k_0 W \sin \theta \sin \phi / 2)}{k_0 W \sin \theta \sin \phi / 2} \cos(k_0 L \sin \theta \cos \phi / 2) \cos \phi \quad [4.13]$$

$$E_\phi = jk_0 V_0 W \frac{e^{-jk_0 r}}{\pi r} \frac{\sin(k_0 W \sin \theta \sin \phi / 2)}{k_0 W \sin \theta \sin \phi / 2} \cos(k_0 L \sin \theta \cos \phi / 2) \cos \theta \sin \phi \quad [4.14]$$

4.5. Determination of the radiation pattern in the principal planes

E-plane: $\phi = 0^\circ$

This plane is called the E-plane as it oriented the same way as the electrical field in the equivalent apertures. Setting $\phi = 0^\circ$ in expressions [4.13] and [4.14], we obtain:

$$E_\theta = -jk_0 V_0 W \frac{e^{-jk_0 r}}{\pi r} \cos(k_0 L \sin \theta / 2) \quad [4.15]$$

$$E_\phi = 0 \quad [4.16]$$

The radiation pattern depends solely on L . For the first resonance, omitting the virtual extensions ΔL , we have:

$$L \approx \frac{\lambda_0}{2\sqrt{\epsilon_{\text{eff}}}} \quad [4.17]$$

from which:

$$k_0 L \approx \frac{\pi}{\sqrt{\epsilon_{\text{eff}}}} \quad [4.18]$$

and:

$$E_\theta = -jk_0 V_0 W \frac{e^{-jk_0 r}}{\pi r} \cos\left(\frac{\pi \sin \theta}{2\sqrt{\epsilon_{\text{eff}}}}\right) \quad [4.19]$$

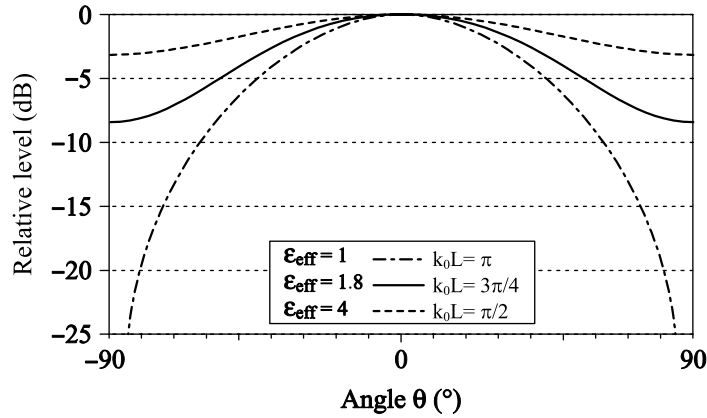


Figure 4.5. Influence of the effective permittivity on the E-plane radiation pattern
 E (--- $\epsilon_{\text{eff}} = 1$; $\epsilon_{\text{eff}} = 1.8$; — $\epsilon_{\text{eff}} = 4$)

In Figure 4.5, we vary the value of ϵ_{eff} between 1 and 4. We see a radiation pattern which widens with increases in ϵ_{eff} and which does not cancel out for low grazing angles. The distance between the radiating slots is reduced at higher levels of permittivity and the array effect is less pronounced.

For higher levels of permittivity, the radiation pattern moves closer to that of a unique slot, i.e. it is uniform in the E-plane.

H-plane: $\phi = 90^\circ$

This plane is orthogonal to the E-plane. Expressions [4.13] and [4.14] reduce to:

$$E_\theta = 0 \quad [4.20]$$

$$E_{\phi} = jk_0 V_0 W \frac{e^{-jk_0 r}}{\pi r} \frac{\sin(k_0 W \sin \theta / 2)}{k_0 W \sin \theta / 2} \cos \theta \quad [4.21]$$

The radiation pattern depends on W throughout the function $\sin X/X$. This dependency results in a widening of the H-plane radiation pattern for reduced values of W (Figure 4.6), which is consistent with radiating aperture theory.

We note that the H-plane radiation pattern is always narrower than the E-plane pattern and that the field cancels out for angles close to horizontal. In the particular instance where the permittivity is close to that of air, the aperture is roughly the same in both planes.

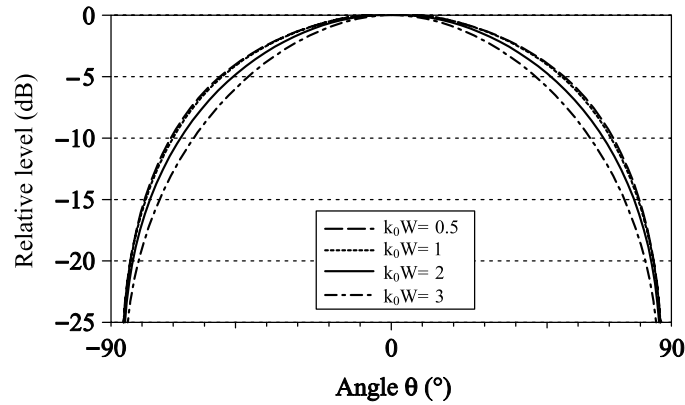


Figure 4.6. Influence of the width W on the H-plane radiation pattern

4.6. Influence of height

Initially, we ignored the influence of h on the radiation pattern in the hypothesis where $h \ll \lambda$, since the product:

$$K = \cos(k_0 h \cos \theta) \quad [4.22]$$

which is common to equations [4.5] and [4.6], tends toward 1.

We note that K is a function which, for a given value of h , increases with θ between $\cos(k_0 h)$ and 1, the value of $\cos(k_0 h)$ reducing in the same proportion as h increases. In other words, the radiation pattern will become narrower as h increases, so long as h remains small enough for approximations to remain valid.

Physically, this increase in h corresponds to field lines which are more open at the extremities, wider equivalent apertures and therefore to a narrower radiation pattern based on aperture theory.

4.7. Influence of the ground plane

In practice, the ground plane and the substrate are necessarily truncated. The finite nature of the lateral dimensions results in a diffraction of the space and surface waves over the ridges of the ground plane. This diffraction leads to parasitic radiation toward the front and back of the antenna.

The front-to-back radiation ratio is typically less than -20 dB for dimensions of the ground plane greater than two wavelengths and for a centered patch. The parasitic radiation toward the front of the antenna generates ripples in the principal radiation pattern (Figure 4.7).

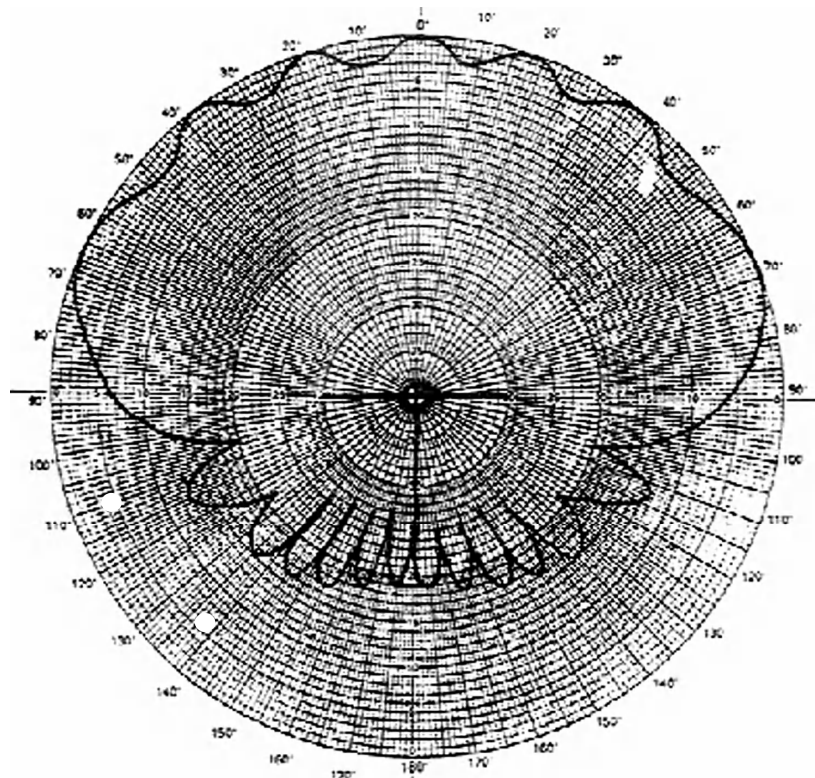


Figure 4.7. Influence of the ground plane on the E-plane radiation

4.8. Polarization

A rectangular patch antenna which is excited along bisector Ox presents a linear polarization of the radiated electrical field. Indeed, we observe in equations [4.13] and [4.14] that field components E_θ and E_ϕ are in phase opposition, which is sufficient to produce a purely linear polarization in all directions. The Cartesian coordinates are easily deduced from equations [4.13] and [4.14]:

$$E_x = -jk_0 V_0 W \frac{e^{-jk_0 r}}{\pi r} \frac{\sin(k_0 W \sin \theta \sin \phi / 2)}{k_0 W \sin \theta \sin \phi / 2} \cos(k_0 L \sin \theta \cos \phi / 2) \cos \theta \quad [4.23]$$

$$E_y = 0 \quad [4.24]$$

$$E_z = jk_0 V_0 W \frac{e^{-jk_0 r}}{\pi r} \frac{\sin(k_0 W \sin \theta \sin \phi / 2)}{k_0 W \sin \theta \sin \phi / 2} \cos(k_0 L \sin \theta \cos \phi / 2) \sin \theta \cos \phi \quad [4.25]$$

Note that component E_y is not present when TM_{10} is the only excited mode. Component E_z cancels out in the H-plane ($\phi = 90^\circ$) and at the antenna axis ($\theta = 0^\circ$). \vec{E} is therefore parallel to the field in the radiating apertures for the maximum direction of radiation.

The purity of polarization depends on the amount of power transmitted in the unwanted cross-polarization E_y . The level of purity is characterized by the cross-polarization ratio τ_p :

$$\tau_p = 20 \log(E_y/E_x) \quad [4.26]$$

The presence of cross-polarization will lead to a mismatch in the polarization between the transmitting and receiving antennas to the detriment of the link budget, but this is not the main consequence.

Let us consider an RF link where the channels are spread between two orthogonal linear polarizations (which are typically called V and H) for a common frequency band.

The diplexing (or filtering) between two orthogonal channels centered over the same frequency depends on the quality of the purity of polarization; the cross-polarization for the V channel constitutes an interference signal for the H channel, and vice versa.

Ratios less than -40 dB are generally required, which are difficult levels for patch antennas to meet, even if setting them into an array improves the purity of polarization of the simple element.

Cross-polarization can result:

- from the contribution of the non-radiating apertures. We have seen that this contribution is weak, notably at the axis of the TM_{10} mode;

- from the excitation of modes which are either orthogonal (TM_{01} and TM_{02}) or which possess an orthogonal component (TM_{11}). This excitation occurs under certain conditions:

- *excitation of the TM_{01} mode*: in order to excite this mode, the feed must be off-center relative to the bisector Ox . The cross-polarization then increases in proportion to the proximity of the matching point of the TM_{01} mode on the bisector Oy and when the resonant frequencies of the TM_{10} and TM_{01} modes are close. In case of limited excitation over the diagonal and of a square patch, the two modes are excited with the same intensity and $\tau_p = 0$ dB,

- *excitation of the TM_{02} mode*: since the maximum of the TM_{02} mode is on the bisector Ox , it can be excited at the same time as the TM_{10} mode, if the resonant frequencies of the two modes are close. This is only possible when the width W is close to double the length L ,

- *from the influence of a feed circuit*: the feed circuit possesses a parasitic radiation which contributes to cross-polarization. It also locally modifies the fields in the antenna. The resulting interference can be modeled by a superposition of higher modes, with each contributing to the cross-polarization according to its weighting.

4.9. Directivity

The directivity D of an antenna radiating a total power P_r , for a given distance r , is expressed as the ratio between:

- the surface density of power radiated by the antenna in the same direction as its maximum radiation:

$$\frac{dP_{\max}}{dS} = \frac{|E_{\max}|^2}{2\eta_0} \quad [4.27]$$

- the surface density of power radiated by an isotropic antenna radiating the same total power P_r as the considered antenna:

$$\frac{dP_{\text{iso}}}{dS} = \frac{P_r}{4\pi r^2} \quad [4.28]$$

and finally:

$$D = \frac{dP_{\text{max}} / dS}{dP_{\text{iso}} / dS} = \frac{2\pi r^2 |E_{\text{max}}|^2}{\eta_0 P_r} = \frac{r^2 |E_{\text{max}}|^2}{60 P_r} \quad [4.29]$$

According to equations [4.15] and [4.16], it appears that the maximum amplitude of the field obtained for $\theta = 0$ is:

$$|E_{\text{max}}| = \frac{k_0 V_0 W}{\pi r} = \frac{2V_0 W}{\lambda_0 r} \quad [4.30]$$

The power radiated by a slot with conductance G is $GV_0^2/2$. In order to determine the total power radiated by the printed antenna P_r , we need to add together the power radiated by each of the two equivalent slots:

$$P_r = 2 \frac{GV_0^2}{2} = GV_0^2 \quad [4.31]$$

and, by using [2.10] and [2.11], we conclude that:

$$D = \frac{r^2 \left(\frac{2V_0 W}{\lambda_0 r} \right)^2}{60 \frac{W}{120\lambda_0} V_0^2} = 8 \left(\frac{W}{\lambda_0} \right) \quad \text{for} \quad \frac{W}{\lambda_0} \gg 1 \quad [4.32]$$

and:

$$D = \frac{r^2 \left(\frac{2V_0 W}{\lambda_0 r} \right)^2}{60 \frac{1}{90} \left(\frac{W}{\lambda_0} \right)^2 V_0^2} = 4 \quad \text{for} \quad \frac{W}{\lambda_0} \ll 1 \quad [4.33]$$

i.e. D (dB) = 6 dB. The formulae are valid under the hypothesis where the mutual conductance G_{12} between radiating slots is negligible compared with G . If this is not the case, then the directivity can be re-written as:

$$D' = \frac{D}{1 + \frac{G_{12}}{G}} \quad [4.34]$$

However, the approximations necessary for the analytical determination of the conductance G of the slot ($W \ll \lambda_0$ or $W \gg \lambda_0$) limit the usefulness of formulae [4.32] and [4.33].

Figure 4.8 shows the theoretical results highlighting the influence of substrate thickness for several values of relative permittivity. With the effective area of the antenna increasing when its electrical volume increases, the directivity is much higher when the thickness is significant and the permittivity is weaker.

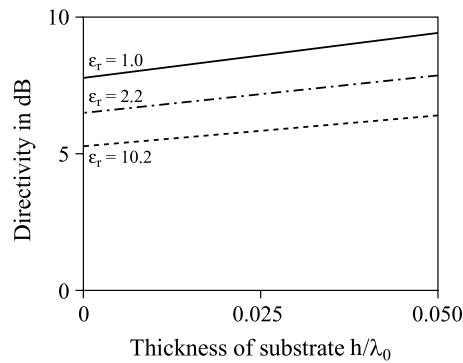


Figure 4.8. Influence of substrate thickness on directivity

4.10. Influence of the substrate on resonant frequency: parametric study based on antenna RCS

The objective is to analyze the influence of the substrate on variations in resonant frequency of a printed antenna. This study is carried out by calculating the equivalent radar area of the antenna. The RCS (Radar Cross Section), which is expressed in m^2 , characterizes the capacity of the target to reflect electromagnetic energy toward the transmitter which illuminates it. It is the expression of a relationship between the re-emitted energy and the density of energy received per unit area.

Since the RCS of a printed antenna is at its maximum when the antenna functions at its resonant frequency f_r , we can determine the value of f_r with commercial software using the following steps:

- for a given substrate thickness and dielectric constant, illumination of the antenna by a plane wave at normal incidence, the component of incident field E corresponds to the polarization of the antenna;
- determination of the field reflected by the antenna in the normal direction;
- calculation of the ratio of the reflected field over the incident field;
- analysis in a frequential band and determination of the frequency at which the RCS is at its maximum.

This method has a double relevance:

- when the thickness of the antenna increases and the resonances are less pronounced, the equivalent RLC model becomes less pertinent and the definition of the resonance is no longer clearly linked to the input impedance Z_a of the antenna (via a maximum value of $\text{Re}(Z_a)$ or $\text{Im}(Z_a) = 0$) or to its minimum reflection coefficient;
- the influence of the feed circuit which modifies the structure of the antenna is released from f_r . We also avoid readjusting the antenna at the impedance of the input port when the substrate's characteristics are modified. Let us take the example of an antenna comprising a 4-mm square patch. In Figure 4.9, we observe a linear decrease in resonant frequency according to substrate thickness.

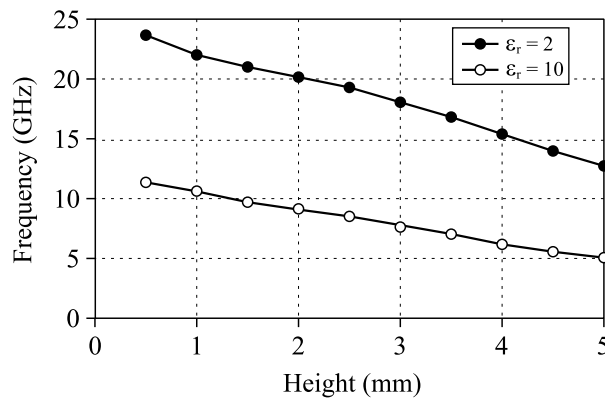


Figure 4.9. Influence of substrate thickness on frequency f_r for $\epsilon_r = 2$ and $\epsilon_r = 10$

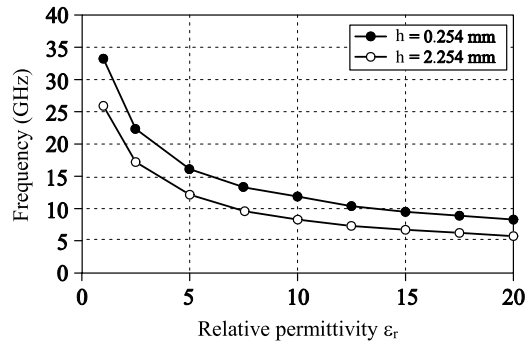


Figure 4.10. Influence of relative permittivity ϵ_r on resonant frequency for two substrate thicknesses, $h = 0.254$ and 2.254 mm

The transmission line model and the concept of the virtual extension ΔL given in equation [2.3] enable us to confirm this dependency, with ΔL showing a first-order increase based on substrate thickness h . In Figure 4.10, we confirm a $1/\sqrt{\epsilon_r}$ decrease. This is in accordance with equation [2.2], the resonant length of the antenna being close to $\lambda_0/2\sqrt{\epsilon_{\text{eff}}}$ where ϵ_{eff} is of the order of ϵ_r .

Chapter 5

Electrical Equivalent Circuit of a Printed Antenna

5.1. Energy considerations

Let us consider a medium of permeability μ_0 , complex permittivity $\varepsilon = \varepsilon' - j\varepsilon''$, and conductivity σ , containing one or more electrical sources labeled J_i (Figure 5.1). We know that Maxwell's equations for time-harmonic fields notably lead to the following two relationships:

$$\nabla \times \vec{E} = -j\omega\mu_0\vec{H} \quad \text{Faraday's Law} \quad [5.1]$$

$$\nabla \times \vec{H} = j\omega(\varepsilon' - j\varepsilon'')\vec{E} + \sigma\vec{E} + \vec{J}_i \quad \text{Ampere's Law} \quad [5.2]$$

where ω is the pulsation. After some effort, we can extract the energy conservation equation from equations [5.1] and [5.2]:

$$\begin{aligned} & \frac{1}{2} \iint_S (\vec{E} \times \vec{H}^*) \cdot d\vec{S} + \frac{1}{2} \iiint_V \sigma |\vec{E}|^2 dV + \frac{1}{2} \iiint_V \omega \varepsilon'' |\vec{E}|^2 dV + 2j\omega \left[\frac{1}{4} \iiint_V \mu_0 |\vec{H}|^2 dV - \frac{1}{4} \iiint_V \varepsilon' |\vec{E}|^2 dV \right] \\ & = -\frac{1}{2} \iiint_V \vec{E} \cdot \vec{J}_i^* dV \end{aligned} \quad [5.3]$$

in which the volume (V) is contained within the closed surface (S).

Note that:

$$P_f = -\frac{1}{2} \iiint_V \vec{E} \cdot \vec{J}_i^* dV \quad [5.4]$$

$$P_r = \frac{1}{2} \iint_S (\vec{E} \times \vec{H}^*) \cdot d\vec{S} \quad [5.5]$$

$$P_j = \frac{1}{2} \iiint_V \sigma |\vec{E}|^2 dV \quad [5.6]$$

$$P_d = \frac{1}{2} \iiint_V \omega \varepsilon'' |\vec{E}|^2 dV \quad [5.7]$$

$$W_H = \frac{1}{4} \iiint_V \mu_0 |\vec{H}|^2 dV \quad [5.8]$$

$$W_E = \frac{1}{4} \iiint_V \varepsilon' |\vec{E}|^2 dV \quad [5.9]$$

where P_f is the total power provided by the sources at volume (V), P_r the power radiated, P_j and P_d the values for power dissipated by the rise in temperature in the conductors and dielectrics, respectively, and W_M and W_E the average values of energy stored in magnetic and electrical forms, respectively. $W_M + W_E$ is the total reactive energy stored in volume (V).

Relationship [5.3] can be rewritten in a more compact form:

$$P_f + P_j + P_d + 2j\omega(W_M - W_E) = P_r \quad [5.10]$$

Expression [5.10] indicates the different active and reactive forms taken by the provided power P_f . Note the analogy with an RLC circuit for which:

- $(P_r + P_j + P_d)$ corresponds to the average power consumed by R ;
- W_M corresponds to the energy $\frac{1}{2}LI^2$ stored in the inductor of inductance L through which the current I flows;
- W_E corresponds to the energy $\frac{1}{2}CV^2$ stored in a capacitor of capacitance C when the voltage V is applied at the terminals.

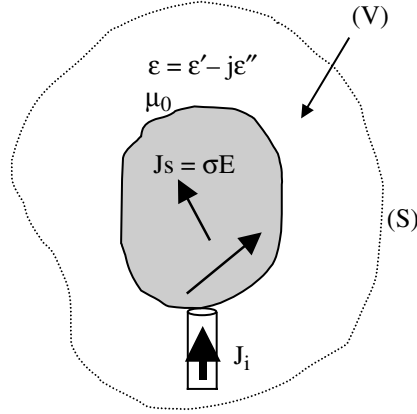


Figure 5.1. Volume (V) characterized by its complex permittivity, permeability, and conductivity containing electrical sources J_i

5.2. Equivalent circuit

From the point of view of the transmission line, the antenna is a load of admittance $Y_A = G + jB$, where G is the conductance and B the susceptance of the antenna. Note the associated impedance $Z_A = R + jX = 1/Y_A$, where R and X are the resistance and the reactance of the antenna, respectively.

Let V_A and I_A be the complex amplitudes associated with the input voltage and the input current of the antenna (Figure 5.2).

The power provided to Y_A is given by:

$$P_f = \frac{1}{2} V_A I_A^* = \frac{1}{2} |V_A|^2 Y_A^* = \frac{1}{2} |V_A|^2 (G - jB) \quad [5.11]$$

which breaks down into active P_A and reactive Q_A power, i.e.:

$$P_f = P_A + jQ_A \quad [5.12]$$

with:

$$P_A = \frac{1}{2} G |V_A|^2 \quad [5.13]$$

$$Q_A = -\frac{1}{2} B |V_A|^2 \quad [5.14]$$

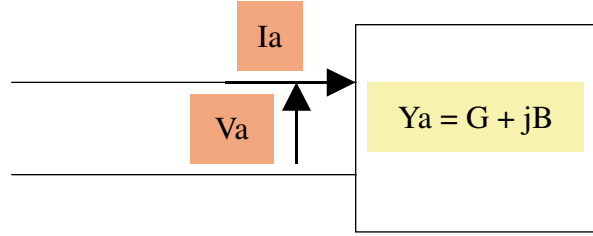


Figure 5.2. Equivalent antenna at an admittance charge $Y_A = G + jB = I_A/V_A$

By comparing equations [5.10] and [5.11], we can ultimately identify G and B with:

$$G = G_r + G_j + G_d \quad [5.15]$$

where:

$$G_r = 2P_r / |V_A|^2 \quad [5.16]$$

$$G_j = 2P_j / |V_A|^2 \quad [5.17]$$

$$G_d = 2P_d / |V_A|^2 \quad [5.18]$$

and:

$$B = -\frac{4\omega}{|V_A|^2} (W_M - W_E) \quad [5.19]$$

5.3. Determination of W_E , W_M , and B for a rectangular patch

From the expressions given in equation [3.17] for the E field for a TM_{mn} mode in a rectangular cavity, we can determine first the general expression for W_E by considering that the volume (V) is that of the cavity ($L \times W \times h$):

$$W_E = \frac{1}{4} \iiint_V \epsilon' |\vec{E}|^2 dv = \frac{1}{4} \int_0^L \int_0^W \int_0^h \epsilon' E_0^2 \cos^2 \frac{m\pi x}{L} \cos^2 \frac{n\pi y}{W} dx dy dz \quad [5.20]$$

from which we can extract:

$$W_E = \frac{\varepsilon' E_0^2 W L h}{8 \delta_{mn}} = \frac{\varepsilon' V_0^2 W L}{8 \delta_{mn} h} \quad [5.21]$$

where:

$V_0 = E_0 \cdot h$ is the electric potential difference between the patch and the ground plane for the maximum value of the field beneath the cavity E_0 ;

$$- \delta_{mn} = 1, \text{ if } m = 0 \text{ or } n = 0, \text{ else } \delta_{mn} = 2.$$

From equation [5.21], we can deduce that the electrical energy stored in a mode increases with the volume ($L \times W \times h$) of the antenna for a given applied electrical field.

Similarly, and by using equations [3.22] and [3.23] for the H field, we have the following expression for W_M :

$$\begin{aligned} W_M &= \frac{1}{4} \iiint_V \mu_0 |\vec{H}|^2 dv \\ &= \frac{\mu E_0^2 h}{4 \omega^2 \mu_0} \int_0^L \int_0^W \left[\left(\frac{n\pi}{W} \right)^2 \cos^2 \frac{m\pi x}{L} \sin^2 \frac{n\pi y}{W} + \left(\frac{m\pi}{L} \right)^2 \sin^2 \frac{m\pi x}{L} \cos^2 \frac{n\pi y}{W} \right] dx dy \end{aligned} \quad [5.22]$$

which simply reduces to:

$$W_M = \frac{V_0^2 W L}{8 \delta_{mn} h \omega^2 \mu_0} \left[\left(\frac{n\pi}{W} \right)^2 + \left(\frac{m\pi}{L} \right)^2 \right] \quad [5.23]$$

where we observe that the influence of W and L on the stored magnetic energy depends on the mode considered. Note that if we make $W_M = W_E$, we even arrive at the resonance condition [3.19] obtained with the cavity model.

Now we calculate the expression for the susceptance B of the antenna. By combining [5.19], [5.21], and [5.23], we find:

$$B = - \frac{4\omega}{|V_A|^2} (W_M - W_E) = \frac{V_0^2}{2\delta_{mn} |V_A|^2} \left(\varepsilon' W L \omega - \frac{W L}{\omega \mu_0} \left[\left(\frac{n\pi}{W} \right)^2 + \left(\frac{m\pi}{L} \right)^2 \right] \right) \quad [5.24]$$

It appears that the positive part of the expression for B corresponds to a capacitive part $jC\omega$, while the negative part corresponds to an inductive part $1/jL\omega$. This result could be extended to a patch of any shape.

5.4. Modeling using a tank circuit

From equations [5.15] regarding G and [5.24] regarding B , we can conclude that the admittance $Y_A = G + jB$ of the patch antenna can ultimately be expressed in the form:

$$Y_A = G_r + G_d + G_j + j(C\omega - 1/L\omega) \quad [5.25]$$

which represents the admittance of an RLC or tank circuit. From this we deduce that each resonant mode can be modeled around its resonance using a tank circuit, which is equally the case for a metallic cavity with losses. Its resonant frequency is given by:

$$f_r = \frac{\omega_r}{2\pi} = \frac{1}{2\pi\sqrt{LC}} \quad [5.26]$$

Note that at the resonant frequency of the mode ($f = f_r$), $B = 0$, $Y_A = G$ is purely real, and $W_E = W_M$.

We can include higher modes in the equivalent circuit of the TM_{10} mode while modeling them through a unique inductance L_f . With these modes working well below their resonance, each one, in effect, presents an inductive feature. This model is only valid close to the resonance of the TM_{10} mode (Figure 5.3). The effect of the higher modes therefore results in essentially non-radiative and non-propagative magnetic energy storage, close to the excitation.

Figure 5.3 also shows the typical evolution of the impedance locus of a patch antenna around its first resonance (the TM_{10} mode). This locus is a circular arc characterized by a cancellation of the imaginary part of the resonant frequency f_r , the inductive behavior (the upper part of the chart) for frequencies that are lower than f_r (f_{\min}), and the capacitive behavior (the lower part of the chart) for frequencies that are higher than f_r (f_{\max}). Note that if we ignore L_f , then the locus is perfectly symmetrical relative to the real axis, while a positive rotation is observed when L_f is included.

In the Smith chart, the impedance locus associated with an ideal resonant circuit is a circle. For a series RLC circuit, which models, for example, the behavior of a radiating slot around its first resonance, the real part of the impedance remains

constant with the frequency; the impedance locus is therefore superpositioned over a constant real part circle on the chart. At the resonant frequency, the intersection of the impedance locus with the real axis (i.e. the cancellation of the imaginary part) occurs to the left of the locus, with the impedance tending toward an open circuit for higher resonant frequencies (Figure 5.4a).

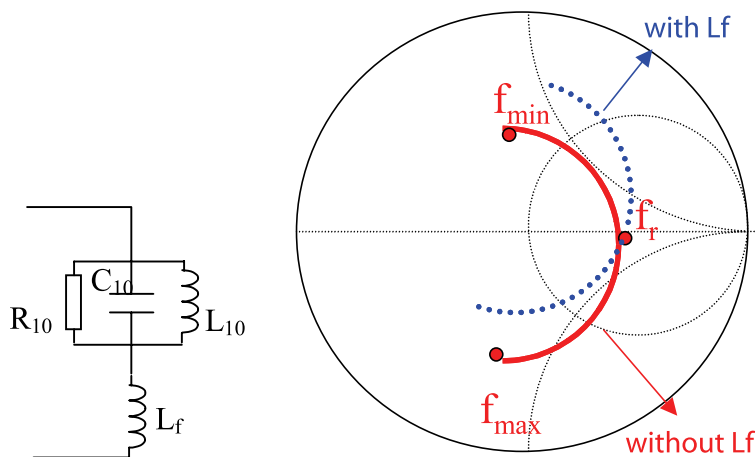


Figure 5.3. Impedance in the neighborhood of the resonant frequency of the TM_{10} mode. Equivalent circuit including the influence of higher modes

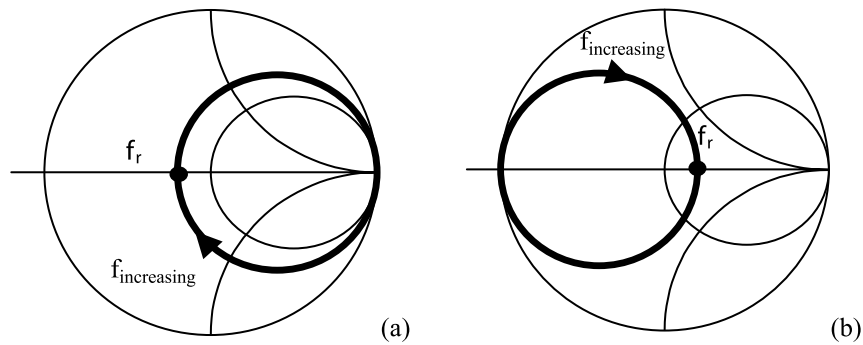


Figure 5.4. Impedance locus characterized for (a) a series RLC circuit and (b) a parallel RLC circuit

For one of the patch modes associated with a *parallel* resonance, the real part of the admittance remains constant. If the Smith chart were to be used for admittance, the impedance locus would be superpositioned over a constant conductance circle.

On an impedance chart, the locus of a parallel circuit does not follow a constant real part circle, but remains a circle by virtue of the symmetrical nature of the Smith chart. The symmetry relative to the center of the chart for a given impedance point is, in effect, the associated admittance, hence the preservation of the circle.

At the resonant frequency, for a parallel resonant circuit, the intersection of the impedance locus with the real axis (i.e. cancellation of the imaginary part) occurs to the right of the locus, with the impedance tending toward a short circuit for higher resonant frequencies (Figure 5.4b).

5.5. Quality factor of an antenna

In general, the quality factor (or Q-factor) is defined as the ratio between the energy stored and the energy lost over a period in a circuit. Using the analogy of the case of a resonant cavity coupled to a feed line, we define the loaded Q-factor Q_{ch} of the antenna using the formula:

$$Q_{ch} = \omega_R \left(\frac{W_a}{P_r + P_j + P_d + P_R} \right) \quad [5.27]$$

where $P = P_r + P_j + P_d + P_R$ is the total feed power, with P_R the power reflected by mismatching. W_a is the total energy stored by the antenna *at resonance*, i.e. $W_a = 2W_E = 2W_M$.

The quality factor for losses other than through mismatching is:

$$Q = \omega_R \left(\frac{W_a}{P_r + P_j + P_d} \right) \quad [5.28]$$

The quality factor for losses through mismatching is:

$$Q_R = \omega_R \left(\frac{W_a}{P_R} \right) \quad [5.29]$$

hence:

$$\frac{1}{Q_{ch}} = \frac{1}{Q_R} + \frac{1}{Q} \quad [5.30]$$

Let R be the resistance for losses from the cavity in the equivalent tank RLC model. R contains losses through radiation and the ohmic losses in the conductors and in the dielectric. Let Z_0 be the characteristic impedance of the feed line. Let us suppose $\beta = R/Z_0$. We can show from [COM 97] that if the Voltage Standing Wave Ratio (VSWR) of the antenna for an antenna frequency $f = f_r \pm \Delta f$ is expressed as ρ , then:

$$\frac{\Delta f}{f_r} = \frac{1}{Q} \sqrt{\frac{\rho^2 + 1}{\rho}} \beta - (\beta^2 + 1) \quad [5.31]$$

which is valid for low values of Δf , where f is close to f_r . The ratio $\Delta f/f_r$ is called the impedance bandwidth of the antenna. It corresponds to the percentage of the frequency band around f_r for which $\text{VSWR} < \rho$, typically $\rho = 2$ or $\rho = 1.5$.

The bandwidth can also be defined from a criterion based on the reflection coefficient Γ , for which a commonly used value is $\Gamma = -10$ dB.

In the case where the antenna is matched to the line ($R = Z_0$ or $\beta = 1$), at patch resonance ($X = 0$) for an adequate feed position, then [5.31] becomes:

$$\frac{\Delta f}{f_r} = \frac{1}{Q} \frac{\rho - 1}{\sqrt{\rho}} \quad [5.32]$$

Note that the bandwidth of the antenna is therefore inversely proportional to Q , i.e. the bandwidth increases with antenna losses, when these are due to radiation or to materials (conductor + dielectric).

5.6. Calculation of radiation quality factor

Let us consider the case where ohmic losses are negligible and where the antenna is matched. We note that $Q = Q_r$ is the quality factor of the antenna that corresponds only to radiation losses and reduces to:

$$Q_r = \omega_R \left(\frac{W_a}{P_r} \right) \quad [5.33]$$

We know that $W_a = 2W_E$. Using [5.9] and [5.21], we can determine the value of the energy stored in the antenna in the case of the TM_{10} mode. We have:

$$W_a = \frac{\varepsilon' V_0^2 WL}{4h} \quad [5.34]$$

On the other hand, according to [4.32], the total power radiated by the two radiating G-conductance slots is given by:

$$P_r = GV_0^2 \quad [5.35]$$

hence:

$$Q_r = \omega_R \frac{\epsilon'WL}{4hG} \quad [5.36]$$

Modeling through an RLC tank circuit, and for a matched antenna, the expression for the quality factor is given by:

$$Q_r = CR\omega_r \quad [5.37]$$

5.7. Calculation of efficiency

If we assume that the antenna is matched, then the efficiency is given by:

$$\eta = \frac{P_r}{P_r + P_j + P_d} \quad [5.38]$$

We will define different types of power as functions of W_a in order to obtain a compact expression for η as a function of the quality factor Q_r .

5.7.1. Losses in conductive walls

$$P_j = 2 \cdot \frac{1}{2} \iint_S R_s I_s^2 dS \quad [5.39]$$

where S is the surface area of the patch and the factor of 2 resulting from the area of the adjoining ground plane. R_s is the superficial resistance of the metallic walls, with conductivity σ and skin depth δ_s , given by:

$$R_s = \sqrt{\frac{\pi\mu_0 f}{\sigma}} = \frac{1}{\sigma\delta_s} \quad [5.40]$$

and I_s is the surface density of current on the walls:

$$\vec{I}_s = \vec{n} \wedge \vec{H} = \vec{H}_t \quad [5.41]$$

hence:

$$P_j = R_s \iint_S |\vec{H}_t|^2 dS \quad [5.42]$$

On the other hand, we have seen that the energy stored at resonance can be expressed as a function of the magnetic field as:

$$W_a = \frac{1}{2} \iiint_V \mu_0 |\vec{H}|^2 dv \quad [5.43]$$

taking into account the fact that H uniquely possesses transverse components and the dependence along z is null, then we find that:

$$W_a = \frac{1}{2} \mu_0 h \iint_S |\vec{H}_t|^2 dS \quad [5.44]$$

from which we determine the expression for P_j as a function of W_a given by:

$$P_j = \frac{2R_s W_a}{\mu_0 h} \quad [5.45]$$

5.7.2. Losses in the dielectric

$$P_d = \frac{1}{2} \iiint_V \omega \varepsilon'' |\vec{E}|^2 dv = \frac{1}{2} \omega \varepsilon_0 \varepsilon_r \text{tg} \delta \iiint_V |\vec{E}|^2 dv \quad [5.46]$$

where $\text{tg} \delta$ is the loss tangent of the substrate.

We have seen that the energy stored at resonance can also be expressed as a function of the electrical field as:

$$W_a = \frac{1}{2} \iiint_V \varepsilon' |\vec{E}|^2 dv = \frac{1}{2} \varepsilon_0 \varepsilon_r \iiint_V |\vec{E}|^2 dv \quad [5.47]$$

from which we determine the expression for P_d as a function of W_a as:

$$P_d = \omega \text{tg} \delta W_a \quad [5.48]$$

5.7.3. Radiated power

Let Q_r be the radiation Q-factor of the antenna given by:

$$Q_r = \frac{\omega W_a}{P_r} \quad [5.49]$$

The radiated power P_r can be expressed as a function of W_a as:

$$P_r = \frac{\omega W_a}{Q_r} \quad [5.50]$$

by substituting expressions [5.45], [5.48], and [5.50] for power as a function of W_a into [5.38], we finally arrive at the following compact expression for radiation efficiency:

$$\eta = \frac{1}{1 + Q_r \frac{\delta_s}{h} + Q_r \text{tg}\delta} \quad [5.51]$$

Note that the efficiency reduces for “bad” conductors (where σ is poor and δ_s is small) and “bad” substrates ($\text{tg}\delta$ is high).

On the other hand, the radiation efficiency is much poorer when the antenna is thin (h is small), with small-sized radiating apertures.

In [5.51], let us compare the terms δ_s/h and $\text{tg}\delta$ for an RT/duroid 5880 substrate for which $h = 0.658$ mm, $\epsilon_r = 2.20$, $\text{tg}\delta = 4 \times 10^{-4}$, and $\sigma = 3 \times 10^8$ mhos.

We know that:

$$\delta_s = \sqrt{\frac{1}{\pi\mu_0 f\sigma}} \quad [5.52]$$

hence for $f = 1$ GHz, of the order of $1 \mu\text{m}$, and $\delta_s/h \approx 1.4 \times 10^{-3}$. The metallic losses are therefore three times more significant than the dielectric losses in this configuration. They become equivalent at the same frequency for a thickness of 2 mm, or for the same thickness at a frequency of 9 GHz. Note that for a typical Q-factor of the order of $Q_r = 100$ at 1 GHz, then the efficiency is 85% for $h = 0.658$ mm and 92% for $h = 2$ mm.

5.8. Influence of surface waves on bandwidth and efficiency

This section summarizes the results presented in [GOD 02]. Figure 5.5 shows the influence of substrate thickness on impedance bandwidth (defined for a reflection coefficient < -10 dB) for different permittivity values. Bandwidth widens when thickness increases and permittivity decreases, for an increasing electrical volume of the antenna.

Figure 5.6 shows how efficiency evolves as a function of substrate thickness. We specifically want to highlight the influence of thickness and permittivity on losses from surface waves while ignoring the lesser noted modifications on losses as a result of the Joule effect.

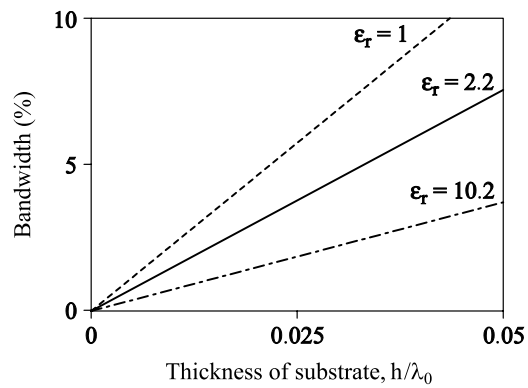


Figure 5.5. Bandwidth as a function of substrate thickness for different values of relative permittivity

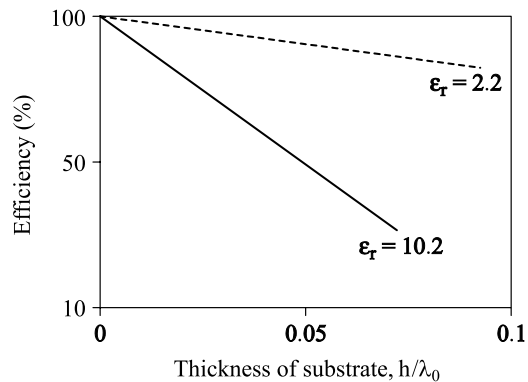


Figure 5.6. Drop in efficiency linked to surface waves as a function of substrate thickness for two values of relative permittivity

In the definition of efficiency [5.38], we therefore replace the ohmic losses P_j and P_d , which are thought to be null in the conductors and substrates, by the power P_{SW} lost into surface waves in the substrate. For these waves, the cutoff frequency of the fundamental TM_0 mode is null, with higher modes appearing when the frequency increases in the sequence TE_1 , TM_1 , TE_2 , etc. Note that for $h = 0.640$ mm, $\epsilon_r = 9.8$, the cut-off frequency of the first-higher order is $f_{TE1} = c/4h(\epsilon_r - 1)^{1/2} = 40$ GHz.

The energy carried by the surface waves is much more significant when the permittivity and thickness of the dielectric are high. The surface waves must be specifically taken into account during the design of MMIC antennas. The use of GaAs or AlGaInP substrates with a permittivity of 12–13 in effect leads to a significant excitation of the fundamental mode from the X band for several hundred microns of thickness.

Chapter 6

Feeding Circuits for Microstrip Antennas

6.1. Introduction

Even if it is effectively susceptible to radiation, an antenna is only usable if there is a feeding circuit enabling an acceptable transfer of guided energy toward the antenna. The optimum excitation of the antenna, or optimum coupling of the antenna to the feeding circuit, is a problem found equally in the excitation of microwave cavities and waveguides [GAR 02]. There are essentially three mechanisms for exciting printed antennas (Figure 6.1):

- direct coupling (by coaxial probe or printed line);
- proximity coupling;
- slot coupling.

The choice of feed type depends on constraints, such as the simplicity of the feeding circuit, the isolation between the excitation circuit and the antenna, or the eventual arrangement into an array of the radiating element. Whichever type of excitation is chosen, there are some general rules for optimizing the circuit between the feed and the antenna:

- define the mode of the antenna that needs to be excited;
- define the field distribution near to the excitation;

- determine the component(s) of the excitation field ($E_{x,y,z}$ or $H_{x,y,z}$) that will effectively contribute to the coupling (the excitation/antenna field distributions must correspond);
- determine the position for the excitation, which allows for optimum matching (this position does not necessarily correspond to a maximum field under the patch);
- take account of the parasitic effect of feed (degradation in the purity of polarization, pattern distortion, back radiation, shift of the resonant frequency, etc.).

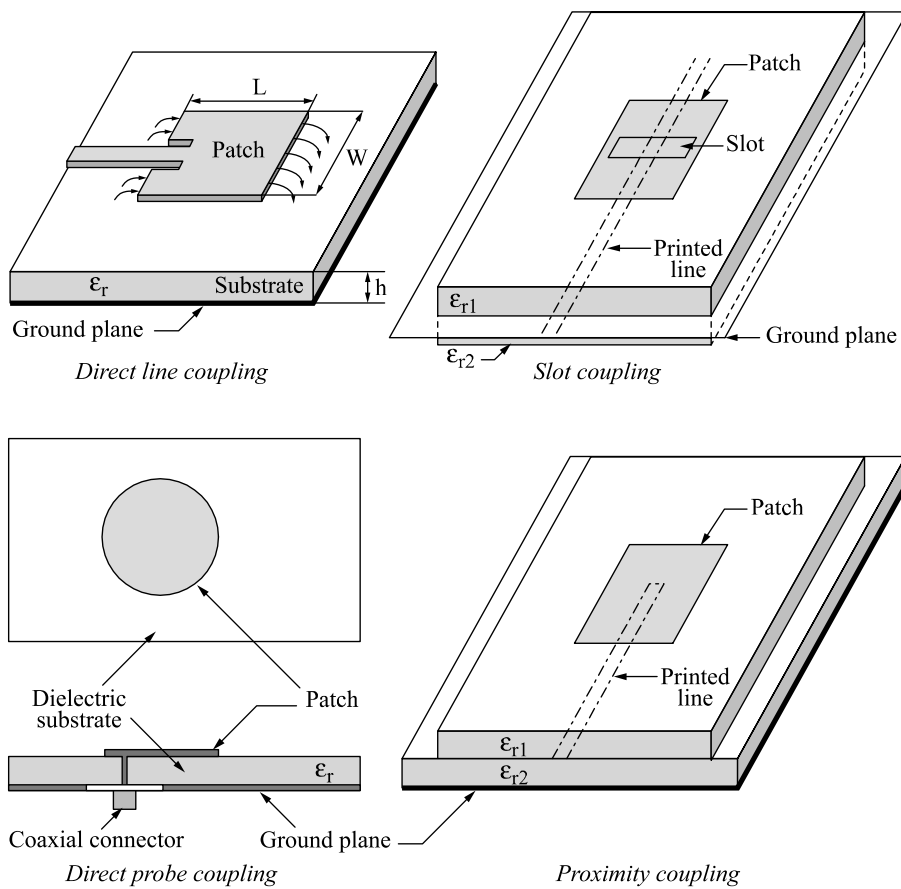


Figure 6.1. Different excitation mechanisms for planar antennas

We will briefly describe probe excitation and proximity coupling by printed line before detailing slot coupling.

6.2. Direct coupling by coaxial probe

A coaxial probe is composed of an SMA connector possessing a two- or four-hole screwable base (female part) and an extended inner conductor, i.e. with its insulator and external sheathing removed. For simplification, we often call the extension itself a probe, which we will do for the rest of the chapter. The SMA standard for coaxial cables at microwave frequencies requires a Teflon ($\epsilon_r = 2.2$) insulator diameter 4.1 mm, with a central core diameter 1.27 mm.

To feed an antenna directly, a vertical hole is drilled at the impedance point 50Ω under the patch, the base is fixed to the ground plane of the antenna, the probe is cut slightly above the patch, and a spot of solder is attached to assure a continuous electrical contact between the patch and the probe.

Soldering the base makes the structure mechanically robust, notably to cater for the torsion of the coaxial cable screwed to the SMA connector. While it enables us an easy impedance matching, this technique does have a number of disadvantages, such as:

- the necessity to drill a hole and to solder;
- high inductance brought about by the probe when substrate thickness increases;
- an unrealistic array configuration (due to the cost and bulk of the probes and cables).

Note, however, that all technologies that produce metallized holes and/or vertical lines, such as LTCC, enable the generalization of direct coupling with superior integration. Thus, it becomes feasible to feed large-scale arrays using direct coupling.

The series reactance X_f , added by the probe to the antenna impedance, results from the magnetic field created by the wiring through which an electric current flows.

Within the specific environment of the printed antenna, some more or less refined X_f approximations have been proposed. In [ZHE 91], we assume that the probe is positioned between two infinite metallic plates, which leads us to the analytical expression:

$$X_f = \eta_0 (h/\lambda_0) \left[-\gamma + \ln \left(\frac{1}{\pi(a/\lambda_0)\sqrt{\epsilon_r}} \right) \right] \quad [6.1]$$

where $\gamma = 0.577216$ is the Euler constant, a is the diameter of the probe, h is the substrate thickness, ϵ_r is its relative permittivity and η_0 is the impedance of

the vacuum. This expression ignores the position of the probe under the patch as well as the patch shape.

We observe that X_f increases if the radius of the probe is small and its length is significant. When $\epsilon_r = 10.5$ and $h = 1.3$ mm, reactance is approximately 10Ω at 3 GHz.

The influence of the probe on the input impedance of a rectangular patch can be seen in Figure 6.2 for several positions of a probe placed on the perpendicular bisecting line. We observe a rotation of loci toward the inductive part of the chart.

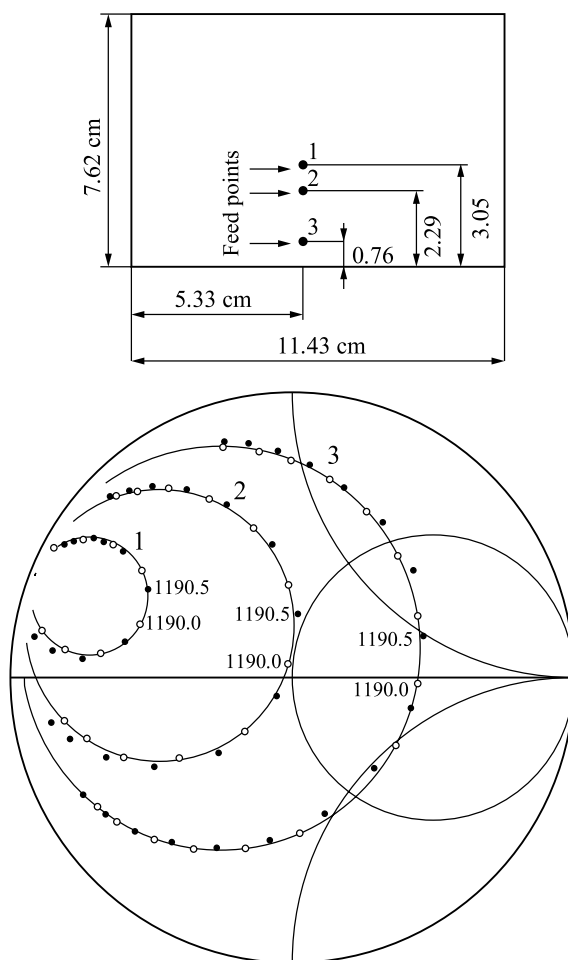


Figure 6.2. Positions of the probe exciting a rectangular patch. Impedance locus for three positions [RIC 81]. Substrate of thickness 1.58 mm and relative permittivity 2.62

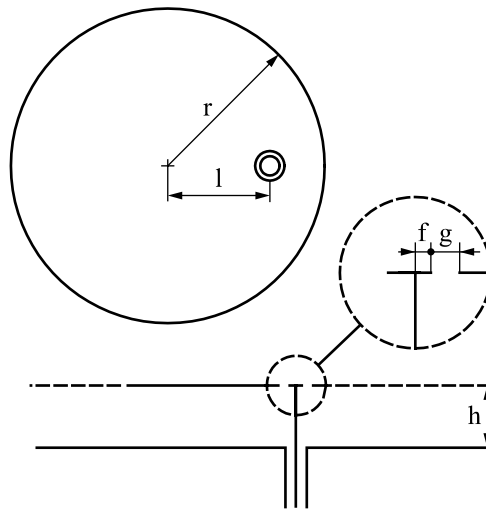


Figure 6.3. Compensation for the reactance of the probe by inserting a capacitive effect at the end of the probe [HAL 87]

This rotation, which is linked to the reactance added by the probe, can be compensated for narrow frequency bands with the aid of a local capacitive effect such as that proposed in Figure 6.3.

In Figure 6.2, we observe that position 2 of the probe enables us to match the TM_{10} mode at 1,190 MHz for a frequency close to the resonance. For this frequency, the impedance circle passes right through the center of the chart, which corresponds to an optimum transfer of energy from the source toward the antenna (matching) and therefore to an optimum coupling from the source to the antenna.

As for the excitation of metallic cavities [GAR 02], we recognize the concepts of optimum critical coupling (route of the locus through the center of the chart), of undercoupling (small circle) and overcoupling (large circle).

6.3. Excitation by proximity coupling

Proximity coupling enables us to excite the antenna while avoiding a direct connection between the feed and the patch. For this purpose, a feed line is positioned between the ground plane and the patch (Figure 6.4). We are therefore referring to a two-layer structure for which the substrates supporting the line and the patch do not necessarily have the same permittivity.

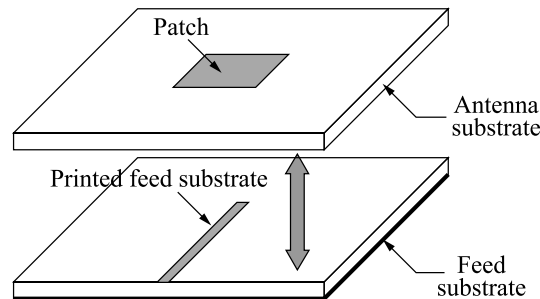


Figure 6.4. *Antenna fed by proximity coupling*

The lack of contact leads to capacitive coupling unlike the direct feed by probe or printed line, which is inductive in nature. While direct coupling necessitates moderate substrate thicknesses (which the characteristic impedance of the line or the reactance added by the probe depend on), capacitive coupling allows us to have more significant thicknesses and therefore much wider bandwidths.

We also observe the lesser parasitic radiation. The thickness ratios between the substrate layers must be chosen in such a way as to optimize coupling. As for slot coupling, fabrication must take place with care to avoid misalignments or parasitic layers of air.

Matching is regulated through adjustment of the depth of penetration of the line under the patch.

6.4. Excitation by slot coupling

Excitation of a patch antenna through a slot was proposed by Pozar [POZ 85]. In this structure (Figure 6.5), a slot etched into the ground plane ensures the transfer of energy by magnetic coupling between the feed line and the radiating element.

This type of feeding enables us to optimize independently the performances of the circuit and radiating parts of the antenna. The substrate of the circuit part possesses strong permittivity, which limits the losses through radiation and optimizes the transfer of energy from the transmission lines.

The upper substrate possesses low permittivity and a higher thickness to increase the bandwidth and gain of the antenna.

Since the feeding line is isolated from the radiating element by the ground plane, the radiation pattern and the polarization are barely disturbed by the excitation.

The observed distortions of the radiation pattern in the E-plane for other types of excitation are notably reduced for excitation through a slot.

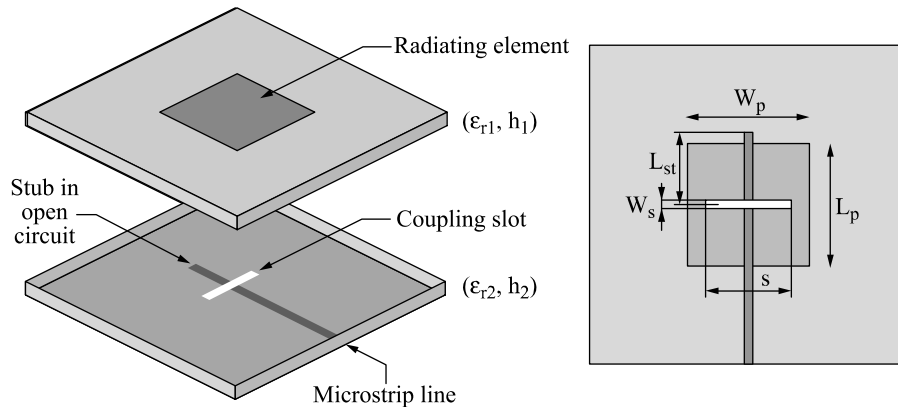


Figure 6.5. Antenna fed by slot coupling

In the canonical case of a slot inserted into an infinite conductive plane illuminated by an electromagnetic field, [COL 66] highlights the presence of two types of coupling, magnetic and electrical. A small aperture is therefore equivalent to the combination of an electrical dipole normal to the aperture (and proportional to the normal E-field) and a magnetic dipole in the plane of the aperture (and proportional to the tangential H-field). Figure 6.6 describes the two potential couplings linked to the presence of the slot.

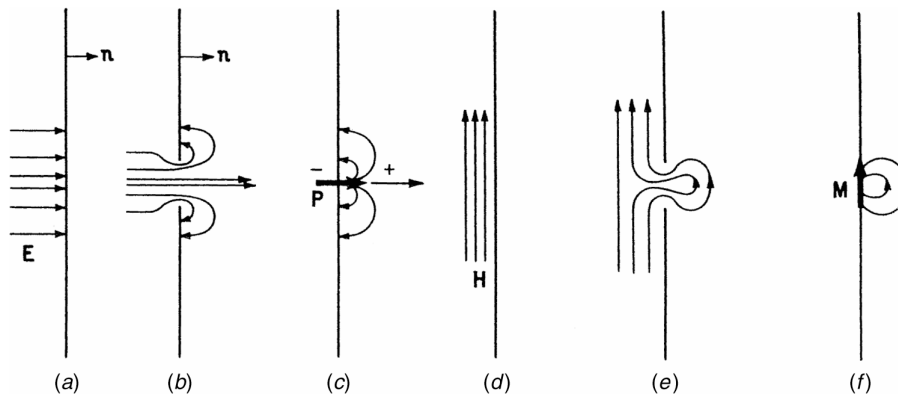


Figure 6.6. Coupling of the electromagnetic field through a slot in a metallic plane [COL 66]

From this model and from our knowledge of the analytical expression for the near field around the microstrip line, [POZ 85] analyzes the nature and intensity of line/aperture coupling as a function of the relative position (in the E-plane) of a slot that is electrically small relative to the patch. The conclusions enable us to estimate the conditions for the optimum transfer of energy between the microstrip line and the antenna.

When the aperture is situated at the center of the patch, coupling is uniquely magnetic in nature and at maximum intensity. When the aperture is near to the radiating slots of the antenna, then electrical coupling is dominant. If, however, the aperture is moved along the bisector in the E-plane between these two positions (the center and edges of the patch), then the two types of coupling occur simultaneously. It appears that the intensity of magnetic coupling is always stronger and that a rectangular shape of the aperture leads to optimum coupling. When the rectangular aperture is moved along the H-plane of the antenna, the level of coupling drops according to the distance to the center. Moreover, it is preferable to center the microstrip line along the symmetry plane of the aperture, whatever the position of the aperture relative to the patch.

Optimum coupling is therefore obtained by centering the rectangular slot relative to the two axes of symmetry of the patch. Under this configuration, the magnetic coupling will be optimized by maximizing the current (and minimizing the impedance) on the printed line, near to the slot. This is achieved by using the open circuit stub of length L_{ST} from Figure 6.5.

To avoid the emergence of significant back radiation, the coupling slot must remain electrically small, or in any event small compared with its resonant length. Moreover, good coupling requires a significant aperture area, and this becomes all the more effective when the field is uniformly distributed in the slot. This efficiency compromise between the coupling and reduction of back radiation is obtained with H slot geometries.

The structure analysis for a slot that is centered relative to the patch can be made by using the electrical circuit as shown in Figure 6.7. The radiating element is modeled using two parallel lines of length L_1 and L_2 loaded by admittances representing two radiating slots, with the equivalent admittance of the patch denoted by Y_{pa} .

The essentially magnetic couplings between the slot and the radiating element on the one hand and the line and slot on the other are represented by transformers with transformation ratios n_1 and n_2 . The rectangular slot is characterized by its admittance Y_s , which is essentially inductive as a result of its reduced length.

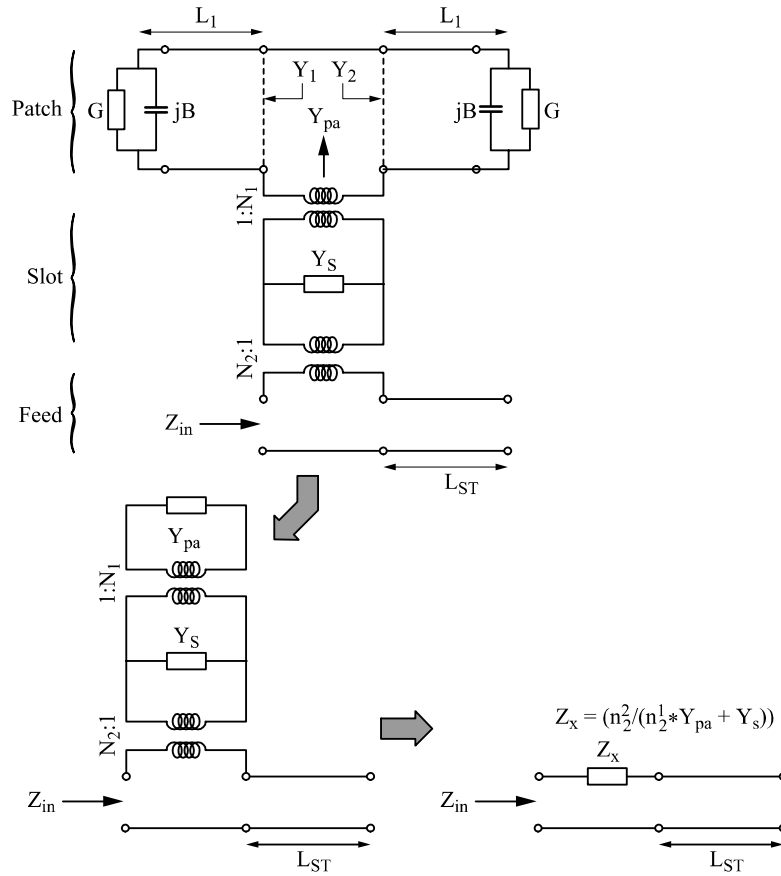


Figure 6.7. Equivalent electrical circuit and simplifications

The simplification of the electrical circuit enables us to establish a significant result: the input impedance of the antenna “seen” at the slot position is the series association of the derived impedance Z_x , which is a function of Y_{pa} , Y_s , n_1 , and n_2 with an open circuit stub of length L_{ST} .

The transformation ratios n_1 and n_2 are given by the following formulae:

$$n_1 = \frac{L_s}{L_p} \quad [6.2]$$

$$n_2 = \frac{L_s}{\sqrt{W_{Leff} h_2}} \quad [6.3]$$

where W_{Leff} is the effective width of the microstrip line. The following points can be drawn from equation [6.2]:

- the coupling between the patch and the slot is strengthened by increasing the length of the slot or decreasing the resonant length of the patch;
- for a given operating frequency, the reduction in the resonant length of the patch is obtained by increasing the permittivity ϵ_{r1} and/or reducing the height h_1 of the substrate of the patch;
- using a high value of h_1 and/or a low value of ϵ_{r1} to promote the gain and bandwidth of the antenna results in a long slot length to preserve a strong coupling, i.e. a reduction of the resonant frequency of the slot. This solution, therefore, carries the risk that significant back radiation will occur.

In consequence, the choice of substrate of the radiating element is the determining factor for a correct transfer of energy between the slot and the patch. According to equation [6.3], line/slot coupling also increases according to the length of the slot.

For a given characteristic line impedance Z_C , this coupling is improved for low thickness substrates via h_2 and W_{Leff} (for $Z_C = \text{const}$, if $h_2 \uparrow$ then $W_{\text{Leff}} \downarrow$) and high permittivities via W_{Leff} (for $Z_C = \text{const}$, if $\epsilon_{r2} \uparrow$ then $W_{\text{Leff}} \downarrow$).

From the expression for the impedance Z_x given in Figure 6.7, we analyze the resonance characteristics of the antenna.

The resonance condition is obtained for a purely real value of Z_x , namely:

$$n_1^2 B_{\text{pa}} + B_s = 0 \quad [6.4]$$

B_{pa} and B_s correspond to the patch and slot susceptances, respectively, with an approximate formula for the patch susceptance given by:

$$B_{\text{pa}} = \frac{4}{Z_{\text{cs}} k_s L_s^3} \quad [6.5]$$

where Z_{cs} and k_s are the characteristic impedance and propagation constant, respectively, of the slot. According to this formula, the increase in L_s (which contributes to a less increased input inductance) will lead to a reduction in B_{pa} and therefore a reduction in the resonant frequency of the antenna. To determine this frequency, it is therefore advisable to take account of the complete patch and slot device.

The value of the real part of Z_x at resonant frequency essentially depends not only on the level of coupling, and therefore initially on the slot length L_s , but also on its width W_s . The more significant the coupling, the higher the resistance will be at the slot center. The reduction in the width of the patch will also contribute to the increase in the real part of Z_x . This last result remains valid, irrespective of the type of feed used. To summarize, we can break down the design of a patch antenna connected by a rectangular slot aligned at the center of the patch into three stages: design of the circuit part, design of the radiating part, and finally, optimization of the complete antenna. Table 6.1 analyzes each of these stages.

Design of the circuit part		Design of the radiating part		Optimization of the antenna	
1. Choice of substrate	high ϵ_{r2} $h_2 \in (0.01-0.02)\lambda_0$ compromises between losses through radiation and ohmic/dielectric losses	1. Choice of substrate	Low ϵ_{r1} High h_1	1. Analysis of Z_x as a function of the slot dimensions	Adjustment of the slot while preserving a ratio of 1:10 between L_S and W_S to obtain a real impedance at the slot level near to the characteristic impedance of the line.
2. Calculation of W_L (width of the line)	Function of Z_C , ϵ_{r2} , and h_2 . Z_C is generally 50 Ω , (typical generator output impedance)	2. Calculation of L_p (resonant length of the patch)	Essentially function of the substrate characteristics and secondly the patch width	2. Adjustment of L_p	The slot reduces the resonant frequency of the antenna, it is necessary to reduce the length of the patch so that the whole structure operates at the desired frequency.
3. Calculation of L_{ST} (length of the stub)	$\lambda_g/4$, in order to maximize the transfer of current in the direction of the slot, λ_g is a function of ϵ_{r2} , h_2 and W_L	2. Calculation of W_p (width of the patch)	$W_p = L_p$ in the example	3. Adjustment of L_{ST}	If an inductive part is observed in the impedance Z_x at resonance, the reduction in the length L_{ST} will compensate for this effect

Table 6.1. Procedure for calculating the parameters of a patch antenna excited by a coupling slot

Following this procedure, an antenna operating at 5.8 GHz has been designed using HFSS software. The first substrate (S1) is made from Duroid 5880. The radiating element, which is a square patch, is etched on the upper surface of this dielectric. The lower surface is non-metallized. The second substrate (S2) is made from AR 1000. The feed line is printed onto the lower surface. The metallization of the upper surface constitutes the ground plane into which the coupling slot is patterned.

Table 6.2 summarizes the substrate values and selected dimensions for the circuit and radiating parts. The parametric study conducted on the dimensions of the slot (while preserving $L_S/W_S = 0.1$) indicates that for $L_S = 8$ mm, the resonance is fixed at 5.42 GHz, which is a variation of 6.9% relative to the desired operating frequency. From equations [6.4] and [6.5], this shift in frequency was expected.

Characteristics of the circuit part	Characteristics of the antenna part
Substrate (S2): Duroid 5880 $h_2 = 0.7874$ mm, $\epsilon_{r2} = 10$	Substrate (S1): AR 1000 $h_2 = 3.175$ mm, $\epsilon_{r1} = 2.2$
$W_L = 0.75$ mm @ $Z_C = 50 \Omega$	$L_P = 14.8$ mm @ 5.8 GHz
$L_{ST} = 4.9$ mm ($\lambda_g = 19.7$ mm @ 5.8 GHz)	$W_P = L_P$

Table 6.2. Dimensions of the structure

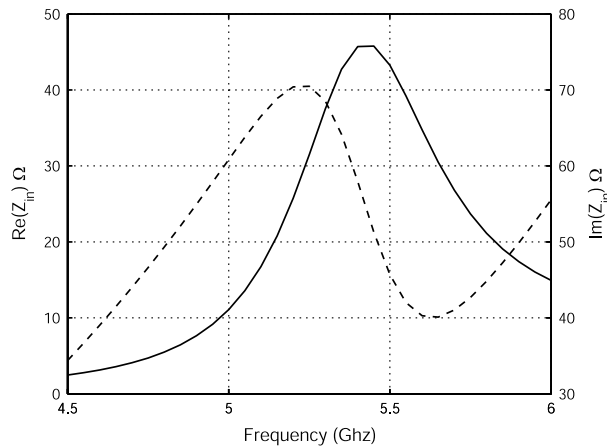


Figure 6.8. Change of impedance at the slot

At this frequency, we observe in Figure 6.8 that the input impedance at the slot location is equal to $Z_{in} = (48.5 + j * 51) \Omega$. In our case, this value directly

corresponds to Z_x since the series impedance added by the stub $\lambda_g/4$ is null. Note that the impedance seen at resonance is non-null and possesses an inductive component. We attribute this inductance to the presence of higher modes, which is not included in the transmission line model.

During the final stage, we adjust the operating frequency to approximately 5.8 GHz by modifying the patch dimensions. By reducing the length of the stub, we compensate for the inductive part of Z_x . The dimensions of the optimized elements are shown in Table 6.3.

W_L Width of line	L_{ST} Length of stub	$L_P = W_P$ Length/width of patch	L_S Length of slot	W_S Width of slot
0.75	2	13.6	8	1

Table 6.3. Optimized parameters of the antenna excited by a coupling slot. Centered microstrip line (units: mm)

In order to compensate for the inductive part, the length of the stub has been reduced by 59% relative to its initial value. The patch is 8% shorter and narrower. The slot has been slightly widened to increase the value of coupling considerably. The matching and impedance simulated at the slot are shown in Figures 6.9 and 6.10, respectively.

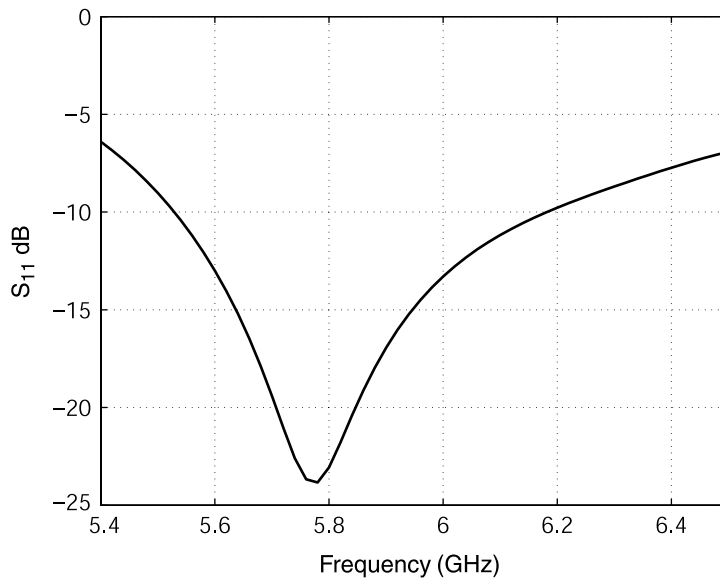


Figure 6.9. Reflection coefficient at the input point of the printed line (feeding port)

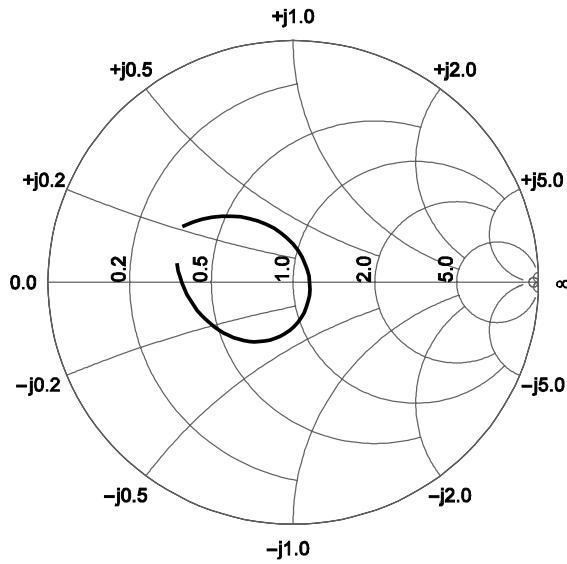


Figure 6.10. Smith chart for the input impedance calculated at the center of the slot

Figure 6.11 shows the normalized field components E_ϕ and E_θ in the E- and H-planes of the antenna at the resonant frequency. Figure 6.12 gives the front-to-back gain ratio at the axis of the antenna. For this structure, the resonant frequency of the slot is set at 9.15 GHz, therefore well beyond the useful frequency band.

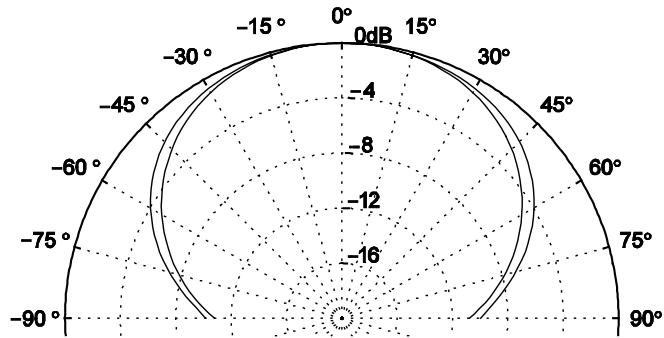


Figure 6.11. Radiation patterns

Figures 6.9 and 6.10 indicate that the antenna resonates at a frequency of 5.78 GHz with a bandwidth at -10 dB of between 5.54 and 6.14 GHz, i.e. 10%. From Figures 6.11 and 6.12 we can deduce the following characteristics:

- -3 dB beamwidth: 108° in the E-plane and 96° in the H-plane;
- cross-polarization level: less than -40 dB in the E- and H-planes;
- gain at broadside greater than 6.1 dB over the whole bandwidth;
- front-to-back gain ratio less than 15 dB.

In order to determine the critical parameters for the antenna, a sensitivity study was led on the dimensions of the patch (L_p , W_p) and the coupling slot (L_s , W_s). The frequency changes in the real part of the input impedance $\text{Re}(Z_{in})$ at the slot, for variations of $\pm 10\%$ in the nominal values of each dimension, are given in Figure 6.13.

The results confirm the theory. Coupling increases when L_s and W_s are increased and when L_p and W_p are reduced. The most influential parameters are patch and slot length. The analysis of results for variations in L_s (Figure 6.13a) shows that resonance shift is limited (less than 3%) in both cases ($L_{S-10\%}$ and $L_{S+10\%}$). Conversely, we observe a significant mismatching, with maximum impedance fluctuating between 33 and 88Ω , which represents variations of 40% and 61% , respectively, relative to the initial value (53Ω) for $L_{S-10\%}$ and $L_{S+10\%}$.

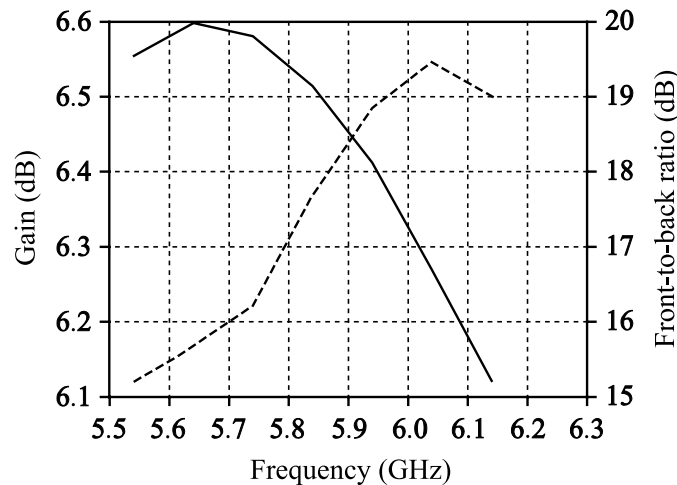


Figure 6.12. Variations in the gain at broadside and in the front-to-back gain ratio as a function of frequency

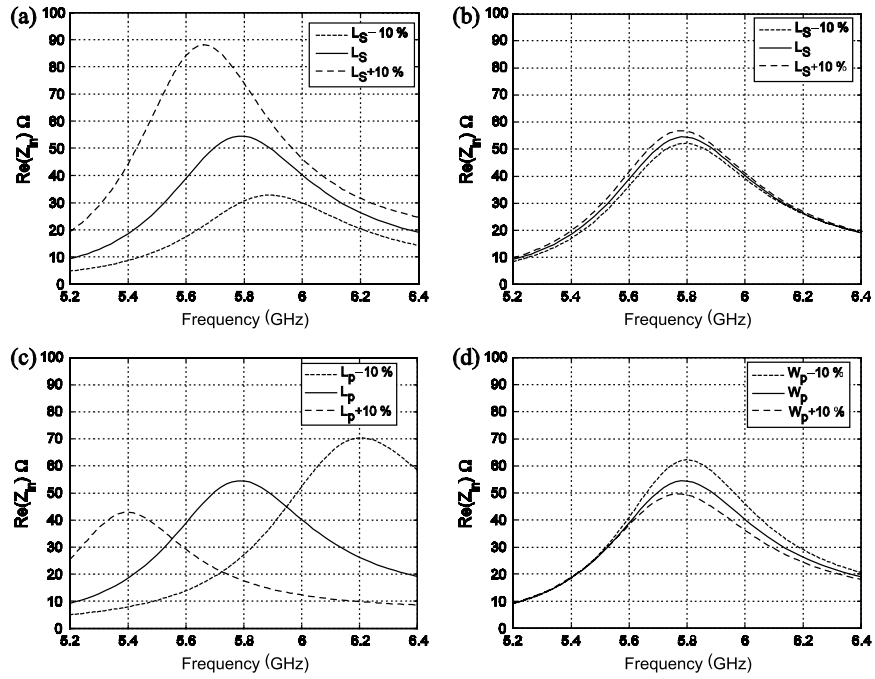


Figure 6.13. Antenna excited by a coupling slot: sensitivity study. Influence of (a) slot length, (b) slot width, (c) patch length, and (d) patch width

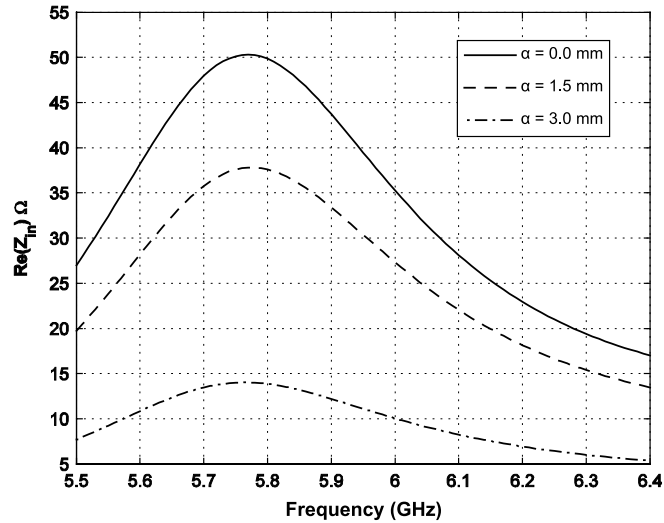


Figure 6.14. Analysis of coupling as a function of the shift of the microstrip line

Operating frequencies and impedance levels are strongly affected by variations in L_p . We see shifts in the resonant frequency of approximately 7% relative to 5.8 GHz for $L_{p-10\%}$ and $L_{p+10\%}$. The maximum value of $\text{Re}(Z_{\text{in}})$ varies by more than 20%, whichever case is proposed, relative to the initial configuration.

Figure 6.14 shows the changes in $\text{Re}(Z_{\text{in}})$ for different shift values a from the center of the feed line, relative to the center of the coupling slot in the H-plane of the antenna. On the basis of these curves, the level of coupling is strongly reduced when the feed line is offset from center. This change happens much faster when the excitation is moved closer to the edge of the slot.

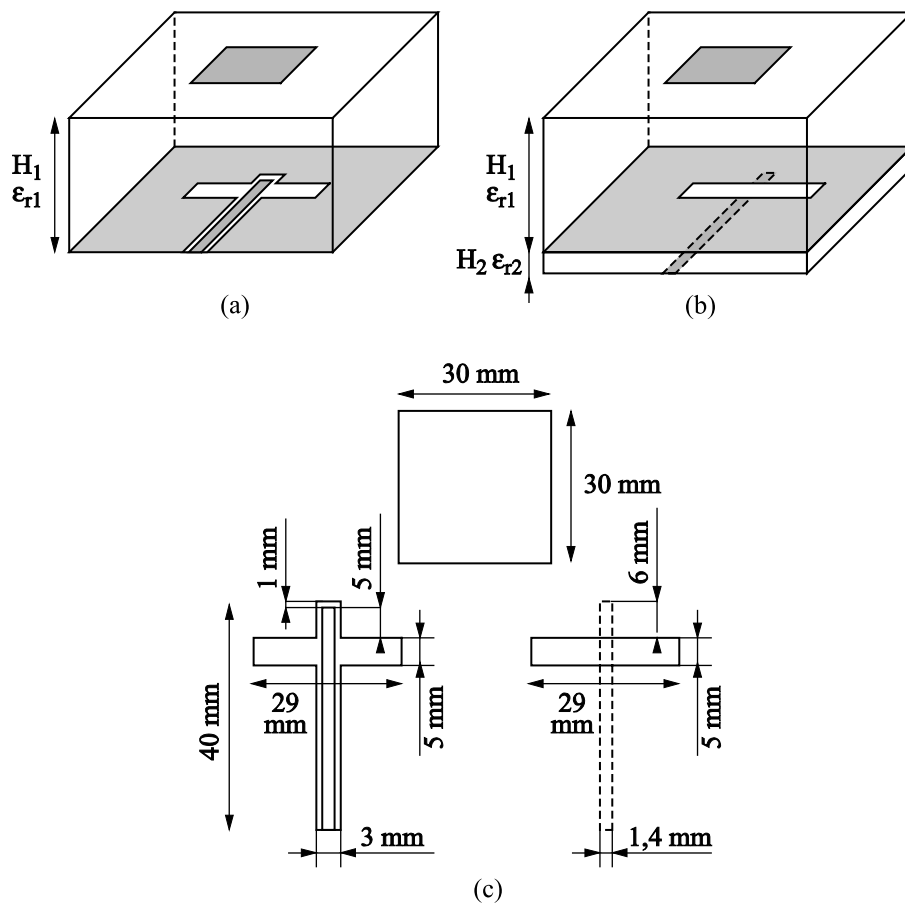


Figure 6.15. Excitation of a printed slot antenna: fed by (a) coplanar line, and (b) microstrip line ($H_1 = 12.5$ mm, $\epsilon_{r1} = 2.2$, $H_2 = 0.762$ mm, $\epsilon_{r2} = 2$)

According to the graph, resonant frequency is not affected by α . Note that moving the line also influences the imaginary part of the input impedance, which becomes more and more capacitive with increases in α .

A variant of excitation by slot coupling utilizes feeding using a coplanar line (Figure 6.15).

The following advantages can be associated with this:

- easier integration of active elements in the line;
- less dispersion and loss from the coplanar line at millimeter frequencies;
- a single substrate for the feeding and radiating element;

and a number of disadvantages, such as more delicate fabrication of feeding circuitries in large antenna arrays, with the resulting need to implement bonding wires or air bridges, short circuiting the even parasitic modes, into the line.

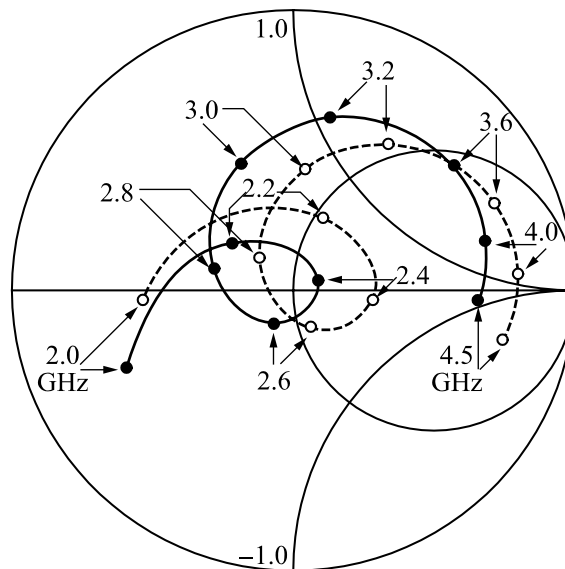


Figure 6.16. Comparison of the impedance loci for feeding by coplanar line (—) and by microstrip line (---)

We formally refer to the same excitation mechanisms as indicated in [GIA 96]. In Figure 6.15, the characteristics of the substrate of the radiating element and the slot and patch dimensions are identical. Figure 6.16 indicates that the resonant

frequency of the slot is higher in the case of coplanar feeding (4.4 GHz as opposed to 4.1 GHz). On the other hand, the size of the coupling loop is wider for microstrip line feeding, which indicates more significant coupling between the slot and the patch. These differences result from the reduction in resonant length of the slot due to the central conductor of the coplanar line. By increasing the slot length with an extension equal to the width of the central conductor, we show that the two impedance loci are superposed.

Chapter 7

Circularly Polarized Antennas

When polarization matching is not necessarily assured for a given orientation of linearly polarized transmitter and receiver antennas, it is preferable to use circular polarization. This is the case, for example, with low Earth orbit or unstabilized satellites, where the antennas are randomly oriented. Similarly, radio-frequency identification (RFID) reader antennas usually present circular polarization in order to enable communication with RFID tags, whatever their orientation. In radar technology, circular polarization is used to minimize interference from rain.

In communications between ground stations and satellites, the Faraday effect causes left and right circularly polarized (or CP) waves crossing the ionosphere to propagate at slightly different speeds. Since a linear polarization can be decomposed into two CP components, the effect of a relative phase shift, induced by the Faraday effect, is to rotate the orientation of a wave's linear polarization. Therefore, low depolarization will be observed if a pure circular polarization is used.

First, we will present the characteristic parameters of circular polarization (axial ratio – AR, polarization ellipse). Then, we will focus on different CP antenna topologies:

- planar microstrip CP antennas that can be categorized in two ways, according to the number of feed points: single- and double-feed antennas;

- sequential arrays, which enable a significant widening of the operating band in which circular polarization is effective – this band generally being reduced for resonant antennas;
- spiral and quadrifilar helix antennas.

7.1. Principles of circular polarization

7.1.1. Elliptical and circular linear polarization

Generally, the electrical field of a progressive plane wave in the positive z-direction can be broken down into two components: E_x and E_y , as a function of time and space, according to:

$$E_x = E_1 \sin(\omega t - \beta z + \phi_x) \tag{7.1}$$

$$E_y = E_2 \sin(\omega t - \beta z + \phi_y) \tag{7.2}$$

The wave is said to be elliptically polarized, as, for a given value of z, the electrical vector E is a function of time, with the extremity of the vector depicting an ellipse called the polarization ellipse (Figure 7.1) [KRA 12]. The ratio between the major and minor axes of this ellipse is called the axial ratio, AR, also known as the ellipticity of the wave, usually expressed in decibels:

$$AR = \frac{\text{major axis}}{\text{minor axis}} \quad \text{and} \quad AR(\text{dB}) = 20\log(AR) \tag{7.3}$$

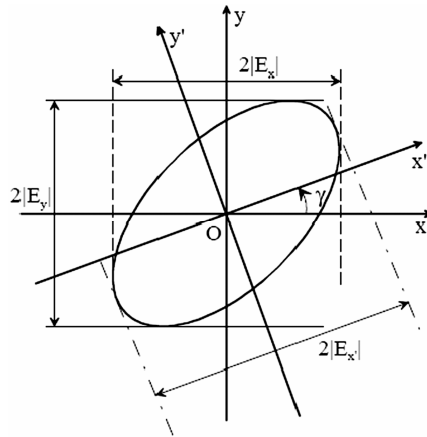


Figure 7.1. Polarization ellipse traced out by the tip of the E vector along its z-direction of propagation

Let $\varphi = \varphi_y - \varphi_x$ be the phase difference between the two components. Two extreme examples of elliptical polarization are:

- circular polarization for which $E_1 = E_2$, $\varphi = \pm\pi/2$, $AR = 1$ (0 dB);
- linear polarization for which $\varphi = 0$ or π , hence $AR = \infty$.

The frequency bandwidth for circular polarization is often defined as being the frequency band at which AR is less than 3 dB.

7.1.2. Right- or left-hand circular polarization

If $E_1 = E_2$ and $\varphi = +\pi/2$, the wave is said to have left-hand circular polarization (LHCP) – the electrical field vector rotating in a clockwise direction toward the reader.

If $E_1 = E_2$ and $\varphi = -\pi/2$, the wave is said to have right-hand circular polarization (RHCP) – the electrical field vector rotating in a counter-clockwise direction toward the reader.

Figure 7.2 shows the change of polarization as a function of the ratio E_y/E_x and of angle φ [STU 97].

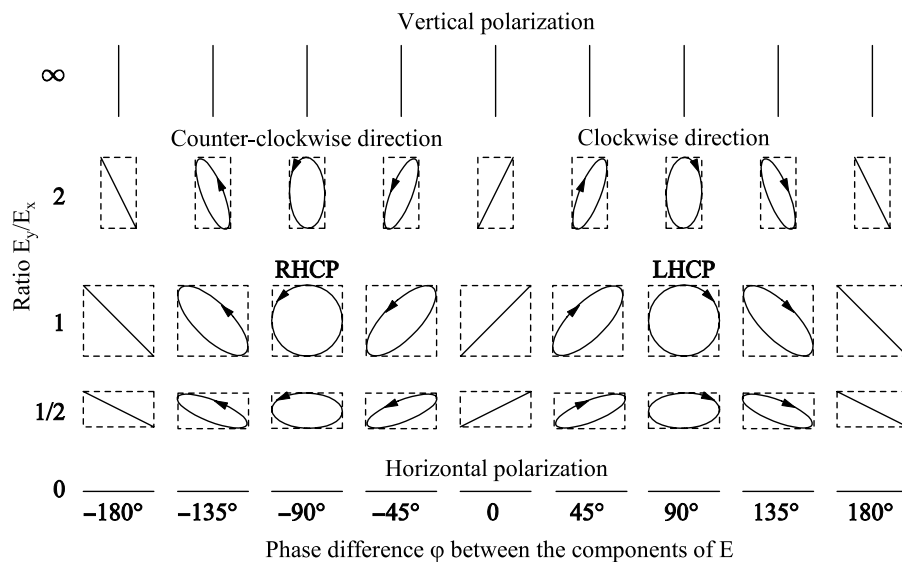


Figure 7.2. Polarization as a function of E_y/E_x and φ .
The wave is directed toward the reader

7.1.3. Axial and cross-polarization ratios

The electrical field radiated by an antenna can be broken down into two terms:

- E_{copolar} : reference CP component;
- E_{cross} : CP component orthogonal to the reference component.

The quality of circular polarization is then expressed by two measurements:

- the cross-polarization ratio:

$$\tau_p = \frac{|E_{\text{cross}}|}{|E_{\text{copolar}}|} \quad [7.4]$$

- the axial ratio, as defined from the ellipse in equation [7.3].

Assuming $E_{\text{cross}} < E_{\text{copolar}}$, these two measurements are then linked by the following relationships:

$$\tau_p = \frac{\text{AR} - 1}{\text{AR} + 1} \quad [7.5]$$

$$\text{AR} = \frac{1 + \tau_p}{1 - \tau_p} \quad [7.6]$$

Some characteristic values for the cross-polarization ratio and axial ratios are given in Table 7.1.

	τ_p	τ_p (dB)	AR	AR (dB)
Linear polarization \rightarrow	1	0	∞	∞
	0.5	–6	3	9.5
	0.17	–15	1.41	3
	0.1	–20	1.22	1.74
	0.01	–40	1.02	0.17
Null $E_{\text{cross}} \rightarrow$	0	$-\infty$	1	0

Table 7.1. Characteristic values for cross-polarization ratio and axial ratios

7.1.4. Measurement of circular polarization

A reference antenna with high purity of circular polarization, where the polarization corresponds to that of the antenna being tested, is usually required in order to measure radiation patterns. However, it is possible to reconstitute the right- and left-hand circular components with measurements performed with a linearly polarized reference antenna, usually a horn antenna. There are two methods for measuring AR.

7.1.4.1. Measurement of the whole ellipse

One method consists of utilizing a linearly polarized transmitter antenna and turning it through 180° in order to measure the electrical field for the two principal axes of the ellipse. The minor and major axes of the ellipse are determined by the minimum and maximum amplitudes of the received electrical field, respectively. The axial ratio can then be calculated by relationship [7.3]. The drawback of this method is that it requires many measurement points.

7.1.4.2. Three-point measurement

Another method enables the mathematical reconstitution of the equation for the ellipse by using three measurement points and by knowing the center of the ellipse (the axis of rotation of the antenna). Theoretically, it is sufficient to use three measurements of amplitude made in three different random directions. In order to minimize errors in measurement, it is in practice advisable to choose these three directions to be as different as possible: at angles of 0° (Ox axis), 90° (Oy axis), and γ° (Ox' axis) (Figure 7.1).

The electrical field E in the coordinate system (O, x', y', z') can be deduced from (O, x, y, z) by a rotation of angle γ around the Oz axis (Figure 7.1):

$$E'_x = E'_1 \sin(\omega t - \beta z + \varphi'_x) \quad [7.7]$$

$$E'_y = E'_2 \sin(\omega t - \beta z + \varphi'_y) \quad [7.8]$$

with $\varphi = \varphi'_y - \varphi'_x = \varphi_y - \varphi_x$. The change of coordinate system from (O, x, y, z) to (O, x', y', z') is expressed by the following relationship:

$$\begin{pmatrix} E'_x \\ E'_y \end{pmatrix} = \begin{pmatrix} \cos \gamma & \sin \gamma \\ -\sin \gamma & \cos \gamma \end{pmatrix} \begin{pmatrix} E_x \\ E_y \end{pmatrix} \quad [7.9]$$

Relationships [7.7], [7.8], and [7.9] enable us to obtain:

$$\cos \varphi = \frac{E'^2_1 - E^2_1 \cos^2 \gamma - E^2_2 \sin^2 \gamma}{2E_1 E_2 \cos \gamma \sin \gamma} \quad [7.10]$$

Thus, the measurement of values E_1 , E'_1 , and E_2 obtained by orienting the reference horn in planes 0° , γ , and 90° , respectively, enable $\cos\varphi$ to be determined using equation [7.10]. The measurements of amplitude do not, however, avoid the uncertainty over the sign of φ , and therefore do not enable the direction of rotation of the wave to be determined.

The following relationships [MOT 86] are then used in order to calculate the axial ratio:

$$AR = \text{tg}(\delta) \quad [7.11]$$

$$\text{with } \delta = \frac{1}{2} \text{Arcsin}(\sin(2\alpha)\sin\varphi) \quad [7.12]$$

$$\text{and } \alpha = \text{Arc tan}\left(\left|\frac{E_x}{E_y}\right|\right) \quad [7.13]$$

7.2. Parasitic radiation – degradation of circular polarization

In printed circular polarization arrays, several types of parasitic radiation can lead to degradation of circular polarization. Principally:

- generation of higher modes on patches;
- discontinuities in the feed circuit;
- transitions as a result of the connectors;
- surface waves;
- secondary currents at the edges of the ground plane.

We will quantify here the degradation in the axial ratio brought about by a parasitic electrical field component which has been superposed to the component E_x of a CP field. The total field can equally be expressed as a function of (E_x, E_y) or (E_R, E_L) :

$$\vec{E}_t = E_x \vec{u}_x + E_y \vec{u}_y \quad [7.14]$$

$$\vec{E}_t = \frac{E_R}{\sqrt{2}}(\vec{u}_x - j\vec{u}_y) + \frac{E_L}{\sqrt{2}}(\vec{u}_x + j\vec{u}_y) \quad [7.15]$$

where E_R and E_L are the components of right- and left-hand circular polarization of the radiated field, respectively. We can simply deduce:

$$E_L = (E_x - jE_y)/\sqrt{2} \quad [7.16]$$

$$E_R = (E_x + jE_y) / \sqrt{2} \quad [7.17]$$

Note that a pure LHCP polarization ($E_R = 0$) is obtained for $E_x = -jE_y$ and a pure RHCP polarization ($E_L = 0$) for $E_x = +jE_y$.

Let $E_p \cdot \exp(jp)$ be the expression for the parasitic field superposed to E_x , resulting, for example, from the presence of higher modes (see above). In order to evaluate the influence of the parasitic field on the axial ratio, and assuming a purely real E_x , we define the ratio:

$$R_p = E_p / E_x \quad [7.18]$$

By introducing R_p into expressions [7.16] and [7.17], we arrive at:

$$\frac{E_R}{E_L} = \frac{E_x(1 + R_p e^{jp}) + jE_y}{E_x(1 + R_p e^{jp}) - jE_y}$$

If left-hand polarization is needed, then $E_x = -jE_y$, and the cross-polarization ratio is expressed as:

$$\tau_p = \left| \frac{E_R}{E_L} \right| = \frac{R_p}{|2 + R_p e^{jp}|} \quad [7.19]$$

$$\text{AR} = \frac{|2 + R_p e^{jp}| - R_p}{|2 + R_p e^{jp}| + R_p} \quad [7.20]$$

Figure 7.3 shows the degradation in the axial ratio caused by parasitic radiation. The dashed and plain curves correspond to the change in AR for increasing values of R_p when $p = \pi$ (worst case) and $p = \pm\pi/2$ (best case), respectively.

We note that the influence of parasitic radiation is significant since we obtain an axial ratio of the order of 1 dB (the interference has a power equivalent to a 10th of the power contained in component E_x) for a low value of $R_p = -20$ dB. AR is about 3 dB when $R_p = -10$ dB. We note that the influence of the parasitic phase is relatively low.

From this study we conclude that low levels of parasitic radiations strongly degrade circular polarization. In particular it is recommended that a feed circuit be produced at the back of the ground plane of the array, and not in the plane of the array, in order to restrict its influence.

The methods described in the rest of this chapter (excitation using symmetrical pairs and sequential rotation) enable parasitic radiation to be reduced.

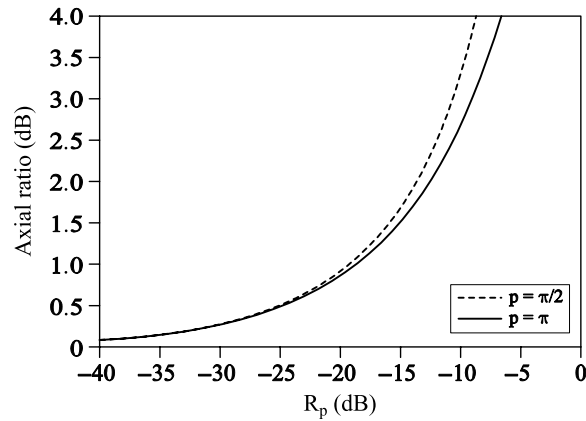


Figure 7.3. Degradation in the axial ratio as a function of the relative level of interference

7.3. Patch fed by single or dual excitation

Rectangular or elliptical patches radiate linearly polarized waves. Circular polarization can be obtained if two linearly orthogonal modes of equal amplitudes are excited with a temporal phase difference of $\pm\pi/2$. For this to happen with a single feed, the physical dimensions of the patch must be properly adjusted. For a patch excited by two feeds, square or circular geometries should be used [HIR 92].

7.3.1. Single excitation

Square or circular microstrip patch antennas that are excited over a diagonal give rise to pairs of degenerated orthogonal modes (with a square patch, TM_{100} and TM_{010} modes). The introduction of disturbances at the corners of the patch (Figure 7.4a) enables the resonant frequencies f_a and f_b of the two modes to be lightly separated (Figure 7.4b).

For the frequency f_0 , which is between the two resonant frequencies, the excitation of the modes occurs with the same amplitude and in phase quadrature. The resulting field is circularly polarized for this frequency without the use of an exterior polarizer [BAL 05]. The same figure illustrates the principle by representing the relative amplitude and the phase of two orthogonal modes. The major drawback of this solution is a very low axial ratio bandwidth (less than 1%).

Circular polarization can also be generated using a square patch antenna fed by coupling from a microstrip line across two crossed slots [ALO 94], as shown in Figure 7.5. These two slots can be fed by two lines branching out of a power splitter

[TAR 93] or by a single line that excites the antenna at four points in series. Following the chosen branch-line, right- or left-hand polarization can be generated, with the other branch of the line being closed by a matched load. The bandwidth is very wide (14%), but efficiency falls due to the power consumed by the matched load.

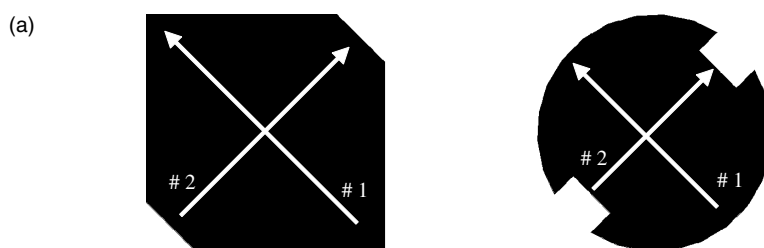


Figure 7.4a. Amplitude and phase of orthogonal modes excited in diagonal planes

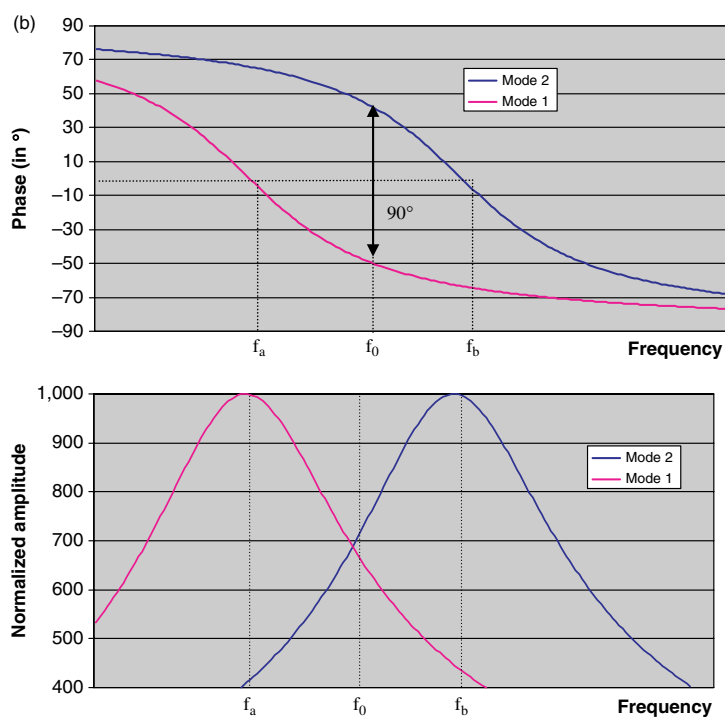


Figure 7.4b. Amplitude and phase of orthogonal modes excited diagonally

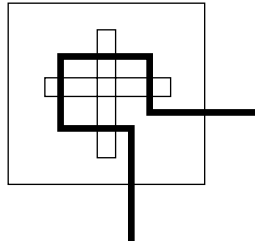


Figure 7.5. Example of circularly polarized antenna with a single feed

Note that it is also possible to generate circular polarization from two non-orthogonal linear polarizations with a lower radiation efficiency [AIS 04].

7.3.2. Dual excitation

Circular polarization can be obtained by combining two linearly polarized waves. If the linear polarizations are orthogonal to each other, present a phase difference of $\pm\pi/2$, and are equal in amplitude, then the polarization is perfectly circular.

Circular polarization is easily produced using a microstrip power splitter (Figure 7.6a) or a $\pi/2$ hybrid coupler (Figure 7.6b). Since two lines are feeding the patch, this is called dual-feed excitation.

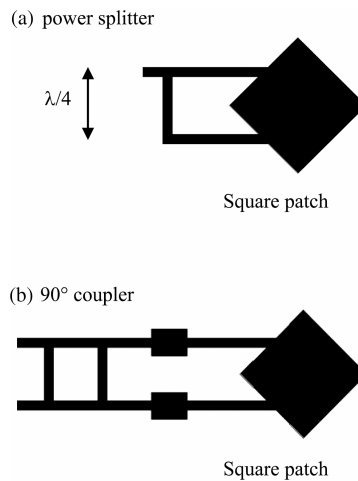


Figure 7.6. Dual-feed circularly polarized antennas: (a) with $\lambda/4$ power splitter and (b) with 90° hybrid phase shifter

The microstrip line power splitter leads to a phase difference of $+\pi/2$, but within a relatively restricted frequency band. Moreover, it does not isolate the two ports from each other, and is not able to prevent the wave reflected by one branch from interfering with the incident wave on the other branch. That restricts the CP bandwidth, which is much less than the matching bandwidth. Conversely, the hybrid coupler, which isolates each of the ports from each other, enables a CP bandwidth to be obtained, which is comparable to the matching bandwidth.

7.4. Sequential array

In a planar array made up of identical radiating elements, a CP wave can be generated using radiating elements which are linearly polarized, elliptically or circularly. In this type of array, circular polarization is obtained by temporal and spatial dephasing the radiating elements, which leads to a circular polarization of excellent quality around the axis and within a wider frequency band than for a simple element.

7.4.1. Principle of sequential rotation: initial analysis

The technique of sequential rotation was first described by Teshirogi in 1985 [TES 85], and then examined by Hall in 1989 [JAM 88].

The first-order analysis illustrates the mechanisms for the sequential feed technique, as well as the relationship between the number of radiating elements, the angular position of the feed point, and the required phase difference.

In the sequential array, the angular orientation and electrical excitation phase are sequentially incremented for each element.

The sequential configuration of M elements of the array is illustrated in Figure 7.7. The n th element is in an arbitrary position on the array plane, but has an angular orientation of:

$$\phi_n = p(n-1)\pi / M \quad [7.21]$$

where p is a whole number where $1 \leq p \leq M-1$. The n th element is fed with phase Φ_n .

Figure 7.8 presents the principal configurations for linear arrays. The arrangement of the elements influences the radiation patterns (width of the principal beam, sidelobes).

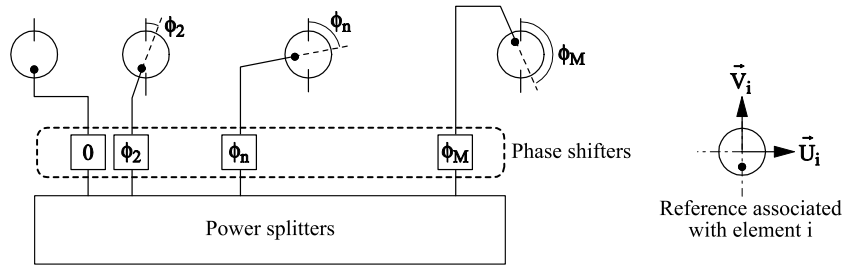


Figure 7.7. Illustration of the sequential array principle

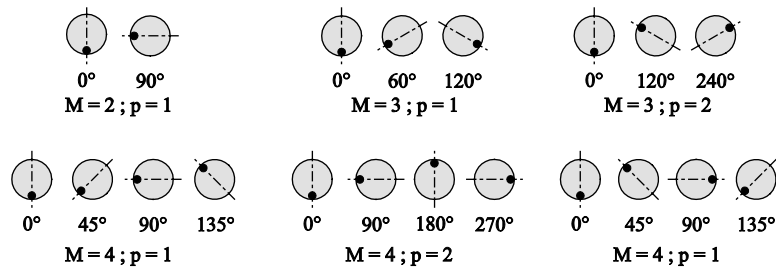


Figure 7.8. Principal configurations of sequential arrays for a linear arrangement of elements. The angles give at the same time the orientation and feed phase for each of the elements

Let U_1 and V_1 be the orthonormal vectors that allow Element 1 to be referenced in the array plane. Other elements are referenced by the orthonormal vector pairs (U_i, V_i) that are deduced from (U_1, V_1) by:

$$\vec{U}_i = \cos \phi_i \vec{U}_1 - \sin \phi_i \vec{V}_1 \quad [7.22]$$

$$\vec{V}_i = \sin \phi_i \vec{U}_1 + \cos \phi_i \vec{V}_1 \quad [7.23]$$

The field radiated by the elliptically polarized Element 1 is expressed as:

$$E_1(\theta, \varphi) = a(\theta, \varphi) \vec{u}_\theta + jb(\theta, \varphi) \vec{u}_\varphi \quad [7.24]$$

where a and b correspond to the axes of the polarization ellipse. For circular polarization, $a = \pm b$.

By combining the radiation of the M elements of the array, we obtain the total field radiated by the sequential array.

Consider a linear array of elements aligned in the plane $\varphi = 0^\circ$ (Figure 7.7).

The total electrical field $E_T(\theta, 0)$ is given by the following equation:

$$E_T = \sum_{n=1}^M E_n(\theta, 0) \quad [7.25]$$

$$= \sum_{n=1}^M \left\{ \begin{aligned} & [a(\theta, 0) \cos \phi_n - jb(\theta, 0) \sin \phi_n] \vec{u}_\theta \\ & + [a(\theta, 0) \sin \phi_n + jb(\theta, 0) \cos \phi_n] \vec{u}_\varphi \end{aligned} \right\} \times e^{-j(\phi_n - \psi_n)}$$

where:

$$\psi_n = (n-1)k_0 d \sin \theta \quad [7.26]$$

We assume all the elements are identical, each pair separated by a distance d , fed with the same amplitude, and we ignore mutual coupling. An example is given in Figure 7.9 for a linear array of four isotropically radiated elements ($a = b/2$ for all angles).

We observe that the sequential array perfectly radiates circular polarization waves at broadside, whatever the polarization of the radiating element. This improvement remains sensitive relative to a conventional array outside the axis for angles less than 20° in this example.

This angle strongly depends on M and p , as well as on the type of radiating element. Even if the polarization of the elements varies as a function of the frequency, the circular polarization in the axis will be assured over a wide band.

Additionally, the sequential array enables matching to be promoted. The wave reflected from the n th element toward the input point of the array possesses a differential phase shift of $2\phi_n$. If the reflection coefficients Γ of each of the elements are equal, then we can easily see that the sum of the waves V_r reflected in the direction of the input point of the array is null.

$$V_r = V_0 \Gamma \sum_{n=1}^M \exp(j2\phi_n) = 0 \quad [7.27]$$

The mismatching flows from the impossibility to keep the correct phase difference when the frequency changes, failure of which will lead to a limitation of bandwidth in impedance.

In addition to guarantee perfectly circular polarization at broadside, the sequential array therefore enables reflection to be minimized at the input port of

the array, whatever the polarization of the array element. Conversely, the radiation pattern outside the axial zone will depend on the purity of polarization of the element used.

The purity of polarization away from the axis is much better in sequential rotation when the base element possesses better circular polarization. This point can be controlled by comparing Figures 7.9 and 7.10, which correspond to $a/b = 0.5$ and $a/b = 0.8$, respectively, for elements which present homogeneous polarization in all directions.

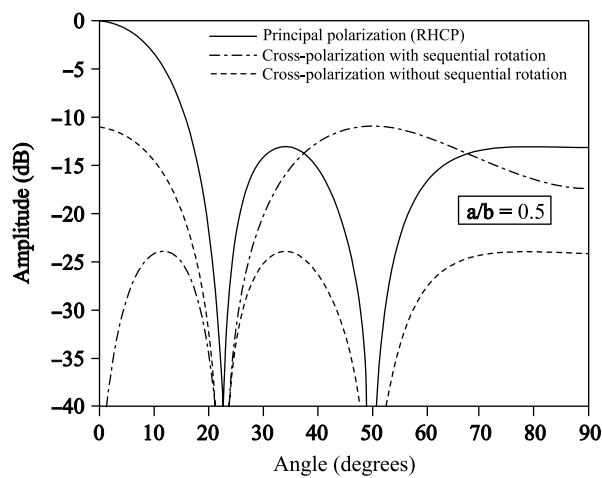


Figure 7.9. Four elements in line with and without sequential rotation, $a/b = 0.5$, $d = 0.65\lambda$

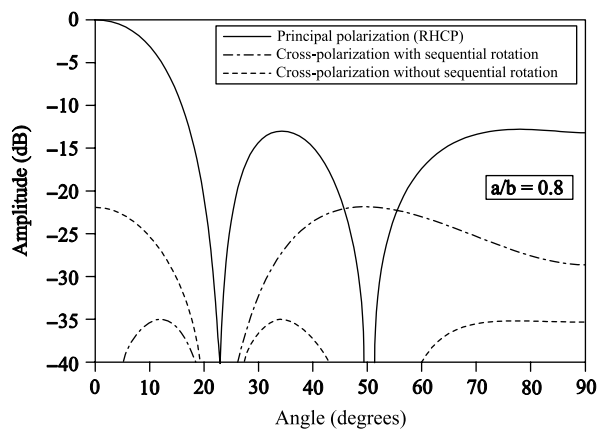


Figure 7.10. Four elements in line with and without sequential rotation, $a/b = 0.8$, $d = 0.65\lambda$

In practice, if a radiating element usually presents good circular polarization around the axis, then the rate of degradation away from the axis depends much on the type of element considered.

In the case where phase differences are obtained according to the feeding line lengths, the behavior of the array differs according to the values of p and M , which impacts on axial ratio and matching bandwidths.

For a frequency gap δ (expressed in %) relative to the central frequency, the cross-polarization improvement factor F between a conventional and sequential array is defined by [HAL 89]:

$$F = \frac{\tau_p \text{ sequential}}{\tau_p \text{ conventional}} \quad [7.28]$$

where τ_p represents the ratio between the amplitudes of the reference and cross polarized boresight electric fields. We show that equation [7.28] can be re-written:

$$F = \frac{2M}{p\pi\delta} \sin\left(\frac{p\pi}{M}\right) \quad [7.29]$$

The change in this factor is given in Figure 7.11. We observe that the purity of polarization is improved when M is large and at its best when $p = 1$.

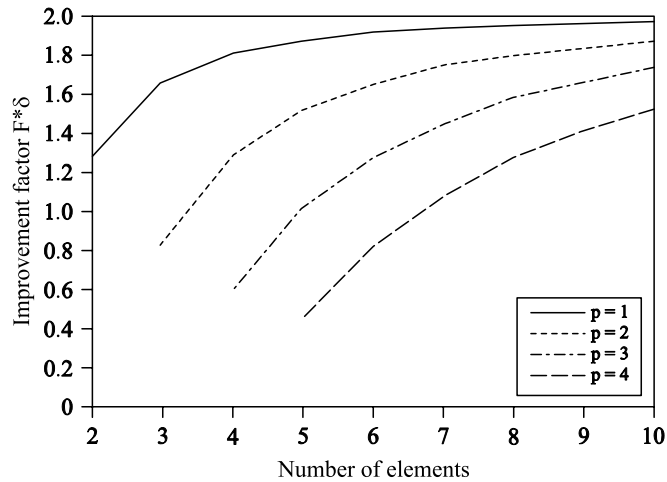


Figure 7.11. Cross-polarization improvement factor [HAL 89]

A two-dimensional array can be obtained by combining two linear arrays where each line and each column is a linear sequential array. In this case, the physical orientation angle and the phase difference angle applicable to the (n, m) element is defined as:

$$\Phi_{nm} = \frac{(n-1)\pi}{N} + \frac{(m-1)\pi}{M} \quad [7.30]$$

When the elements are circularly polarized, the 2-D sequential arrays enable the performance of a conventional array to be increased by:

- multiplying the 3 dB axial ratio bandwidth by 3–6;
- multiplying by 2 the matching bandwidth defined as the frequency bandwidth for which voltage standing wave ratio (VSWR) < 1.5.

In Figure 7.12, we give the characteristics of a 4×4 array, made up of subarrays sequentially fed about 11 GHz [DUS 01]. The band-widening performances are of order of magnitude predicted previously (Figure 7.13). The radiation patterns indicate good cross-polarization performance (<20 dB) in the principal and diagonal planes (Figure 7.14). Finally, the change of gain with frequency indicates good performance stability between 10.8 and 11.8 GHz (Figure 7.15).

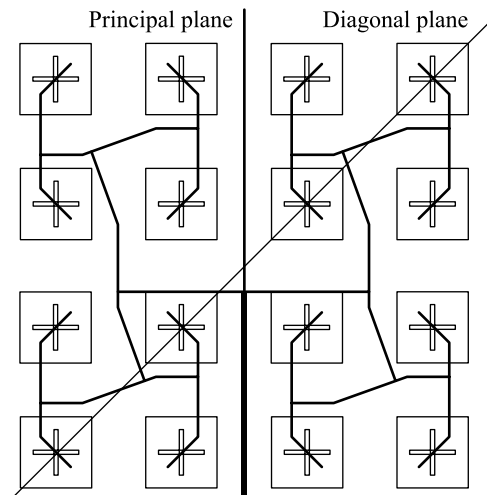


Figure 7.12. 4×4 array obtained by the phase feeding of four 2×2 subarrays presenting sequential rotation

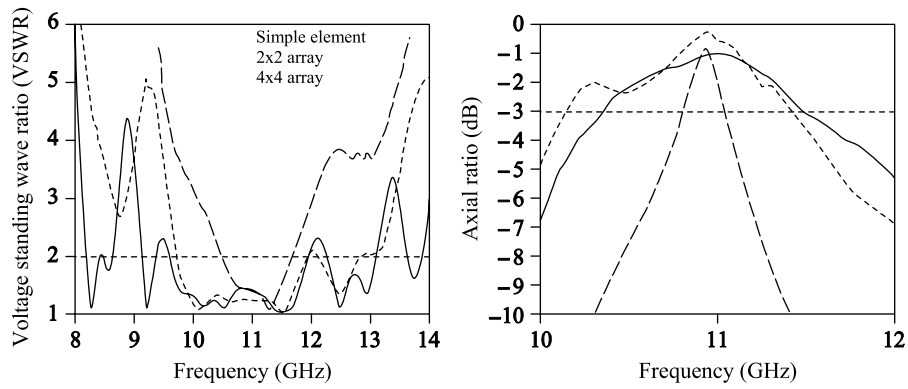


Figure 7.13. Experimental VSWR and axial ratio at broadside.
Simple element (—), 2×2 array (-----), 4×4 array (.....)

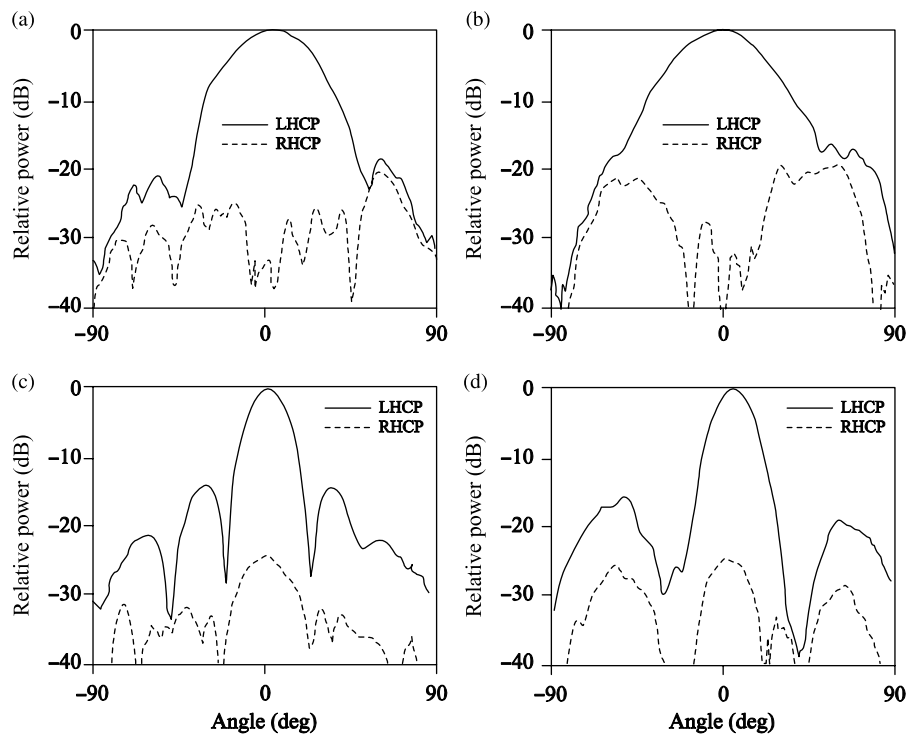


Figure 7.14. Radiation of 2×2 and 4×4 arrays in the principal and diagonal planes at 11 GHz: (a) 2×2 principal plane, (b) 2×2 diagonal plane, (c) 4×4 principal plane, and (d) 4×4 diagonal plane (—) LHCP, (---) RHCP

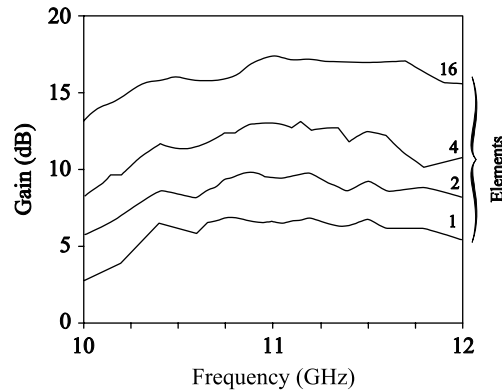


Figure 7.15. Gain as a function of frequency for different array dimensions

7.4.2. Sequential rotation applied to a radiating element fed by multiple feeds

The concept of sequential rotation can be applied to different excitation points of a single radiating element (Figure 7.16), with phase differences dependent on their positions [HAL 89].

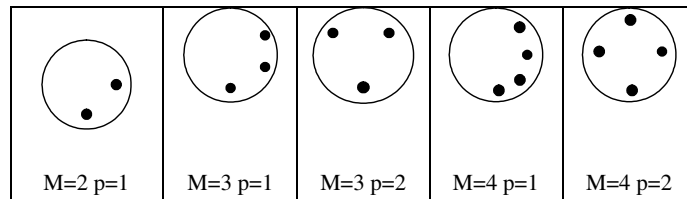


Figure 7.16. Circular radiating element fed by multiple feeds – configuration for different arrangements of sequential rotation

However, the significant level of mutual coupling between the feed probes, which is associated with a variable phase difference of the feeds when the frequency is extended beyond the resonant frequency, leads to a mediocre axial ratio and a reduced bandwidth for most pairs (p, M).

For certain configurations, such as the four-point feeds for p = 2 (Figure 7.17), the sequential rotation of the feeds is, on the other hand, beneficial. The higher modes are then markedly less pronounced, which promotes widening of the circular polarization bandwidth. We will use the example of the circular patch to prove this attenuation.

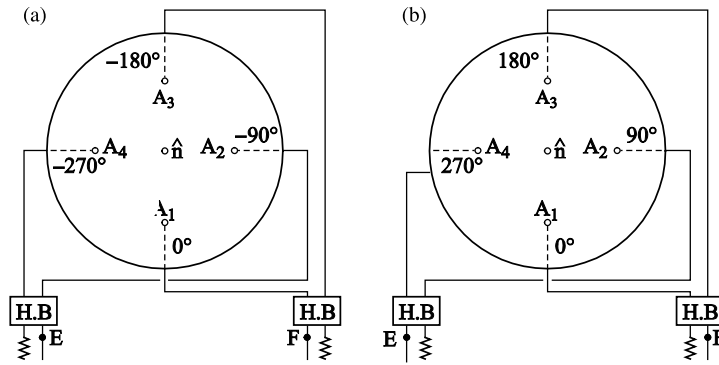


Figure 7.17. Right-hand (a) or left-hand (b) circular polarization and limitation of the higher TM_{21} mode

For the circular element, the TM_{10} and TM_{01} modes are dominant and the first higher order mode is the TM_{21} . The TM_{21} mode is all the more excited when the substrate thickness is significant and its permittivity is low (low quality factor).

Owing to its structure, this mode creates cross-polarization. It also increases the coupling between ports if the TM_{10} and TM_{01} modes are individually excited by two orthogonal branch-lines.

The distribution of currents on the surface of the radiating element for the different modes is illustrated in Figure 7.18. The feed topology consisting of four phase sources: 0° , 90° , 180° , and 270° (Figure 7.17), enables the TM_{10} and TM_{01} modes to be strengthened and the TM_{21} mode to be destroyed due to the symmetry of these modes and the antisymmetry of the excitations.

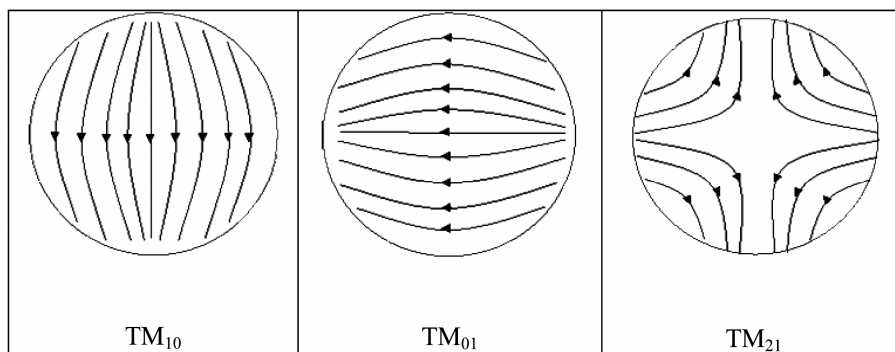


Figure 7.18. Current modes on a dual-feed circular patch

However, placing this element into an array structure can be a very delicate operation with four simultaneous excitations, and for this we tend to favor a dual-feed antenna using two notches to reduce the excitation of the TM_{21} mode.

7.5. Spiral and quadrifilar helix antennas

7.5.1. Spiral antennas

Spiral antennas, and particularly planar two-arm spiral antennas, naturally create circular polarization around the normal of the spiral plane. This polarization remains of good quality in a significant angular cone and for a wide frequency band. Their planar shape and relatively reduced size enable easy integration of spiral antennas on existing surfaces (such as aircraft fuselages).

7.5.1.1. Frequency independent antennas

When the dimensions of the radiating zones relative to wavelength are unchanged when the frequency is modified, the antenna is said to be frequency-independent [TER 71, BAL 05, DYS 59]. Spiral antennas satisfy this definition with dimensions included between two circles of radius: r_1 and r_2 , setting the high and low frequencies of the operating frequency band. The current weakens through radiation as the distance to the feed point is extended. As a consequence, with the energy reflected at the end of the arms being low, the input impedance and the input current vary little over a wide frequency band.

7.5.1.2. Principle of operation in order to obtain circular polarization

A two-arm spiral can be modeled by a bifilar line, which is gradually transformed into a radiating structure owing to its geometry. In a spiral, the path difference between the currents considered on each arm at adjacent points increases with the distance relative to the center of the spiral. When the path difference corresponds to $(n + 1/2) \lambda$ with excitation in phase opposition between the two arms (odd mode) or $n \lambda$ with excitation in phase between the two arms (even mode), there is strong local radiation around the adjacent points. The feed occurs as a result of a wideband balun, which separates the current into two and produces the required phase difference between the arms.

Let us consider the flat two-arm spiral antenna (Figure 7.19) fed via A and B. This antenna has been simulated using the high-frequency structural simulator (HFSS) software package. The point O is the center of symmetry of the antenna. P and Q are situated on the origin arms A and B, respectively, with $OP = OQ = r$.

We note that P' and Q' are the points adjacent to P and Q , respectively, on the other arms. If the space between the lines Δr is much less than r , then the arc QP' is equal to πr .

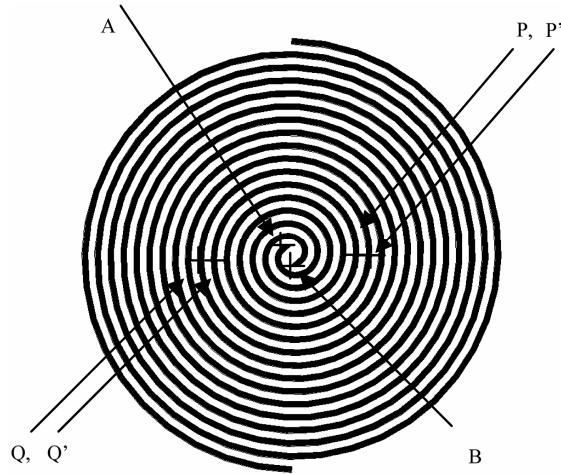


Figure 7.19. Two-arm spiral

The path difference for two neighboring points is therefore πr . For $\pi r = \lambda/2$ (circumference equal to λ) and excitation in phase opposition in A and B , we observe that the currents in P and P' are in phase (phase φ) and that the currents in Q and Q' are also in phase (phase $\varphi + 180^\circ$), with an opposite orientation to the currents in P and P' .

As a result, the currents in (P, P') and (Q, Q') are combined for a radiation maximum at the axis. Since the radiation of adjacent arcs is equal in intensity but in phase quadrature ($\pm 90^\circ$), the polarization is therefore circular at the axis.

The spiral antenna presented for this study is matched in the band [0.7 GHz, 5 GHz]. The simulation has been produced using the HFSS software package. The antenna is excited by two ideal voltage generators in phase opposition.

The parametric equations characterizing an arm of the antenna are given by:

$$\begin{aligned} x &= R_1 + R_0 t \cos(t) \\ y &= R_1 + R_0 t \sin(t) \\ R_0 &= (S + W) / \pi i \end{aligned} \quad [7.31]$$

where $R_1 = 3$ mm, $S = 3$ mm, $W = 3$ mm, and π ranges from 0 to 16π , where S and W correspond to the width of the slot between two metallic arms and the width of the metallic arm, respectively.

In Figure 7.20, we present the surface currents on the arms of the spiral for four frequencies included in this operating band.

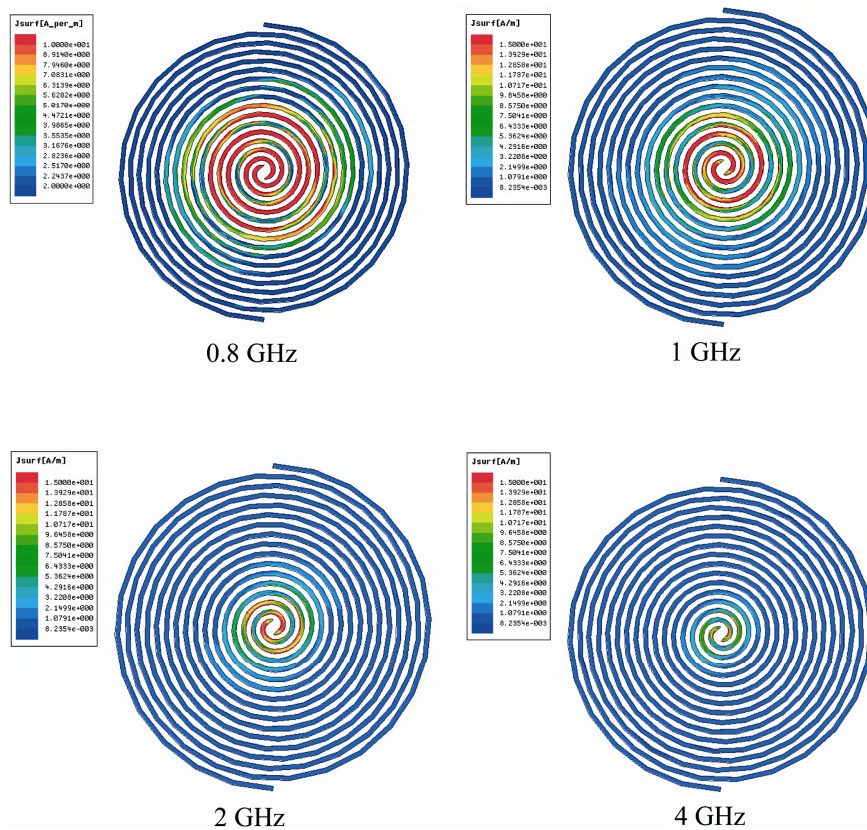


Figure 7.20. Surface currents for frequencies 0.8, 1, 2, and 4 GHz

The area of the spiral, which contributes to the radiation, is a ring whose diameter is reduced at high frequencies. We will therefore observe a displacement of the phase center of the antenna, which is characteristic of a dispersive antenna.

With the currents being strongly attenuated before reaching the ends of the arms for each frequency, good matching ($S_{11} = -30$ dB) is observed over the operating

band. When the length of the arms is small relative to the wavelength, the reflected current causes the circular polarization to deteriorate. For frequencies less than 0.7 GHz, the antenna is no longer matched ($S_{11} = -7\text{dB}$ at 0.5 GHz) and presents an average quality of polarization at broadside with $\text{AR} > 3\text{ dB}$ (Figure 7.21).

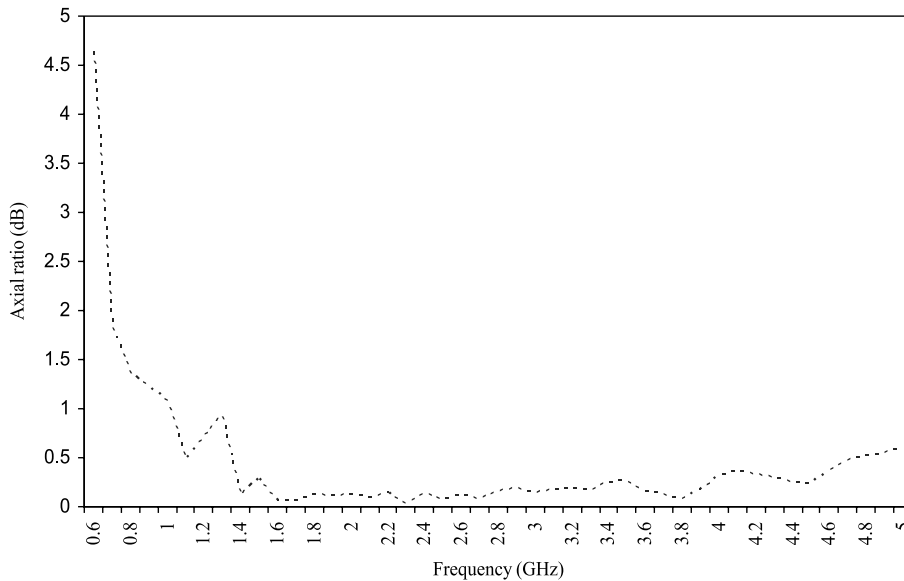


Figure 7.21. Polarization at broadside as a function of frequency for a spiral antenna

For each frequency examined, we can trace the axial ratio as a function of the angle of elevation θ in the xOz plane normal to the plane of the antenna. It appears that polarization remains circular ($\text{AR} < 3\text{dB}$) in a cone ranging from 100° to 130° around the perpendicular (Figure 7.22) depending on frequency. The cone becomes wider as the frequency increases.

The gain and aperture angle determined from Figure 7.23 vary between 2.7 dB and 80° at 1 GHz and 4.6 dB and 48° at 2 GHz.

The change in spiral antenna gain as a function of frequency in Figure 7.24 shows a strong variation in gain between 2 and 4.5 dB over the band (0.7–5.0 GHz).

Spiral antennas are therefore characterized by circular polarization at the axis perpendicular to the spiral within a solid angle of $60\text{--}80^\circ$, bidirectionality of the radiated field, as well as by matching and circular polarization in a very large bandwidth of up to a decade.

One of the major disadvantages is the dispersive nature of the spiral with a moving phase center and a strong gain variation, which renders these types of antennas of little use for pulsed applications.

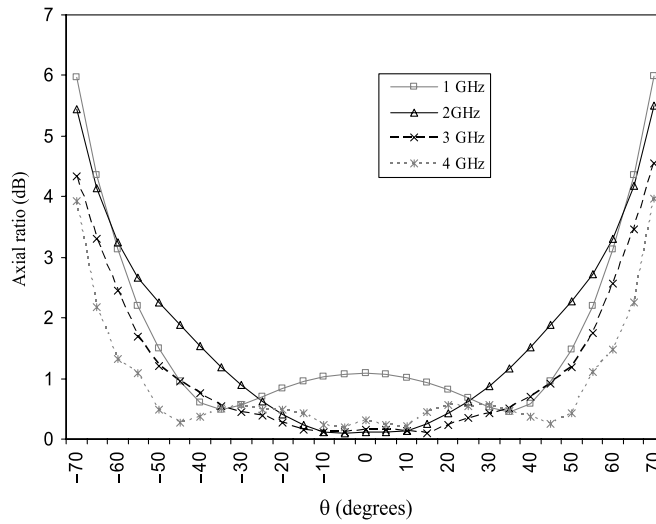


Figure 7.22. Axial ratio as a function of the angle of elevation for 1, 2, 3, and 4 GHz

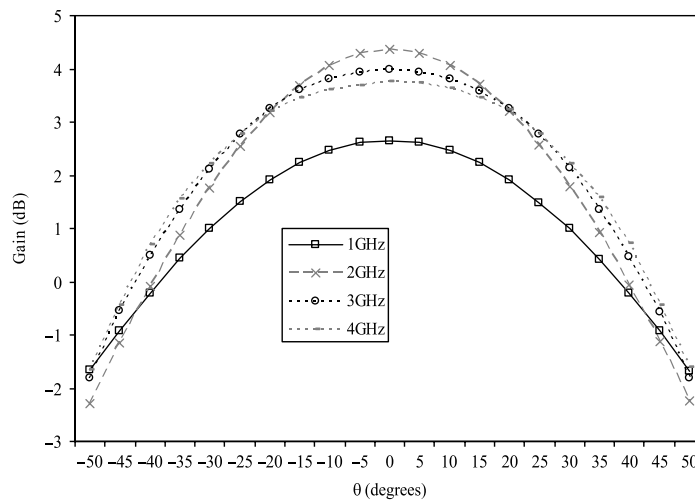


Figure 7.23. Gain as a function of the angle of elevation for 1, 2, 3, and 4 GHz

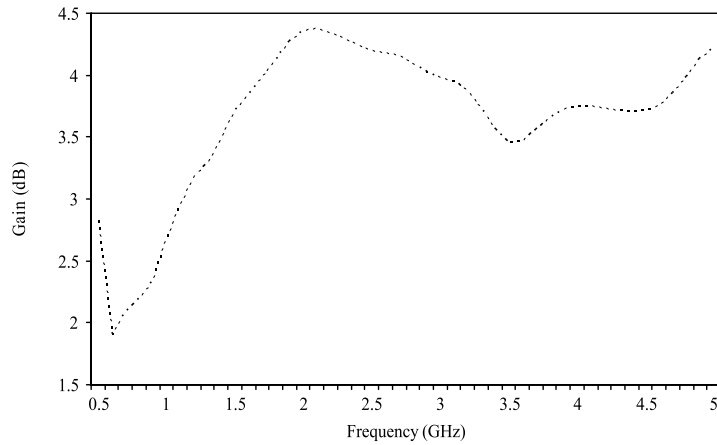


Figure 7.24. Gain as a function of frequency for $\theta = 0^\circ$ and $\phi = 0^\circ$

7.5.2. Quadrifilar helix antennas

The quadrifilar resonant antennas studied by Kilgus [KIL 69] provide a quadri-hemispheric radiation pattern and virtually perfect circular polarization. These characteristics make them attractive for navigation satellite terminals or telephony with orbital satellites.

7.5.2.1. Monofilar helix antenna

7.5.2.1.1. Sizing – normal and axial operating modes

A cylindrical helix can be defined by a circular cylinder of radius a , oriented along axis z , and with a base in the plane xOy (Figure 7.25, where only one of the wires is considered, such as that fed by the 0° phase).

Considering the cylindrical coordinate system, the equations of the helix are as follows:

$$x = a \cos \phi; y = a \sin \phi; z = a \phi \tan \alpha \quad [7.32]$$

where α is the angle of inclination of the helix, i.e. the angle between the helix and the uncoiled base of the cylinder on which it stands. Let $D = 2a$ be the diameter of the helix, C its circumference, L the length of one turn, S the axial distance between two consecutive points of the helix with the same ϕ , and N the number of turns. C_λ , S_λ , and L_λ represent the respective distances in wavelength. These three parameters are enough to completely describe the helix.

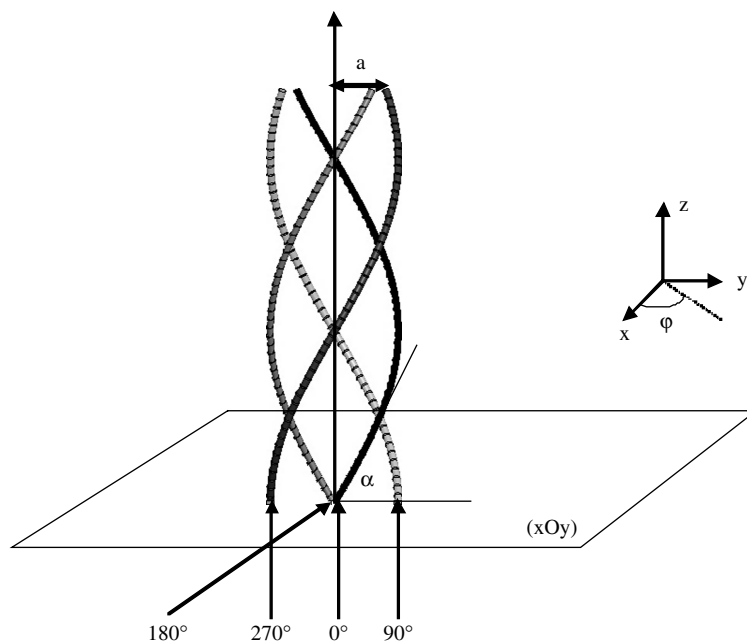


Figure 7.25. Quadrifilar helix

Let us consider first of all a monofilar helix antenna. On the basis of electrical size of the antenna, the helix operates either in its normal or axial mode. If the dimensions of the antenna are small relative to the wavelength ($D \ll \lambda$, $NS \ll \lambda$, $C_\lambda < 0.75$), then the maximum radiation is normal at the axis of the helix and the antenna is in its normal mode.

If, on the other hand, the circumference of the helix is of the order of one wavelength ($0.75 < C_\lambda < 1.25$), then the maximum radiation occurs along the axis of the helix and the antenna is in its axial mode.

7.5.2.1.2. Study of the normal mode of the monofilar helix

The geometry of the helix is reduced to a ring when angle α is near to 0, and a wire when α approaches 90° . Since the geometric limits of the helix are either a ring or a dipole, the field radiated by a small helix (small relative to the wavelength) can be modeled by combining the radiated fields of small rings and short dipoles placed in series.

The diameter of a ring is the same as that of the helix (D) and the length of a dipole is in the first instance identical to the distance between the rings S . As the

helix is small and short, we consider that the distribution of the current is uniform in amplitude and phase along the whole length of the helix and that the far-field radiation pattern, which is independent of the number of turns, is obtained from a single turn of the helix, modeled by a ring of diameter D and a dipole of length S .

Let I be the complex amplitude of the current and ω its angular pulsation. The sole non-null component of the electrical field radiated by the small ring of diameter D is E_ϕ , given by:

$$E_\phi = \eta k^2 I A \frac{e^{-jkr}}{4\pi r} \sin \theta \quad [7.33]$$

where $A = \pi D^2/4$ is the area of the ring, $k = \omega(\mu\epsilon)^{1/2}$ is the propagation constant, and $\eta = (\mu/\epsilon)^{1/2}$ is the intrinsic impedance of the medium. For the small dipole of length S , the single component of the electrical far-field is E_θ , given by:

$$E_\theta = j\omega\mu S \frac{e^{-jkr}}{4\pi r} \sin \theta \quad [7.34]$$

The total field radiated for one turn is therefore:

$$\overline{E} = \overline{a}_\theta E_\theta + \overline{a}_\phi E_\phi = (\overline{a}_\theta j\omega\mu S + \overline{a}_\phi \eta k^2 A) I \frac{e^{-jkr}}{4\pi r} \sin \theta \quad [7.35]$$

The normalized pattern of the field radiated from the helix in normal mode is:

$$f(\theta) = \sin(\theta) \quad [7.36]$$

The field is null along the axis and at its maximum in the plane $\theta = 90^\circ$ normal to the helix. As E_θ and E_ϕ are out of phase by 90° , the radiated wave is elliptically polarized. The axial ratio of the far-field polarization ellipse is obtained by dividing the amplitudes and is equal to:

$$AR = \frac{|E_\theta|}{|E_\phi|} = \frac{\omega\mu S}{\eta k \frac{2\pi}{\lambda} A} = \frac{S\lambda}{2\pi A} = \frac{2S\lambda}{(\pi D)^2} \quad [7.37]$$

where $k = 2\pi/\lambda$ and $\eta k = \omega\mu$. Polarization is purely circular for $|E_\theta| = |E_\phi|$ or $AR = 1$ obtained with:

$$C = \pi D = \sqrt{2S\lambda} \quad [7.38]$$

Under this condition, the radiated field is circularly polarized in all directions, except for along the axis, where the radiation is null.

7.5.2.2. *Quadrifilar helix antenna*

A quadrifilar helix is constructed by adding three monofilar antenna wires. The four wires are positioned equidistant apart and are fed by signals of the same amplitude but out of phase by 0° , 90° , 180° , and 270° , respectively (Figure 7.25).

The experimental data [ARL 74] indicate that:

- the quadrifilar helix antenna operates in axial mode for C_λ between 0.4 and 2, whereas for the monofilar helix its value must be between 0.75 and 1.25;
- it operates in normal mode when C_λ is smaller than the lower limit of the frequency band defined in axial mode.

Quadrifilar helices have been simulated using the HFSS software package in order to emphasize these two modes.

The helices comprise 0.1 mm diameter wires using an electrically perfect conductor. The cylinder on which they rest is made of air.

We obtain a normal radiation mode in the case where the parameters of the helix are such that $\alpha = 72^\circ$, $N = 1.8$, $C = 38 \text{ mm} = 0.3\lambda_0$ (at 2.35 GHz, $\lambda_0 = 127 \text{ mm}$) and an axial radiation mode for parameters of the helix such that $\alpha = 60^\circ$, $N = 0.6$, $C = 105 \text{ mm} = 0.62\lambda_0$ (at 1.76 GHz, $\lambda_0 = 170 \text{ mm}$) [SHA 93].

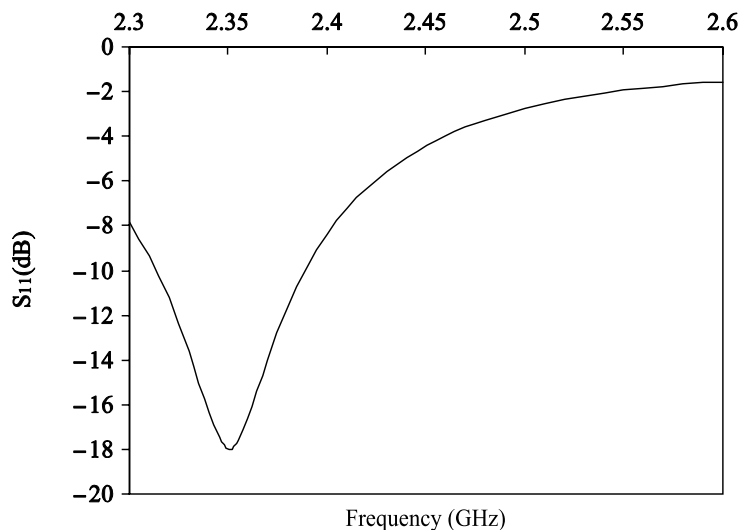


Figure 7.26. S_{11} (dB) as a function of frequency (normal mode)

In normal mode, the quadrifilar antenna presents maximum radiation in the vertical plane when the angle of elevation is equal to 90° , and circular polarization for $63^\circ < \theta < 107^\circ$ (the axial ratio is less than 3 dB for these angles of elevation) while the side lobes are 20 dB below the principal lobe (Figures 7.26, 7.27 and 7.28).

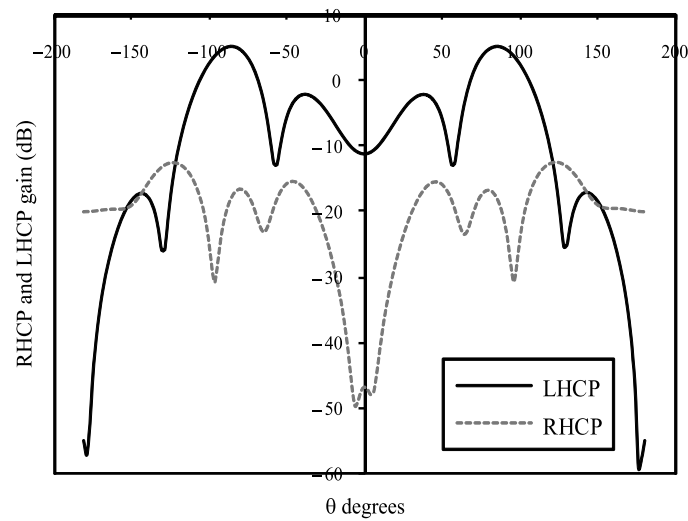


Figure 7.27. Gain (dB) in right- and left-hand polarization as a function of the angle of elevation at 2.35 GHz (normal mode)

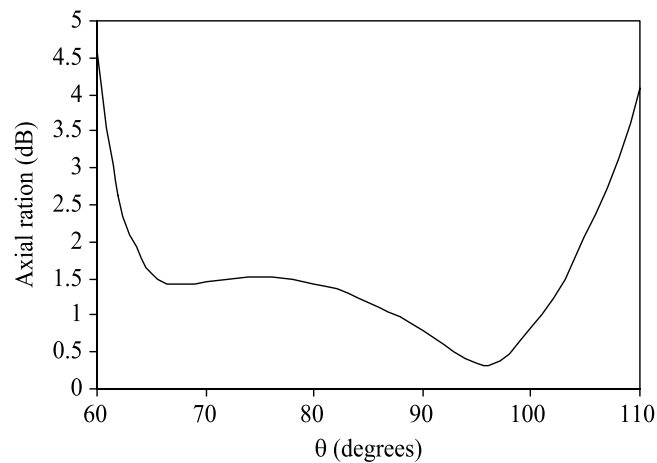


Figure 7.28. Axial ratio (dB) as a function of the angle of elevation at 2.35 GHz (normal mode)

These characteristics respond to the specificities required for communications between a lighthouse and seagoing vessels: CP radial radiation with a good axial ratio ($AR < 3$ dB for $75^\circ < \theta < 105^\circ$) as well as low levels of side lobes in the operating band.

In axial mode, the quadrifilar antenna presents maximum radiation at mid-power in a 200° range around the axis in the vertical plane and circular polarization in a 100° range around the axis.

Cross-polarization is at least 10 dB below the principal polarization with the most restrictive band (Figures 7.29, 7.30 and 7.31). This antenna follows the main specificities required for satellite communications: 360° coverage in azimuth for circular polarization guaranteeing an axial ratio of less than 5 dB as well as low levels of side modes in the operating band.

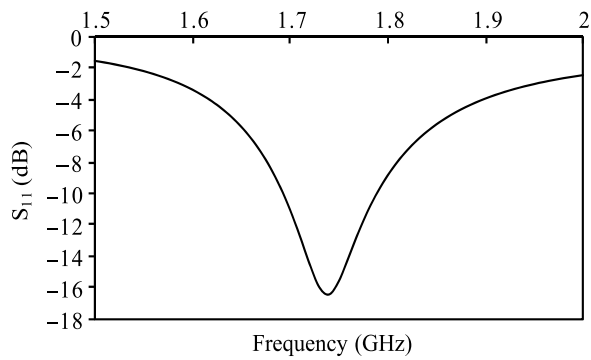


Figure 7.29. S_{11} (dB) as a function of frequency (axial mode)

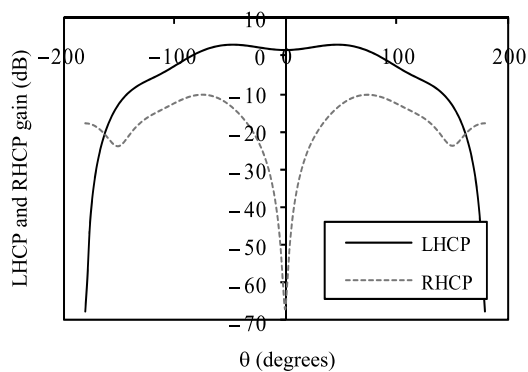


Figure 7.30. Gain (dB) in right- and left-hand polarization as a function of the angle of elevation at 1.76 GHz (axial mode)

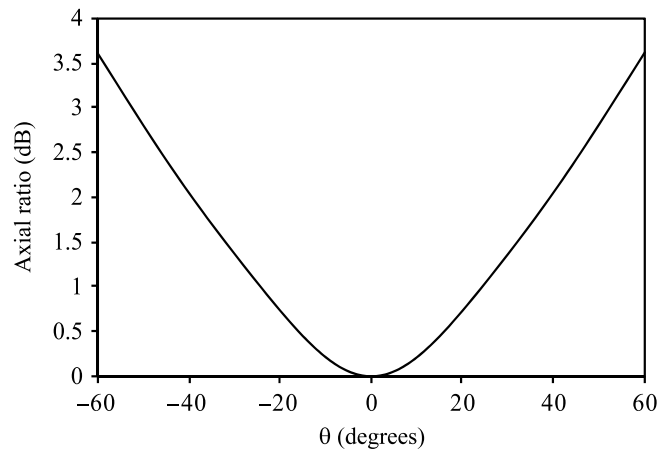


Figure 7.31. Axial ratio (dB) as a function of the angle of elevation at 1.76 GHz (axial mode)

Quadrifilar helix antennas have two advantages over monofilar helix antennas: an increase in bandwidth and low operating frequency in axial mode. The main disadvantage is the complexity of the feed system, with the quadrifilar helix antenna requiring a feed system of signals with similar amplitudes, but out of phase by 90° for each of the branches. There are several solutions:

- a circuit comprising 3 dB/ 90° couplers and a hybrid ring implanted at the base of the antenna, which is simple to design but not very compact;
- feeding of each bifilar helix using a “folded balun”, which enables currents of the same amplitude and in phase opposition to be excited, with each bifilar helix being fed in phase quadrature using a hybrid coupler (a complex and bulky circuit resulting from the assembly of balun and adapter, further reducing the operating band);
- a [KIL 69] circuit, consisting of a coaxial line, split at its extremity in order to create a balun (phase quadrature is thus assured by adjusting the length of the branches, which makes tuning a delicate operation and reduces the operating band).

7.6. Conclusion

Having recalled the characteristic antenna parameters of circular polarization, we have presented a number of CP antennas while qualitatively and/or quantitatively explaining their principles of operation. We have particularly examined a linearly or circularly polarized radiating element, where arranging in an array enables the

axial ratio bandwidth to be widened, a spiral antenna which, despite a bandwidth of one decade, is poorly matched to ultra-wideband pulse radios because of the frequency dispersion that it presents, and quadrifilar helix antennas in normal and axial mode. The principal characteristics of the last two antennas were illustrated using the HFSS software package.

Chapter 8

Wideband Antennas

Wideband is a relative term used to describe a wide range of frequencies in a spectrum, typically from 10% to one octave and sometimes more than a decade bandwidth. This bandwidth is related to a characteristic of the antenna; in general this refers to matching, but it can also equally refer to polarization or radiation pattern.

There are essentially two main applications for wideband antennas. The first is related to the world of radar. In order to detect an object which would be hidden at certain frequencies, it is important to illuminate the targets with a wideband signal. Similarly, for reasons of accuracy in localization with pulse radars, as narrow a pulse as possible must be produced in order to increase the range resolution. It is therefore necessary in this case to widen the frequency bandwidth.

The second reason is linked to the definition of channel capacity [SHA 49]. With a workable signal-to-noise ratio, capacity is thus proportional to bandwidth. The new video signal standards, such as MPEG-4, require high transmission rates and therefore a wide frequency band. Spread spectrum modulation techniques similarly require wide frequency bands. In recent years, applications classified under the acronym UWB (ultra-wideband) have become known as a result of numerous developments in localization and communication for the two reasons stated above.

There are several possible strategies for antenna design. The choice of design approach depends on the application, particularly the available space for the antenna and then by implication the frequency band and the desired gain.

The principles of antenna design will be detailed for the following:

- wideband antennas that couple the intrinsic resonances of the radiating element;
- traveling wave antennas;
- frequency independent antennas;
- UWB antennas.

8.1. Multiresonant antennas

8.1.1. Principle

In previous chapters, we have shown that microstrip antennas could be modeled using the cavity method. As the name indicates, this refers to a model using resonances of a cavity-type antenna, which is therefore intrinsically of low bandwidth. However, it is possible to attenuate this resonance with the coupling of one or more neighboring resonances in order to form a wideband antenna.

8.1.2. Widening bandwidth through resonance coupling

Figure 8.1 shows two methods which enable the bandwidth of a patch antenna fed via a coaxial connector to be widened. A slightly differently sized passive antenna (or even two for reasons of symmetry), set to a close frequency, is placed in proximity of the antenna. The proximity of this new resonance enables the bandwidth of the original antenna to be widened. This operation can be carried out either in the same plane as the antenna (a) or in superposition (b).

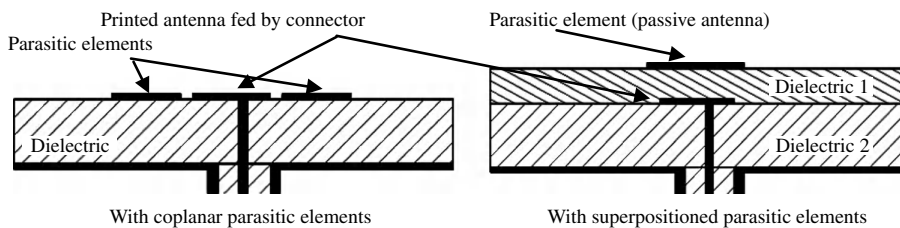


Figure 8.1. Different mechanisms for widening bandwidth using resonance coupling

The bandwidth obtained is thus much greater [WOO 80, SAB 83] than that observed for a microstrip structure, that can be considered as a cavity which intrinsically restricts the bandwidth of the antenna. Another method for widening bandwidth involves moving this ground plane far from the radiating part, which then becomes a reflector for the antenna.

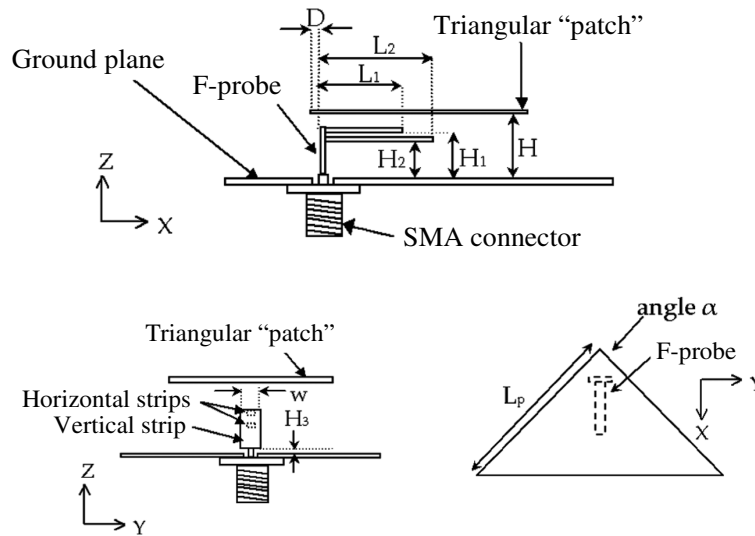


Figure 8.2. Description of an F-probe triangular antenna

In Figure 8.2, the ground plane has been moved far from the antenna. The inductive effect created as a result of the length of the connector must therefore be balanced out. This balancing is possible using a U slot [HUY 95] or by modifying the shape of the connector. The latter solution [LEP 05, LEP 08] is shown here. The F-probe is made up of a coaxial connector and two metallic strips which are welded to its inner conductor. This passes through the ground plane. The triangular radiating element is placed over the F-probe and is fed by electromagnetic coupling.

If we calculate the input impedance of the F-probe alone and compare it to the input impedance of its two constituent L-probes, we obtain the curves represented in Figures 8.3.

We note that the F-probe strongly indicates two distinct resonances resulting from the separately considered L-probes: (H_1, L_1) and (H_2, L_2) . We must also bear in mind that the coupling between the two parts of the F-probe tends to raise the values of the real and imaginary parts of the input impedance and then, as a result, make matching difficult.

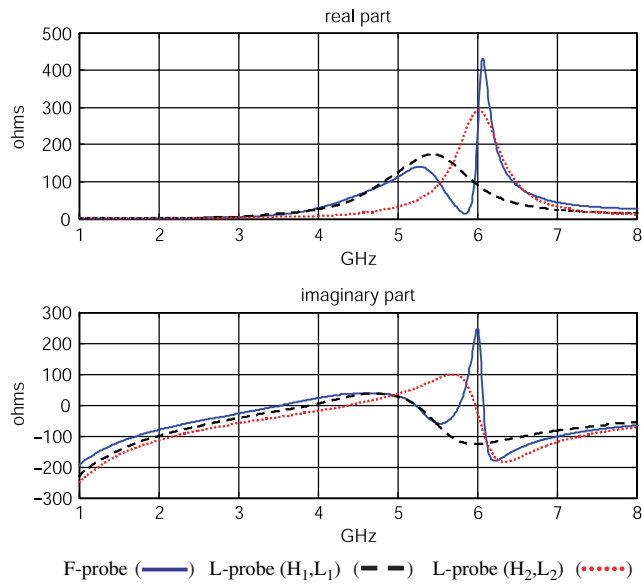


Figure 8.3. Real and imaginary parts of the input impedance of F- and L-probes

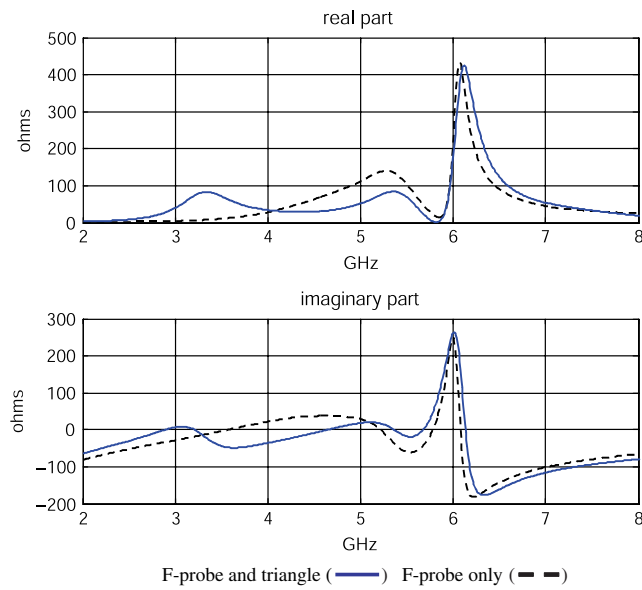


Figure 8.4. Real and imaginary parts of the input impedance of F-probe with and without triangle

If we now place the metallic triangular plate over the F-probe (Figure 8.4), we see the resonance of the triangle appears, which enables the real part of the input impedance to be increased between 3 and 4 GHz, and leads to an antenna matched to 50 ohms between 3 and 5.8 GHz.

The direction of the probe and the geometry of the triangle enable a radiation similar to that of a printed wideband antenna.

8.2. Traveling wave antennas

We have just seen that widening the bandwidth of a multiresonant antenna is tricky. These resonances are linked to standing waves trapped in the antenna. If we now consider that the antenna forms a transition between a guided structure and free space, we can construct a traveling wave antenna which does not therefore produce standing waves.

The best known structure is the horn antenna. When the transition between the waveguide and free space is progressive and over a greater distance than the wavelength, there is no obstacle to propagation and the antenna is then very well matched.

8.2.1. Tapered slot antennas

Waveguides, but more so transmission lines, support wideband propagation. A transmission line is therefore the ideal support for designing a wideband antenna.

Slot antennas with progressive transitions (TSA, tapered slot antenna) provide a good example of this principle [LEW 74, GIB 79], which involves progressively widening the slot (dual slots in the case of a microstrip line) in order to be matched to the free space impedance. This transition must be as smooth as possible in order to maintain good impedance matching and leads to an aperture near to the wavelength and therefore to a directional antenna. On the basis of the geometry of their slots (see Figure 8.5), we distinguish antennas whose slots are linear (LTSA, linear tapered slot antenna), broken linearly (BLTSA, broken linear tapered slot antenna), exponential then constant (CWSA, continuous width slot antenna), or exponential (Vivaldi).

TSA antennas are matched over very wide bandwidths, from 125% to more than 170% [GUI 98]. Radiation from these is unidirectional in the substrate

plane and presents a low cross-polarization level. Their directivity increases with frequency and the gains obtained by these antennas are in the range between 7 and 10 dB, depending on the type of TSA. These qualities, linked to a low dispersion in time domain, make them ideal candidates for subsurface radar applications, electromagnetic compatibility, or in metrology, since they can be arranged in an array with small gaps between antennas. They can also be used as a primary source for wideband reflectors.

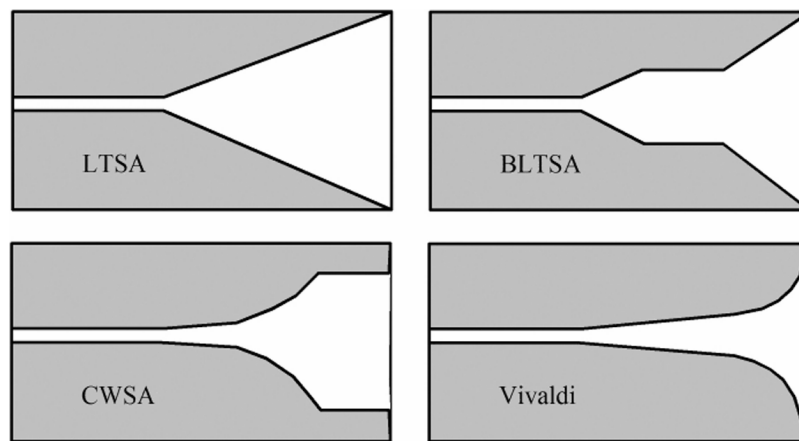


Figure 8.5. Variants of tapered slot antennas

8.3. Frequency independent antennas

8.3.1. Introduction

This category of antenna covers those whose characteristics (radiation pattern, input impedance, and polarization) remain unchanged over theoretically infinite bandwidths. We saw in previous chapters how the “useful” behavior of an antenna was obtained for antenna dimensions close to the wavelength (more precisely, a half or a quarter of the wavelength). In other words, if we reduce the dimensions of an antenna by a factor of α , just its working frequency will be increased by α , but the rest of its characteristics will remain unchanged. In 1957, Rumsey [RUM 57] published a general theory on frequency independent antennas, which was based on results obtained using equiangular antennas. He showed that an antenna formed of elements, which can be deduced from each other using homothety, and uniquely defined by its angles, is frequency independent.

8.3.2. Equiangular antennas

The mathematical equation which satisfies the two preceding conditions is a logarithmic spiral.

Let $\rho(\theta) = \rho_0 \exp(\alpha \theta)$ where ρ_0 is the radius centered at $(\theta_0 = 0)$, and α is the coefficient regulating the expansion of the spiral (Figure 8.6).

If a section ρ_0 radiates at λ_0 , then, for $\lambda_1 > \lambda_0$, there is further a rigorously homothetic part ρ_1 , in the ratio λ_1/λ_0 , which will then radiate at λ_1 , as ρ_0 radiated at λ_0 .

In order for the antenna to have a constant impedance, independent of frequency, the width of the radiating section must remain proportional to the length of the arms, and therefore increase according to the distance of the feed point of the antenna from the center of the spiral.

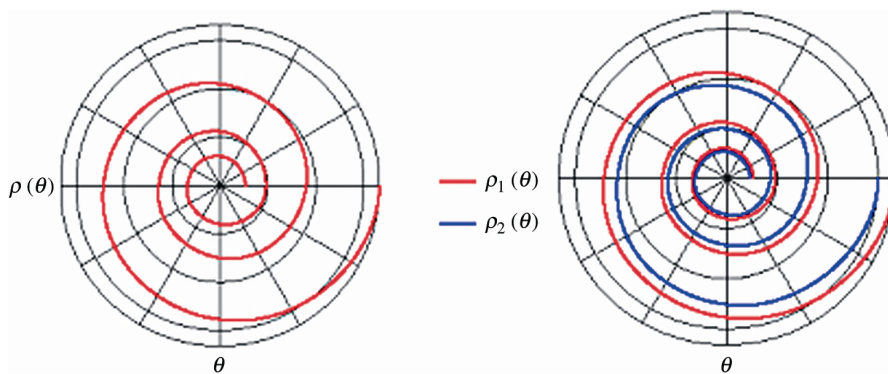


Figure 8.6. Construction of a logarithmic spiral

To define a plane antenna, it is therefore advisable to define the equations of two spirals which form the edges of a metallic strip: $\rho_1(\theta) = \rho_0 \exp(\alpha \theta)$ and $\rho_2(\theta) = \rho_0 \exp(\alpha (\theta - \delta))$ (Figure 8.7). We could equally use the same principle to construct a conical spiral [DYS 59].

The antenna is usually formed from two spirals, with the same center and with the second spiral having been obtained after a rotation of π , which result in a symmetrical structure. It is thus defined solely by its angle of rotation θ , the length of its arms, and the spiral rate $1/\alpha$ (Figure 8.7).

The bandwidth of this antenna is theoretically uniquely limited by its dimensions. The central section fixes the high operating frequency, which must be low compared to the shortest wavelength (usually less than $\lambda/8$). The low operating frequency is given by the maximum length of the radiating arms. We can simply explain the principle of radiation from the antenna as follows: at the feed point, two distributions of currents in phase opposition each spread along one of the arms. The proximity of the two arms in the central area is therefore identical to a transmission line where there is no radiation. When the current propagates and moves away from the central section, radiation is produced, which reaches its maximum when these same currents are in phase. This condition is verified over a ring with a circumference equal to the wavelength. Through construction, this spiral produces a circular, or even elliptical polarized radiation when the current has not been totally radiated at the extremities of the arms (see Chapter 7). Finally, in order to excite this symmetrical antenna structure with the help of an SMA connector, a balun is very often required. Indeed, the input impedance of a logarithmic spiral antenna is typically between 75 and 100 Ω and varies depending on the thickness of the arms and the substrate used; that of a self-complementary slot spiral antenna is 188.5 Ω (60π), in accordance with Babinet's principle. This type of wideband balun sometimes affects the performance of antennas by adding losses and limiting their bandwidth. There is however some very wideband baluns with low loss levels, for which the design has nowadays been perfected [BEG 96].

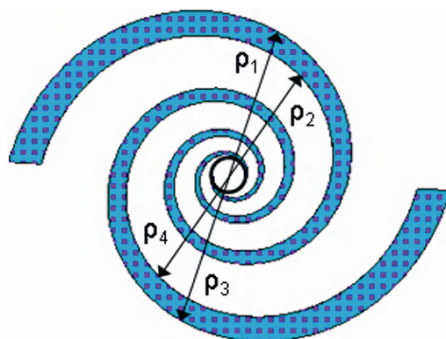


Figure 8.7. *Two-arm logarithmic spiral antenna*

8.3.3. Log-periodic antennas

We have seen that the relative dimensions of an equiangular spiral antenna are found to be equal for all wavelengths via a continuous transformation with properties which are preserved at all frequencies. If this transformation is periodic, rather than continuous, with a logarithmic gap between each frequency, then a log-periodic antenna is designed.

8.3.4. Sinuous antennas

Archimedean spirals (see Chapter 7) and log-spiral antennas have been used for several decades over some extremely wide bandwidths, but, in his document [DUH 87], R.H. Duhamel shows that previous attempts at utilizing more than four periodic elements in order to provide two orthogonal polarizations with radioelectrical properties and similar dimensions have been fruitless.



Figure 8.8. Dual polarized sinuous antenna

The geometry of the sinuous antenna (Figure 8.8) can be presented as a hybrid of spiral and log-periodic antennas. The geometry of the arms resembles the log-periodic antenna and allows dual polarization. When the sinuous antenna is self-complementary, its input impedance is frequency independent, as we have seen previously.

Usually, this planar antenna is positioned over a cavity containing the feeding system and an absorbent whose principal function is to remove back radiation. The antenna is printed onto a substrate of low permittivity. The sinuous antenna is made of p cells, with each cell being defined by the two parameters α_p and τ_p (Figure 8.9).

Equation for the average fiber (Figure 8.9) of the p th cell for $|\phi| \leq \alpha_p$:

$$\phi = \frac{2\alpha_p (-1)^p \ln\left(\frac{r}{R_p}\right)}{\ln \tau_p} \quad \text{and} \quad R_{p+1} \leq r \leq R_p \quad \text{with} \quad \tau_p = \frac{R_{p+1}}{R_p} \quad [8.1]$$

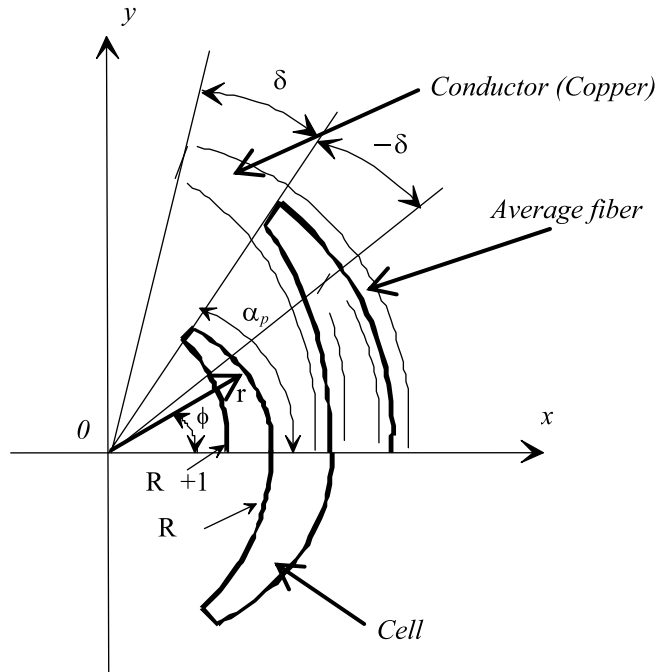


Figure 8.9. Construction of the geometry of the sinuous antenna

Equation of the average fiber of the p th cell for $\alpha_p \leq |\phi| \leq \alpha_p + \delta$:

$$r = \sqrt{\tau_p} R_p \quad [8.2]$$

[JOH 93] presented an approximate formula in order to calculate the lowest operating frequency of such an antenna:

$$2r(\alpha_p + \delta) \approx \frac{\lambda}{2} \quad [8.3]$$

where the angles are expressed in radians. This lowest frequency is thus limited by the exterior radius of the antenna R_1 , where $\lambda_L = 4R_1(\alpha_1 + \delta)$.

As for high frequency, this is limited by the dimensions of the feeding zone. For good performance, the smallest segment of the feeding zone must be less than $\lambda_H / 4$ in order to provide a good transition between the feeding zone and the radiating zone of the antenna.

The highest operating frequency can then be calculated from:

$$2R_p(\alpha_p + \delta) \approx \frac{\lambda_H}{2} \quad [8.4]$$

The bandwidth of the antenna can therefore be controlled by adjusting the interior and exterior diameters of the antenna. The dimensions of the feeding system limit high operating frequencies.

The radiation pattern is bidirectional (without the cavity) and symmetrical in relation to the plane of the antenna, with maximum values perpendicular to the plane and null values at the level of the plane. The half-power beamwidth varies from 60° to 100° in planes E and H. The polarization is linear and the maximum gain is typically equal to 5 dB.

Since this antenna is self-complementary, its impedance is frequency independent, while remaining raised and close to 188.5Ω (60π), and it would be difficult to produce a very wideband feeding system enabling the transformation of characteristic impedance from 50 to 188.5Ω .



Figure 8.10. *Modified dual polarized sinusoidal antenna*

The geometry of this sinuous antenna can be modified [BEG 00] and so it is no longer self-complementary, but even so possesses a low fluctuating input impedance, which enables matching to a far weaker characteristic impedance approaching 100 ohms (Figure 8.10). Other radiation characteristics are similar to those of the sinuous antenna.

8.4. Ultra-wideband antennas

This final category, UWB, covers a diverse range of antennas. Development of all of these antennas is linked to the publication in 2002 of a recommendation of the US Federal Communications Commission (FCC), authorizing the transmission and reception, under a certain level, of signals in a frequency band ranging from 3.1 to 10.6 GHz. This radio transmission technique consists of utilizing signals whose spectrum is spread over a wide frequency band, typically between 500 MHz and several GHz. This spectral availability enables us particularly to reach high data-rates communications and also leads to a high spatial resolution for radars.

However, the current restrictions imposed by regulatory organizations on the power transmission level limit the range of UWB communications to a few meters for high data-rates, and just a few hundred meters for low data-rates. UWB technology therefore seems naturally well placed for short-range communications (WLAN, WPAN), which offer an alternative which is at the same time low cost and low power among the existing standards.

Today, the acronym UWB brings together two standards but distinct technologies. The first has its foundations in very short pulse transmission; this is known as a monoband or *Impulse Radio* approach. As for the second approach, this is based on the simultaneous utilization of several carriers. This is known as the multiband technique, where the frequency band is subdivided into several subbands. The modulation used in each subband is OFDM (orthogonal frequency division multiplexing).

The pros and cons of the mono- and multiband approaches are sensitive issues and have been the subject of many debates within the regulatory organizations. One particularly significant question concerns the minimization of interference during transmission and reception in the UWB system.

The multiple band approach is particularly interesting, since carrier frequencies can conveniently be chosen in order to avoid interference with narrowband systems. It thus offers more flexibility, but requires a greater level of control in the physical layer. UWB signals in the impulse radio technique require high performance RF

components (very short switching times) and very precise synchronization. UWB systems can then be developed at a relatively low cost.

Contrary to the multiband approach, which depends on techniques which are tried and trusted and readily available, impulse radio communication system architecture has given rise to numerous developments and has specifically necessitated the putting into place of new definitions and characteristics of antennas [BEG 10].

There are therefore two constraints which are strongly linked to the emergence of UWB technology: the first is the need to design compact antennas which are compatible with integration onto mobile or small-sized objects (WLAN, WPAN), and the second, for those antennas used in impulse radio mode, is not being able to change the shape of radiated pulse.

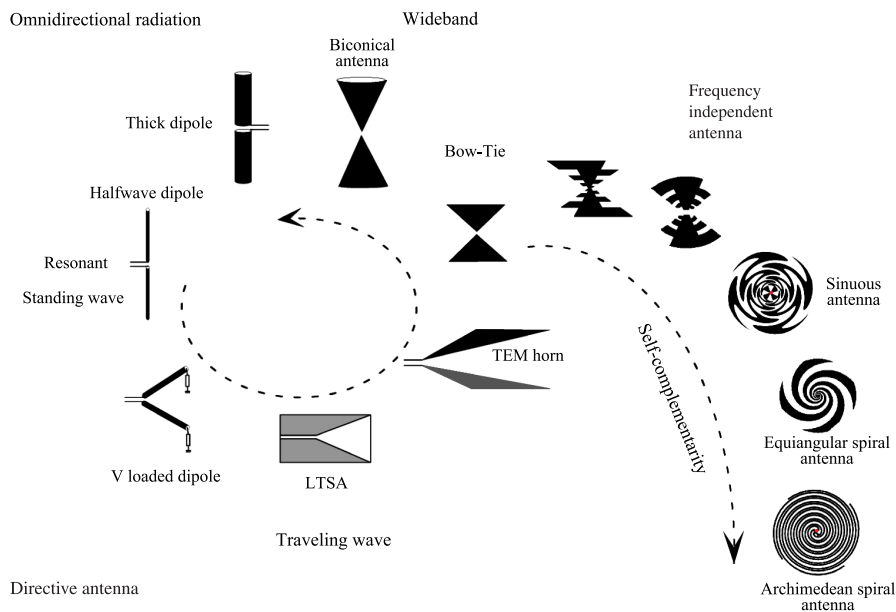


Figure 8.11. *Antenna metamorphosis: from resonant to frequency independent antenna*

The process of antenna “metamorphosis”, shown in Figure 8.11, allows the design choice to be guided toward a *Bow-Tie* type of geometry, to take account of the two constraints, above.

In fact, if we examine the process which enables the transformation of a standing wave antenna into a traveling wave one, i.e. folding a dipole, loading it, transforming it in a slot line and then in a transverse electro magnetic (TEM) horn, then we observe that the size of this type of antenna becomes significant. By shortening the length of this horn and straightening the two planes, we arrive at the so-called *Bow-Tie* geometry.

If we now carry out a transformation of, first, a thick dipole, then a bicone one, we come back again to *Bow-Tie* geometry. It is interesting to observe that when the aperture angle of the *Bow-Tie* is 90° , this geometry is self-complementary and therefore particularly well matched to stabilizing the input impedance of a wideband antenna. We must therefore come back to *Bow-Tie* geometry in order to work within the two constraints which were previously set out. It goes without saying that it would be preferable to opt for a monopole structure in order to minimize the size of the antenna.

The geometries considered can be tapered, triangular, circular, elliptical, or even rectangular. This class of UWB antennas is certainly the most representative and most used in telecommunications, since they preserve the interesting characteristics of omnidirectional radiation, as well as the principles of sizing of monopole or dipole antennas, which result in relatively compact structures.

The following section is a summary of the 3rd paragraph of Chapter 5 [BEG 10].

8.4.1. *Biconical and Bow-Tie antennas*

The infinite biconical antenna [STU 97] can be considered to be an infinite transmission line (Figure 8.12).

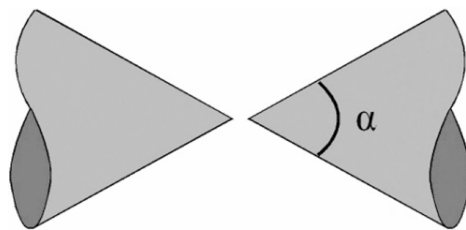


Figure 8.12. *Infinite biconical antenna*

The input impedance of such an antenna is given by:

$$Z_{in} = 120 \ln [\cot (\alpha/4)] \quad [8.5]$$

In reality, the antenna is not infinite and reflections appear at the extremities of the bicone, which limit the antenna's bandwidth. The bandwidths obtained with biconical antennas are typically from 120 to 150%. The radiation pattern is dipole-like, omnidirectional in the plane which is perpendicular to the axis of the cones and null at this axis and linearly polarized. The maximum gains are between 0 and 4 dB.

In a monopole configuration where we add a ground plane perpendicular to the axis of the half-cone, the antenna is called a discone antenna.

The *Bow-Tie* antenna is a planar version of the finite biconical antenna, which can be printed onto a substrate. This is a symmetrical structure where the currents are principally concentrated at its edges.

The *Bow-Tie* antenna performs less well in terms of bandwidth than the biconical antenna, being limited by the truncation of the antenna. Its input impedance varies more with frequency than that of the finite biconical antenna with the same dimensions [BAL 05]. A poorer quality of matching results from this, as well as lower bandwidth, but one which can nevertheless reach values greater than 100%.

Studies have been carried out in order to evaluate the influence of the flare angle α for a *Bow-Tie* antenna formed from two triangles of height $H = 3$ cm (Figure 8.13).

This study has been compared with the results obtained by Brown and Woodward [BRO 52] and shows the significance of this parameter on the lowest matching frequency and impedance stability of the antenna.

From this study, it is interesting to trace the length L in terms of the wavelength to the maximum of the real part of the impedance, as a function of the flare angle (Figure 8.14): we then observe that it is virtually equal to a half-wavelength, whatever the value of α .

In terms of radiation, the antenna presents a dipole-like radiation, i.e. omnidirectional in the plane perpendicular to that of the antenna. The resulting gains are therefore between 0 and 3 dB.

The *Bow-Tie* antenna can also be produced using slots in a metal plate or on a substrate [DIN 95], which enables a structure which is no longer symmetrical to be obtained. In this way, its feed can be ensured by the use of a coaxial cable without the use of a balun. However, the input impedance of such an antenna typically remains around 80Ω .

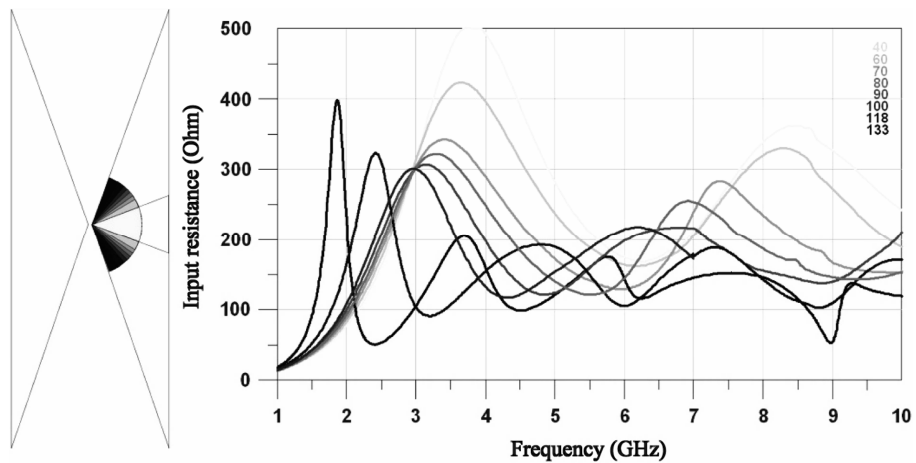


Figure 8.13. Influence of the value of the flare angle ($^\circ$) of the Bow-Tie antenna on the real part of the input impedance [BEG 10]

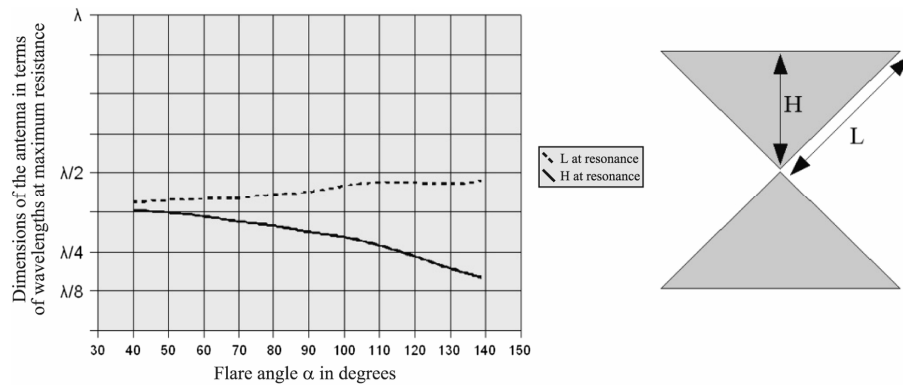


Figure 8.14. Height H and vertex L of the antenna, expressed in terms of wavelength at maximum resistance as a function of angle α [BEG 10]

8.4.2. Planar monopoles

8.4.2.1. Planar monopoles mounted over infinite ground plane

There are many works on planar monopoles mounted over infinite ground planes (or those which can be considered as infinite). Triangular and circular, and to a lesser extent square (Figure 8.15) structures are potentially antennas with wideband characteristics and their optimization leads to a wide variety of monopoles. The shape of the radiating element can also be elliptical, but too great an ellipticity ratio is detrimental to bandwidth [AGR 98].

The tilt of these elements modifies the symmetry of the unit and reduces the performances of the antenna [CHE 03]. In this section, therefore, we will solely concentrate on ground plane perpendicular planar structures.

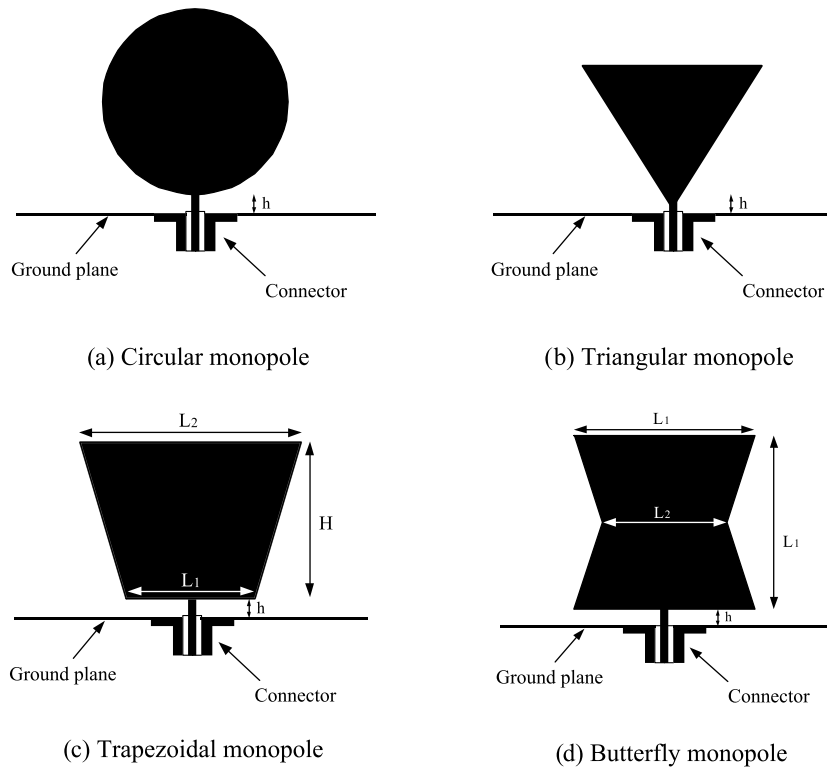


Figure 8.15. Planar monopoles mounted over ground plane

Aside from a few variations, it is easy to size up these antennas. Inherently, the low frequency is given by the height of the monopole and corresponds to a quarter wavelength. A critical parameter is the gap (h) between the monopole and the ground plane [HAM 93]. By making use of this distance, the designer can set the average input impedance of this antenna. Table 8.1 summarizes bandwidths obtained in terms of matching.

Type of monopole	Circular	Triangular	Trapezoidal	Butterfly
<i>Bow-Tie</i> Bandwidth (50 ohms)	160%	120%	80% for $L_1 = \frac{3}{4}L_2$	75% for $L_2/L_1 = 0.8$

Table 8.1. Summary of performances of planar monopoles

In general, the radiation from these antennas is quasi-omnidirectional in the azimuthal plane. In the elevation plane, variations in the pattern can be significant as and when the frequency grows. A minimum of radiation appears perpendicular to the ground plane.

For all of these antennas, we must be watchful so as to preserve sufficient dimensions for the ground plane (at least greater than one wavelength at the lowest operating frequency), so as not to degrade performance of the antenna in terms of bandwidth or radiation.

However, this last condition implies that, even if the radiating part of the antenna is small, the ground plane occupies a significant space. The following section presents some examples of reduced ground plane monopole planar antennas.

8.4.2.2. Reduced ground plane planar monopoles

From the moment when the size of the ground plane is reduced, the image principle is no longer matched with the understanding of these antennas. The ground plane becomes an integral part of the antenna and can, if we pay attention to it, also radiate it.

The following figures show different strategies for reducing the size of this ground plane. There are principally two feeding methods for these antennas: using a microstrip line (Figure 8.16a), or using a coplanar waveguide (Figure 8.16b).

In reality this is not really a microstrip line or a coplanar waveguide, as these propagation supports have limited dimensions. This implies that the length of these lines will have an effect on antenna performance. It will therefore be necessary

to watch that these propagation modes which are suitable for supports have had time to be established, in other words, to preserve minimum lengths for these feed lines.

Since the first solution works within this constraint, it consists of isolating the radiating part from the feeding line by using a particular T shape [FOR 04] for ground planes lateral to the coplanar waveguide (Figure 8.16c).

Decoupling between the radiating element and the feeding line limits the back current in the direction of the connector and facilitates integration with the antenna.

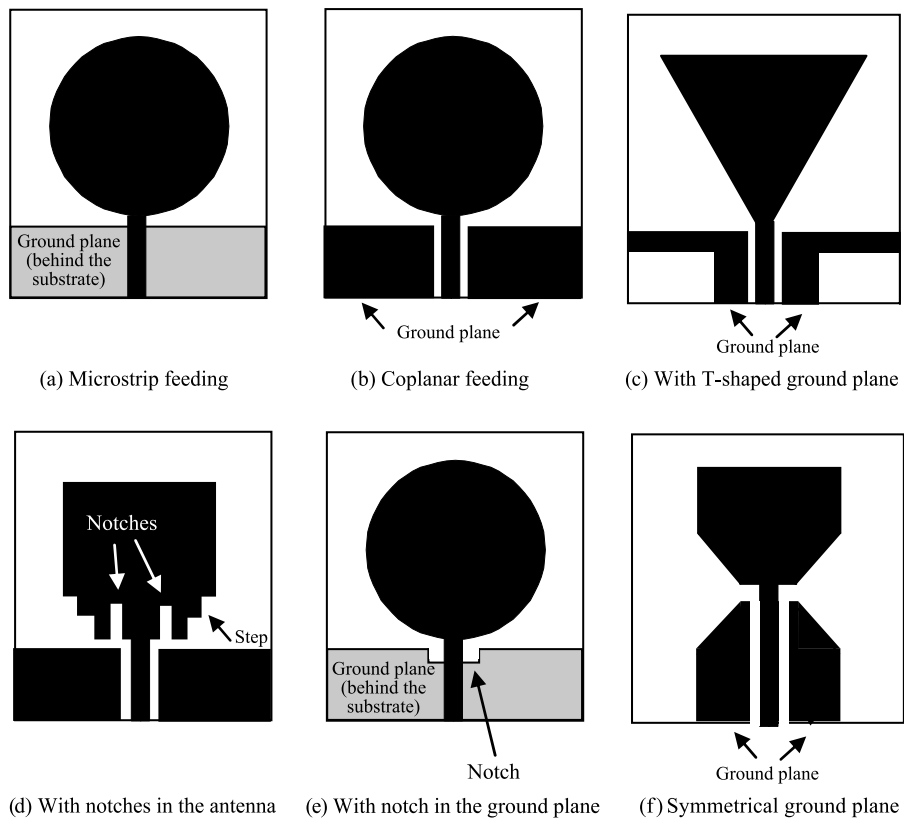


Figure 8.16. Strategies for optimizing the size of the ground plane

However, a minimum line length of around a quarter wavelength at the lowest frequency is nevertheless required so that the mode can be correctly established in the line. The lateral bulk of the antenna then becomes significant again and corresponds to around $2/3$ of a wavelength at low frequency.

As we have underlined above, the impedance matching is dependent on the distance between the radiating part and the ground plane. One technique used to optimize matching bandwidth of the antenna is to modify the radiating part in front of the ground plane with the aid of *steps* or *notches* (Figure 8.16d) [CHO 06].

The increase in bandwidth can be spectacular, but occurs to the detriment of the radiation pattern [SU 04]. A notch in the ground plane (Figure 8.16e) also enables widening of the bandwidth [BIB 10].

Another design approach consists of designing ground planes of the same shape and size as the radiating element (Figure 8.16f) [ROB 05]. In such a case, the line no longer possesses a ground plane capable of being considered as infinite. This therefore acts uniquely as an image for the radiating element: the doublet formed as a result of this is a dipole antenna.

Thus, for this type of structure, the feed line is an integral part of the antenna and its length governs the bandwidth, which acts as a dipole.

Whether for monopole mounted over ground plane or reduced ground plane antennas, the optimization of the characteristics of radiation leads to changes in the geometry of the antenna. Today, there are a multitude of studies on the subject [PEY 05]: slot (s) insertion, trident-shaped feeding, fractal geometry, etc. However, all of these studies rely on the sizing principles that we have previously set out, and which enable any designer to initiate the design of a planar wideband antenna.

8.5. Conclusion

The design of a planar or printed antenna over a very wide frequency band is naturally more complex. The choice of geometry is guided by the application and for antennas able to transmit or receive pulses, it is advisable to consider additional parameters, such as dispersion or the fidelity factor [BEG 10].

For more classic applications, the challenge to be taken up is the necessary compromise between aperture area, gain, frequency, and bandwidth (see Chapter 9). For a compact, directive antenna, a solution favoring the resonances of the structure being studied is a good one. If the bandwidth becomes greater than the octave, it is

then advisable to turn to the principles of Rumsey (defining geometry according to angles) and Babinet (self-complementary utilization) in order to guarantee performance stability as a function of frequency.

While the objective now is to design an omnidirectional and compact antenna, printed monopoles with reduced ground plane solutions are the best candidates. In terms of theoretical limits for miniaturization, let us add finally that the McLean limit remains valid for UWB, but not the Chu-Harrington limit [SCH 03].

Chapter 9

Miniature Antennas

9.1. Introduction

The surge in new technologies is enabling more and more features for compact mobile terminals to be presented. Numerous wireless communication standards are being developed, some concurrent, some complementary. For example, it is well known that standards in mobile telephony present a wide coverage and allow a high mobility, while standards in wireless local area networks, such as the IEEE 802.11 standards, enable much higher throughputs, but with poorer coverage and more reduced mobility. A terminal claiming to offer a large range of services with variable throughputs and dynamics should therefore integrate send/receive modules working with several intrinsically different characteristic standards. A common characteristic will, in the case of mobile terminals, always be bulk: with user acceptance assuming a practical and aesthetically pleasing object, then, this being the case, antennas must be as discreet as possible.

Furthermore, each communication standard has been allocated a band of defined working frequencies by the regulatory authorities. As we will see later, the width of the allocated spectrum will directly influence the bandwidth of the antenna and therefore its size. The standards also induce particular characteristics in the performance of the antenna, such as its matching level, the form of radiation created, field polarization, or even a multiplication of the number of antennas for the same standard, as is the case in multiple input, multiple output (MIMO) technologies.

We are going to look at the design principles for small-sized antennas, their physical limitations, the compromises to be found, as well as the most used structures of compact antennas with their advantages and disadvantages. We will also discuss possible strategies for conforming these antennas and integrating different operating modes into one structure.

9.2. Which types of antennas should be used for integration?

Among the numerous families of antennas, not all are appropriate in the context of highly integrated structures where the antennas must be most compact. In summary, we can consider two principal families of antennas: non-resonant and resonant.

9.2.1. *Non-resonant antennas*

At the heart of the grand family of non-resonant antennas we find two subgroups: very small size of the antenna (compared to wavelength) and those that are relatively large in terms of wavelength. We must *a priori* eliminate very large antennas (traveling wave antennas, which we would assume to have at least one very significant dimension) that are not intrinsically matched to applications requiring low profile. Nevertheless, some antennas can be used in ultra-wideband (UWB) applications, but this particular case is dealt with in Chapter 8.

Antennas with very small sizes (compared to wavelength) appear attractive where strong integration is needed. This is the case, for example, with magnetic loops (very small loop conductor wire elements) or non-resonant dipoles (small wired elements that are symmetrical in open circuit). These antennas are used when the wavelength is so large that no resonant system can be envisaged. If we take, for example, a 125 kHz radio-frequency identification (RFID) reader, this has a wavelength of 2,400 meters and, indeed, a resonator cannot be integrated into a receiver.

However, we will not deal with non-resonant antennas in this chapter for two principal reasons: their low gain and the problems with matching. Considering solutions to currents that can settle on the surfaces of such antennas, it appears indeed that the impedance at the feed point is essentially imaginary (strongly inductive or capacitive) and that the radiation resistance is very low. This results in antenna matching difficulties in classic systems, leading to the necessity for matching networks, where losses lead to very limited radiation efficiency. The great majority of applications in modern telecommunications work at minimum frequencies of several hundreds of MHz and so it is marginal whether it is worth resorting to this low performance category of structures.

9.2.2. Resonant antennas

Equations governing the behavior of an electromagnetic wave propagating in a finite medium contain solutions comprising traveling waves (which flow perfectly in the medium), stationary waves (which remain oscillating at fixed points in the medium), or combinations of both. Instances of stationary waves appear when the traveling wave hits a strong discontinuity of the medium (or impedance rupture). In this situation, any signal injected into the medium presenting strong discontinuities can create a stationary wave. This medium can be restricted following one, two, or even three dimensions (linear, planar, or volume elements). When the path produced by the wave between two extremities of the structure (two impedance ruptures within the medium) is a multiple of the half-wavelength, the solutions of these stationary waves are superimposed and the element is then the center of a resonance phenomenon (or resonance mode). Of interest is that the resonators enable a strong energy concentration (relative to the quality factor of the said resonator), and the permanent oscillation of currents and charges (for conductive elements) enable the particularly efficient production of electromagnetic radiation.

Resonant antennas must therefore adhere to criteria regarding the proportionality of their dimensions, relative to the wavelength of the signal, in order to offer good radiation efficiency. While going by this assessment we will essentially deal with the case of resonant antennas by detailing the possible approaches for making them compact when their dimensions are proportional to the wavelength. We will consider the cases of wired, planar, or volume resonators. In the following section, we discuss the compromise between optimum integration and required performance.

9.3. Integration limits in a finite volume

As we have just seen, antennas that enable an association between strong compactness and efficient radiation are generally resonant structures. Numerous theoretical studies into miniature antennas have enabled us to define a so-called electrically small antenna and its associated behavior [WHE 47, CHU 48, MCL 96, GEY 03]. The aim of these studies has been to demonstrate the necessary compromise between the bulk of the antenna, its quality factor, and its radiation.

An electrically small antenna is one that stands in a sphere with radius a , such that:

$$a = 1/k = \lambda/2\pi \quad [9.1]$$

[MCL 96] gives an approximation of the quality factor of the antenna for a fundamental resonance mode:

$$Q = \frac{1}{k^3 a^3} + \frac{1}{ka} \quad [9.2]$$

We can therefore deduce that, for a given wavelength, reducing the antenna's dimension (and therefore a) will increase the quality factor and therefore reduce the bandwidth of the antenna.

Moreover, we show that the nominal, i.e. maximum gain obtainable in this mode, is given by:

$$G_{\text{norm}} = ka(ka + 2) \quad [9.3]$$

It follows, then, that reducing the size of the antenna relative to the wavelength will reduce its gain. Conversely, we can demonstrate that for a more complex antenna (for modes other than the fundamental mode), the gain of the antenna may increase.

These theoretical formulae therefore illustrate well the necessary compromise linked to the laws of physics: reducing the size of the antenna will necessarily reduce its gain and/or its bandwidth. A miniature antenna is electrically small since its greatest dimension is far less in terms of wavelength. However for efficient radiation we have seen that it is preferable to use resonant antennas. We therefore need to find the best strategies for creating a resonance mode within the lowest possible finite volume; this integration needs to take place based on a compromise between size, bandwidth, and radiation efficiency.

We will therefore present, first of all, the different types of structures enabling the production of a resonant antenna, to subsequently see how these structures can be matched at a given volume and the impact on the characteristics as a result of impedance and radiation.

9.4. Resonant antennas in fundamental mode

9.4.1. *General considerations*

As previously discussed, the same antenna topology can be the center for a multitude of resonance modes that appear at each frequency where the structure becomes a multiple of the half-wavelength. Each resonance mode presents its own characteristics of radiation. The fundamental mode of an antenna corresponds

to the lowest frequency instance of resonance. The greatest compactness of antenna at a given working frequency is attained in order to achieve the fundamental mode.

We are therefore starting from the premise that compact antennas can be obtained based on the fundamental mode of a base structure. Whether for one, two, or three dimensions, for metallic, dielectric, or mixed structures, the fundamental mode will correspond to length $\lambda_g/2$ or a half-wave. Here, λ_g represents the wavelength of the signal in its medium that is represented as the guided wavelength. It is important to note that this guided wavelength depends on the medium in which the wave is propagated. In particular, in the case of antennas using a dielectrical material (whether or not associated with conductors), the guided wavelength becomes less than the wavelength in the vacuum, in response to the following relationship:

$$\lambda_g = \frac{\lambda_0}{\sqrt{\epsilon_{\text{eff}}}} \quad [9.4]$$

where λ_0 is the wavelength in the vacuum and ϵ_{eff} is the effective permittivity of the medium. This effective permittivity represents either the relative permittivity in the case of a homogeneous medium, or an equivalent permittivity in the case of heterogeneous media, where one approximation remains pertinent (for instance, for patch antennas). The same applies for magnetic materials, permittivity being replaced by permeability, but with the need to resort to these materials being much more marginal, we will continue to focus here on the unique consideration regarding permittivity. It is evident that an increase in permittivity enables a reduction in the guided wavelength, and therefore that a dielectrical material-based antenna may have more compact dimensions for the same working mode. However, this principle does have its compensations, which will be detailed in section 9.5.1.

Finally, another important point to note is the two types of resonances found following the topology of the antenna: series and parallel (or anti-) resonance. The terms “series” and “parallel” are explicit, since they refer to the equivalent circuits that can be constructed in order to reflect the behavior in impedance of the antenna on this resonance mode. Indeed, an antenna presenting series resonance can be represented by an RLC circuit, which contains three components R, L, and C (representing resistance, inductance, and capacitance), placed in series, while a parallel resonance antenna is equivalent to its three components placed in parallel. It follows that, for series resonance, the antenna will present very low (or even virtually null) impedance, while in the case of parallel resonance, on the other hand, this impedance will be very high. Whether resonance is series or parallel will depend on the topology of the antenna and on its feeding method.

In the following sections, we will present base structures working in fundamental mode, before detailing some techniques allowing the bulk of these structures to be reduced in section 9.5.

9.4.2. *Wire antennas*

Wire antennas are structures based on linear conductors, with a generally circular or square cross-section. This cross-section is considered to be poor, relative to the length of the conductor, which is why the base theory of these antennas assumes a linear distribution of the current sources. We can therefore easily analytically calculate the radiation produced by this type of antenna.

9.4.2.1. *Half-wave dipole*

The best known of the wire antennas, which is historically very old, but still very much in use, is the dipole antenna. This antenna comprises two metallic arms, which are aligned along the same axis and fed from the center (see Figure 9.1). Since these arms are left in open circuit at their free extremities, the resonance solutions of the currents set the null values of these currents at the extremities. The fundamental mode of the dipole antenna is therefore the half-wave mode. This half-wave dipole, which is often used as a canonical reference, presents a maximum envelope of currents at the location of the source of the voltage (see Figure 9.1), which leads to an instance of series resonance.

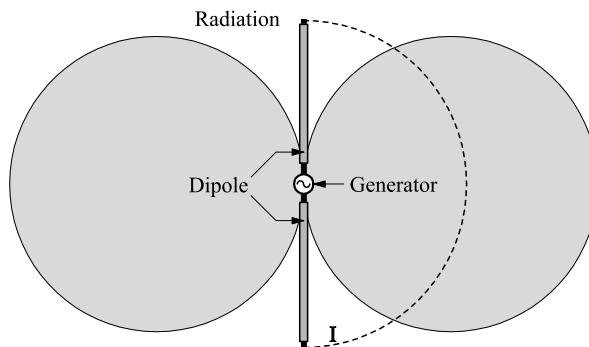


Figure 9.1. *Half-wave dipole with envelope of currents at its surface (I) and the shape of far-field radiation produced*

From a radiation perspective, there are two principal characteristics: this antenna does not radiate any field along its axis and presents a radiation pattern symmetrical about its axis. Indeed, this antenna is said to be omnidirectional, i.e. that it radiates a perfectly equivalent level of field magnitude, whatever the direction considered

in a plane which is perpendicular to its axis (horizontal if the dipole is vertical, for instance).

From the perspective of bulk, since this antenna comprises only metal, and a single axis, its largest dimension is strictly equal to the half-wavelength in the vacuum.

9.4.2.2. Monopole antenna

Using image theory, we can reduce the bulk of a dipole antenna, subject to associating the antenna to a ground plane of large dimensions (typically several wavelengths). This is the case, for example, for vehicle antennas where large metallic surfaces are available.

Virtual imaging enables the creation of the equivalent of a dipole from a single one of its arms. As such we refer to a monopole. The monopole has a fundamental mode, corresponding to a total size of $\lambda/4$ (see Figure 9.2). This quarter-wavelength monopole offers the same radiation characteristics as the dipole, namely zero radiation at its axis and omnidirectional behavior in the perpendicular plane, but in theory no radiation in the half-space situated below the ground plane.

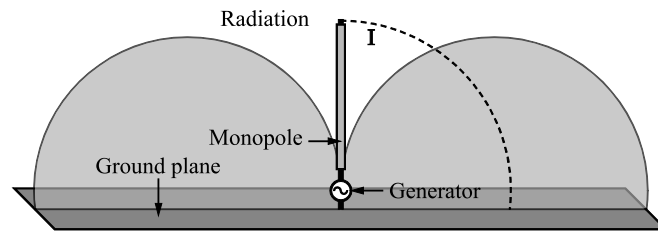


Figure 9.2. *Quarter-wavelength monopole*

9.4.2.3. Resonant loop

A resonant loop can also be considered as formed from two metallic arms, fed from the center, but this time closed in on themselves, with now a short circuit and no longer an open circuit condition (see Figure 9.3).

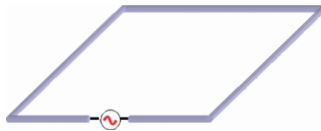


Figure 9.3. *Structure of the resonant loop*

This structure is principally used in two forms: one with four equal sides, one with two parallel arms (one of which contains the source) clearly larger than the others. This latter form, also called a folded dipole, behaves in the same way as the classic half-wave dipole, the total path of the loop being this time equal to the wavelength. The advantage of this folded dipole is that the fundamental mode resonance offers a poorer quality factor and therefore a wider operational bandwidth to compensate for a very slightly larger bulk. In the first form, a loop with a total path equal to $\lambda/2$ is not used in practice, since, on the one hand, the resonance, which is parallel this time, produces an impedance that is very difficult to match, and on the other hand the distribution of the currents does not enable very effective radiation efficiency. Conversely, loops with total size λ can be used in a series resonance, offering a radiation pattern that is less omnidirectional than classic dipoles, but with a higher maximum gain and a bulk spread along two dimensions (a square with sides equal to $\lambda/4$).

However, loops are generally superseded by planar patch antennas that offer the same advantages while having more degrees of flexibility.

9.4.3. Planar antennas

In this category of planar antennas, we will consider two principal families: slot and patch antennas. We do find within the planar versions dipole antennas in printed circuit technology, but the general behavior remains identical to that previously described.

9.4.3.1. Slots

Slot antennas are vacuums created in plain metal: sheet metal, edge of a waveguide, metallization of a printed circuit board, etc (see Figure 9.4). The Babinet principle established the duality between the vacuum in a conductor and a conductor in a vacuum. It follows then that a slot will present exactly the same characteristics of radiation as its “negative”.

Indeed, in the case of the most classic of the linear slots, these antennas will present the same radiation as the equivalent dipole. The fundamental structure in this case will therefore be a slot of size $\lambda/2$, which will present the same radiation pattern as the half-wave dipole, except that here, still following the Babinet principle, the polarization of the radiated field will be orthogonal.

Furthermore, as the metallic and vacuum parts are inverted, the laws of voltage and currents are too, as is the behavior under impedance. This being the case, the fundamental mode $\lambda/2$ of the slot corresponds to a very high impedance parallel resonance.



Figure 9.4. Structure of a slot antenna

9.4.3.2. Patches

Printed patch antennas have been widely detailed in previous chapters. They are said to be planar as their vertical dimensions are negligible relative to the other dimensions of the structure that take shape in two dimensions. The most classic patch antennas are rectangular in shape, even though all types of geometry exist.

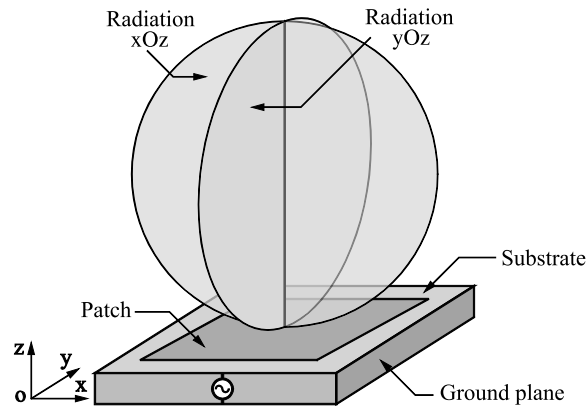


Figure 9.5. Model of a rectangular patch and its radiation in fundamental mode

The fundamental mode of this type of structure, the TM_{10} , corresponds equally well to a larger dimension equal to $\lambda g/2$. For a patch placed in the horizontal plane (see Figure 9.5.), the maximum radiation in fundamental mode is produced at the zenith, with a horizontal polarization.

The patch is a directive antenna with quite a wide aperture. Matching in impedance is easy (see Chapter 6) and the bandwidth is directly linked to the height of the substrate.

Indeed, when the fundamental mode corresponds to a parallel resonance for classic feeding, the quality factor reduces as the height of the patch increases, since the value of capacitance created between the top of the patch and the ground plane reduces (see Chapter 5).

9.4.4. Comparison

We are now able to compare the principal characteristic base antennas. If we take a system working at 1 GHz, the wavelength is thus 30 cm. A half-wave dipole antenna will therefore have a total length of 15 cm, and will offer an omnidirectional radiation pattern (with a maximum theoretical gain of 2.15 dBi).

If the application enables a large ground plane to be used, a quarter-wave monopole will therefore be only 7.5 cm, also with omnidirectional radiation (and a maximum gain of 5.15 dBi).

For the same application, a patch antenna only offers a minimal vertical bulk (typically of the order of 1 mm or even 1 cm for wider band applications). If we use a substrate of relative permittivity equal to 4 (which is a common value), then the patch will have a length of 7.5 cm and a smaller width.

In contrast, it is important to note that the ground plane will need to be bigger than the longest dimension of the patch. This antenna will thus be directive, with a maximum gain of about 8 dBi.

All these antennas can be relatively easily matched over a 50 ohms standard, but offer quite low bandwidths. Choosing between one and another of these structures therefore depends on the application, between linear and surface bulk. As we will see later, the evolution of these base antennas will enable aerial compactness to be increased.

9.4.5. 3D antennas

In the context of strong integration of the antenna in a general device (a terminal housing, for example), it is interesting to make the most of the fact that there are three dimensions. As discussed in section 9.3, limits are given in terms of volume. In the next part we will detail the case of antennas that are conformed in three dimensions, while emphasizing the various techniques that enable the reduction in bulk of aerials.

9.5. Bulk reduction techniques

The base structures presented previously enable a resonant element to be created in a fundamental mode. In this section we describe the different possible methods of going beyond the limits of classic structures through the use of materials with strong permittivity, the modification of resonator profiles and the utilization of loads or

short circuits. Some example structures that allow compactness to be combined with good control of radiation pattern are presented.

9.5.1. Use of dielectrics with strong permittivity

Expression [9.4] shows that we can resort to using a dielectric with strong permittivity as a substrate in order to obtain a resonator with very small dimensions. For example, ceramic materials are able to offer very high values. A relative permittivity of 90 will thus enable a fundamental mode in a dimension of $\lambda_0/20$.

Unfortunately, the physical properties discussed in section 9.3 show that the bandwidth and gain of the antenna will be severely limited when the permittivity of the substrate is increased. This same behavior can also be seen in relation to patch antennas in Chapter 5 (section 5.8). We therefore need to find a compromise: the increase in permittivity may lead to very compact antennas, but this will be offset by poor characteristics of bandwidth and gain being offered.

9.5.2. Modification of wave path

Another approach toward better integration of antennas within compact structures is to modify their profile. Here we are still working on resonators, but we are looking to conform them in such a way that the wave will then follow a path that is no longer linear but best fits the available volume. However, we must not forget that the antenna must not only be brought into resonance, but it must also be an efficient source of radiation. Thus, folding the resonator may lead to a loss in efficiency if the currents on the antenna contribute to the radiation in a destructive way (sources in phase opposition). We are going to describe some structures of conformed antennas, together with the impact on their characteristics of radiation.

9.5.2.1. Inverted L antenna

The so-called inverted L antenna (or ILA) is a quarter-wave monopole where the vertical arm has been bent (Figure 9.6). This very simple structure enables the vertical bulk of the structure to be reduced. However, this change in topology has two impacts. Firstly, the horizontal arm, which is close to the ground plane, is susceptible to instances of coupling; the impedance obtained is therefore different to that of the classic monopole. Secondly, the source radiation currents are now along two orthogonal axes (one vertical and one horizontal arm); the radiation produced is therefore also different, notably with a mixture of vertical and horizontal polarizations.

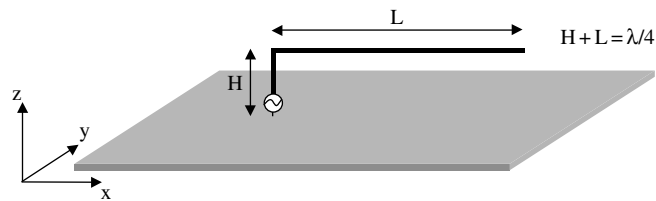


Figure 9.6. *ILA antenna*

9.5.2.2. *Helical antenna*

The helical antenna is also a derivation of a quarter-wavelength monopole. The total path of the helix-conformed conductor (see Figure 9.7) is at least a quarter-wavelength. However, here the vertical dimension is reduced since the monopole is “compressed”, i.e. wound around a cylindrical shape. The spires created by this winding will also change the impedance, leading to a very low resistance, which generally necessitates an impedance transformer.

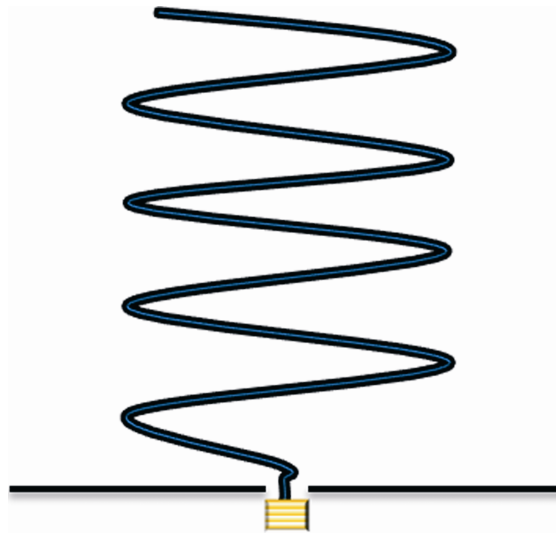


Figure 9.7. *Helical antenna*

In spite of this, the helical antenna is particularly interesting: a correct sizing of the structure enables radiation pattern to be virtually identical to that of the monopole, i.e. perfectly omnidirectional. This structure therefore typically offers a height a quarter of the size, relative to an equivalent monopole.

We note that helical antennas can also be used in another working mode, namely the axial mode, which conversely necessitates an antenna that is large relative to λ , and which therefore is not relevant when discussing compact antennas.

9.5.2.3. Conformed patch antennas

As with wire structures, patch antennas can also be designed in such a way as to extend the path of the currents. Two simple examples are shown in Figure 9.8. The H antenna presents a patch roof, into which two notches are cut. The resonant wave in the structure will then need to follow a longer path between the extremities of the patch, the length of which becomes less than $\lambda/2$. The same approach is valid when slots are cut into the patch roof. Notches and slots will modify the imaginary part of the patch impedance in different ways.

The choice of structure may therefore depend on the feed type or the environment near to the antenna (for example, correcting inductive or capacitive coupling). As with the ILA antenna, modification of the current paths will imply a modification of the characteristics of radiation, and particularly the radiation efficiency and purity of polarization.

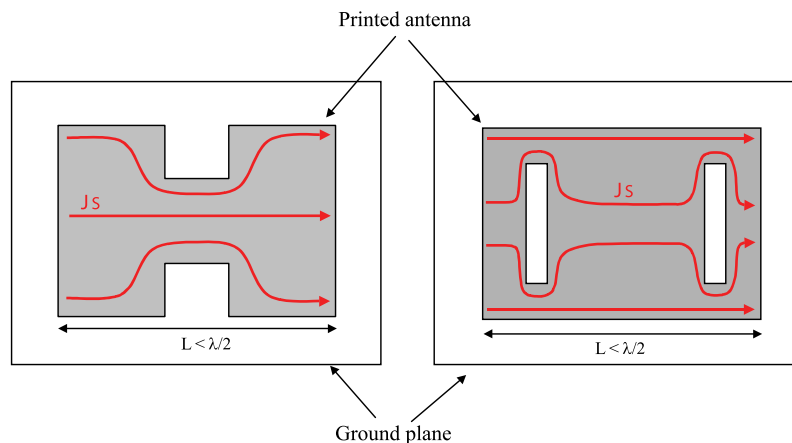


Figure 9.8. Extending the path of the wave: H antenna (left) and slot-patch antenna (right)

9.5.2.4. C-patch antenna

The C-patch antenna (Figure 9.9) is also a patch antenna whose roof shape has been modified. This particular shape allows an important extension of the path of the wave, which offers a reduction in surface occupied by a factor of 3–4, relative to a classic patch. As before, this strong gain during winding has its compensations: a reduction in the antenna's bandwidth, as well as an important degradation of

the purity of polarization (which is again more significant than in the case of the H antenna).

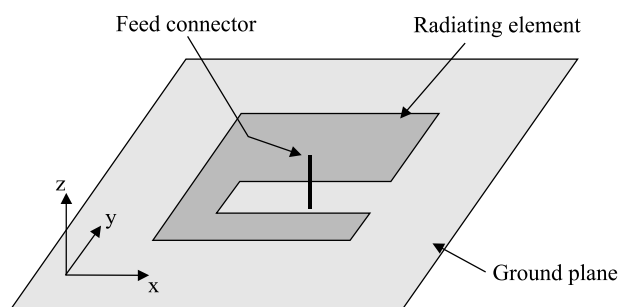


Figure 9.9. *C-patch antenna*

9.5.3. Utilization of inductive, capacitive, and short-circuit effects

As with all resonators, the resonant frequency of antennas depends on the value of the equivalent components L and C (inductive and capacitive). One approach for reducing the bulk of antennas is therefore to try to add inductive or capacitive effects that enable the value of the frequency to be lowered, thereby rendering the antenna proportionally smaller relative to the wavelength. Making use of capacitor- or inductor-types of components may be a solution, but the general preference is to modify the topology of the antenna in order to create this capacitive or inductive effect locally.

Furthermore, we have seen that the use of the ground plane may allow a reduction in the bulk of antennas. Generally, the use of short circuits in a structure is truly a key factor in reducing bulk. But now, the combination of a short circuit and the effect of the inductive or capacitive coupling that it can produce as a result of being judiciously positioned in the structure lead to structures of antennas that are more compact.

9.5.3.1. Loaded monopole

As an example of an antenna that uses a capacitive or inductive effect in order to lower the resonant frequency, we now put forward the case of the quarter-wave monopole. Figure 9.10 shows the case of a capacitive roof placed at the top of a monopole, in order to create an overall increase in the value of resonator capacitance, and therefore a reduction in the resonant frequency. The second case, which is presented in Figure 9.11, is of a monopole consisting of a series induction coil at the base of the radiating arm that also enables a shorter antenna to be obtained.

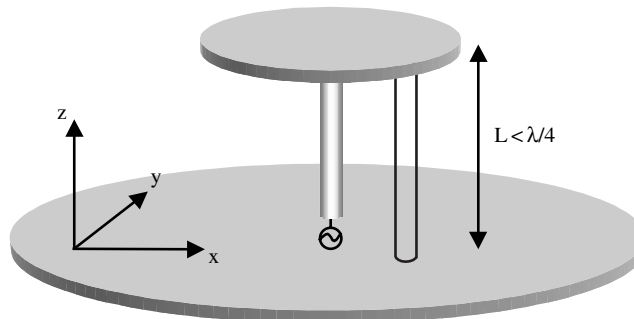


Figure 9.10. *Monopole loaded by capacitance*



Figure 9.11. *Monopole loaded by inductor (whip monopole)*

9.5.3.2. *Quarter-wave patch*

As its name suggests, the quarter-wave patch uses a short-circuit plane in order to enable the transformation of the half-wave resonance mode of the classic patch in quarter-wave mode (being based therefore on the electrical image created by the ground plane as a result of image theory). A patch that is twice as short results from this, but with a degradation of radiation characteristics.

As we can see in Figure 9.12, the short-circuit plane, which contains strong current densities, will produce a significant vertical component to the detriment of the pure horizontal polarization of the half-wave patch.

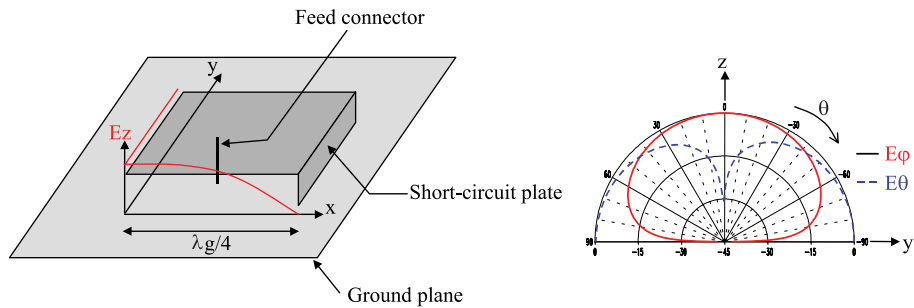


Figure 9.12. Quarter-wave patch and associated radiation pattern in the plane xOz

9.5.3.3. Inverted F antenna

The inverted F antenna (Figure 9.13), or IFA, is the equivalent of an ILA antenna with a short circuit added. Not only will this short circuit allow the virtual extension of the wave path, but furthermore the positioning of the feed wire in parallel with this short circuit enables the creation of an inductive coupling effect.

As with loaded monopoles, this additional self-inductance enables a lowering of the resonant frequency of the structure, and therefore the achievement of a shorter antenna.

We will detail the evolution of the IFA antenna in terms of planar technology, the PIFA, in the next section.

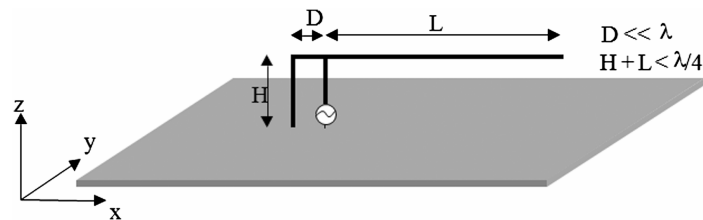


Figure 9.13. Inverted F antenna

9.5.3.4. PIFA

The acronym PIFA stands for planar inverted F Antenna as the antenna when viewed from the side is always in the shape of an overturned letter F [DRE 05]. A common PIFA (see Figure 9.14) comprises a rectangular plate of dimensions $L_1 \times L_2$, a ground plane and a short-circuit plane that links the plate to the ground plane. The width of the short-circuit plane W varies from L_1 to 0 (wire). Since this

antenna is nowadays one of the most used structures in the integration of very compact antennas, we are going to focus a little more on the details.

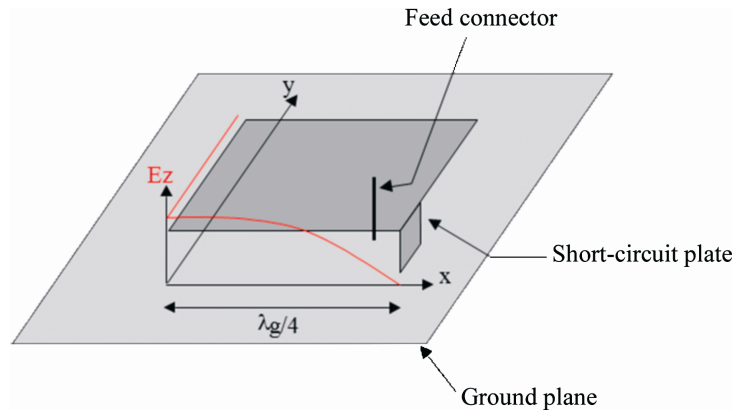


Figure 9.14. PIFA antenna

The resonant frequency of a PIFA depends on a number of parameters. If we consider the PIFA on an infinite ground plane, the resonant frequency of the antenna varies according to the width of the short-circuit plane, relative to the width of the plate (W/L_1) and according to the ratio between the length and width of the plate [HIR 92]. In practice, we hardly ever encounter an infinite ground plane. As a consequence, the dimensions and shape of the ground plane may strongly affect the value of the resonant frequency. Furthermore, the position of the feed point also has a strong bearing on the resonant frequency of the antenna.

When $W/L_1 = 1$ (i.e. the width of the short-circuit plane is equal to the width of the plate), the resonant frequency is defined by the following expression:

$$L_2 + H = \lambda/4 \quad [9.5]$$

When $W = 0$ (i.e. the short circuit is effected by a wire), the resonant frequency is defined by the following expression:

$$L_1 + L_2 + H = \lambda/4 \quad [9.6]$$

When $0 < W/L_1 < 1$, the resonant frequency is defined by the following expression:

$$f_r = r.f_1 + (1-r).f_2 \text{ when } L_1/L_2 \leq 1 \quad [9.7]$$

and:

$$f_r = r^k \cdot f_1 + (1-r^k) \cdot f_2 \text{ when } L_1/L_2 > 1 \quad [9.8]$$

where $r = W/L_1$, $k = L_1/L_2$, the frequency f_1 is defined by the relationship $L_2 + H = \lambda/4$ and f_2 is defined by the relationship $L_1 + L_2 + H - W = \lambda/4$.

Apart from the resonant frequency, another significant parameter in antenna design is bandwidth. Once more, in the case of PIFA antennas, it is possible to optimize bandwidth by modifying certain parameters: essentially the height and dimensions of the plate and the width of short-circuit plane. The larger the ratio between the width and the length, the greater the bandwidth. Similarly, for a given plate width and length, it is possible to improve the bandwidth by increasing the height of the plate, relative to the ground plane. The principal disadvantage of the PIFA antenna is its poor control over its radiation pattern and a much-degraded purity of polarization. However, this aspect is often masked when strong integration is required.

9.5.4. Control over radiation

As we have just seen, a preference toward extremely compact structures generally induces degradation in the characteristics of radiation. However, some structures are able to be compact and still maintain control over radiating fields. Here we look at two cases: one antenna enabling a tendency toward a perfectly isotropic radiation pattern [VIL 02], and another enabling omnidirectional radiation with very good purity of polarization [DEC 02].

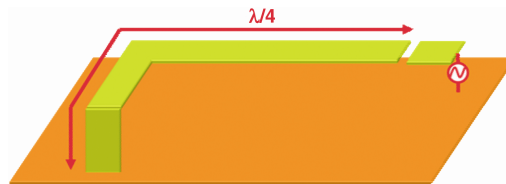


Figure 9.15. 3D folded strip antenna

9.5.4.1. Folded quarter-wave resonator

In order to combine the appeal of the compact resonator with a radiation pattern where we can control the characteristics, the structure is folded along three orthogonal axes (see Figure 9.15). In practice, this type of resonator is usually produced using microstrip technology. In order to maintain the linear current distributions, these strips must be relatively narrow, thus leading to a resonator with

a fairly high quality factor. An approach involving feed by capacitive coupling enables us to easily return to a matched structure.

This structure therefore enables us to simply obtain small lateral dimensions, along with good impedance matching. However, beyond this, imposing three orthogonal axes on the elements of the resonator also offers the option of sizing these elements based on a constraint of radiation, such as isotropic radiation (which is the subject of [JEC 02]), i.e. an equivalent level of radiated field in every direction in the space. This isotropic constraint is expressed through a criterion of maximum variation in the gain in the overall space of the order of 3 dB (which is in reality a half-space if we consider an infinite ground plane). Optimization of the parameters (values h , l_1 , and l_2 in Figure 9.16), while considering each arm of the structure to be a radiating element with the current intensity of current corresponding to a quarter-wave mode, gives the following values: $h = \lambda/24$, $l_1 = \lambda/15$, and $l_2 = \lambda/7$ [VIL 02]. We then obtain an antenna whose biggest dimension is $\lambda/7$, which brings about an isotropic radiation. Nevertheless, it should be noted that this radiation is uniform in terms of power, if not in terms of polarization.

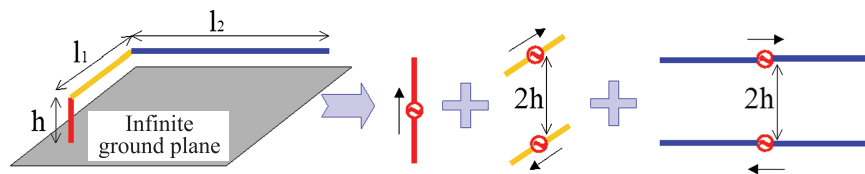


Figure 9.16. Contribution of the different antenna arms on radiation

9.5.4.2. Wire-patch

Another topology that enables compactness and purity of radiation to be combined is the wire-patch antenna [DEC 02]. The principal elements are summarized in Figure 9.17. In its most classic form, the structure of this antenna is identical to that of a printed patch antenna. It comprises an arbitrarily shaped metallic patch that is positioned on the upper surface of a dielectric cell. The lower surface of this cell is entirely metallized and constitutes the ground plane of the antenna. Feeding is achieved by a coaxial connector that crosses the ground plane and the dielectric substrate in order to be connected to the upper metallic element (which is called the capacitive roof).

The characteristic feature of this antenna is that it possesses one or more wires connecting the antenna roof to the ground plane. These wires are often called grounding or short-circuit wires. The presence of these wires close to the connector is the key to the unique workings of the antenna. Without the grounding wire, the antenna behaves as a series resonant circuit due to the self induction from the feed

connector and the capacitance formed by the upper roof. Adding a grounding wire to the antenna then leads to the appearance of parallel resonance at the same point as the series resonance previously quoted (Figure 9.18).

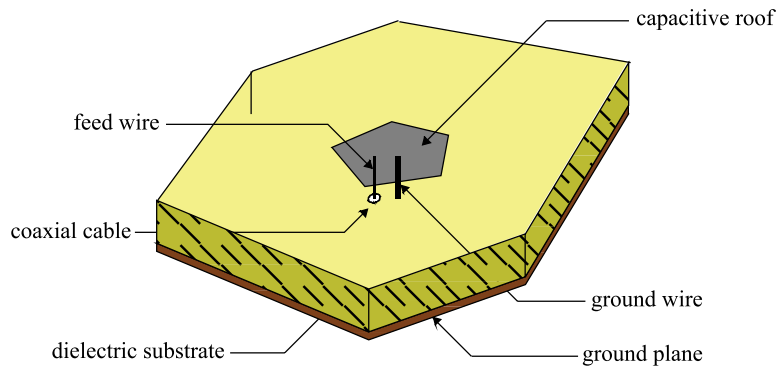


Figure 9.17. Wire-patch antenna

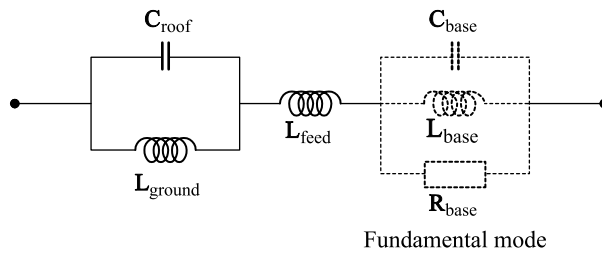


Figure 9.18. Equivalent circuit of wire-patch antenna

This is explained by the fact that induction of the lead-in ground wire shorts the antenna capacitance the antenna capacitance formed between the ground plane and the upper roof. The majority of surface densities of currents circulating around the antenna are, moreover, particularly concentrated on the short-circuit wire.

This resonance mode therefore occurs at a much lower frequency to that of the patch, $\lambda/2$ in fundamental mode (approximately four times lower). The dimensions of the antenna are therefore particularly low relative to the working wavelength, since they are verified according to square antennas of wavelength l and height h :

$$l = \lambda g/8; \quad h = \lambda g/20 \quad [9.9]$$

A complete study of the parameter keys of such a structure can be found in [DEC 02], for which Table 9.1 offers a summary.

Parameters		Resonant frequency	Amplitude at resonance	Quality factor
Height	↗	↘	□	↘
Substrate permittivity	↗	↘	↗	↗
Roof length	↗	↘	□	□
Roof width	↗	↘	□	□
Roof area	↗	↘	□	□
Length–width of ground plane	↗	↘↔	↘↗↔	↘↗↔
Radius of coaxial connector	↗	□	□	□
Radius of grounding wire	↗	↗	↘	↘
Displacement of coaxial connector	Center to extremity	□	↗	↗
Displacement of grounding wire	Center to extremity	↘	↗	↗
Linked displacement of wires	Center to extremity	↘	□	↗

Note: ↘, reduction; □, stability; ↗, increase.

Table 9.1. Influence of the parameters of the wire-patch antenna

An additional point about this wire-patch antenna concerns its characteristics of radiation. Effectively, its topology causes the short circuit to condense the strongest current densities. This results in radiation that is virtually equivalent to that of a classic quarter-wave monopole (see Figure 9.19). We therefore obtain a perfectly omnidirectional antenna, with a maximum gain of the order of 5 dBi and a very pure vertical polarization. It is interesting to note that the wire-patch antenna can be used with a reduced ground plane, which is barely bigger than the roof, and that in this situation we can move toward a dipolar pattern (which is equivalent to that of a half-wave dipole).

9.5.4.3. Coplanar wire-patch

A declination of the principle of the wire-patch antenna is the coplanar wire-patch (see also [DEC 02]). This refers to a structure where all of the elements of the wire-patch are transposed into a single plane in order to obtain a 2D structure (see Figure 9.20). Instead of having a ground plane positioned under the roof of the antenna, the bulk of the structure occurs around the capacitive roof, and the feed and short-circuit wires are replaced by strips, all within the same plane. As with

the classic wire-patch, the essential currents are concentrated in the short-circuit strip. As the ground plane is heavily reduced, the antenna offers dipolar radiation. Conversely, as the ground plane is around the antenna, its bulk is increased, and we obtain maximum dimensions of the order of $\lambda/3.5$ (which remains clearly less than a classic patch antenna).

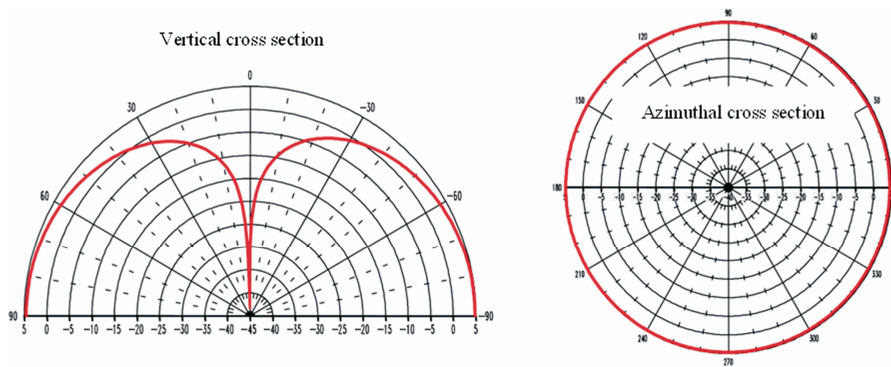


Figure 9.19. Radiation of the wire-patch antenna over an infinite ground plane

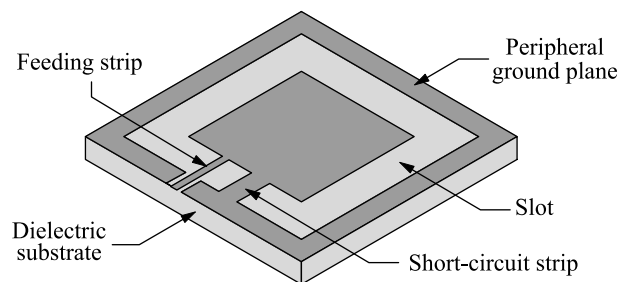


Figure 9.20. Coplanar wire-patch antenna

We can also see that this coplanar principle can be transposed to other topologies (such as PIFA, folded quarter-wave, etc.), which also leads to an increase in area but which also enables the lower ground plane to be suppressed.

9.6. Multiresonant antennas

In the context of the integration of antennas in a communicating housing, it is quite often necessary to multiply the range of frequencies, in order to offer access to several communication standards or to widen the general operating band of the

system. Although they are practical to integrate, resonant antennas are limited in terms of bandwidth by their quality factor. It is often the case, therefore, that more than one resonance (or more than one resonator) will be used, in order to enable either the operating band to be widened (as in a wideband system) or multifrequency operation.

In order to widen the bandwidth of an antenna, we look for the structure to present two resonances (which would usually be parallel) that are sufficiently close in frequency for the impedance of the antenna to remain matched over a wider spectrum. For example, we can refer to the example of the U slot patch antenna (see Figure 9.21). The patch offers its classic $\lambda/2$ resonance mode, but the slot fitted into its roof will also come into resonance. If the slot path is correctly adjusted then the coupling of these two resonances enables us to obtain a unit-operating band that is clearly wider. However, we must pay attention here to the characteristics of radiation. We will therefore attempt to bring together resonance modes providing similar characteristics of radiation, so that the final antenna keeps an identical radiation pattern over the whole range of frequencies.

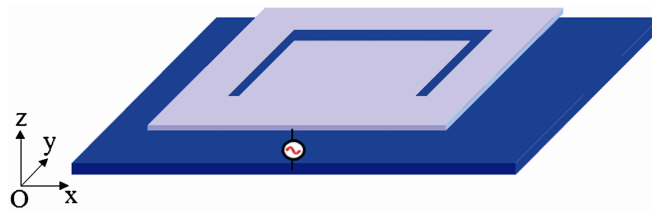


Figure 9.21. *U slot patch*

Clearly this principle can be extended to cater for more than two resonances. In the context of applications such as those defined for UWB, which by definition cover a very wide spectrum, some antenna structures can be based on a combination of multiple resonances with severely degraded quality factors. A first example is the use of fractal structures, where the motif, which is repeated over a range of scales, therefore offers multiple resonances within the spectrum (see Figure 9.22).

However, we can equally use a combination of resonators in order to offer several distinct operating bands. The logical approach is first to design an antenna that can operate in the lowest band, which can subsequently be integrated (without increasing the general bulk) with another resonator for a higher frequency band (which is therefore *a priori* less bulky). Still with the example in Figure 9.21, we can deliberately design a shorter slot, which will present a resonance mode with a higher frequency.

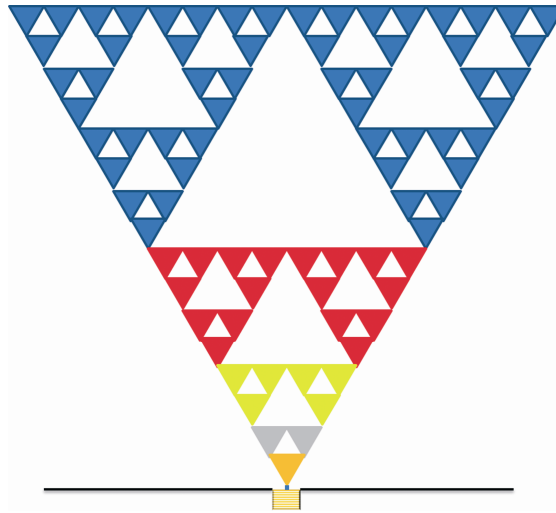


Figure 9.22. *Fractal antenna (Sierpinski)*

Within this logic of integrating several resonators, we can also differentiate between multiband designs (where all resonators should have equivalent radiation in different bands) and multifunction designs (where resonators are able to offer completely different types of radiation). Moreover, within a single structure, we look for the different modes to be fed from one single connector (as with the U slot patch), or conversely to have a feeding port for each operating mode. It is useful to be able to design antennas with a single port, but that then assumes that it is possible to filter out the different bands received.

In the case of diversity systems, which therefore require several antennas to provide several independent copies of the same signal, it is imperative that we separate the ports, but also that we see to it that the coupling between these modes is as low as possible. In order to enable assistance in the integration of diversity systems in reduced bulk, priority will be given to either pattern diversity (thus two resonators with complementary radiation patterns) or polarization diversity (two modes with perfectly orthogonal polarizations). For example, dual-polarized patches can offer two perfectly uncorrelated channels, without having to increase the bulk of the antenna.

9.7. Synthesis and discussion

This chapter has enabled us to work our way through the range of principal structures of antennas that are used in order to integrate wireless links into

compact devices. The elements best suited to this type of integration are essentially resonators. Whatever the choice of resonant system, a compromise is necessary between general size of the antenna, its bandwidth, and its characteristics of radiation. It is possible to move toward extreme miniaturization, for example by using dielectrics with very high permittivity, but that would inevitably have an effect on the antenna performance, in terms of impedance or efficiency of radiation.

Over and above the different families of antennas described, some common approaches can be retained: conforming the antenna in three dimensions, resorting to short circuits and modifying the inductive and capacitive effects within the body of the structure. One of the most popular structures, which combines these three approaches, is the PIFA antenna. However, the wire-patch antenna also allows very strong compactness while preserving a better control of radiation.

Finally, the combination at the core of a single structure, with several elements being in resonance, is key in developing new multistandard or diversity systems. The more these systems increase in complexity, the more it is necessary to very precisely design their structure, while taking into account their working environment: a housing in which they will be integrated, related elements (radio card, batteries, etc.), CEM constraints, etc.

New approaches exist that have not been mentioned here: utilization of purely dielectric resonators, magneto-dielectric substrates, or even meta-materials. We hope from this that a number of these techniques will enable the compactness of future antennas to be improved still further.

Chapter 10

Reconfigurable Antennas

10.1. Introduction

The concept of reconfigurability suggests the ability of a system to dynamically modify its performance. We define a reconfigurable antenna (RA), as one which internally, or in the immediate neighborhood, uses active components that are able to change their base characteristics. The changeable parameters are:

- frequency (central frequency, bandwidth);
- polarization (type of polarization, orientation);
- radiation pattern (beamwidth and direction, shape of the pattern).

Reconfiguration circuits that are distant or isolated from the antenna are outside the scope of the subject of RAs. This is the case with active, phased array antennas, whose radiating elements are fed by phase shifters and programmable amplifiers.

A characteristic of reconfiguration does not signify that the antenna is intelligent, i.e. capable of automatically adapting to its environment. A decision-making and feedback process must be added, usually to the exterior of the antenna. This can take the form of a micro-controller or a field-programmable gate array (FPGA) that drives the negative feedback circuit containing the reconfigurable component.

There are also examples of simple decision circuits, which are based on phase comparison systems used to self-adjust resonant frequencies [TUR 99].

The dynamic modification of the operating parameters of an antenna brings flexibility to communication systems. Antennas with pattern and/or polarization diversity enable us to increase the efficiency of indoor communication systems, by significantly reducing the levels of fading. Frequency reconfigurable antennas (FRAs) enable multistandard functions to be maintained while preserving the inherent characteristics of filtering in narrowband.

This chapter is organized as follows: in section 10.2, we will describe the basic topologies, while providing the general constraints applicable to RAs. In section 10.3, we will present the basic switchable radio-frequency (RF) components. Examples of frequency reconfiguration are given in section 10.4, examples of polarization reconfiguration are given in section 10.5, and examples of pattern reconfiguration are given in section 10.6, while stressing the modeling strategies and the constraints imposed by biasing circuits.

10.2. Basic topologies and constraints

We will limit our study to topologies based on the integration of components of variable impedance. We will therefore not consider substrates with variable electrical permittivity or magnetic permeability (ferroelectric [BRO 99], ferromagnetic [LOV 06], and liquid crystal [DEJ 05] materials). For low-cost applications, being able to switch on and off is generally the limit of the requirement for microwave electronics. We will therefore not cover many examples of continuous-adjustment antennas with basic varactor diodes. The active components can be semiconductor (PIN diodes, transistors) or micro-mechanical (MEMS, micro-electro-mechanical systems) elements, directly integrated with or mounted on the antenna. Although we generally deal with single switches or single-port double-throw (SPDT), we also find instances of switched inductors or capacitors.

The topologies of RAs can be classified into three categories, depending on the position of the active component (Figure 10.1):

- component integrated into the body of the radiated element (Figure 10.1a);
- component incorporated into a stub connected to the antenna (Figure 10.1b);
- component inserted into the feed line of a single antenna or an antenna array (Figure 10.1c).

The first category leads to compact structures. However, it requires the component to be inserted in the neighborhood of a maximum of current in order

to ensure both a significant alteration in the behavior of the antenna and a significant dynamic adjustment. From this we obtain significant coupling between the component and the near field of the antenna, and therefore, a strong sensitivity to the parasitic elements of the component. The influence of coupling is difficult to quantify because of the non-ideal behavior of the component, which is not reduced to a short circuit in the *on* position or to an open circuit in the *off* position. We observe [LAH 02]:

- a drop in antenna efficiency, particularly in the *on* position, due to the non-null resistance of the component;
- a shift in the simulated resonant frequency, due to the capacitive and/or inductive effects created by the casing and the bonding or internal microchip wires.

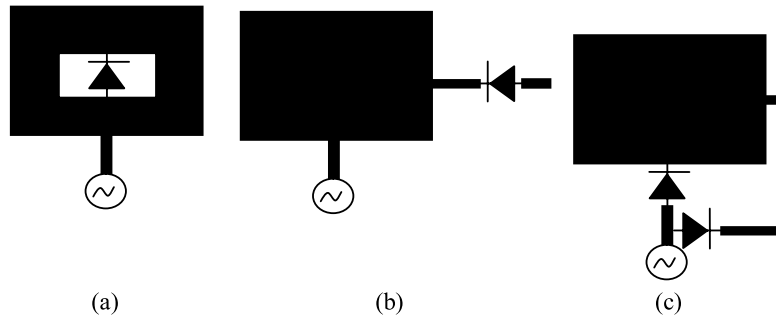


Figure 10.1. Schematic representation of the three categories of RAs

Strictly taking into account the interaction between the antenna and the component means that sophisticated 3D electromagnetic modeling needs to incorporate an equivalent distributed electrical circuit of the component, as well as the casing and its connectivity solution (flip chip, bonding, direct soldering, conductive glue, etc.). Models of this type are not, as of now, available within commercial simulation softwares, so we generally have to satisfy ourselves by introducing an equivalent circuit combining lumped resistor (R), inductor (L), and capacitor (C) into electromagnetic simulation. Yet these circuits are based on component measurements or manufacturer data obtained with probe stations for microstrip or coplanar inputs. Since this guided propagation environment is not that of the antenna in which the component is embedded, it is clear that the simulations produced will be far from realistic.

In the second type of RA, the switched component is positioned outside the radiating zones and loads the antenna across a stub. Depending on the state of the component, the load seen by the antenna may differ, and consequently, the distribution of current on the antenna and the radiation and input impedance characteristics.

This solution is less compact, but reduces the interaction between the component and the field near to the antenna. Moreover, it makes the utilization of a circuit model for the component possible, since its input ports are connected to a transmission line.

In the third type of RA, one or more components are integrated into the feed circuit of one or more antennas. In the example of the two-port antenna (Figure 10.1c), the idea is to select either port to switch to one of the two orthogonal linear polarizations. The same concept can also be extended to distinct radiation patterns for antenna diversity purposes. It is also possible to select n out of N antennas in order to obtain a range of beams of variable width [LEG 04]. A Butler matrix is a more sophisticated example of a switchable feed circuit.

The Butler matrix (Figure 10.2) enables us to select a radiation pattern from N available antennas by switching one of the N inputs using SPDT. The path followed by the signal varies according to the input selected. This leads to a modification of the phase law along the N antennas of the array, and therefore, a scanning of the principal beam.

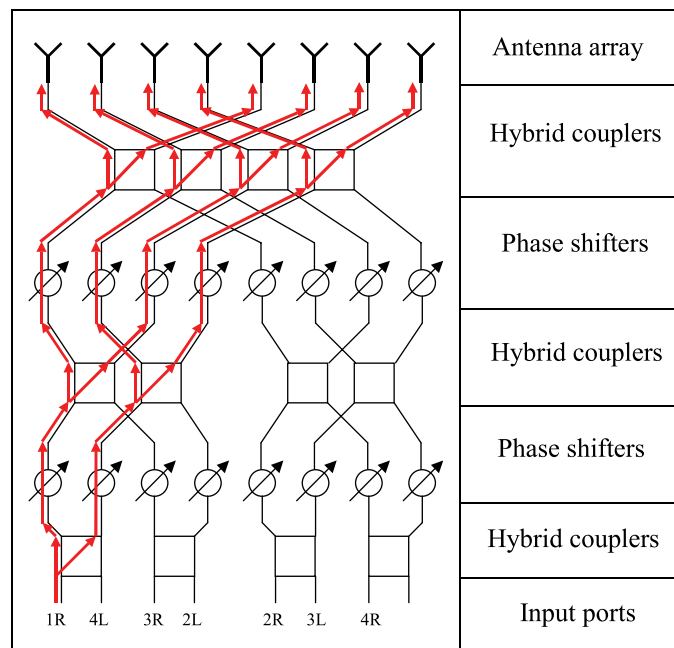


Figure 10.2. Synoptic illustration of an eight-input Butler matrix. Input 1R is selected

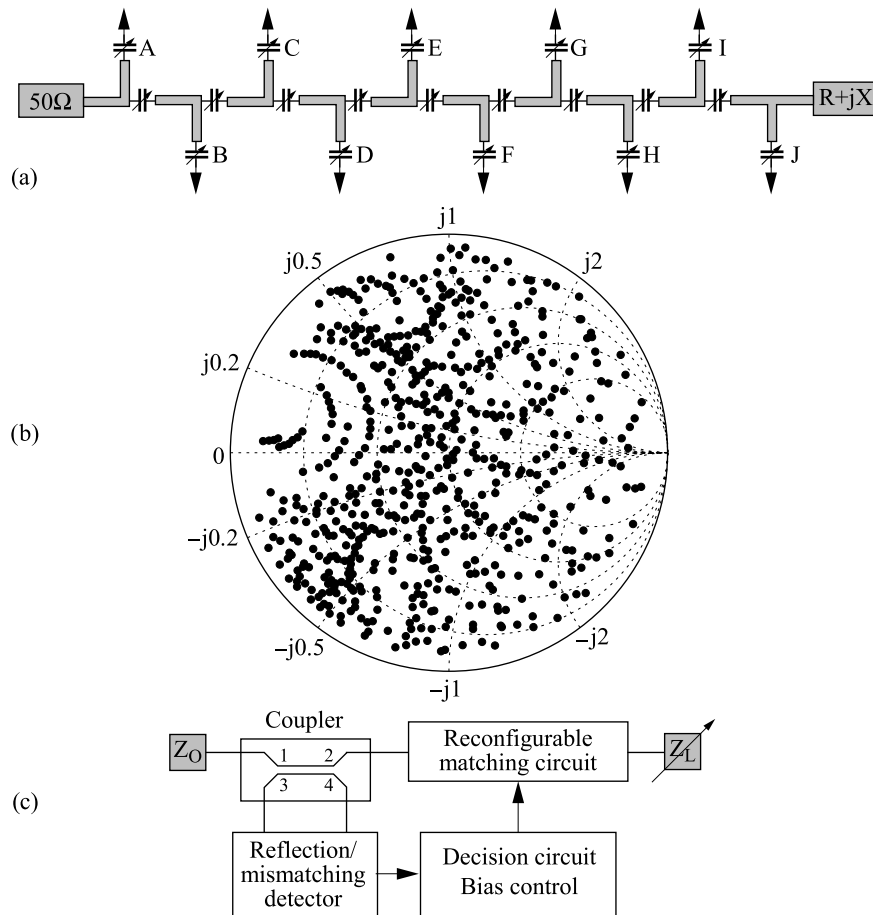


Figure 10.3. Reconfigurable impedance-matching circuit. (a) Illustration of principle [WHA 06] based on a loaded line using switched capacitance stubs. (b) Typical distribution of impedance for 2^8 states [UNL 06]. (c) Concept of automatic reconfiguration

The combination of SPDTs and switches can therefore lead to complex functions, such as the Butler matrix. The automatic matching circuit (Figure 10.3) is another example of a complex circuit positioned along the feed line, enabling the intelligence to be integrated as close as possible to the antenna. Automatic matching is required when the range of frequencies is too wide for a single antenna or when the near environment leads to strong variations in antenna impedance (such as a hand being placed on the antenna of a wireless object, or the influence of the body on the RFID tag). This matching circuit is usually inserted between the power amplifier (PA) and the transmitter antenna. It must enable optimum operation of the

PA in terms of linearity, efficiency, and output power [VAN 08]. The adaptive circuit is usually based on a commutative matching T- or Π -network using the LC components (Figure 10.3a). An impedance measurement and a controller complete the device (Figure 10.3c).

For all RA topologies, biasing circuits must be designed to limit the interaction between the near field of the antenna and the direct current (DC) lines that are likely to generate parasitic radiation from induced currents.

While preferring an RA solution to a classic solution, based on a passive antenna, it must be possible to be able to justify the overspend on circuits and additional connectivity solutions, as well as the energy consumed. For example, a passive multiband antenna eventually possesses reduced radiation efficiency. An electronic frequency reconfiguration can therefore lead to better performance in terms of matching and efficiency for each frequency, but at the cost of increased energy in order to activate the components. If the improvement in efficiency and matching of the antenna, which is beneficial in terms of energy, is wiped out by the RF losses from the components and the requirement for DC energy to energize the components, then it makes no sense to use an RA.

10.3. Switched components: available technologies

The main integrable switches for an RA are presented. We will discuss in the following order: PIN diode, field-effect transistor (FET), and MEMS systems.

A switch is a system governed by two states: *on* or *off*. At low frequency (static or quasi-static regime), its electric circuit is that of a perfect component, with infinite impedance when *off* and null impedance when *on*. When the frequency increases, the equivalent model of the component becomes more complicated and additional parameters appear in the form of capacitance, inductance, and resistance. These parameters must be taken into account in order to precisely determine component performance. A working switch will be characterized by a rapid commutation rate, low insertion losses (S_{12}), strong isolation (S_{11}), low operating voltage, high longevity (measured in numbers of cycles), linear behavior (measurement of the IP_2 and IP_3 points that represent the distortions due to harmonics of the orders 2 and 3), and poor consumption.

PIN diodes are widely used in microwave circuits in order to produce variable attenuators, modulators, or commutators. The PIN diode is an active electronic component produced from semiconductors comprising a strongly positively doped layer (P), an intrinsic (non-doped) layer (I), and a highly negatively doped layer (N) (Figure 10.4a).

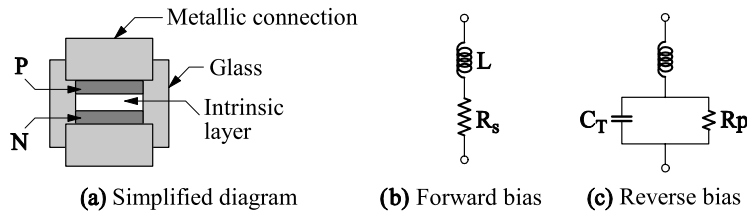


Figure 10.4. PIN diode: (a) physical diagram, (b) forward equivalent model, and (c) reverse equivalent model

Under the effect of forward bias, the positive charges of the P region and the negative charges of the N region are injected into the I region, thereby increasing its conductivity and reducing its resistivity. In the *on* state (Figure 10.4b), the PIN diode possesses an equivalent model containing a parasitic inductance L and a series resistance R_s whose value varies from $1\ \Omega$ to $10\ \text{k}\Omega$, depending on the biasing current I_d and the fabrication process. A good initial approximation is $R_s \approx 1/I_d$ (Figure 10.5b).

When it is reverse biased (Figure 10.4c), the diode is essentially equivalent to a capacitance C_T , which is the sum of the junction capacitance (C_{J0}) and parasitic capacitance (C_p). C_T restricts the isolation performances of switches at high frequencies, but its value remains extremely poor ($0.1\ \text{pF}$ or $1.6\ \text{k}\Omega$ at $1\ \text{GHz}$). At low frequency, this capacitance increases with reverse voltage (Figure 10.5c).

Note that the behavior of the PIN diode only differs from that of the classic PN diode at a frequency above $\sim 10\ \text{MHz}$.

PIN diodes sold commercially are generally encased (Figure 10.5a). There are smaller diodes used in *Beam-Lead* technology (Figure 10.6), which are easily integrated into antennas.

They can be assembled using thermal compression (or *bonding*), soldering, or using a conductive epoxy glue. In Figure 10.6c, we see that typical performance levels for the HPND-4005 diode at $f < 10\ \text{GHz}$ are insertion losses of $0.45\ \text{dB}$ with $I_d = 1\ \text{mA}$ and isolation $> 17\ \text{dB}$ for $V_r = 10\ \text{V}$.

It is useful to compare PIN diode performance with that of RF transistors derived from metal semiconductor field effect transistors (MESFETs) (Table 10.1). The main drawback of the FET results from degradation due to drain-to-source capacitance. We observe that the figure of merit ($\text{FOM}) = 1/(2\pi C_{\text{off}} R_{\text{on}})$ is higher in PIN diodes, due to a lower value of C_{off} for a given value of R_{on} .

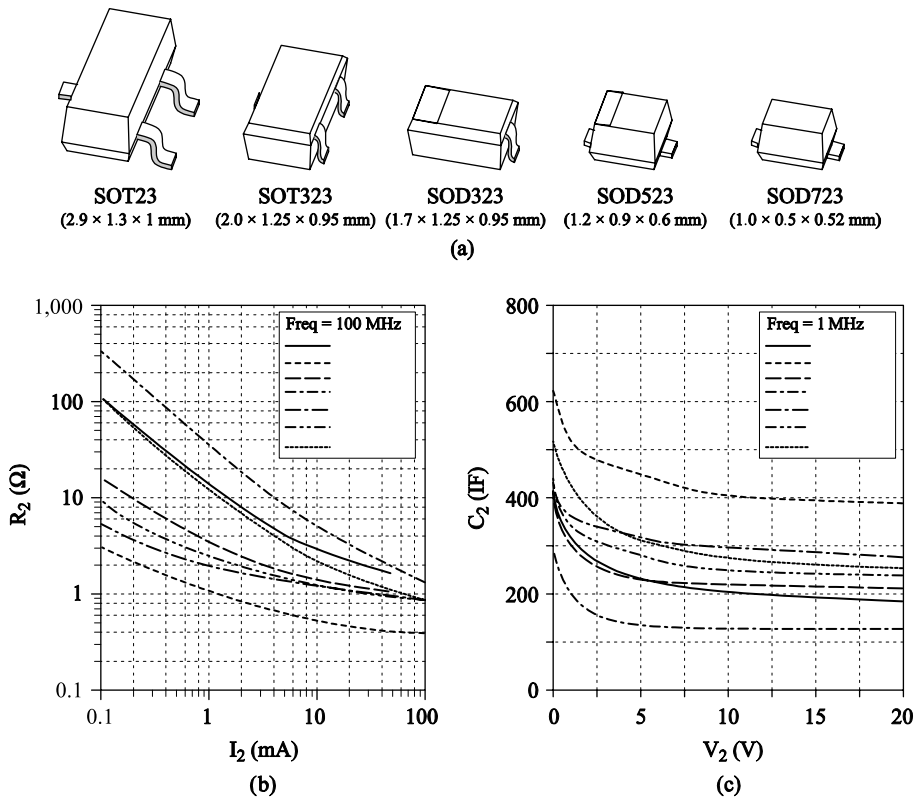


Figure 10.5. (a) Encased diodes, (b) series resistance R_S as a function of the forward-bias current, and (c) diode capacitance as a function of reverse voltage for different diode models

The FOM changes with the maximum operating frequency of the component, which can reach 180 GHz for a PIN diode, while it is about 26 GHz for a MESFET.

On the other hand, it is the voltage applied to the gate that causes the transistor to switch on. This therefore consumes very little current and power, which is contrary to the PIN diode (typically at least 10 mW). This constitutes a fundamental advantage in phase shifters and attenuators for arrays of on-board antennas.

It should be noted that even if the FET is a component with three electrodes, it can function with a voltage $V_{DS} = 0$ V that simplifies biasing circuits. Since the gate is naturally decoupled from the RF source and drain, DC isolation using blocking circuits is not necessary, which simplifies the design even further.

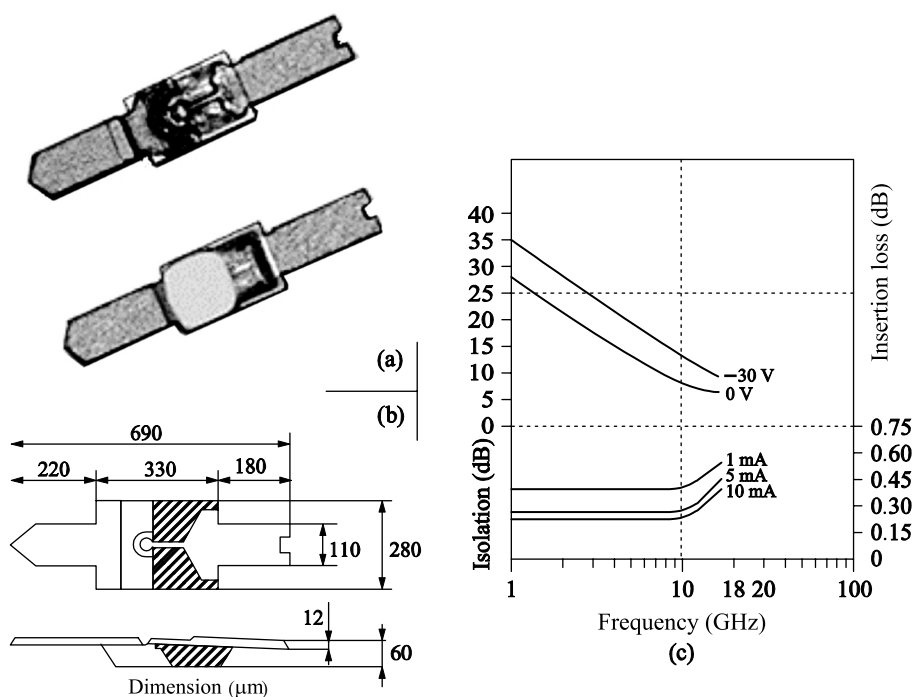


Figure 10.6. Beam-lead PIN diodes: (a) photograph, (b) dimensions, and (c) isolation and insertion losses

	MESFET (1 μm)	PHMET (0.25 μm)	PIN diode	
			Silicon	GaAs
Number of ports	3	3	3	3
Typical R_{ON}	1.5 $\Omega\text{-mm}$	1.2 $\Omega\text{-mm}$	1.7 Ω	1.7 Ω
Typical C_{OFF}	0.40 pF/mm	0.32 pF/mm	0.05 pF	0.05 pF
Figure of merit (GHz)	265	414	1872	1872
Breakdown voltage (V)	15	8	50	30
Low limit frequency	DC	DC	10 MHz	10 MHz
Complexity of driving circuit	Low	Low	High	High
Biasing constraints	0 V on/ -5 V off	+0.5 V on/ -5 V off	5 to 10 mA on/ 0 to -30 V off	5 to 10 mA on/ 0 to -30 V off

Table 10.1. Comparisons of transistor and PIN diode performance

One of the main drawbacks of semiconductors is their nonlinear response at high levels, with interference problems between channels and the degradation of the signal-to-noise ratio. This problem has been overcome with recent developments in MEMS technology (Figure 10.7), which ensures better isolation and insertion losses up to 40 GHz with very low consumption.

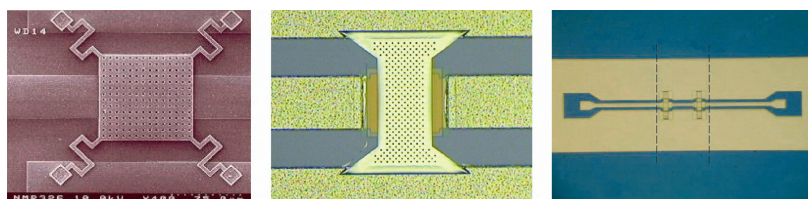


Figure 10.7. Different types of MEMS, micro-machined over silicon

MEMS are micro relays produced using conventional techniques and semiconductor manufacturing processes (layering, patterning, and lithography), to which specific micro-machining stages are added, ensuring that certain so-called sacrificial layers are patterned.

Micro-machining enables us to produce suspended structures. Most MEMS are manufactured on silicon wafers. They enable a range of activities to be realized in domains as diverse as medicine (monitoring blood pressure), the motor industry (speedometers, monitoring compression), and electronics (print heads for inkjet printing).

In the domain of telecommunications, specifically in embedded systems or mobile telephony, low consumption of RF MEMS is a significant advantage. MEMS SPDT and MEMS switches are commercially available, but variable capacitors and inductors are also developed in laboratories.

On the other hand, the limitations are still poor switching speeds (no more than about 10 μ s in recent publications) and high activation voltages, even if recent topologies enable a drop to about 10 V. Reliability also remains a problem.

Typical performances are compared in Table 10.2.

The basic principle of MEMS consists of applying a static electrical field to the mobile elastic membrane in order to create a deflection from the membrane. The example of a capacitive switch is presented in Figure 10.8. The metallic membrane acts as a bridge above the coplanar line, connecting two lateral electrodes that consist here of the lateral ground planes, although independent electrodes can also be used. By applying a continuous voltage between the line (or sometimes a couple

of symmetric electrodes located below the slots) and the membrane, the membrane is drawn toward the line (low state). In order to avoid a DC short circuit between the line and the membrane, a thin dielectric layer, such as a silicon nitride, is deposited on the line at the membrane.

Characteristics	MEMS	GaAs FET	PIN diode
Size	Small	Very small	Small
Resistance (Ω)	0.5	1--5	1--5
Commutation power (CW)	2	0.5	5
Breakdown voltage	Low	Low	Variable
Switching rate (μ s)	0.5--200	$1e^{-2}$ -0.1	$1e^{-2}$ -0.1
Number of cycles	10^{10}	10^{10}	10^{10}
Operating frequency (GHz)	70	4	20
IL Insertion loss (dB)	0.25	0.5	0.5
Isolation (dB min)	40	30	30
IP3 third harmonic	Very good	Low	Low
Consumption	Very low	Low	Low
Control voltage	5 V, 28 V, 48 V	3 V, 5 V	3 V, 5 V
Integration	Very good	Very good	Very good
SPDT cost €	8.0--20.0	0.5--4.0	0.9--8.0

Table 10.2. Performance comparisons for several types of MEMS [GRA 02]

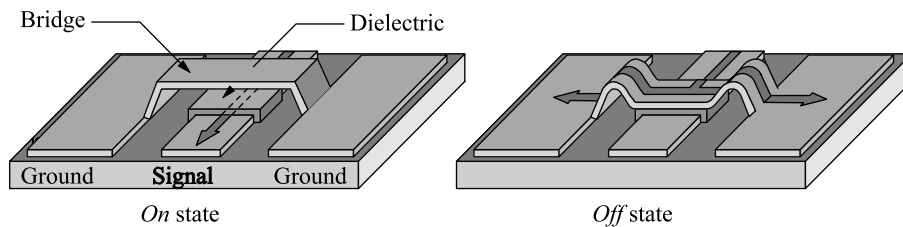


Figure 10.8. Principle of the capacitive parallel MEMS

In low state, the MEMS finally creates an RF short circuit on the line and acts as an open switch. The more significant the equivalent capacitance in low state, the better the isolation will be. The C_{on}/C_{off} ratio of equivalent capacitance in high and low states constitutes an FOM for capacitive MEMS commutators. Nowadays, values of 100 are commonplace.

Note that the low DC current consumption enables RF/DC decoupling to take place using individual RF resistors placed in the bias circuit. In cases where MEMS topology isolates RF line from activation electrodes by design, the design of the bias circuit is even simpler. The simplicity of the bias circuit is an advantage for RAs

where the radiating parts are near the DC lines. In order to limit the electromagnetic coupling between the RF and DC lines, high resistivity lines can be used in order to bias the MEMS.

10.4. Frequency reconfigurable antennas (FRAs)

10.4.1. Introduction

FRA is one whose impedance characteristics are modified electronically. More specifically, it is concerned with shifting the resonant frequency of a planar antenna. Frequency diversity must occur by preserving matching and efficiency of quality throughout the operating band. Frequency diversity can be considered for two types of applications:

1) Delicate adjustment of untuned narrowband resonance: This adjustment can be linked to interference from a hand or head in the near field of the antenna for a cell phone positioned close to the body. It can also result from sensitivity to manufacturing tolerances. This adjustment must be associated with a form of feedback and to a decision circuit in order to enable device intelligence, i.e. adaptation to changes in the environment.

2) Narrowband operation over multiple communication standards (such as Bluetooth + Wi-Fi 802.11a/b/g at 2.4/5.4/5.8 GHz), which presents the following advantages over multiband or wideband passive antennas:

- potential tuning of the operating frequency of the FRA at a standard which either did not exist or was not accounted for during its design. This enables us to increase the lifespan of infrastructures intended to be operational over a long period (communication network infrastructures, military technology, space industry). The cost arising from the accrued complexity is compensated for by the increase in lifespan;

- intrinsic filtering of unwanted channels and noise in non-selected frequency bands. Some filtering takes place at the FRA itself, which eases the effort on the duplexers in the reception stages;

- a compact multiband miniature antenna does not have stable radiation characteristics (radiation pattern, polarization) across all frequency bands. On the other hand, the reconfiguration of certain types of FRA comes back to a homothety of the dimensions of the antenna that enable us to preserve the properties of radiation across all bands.

FRAs are also found in the military domain, where detection and security systems must be able to operate over different frequency bands in order to resist electronic counter-measures.

10.4.2. Examples of radiating slot-based FRA

In the first example [LAH 01], the FRA consists of a radiating slot in which eight beam-lead PIN diodes are periodically inserted (Figure 10.9). The slot is centrally fed by a coplanar line. The antenna functions on the second resonant mode, where the real part of impedance is low enough to be adjusted to 50Ω by regulating the slot width. On the other hand, impedance is too high in the first resonant mode to enable matching.

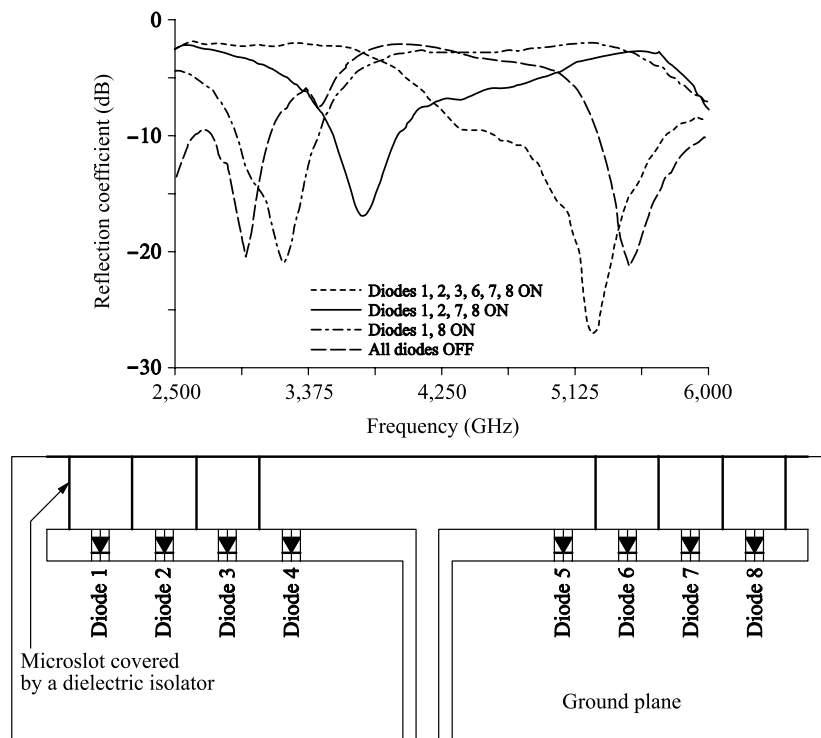


Figure 10.9. Reconfigurable eight PIN diode slot, fed by coplanar line. Reflection coefficient for different combinations of diode states [LAH 01]

The slot antenna is manufactured on a substrate with properties $\epsilon_r = 2.2$, $\text{tg}\delta = 10^{-3}$, $h = 1.524 \text{ mm}$. The radiating slot is $500 \mu\text{m}$ wide, which enables us to connect the beam-lead diodes, total length $800 \mu\text{m}$ (MACOM4P461).

The isolation between biasing voltages applied to each diode is produced by microslots ($100 \mu\text{m}$) cut into the ground plane. These microslots enable us to separate the DC zones corresponding to each bias voltage.

On the other hand, they disturb the operation of the antenna as each microslot acts as an RF load connected to the radiating slot. In order to ensure RF continuity, while preserving the DC isolation, each microslot is completely covered by a dielectric insulator (adhesive strip) which is topped by an adhesive copper strip. The capacitance created from this is enough to produce proper biasing without affecting the antenna's behavior.

The diodes are combined by symmetric pairing and switched in pairs. The resonant slot length is reduced as the diodes are switched in their *on* state, with the current lengthening the slot flowing mostly in the diodes closest to the feeding circuit.

The lowest frequency is obtained when all diodes are *off*. Then, in increasing order of frequency, when diodes 1 and 8 are *on*, then 1, 8, 2, and 7, then 1, 8, 2, 7, 3, and 6, and finally, when all diodes are *on*. We see a definite shift in resonance toward high frequencies when the number of diodes in use increases.

Diodes are switched in pairs so as to preserve a perfectly symmetric load of the coplanar line and to thus avoid the excitation of even modes in the line. This constraint limits the number of frequencies available to be synthesized to 5.

Multifrequency behavior is possible since proper impedance matching is observed for all switched lengths. This property, which results from the low dependency of the resonance on slot width for variable resonant lengths, forms an intrinsic advantage of radiating slots over other types of FRA.

Resonant length can also be regulated by introducing a capacitive effect into the slot [PIO 02]. This effect leads to an artificial increase in the electrical length of the antenna, and therefore a reduction in its resonant frequency.

In Figure 10.10, we present a slot antenna that is loaded using two adjustable capacitive MEMS. Each capacitance is placed in the middle of one of the arms of the slot. Here, we refer to series MEMS, where the height of the bridge above the line can be adjusted using a continuous voltage applied between the electrodes.

The antenna is manufactured from alumina using micro-machining techniques. A thin layer of alumina is introduced under the membrane of the series MEMS in order to avoid a short circuit at low state.

As MEMS are sensitive to humidity, they are produced in a metallic cavity that backs the slot so that it avoids all contact with its environment. The cavity eliminates radiation in a half-space.

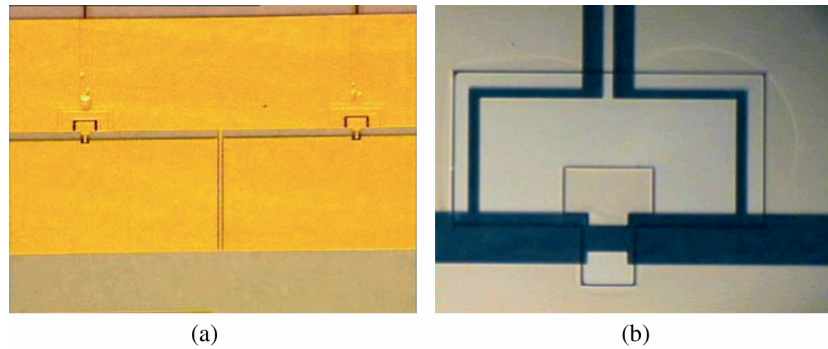


Figure 10.10. (a) MEMS-based reconfigurable radiating slot produced over quartz. (b) Detail of the MEM region and biasing circuit [PIO 02]

The cavity depth is $400\ \mu\text{m}$. The slot is excited by a coplanar line that passes over a hole cut into the cavity. The slot is covered with a thin layer of quartz.

The sidewalls of the cavity have been adjusted in order to shift the fundamental of the cavity beyond 30 GHz. The first slot resonance can theoretically be shifted over frequencies of 20.16 GHz (MEMS *off*) and below, depending on the minimum height of the achievable membrane.

In practice, the height of the membrane cannot be less than $0.6\ \mu\text{m}$, as all applied voltage that is greater than the corresponding voltage leads to the low state of the MEMS. Maximum shift happens at about 15 GHz, which corresponds to a shift of 22%.

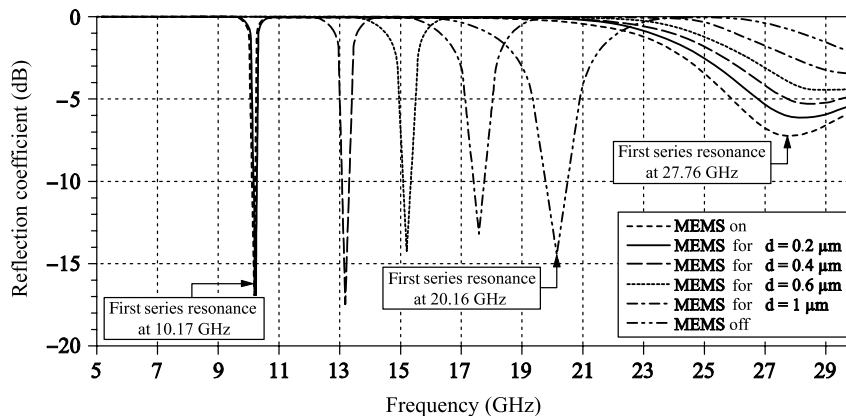


Figure 10.11. Influence of bridge height d on the reflection coefficient for $d = 0.2\ \mu\text{m}$, $0.4\ \mu\text{m}$, $0.6\ \mu\text{m}$ and $1\ \mu\text{m}$, in the on and off states

10.4.3. Examples of patch- or PIFA-based FRA integrating switchable slots

Slots loaded by reconfiguration components enable lines of current in a radiating structure to be disturbed. Figure 10.12 illustrates the disturbed lines of current exciting a patch when a switchable slot is either active or non-active, which is shown by the modification of the excited mode on the patch, and from its resonant frequency [FAN 05].

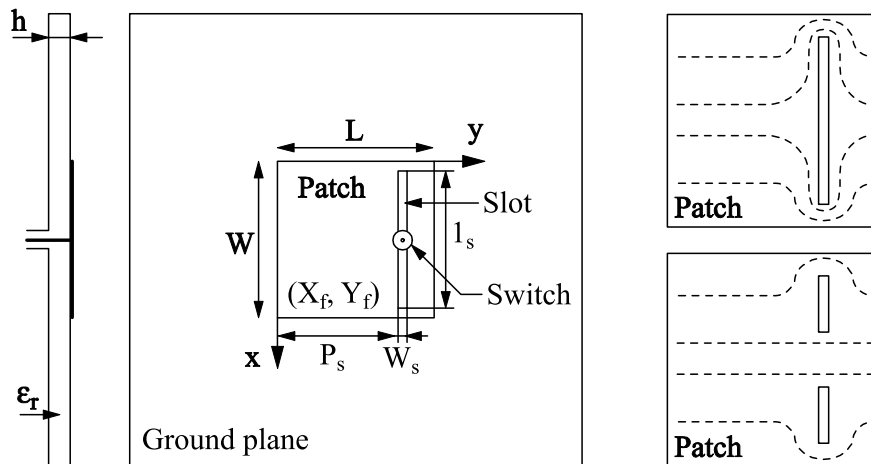


Figure 10.12. Switchable slot on a radiating patch [FAN 05]

Figure 10.13 shows a PIFA antenna to which a switchable slot has been added [PAN 04]. This example illustrates the possibility of placing multiple switched components in the core of a single slot, in order to obtain more than two resonances.

10.4.4. Examples of FRA using switched short circuits

The activation of switched short circuits enables current flowing and, following on, operating frequency(ies) of the antenna to be modified. PIFA antennas have a short circuit between an L-shaped probe (planar) and the common ground plane of the antenna. The position of this short circuit enables us to modify the antenna frequency, and, as a consequence, PIFA antennas are very obvious candidates for additional functionality, while making one or more of these short circuits switchable. Figure 10.14 presents two examples of reconfigurable PIFA antennas.

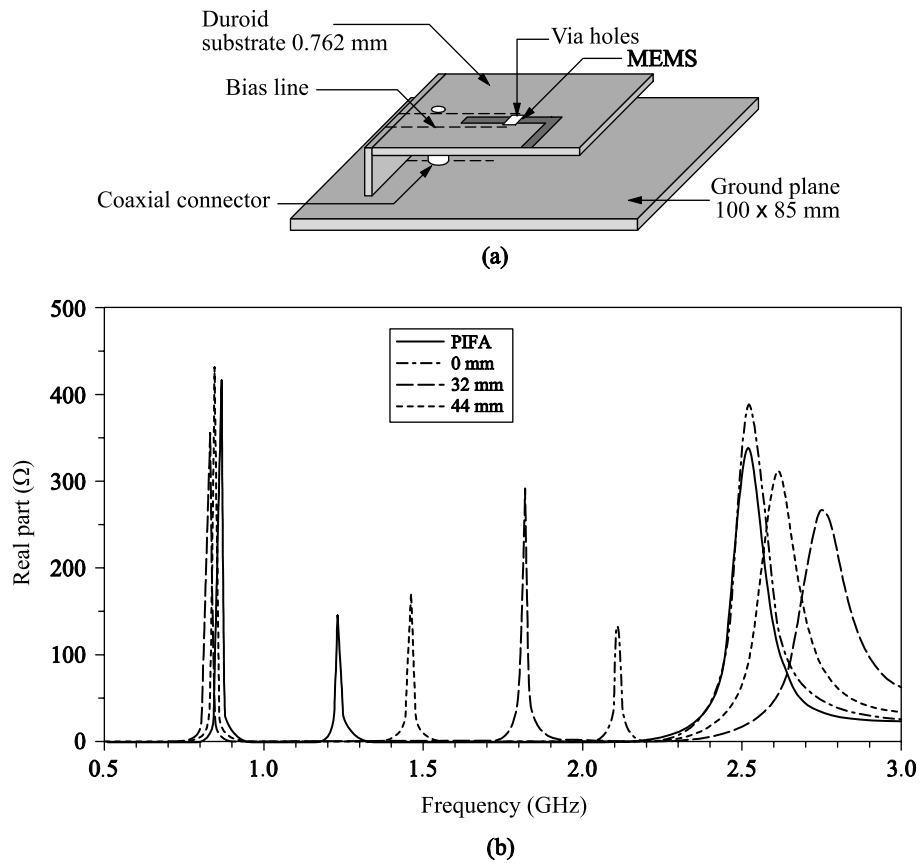


Figure 10.13. PIFA antenna loaded with a switchable slot [PAN 04]

10.4.5. FRA utilizing a loaded stub

The electrical length of the antenna can be modified by utilizing the capacitive impedance presented by a stub loading a patch. The structure in Figure 10.15 is based on a coplanar stub loaded by switched MEMS [ERD 07].

10.5. Introduction to RAs in terms of polarization and radiation pattern

Antennas with pattern and/or polarization diversity enable indoor communication systems to become more efficient by significantly reducing levels of fading. Signals available to the different branches of one or more antennas are combined as much as possible in order to optimize the overall signal-to-noise ratio. The RA is particularly suitable for branch combining by selection or switch of

pattern and/or polarization. The contribution of the reconfiguration is also important in MIMO systems, where an additional degree of freedom linked to pattern selection is combined with pure signal processing [SAR 08].

Finally, we can make use of this reconfiguration in applications where electromagnetic interference signals (scramblers) have to be cancelled by including radiation nulls in the pattern.

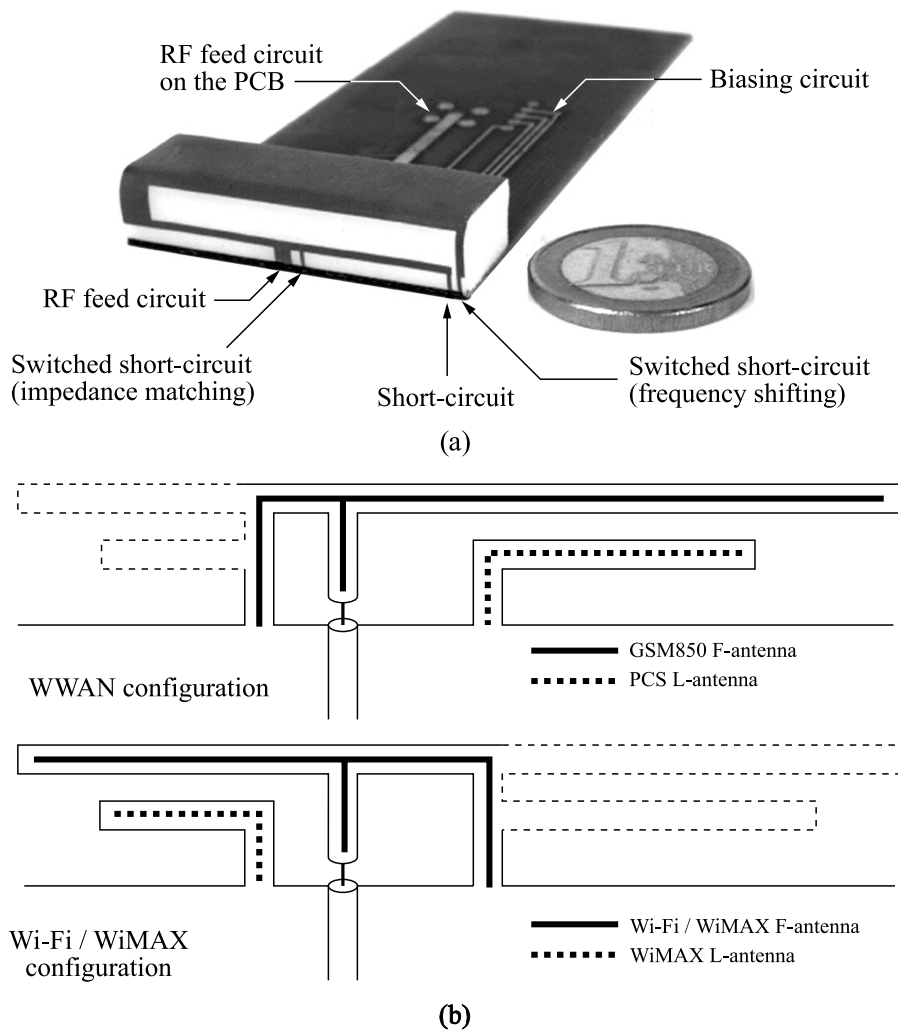


Figure 10.14. Two examples of reconfigurable PIFA

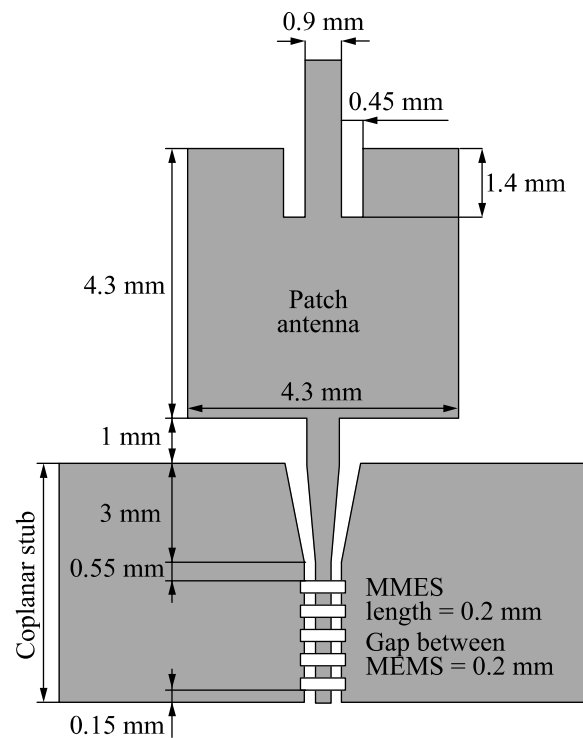


Figure 10.15. Patch loaded by a coplanar stub including MEMS [ERD 07]

10.6. Polarized reconfigurable antennas (PRAs)

The objective is to dynamically reconfigure the polarization of an antenna in order to send or receive a linearly or circularly polarized signal. The need to adjust polarization is found in multiple applications:

- changing antenna specifications during the course of a mission for a satellite or on-board antenna;
- binary modulation based on orthogonal circular polarizations (RHCP = 1, LHCP = 0) for certain types of connections [KOS 99];
- being able to offer polarization diversity for communications affected by variable propagation (rain, ionosphere, etc.) or multipath (indoor) conditions.

Figure 10.16 shows a concept that enables an antenna to continually switch between circular and linear polarizations [LEG 04a].

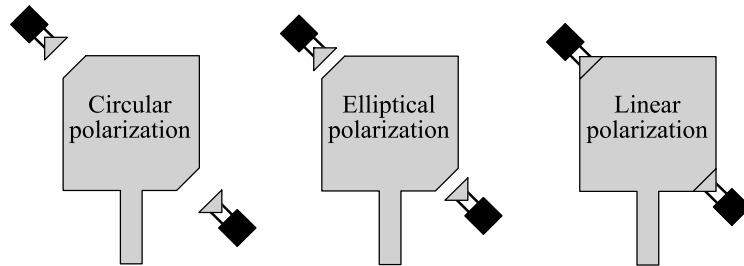


Figure 10.16. Polarization reconfiguration – patch antenna with truncated corners, controlled by SDA

The basic antenna is a patch antenna with truncated corners, i.e. circularly polarized. Knowing that a square patch generates linear polarization, the solution consists of filling in the truncations with metallic elements, put into action by the MEMS actuators. The technology used for this is called Scratch Drive Actuator (SDA). Following the position of the parasitic elements, the polarization can be circular, elliptical, or linear.

An example of polarization reconfiguration of a printed antenna fed by two slots is shown in Figure 10.17 [BOT 00].

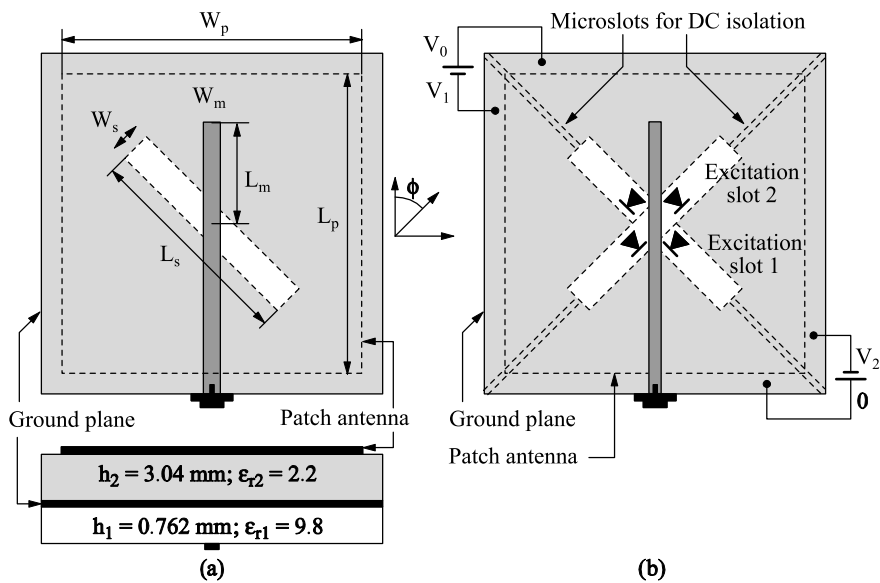


Figure 10.17. (a) Rectangular circularly polarized patch fed using a diagonal slot. (b) PRA fed using two switched cross-slots including the DC circuit

The basic passive antenna (Figure 10.17a) is a rectangular patch excited using a diagonal slot cut into the ground plane of the antenna and excited using a microstrip line. The TM_{10} and TM_{01} modes generated are linearly orthogonal and resonant at different frequencies.

In order to obtain circular polarization, the modes must be excited in phase quadrature with identical amplitudes by adjusting the L_p/W_p (patch length to patch width) ratio.

The RA in Figure 10.17b includes a slot that is identical in length and width along the other diagonal of the patch. A pair of beam-lead diodes is soldered into each slot, 3 mm from the intersection. By switching one pair of diodes *on*, while the other *off*, the rotation of the circular polarization is reversed.

The biasing is represented symbolically in Figure 10.17b, RHCP being selected with ($V_1 = V_0 = 10$ V, $V_2 = 0$ V), while LHCP is obtained for ($V_1 = 0$ V, $V_2 = V_0 = 10$ V). We observe in Figure 10.18 that a common 4% bandwidth defined for $RA > 0.7$ (3 dB) is obtained about 5.0 GHz for the two states of commutation with good matching ($S_{11} < -10$ dB).

The radiation patterns shown in Figure 10.19 at central frequency present few ripples with low cross-polarization.

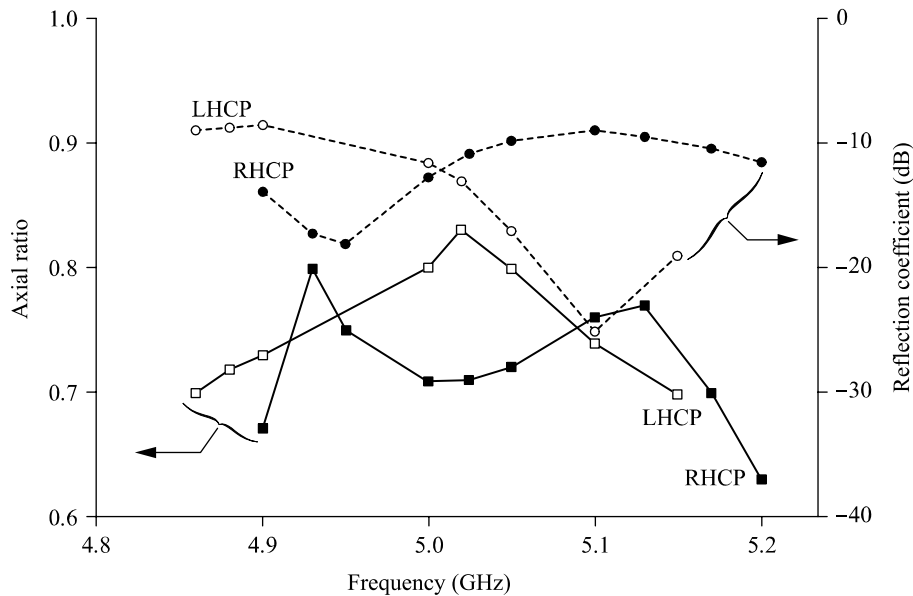


Figure 10.18. Axial ratio at the axis and matching as a function of frequency

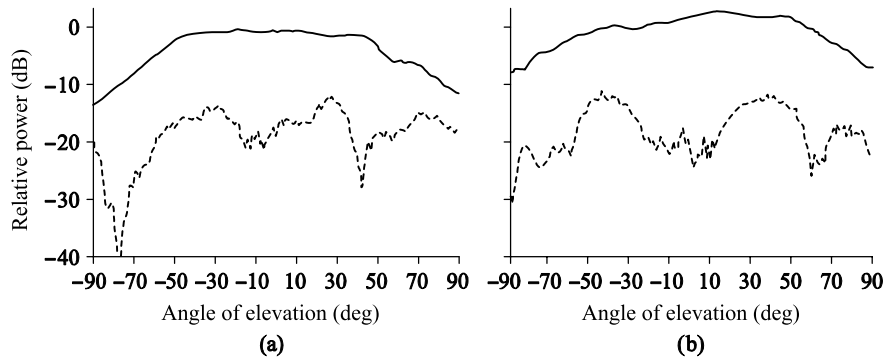


Figure 10.19. RHCP radiation pattern in the two principal planes at 5 GHz

Another example of PRA [FAN 05] is based on a rectangular patch excited by a probe located on the diagonal, which enables the two orthogonal TM_{10} and TM_{01} modes to be excited simultaneously (Figure 10.20). A slot is cut along one of the bisectors with a diode placed in the middle.

When the diode is *on*, the current of the TM_{01} mode flows in the y direction, across the diode, with the frequency of the mode being barely disturbed by the presence of the diode and the slot, relative to the case when there is no slot. When the diode is *off*, the current of the TM_{01} flows along the slot; we observe an increase in the resonant length of the mode and a decrease in its resonant frequency, compared with the *on* state. On the other hand, the TM_{10} mode flowing in the x direction is not affected by the state of the diode. From this, it is possible for the antenna to produce reconfigurability, in the sense of rotation of the circular polarization generated by the structure, provided that the correct sizing of the patch and the slot is realized.

The principle is presented in Figures 10.20b and c. The characteristics of the TM_{01} mode are modified for the two states of the diode and are unchanged for the TM_{10} mode. Thus, at low and high frequency (f_l and f_h , respectively), the conditions of circular polarization are followed with equal and opposite phase quadratures and identical amplitudes for the two modes.

10.7. Radiation pattern reconfigurable antennas (RPRAs)

Switching short circuits for a patch antenna generally modifies the lengths of the lines of current, and therefore, the operating frequency of the antenna. This effect is unwanted in the context of pattern reconfiguration and, in practice, restricts the

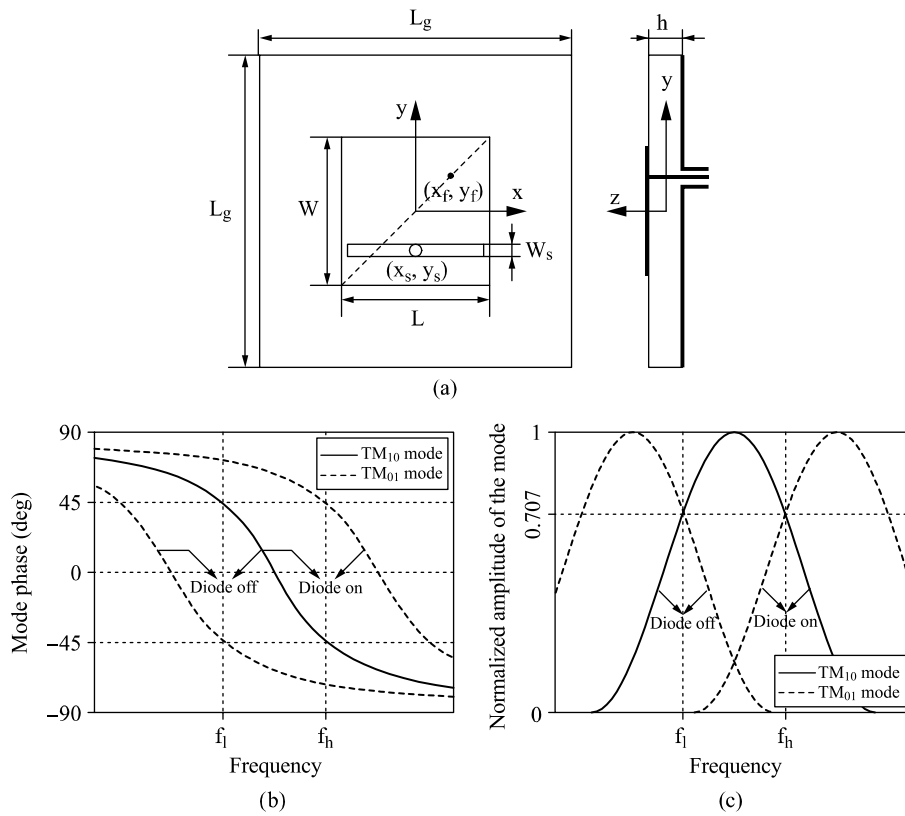


Figure 10.20. Circularly polarized PRA based on a switched slot patch: (a) geometry, (b) phase, and (c) amplitude of the TM_{01} and TM_{10} modes

number of synthesizable patterns to two or three. Here, we will restrict our study to two families of RPRA that present moderate or null variations in matching for each pattern. We will look at:

- antennas with rotational symmetry, where the sequential switching of the parasitic elements leads to rotation of the main-lobe pattern;
- antennas with parasitic elements and switched loads, which combine the intensity of coupling between elements with the values of reactance loading each parasitic element so that it can scan the pattern.

Finally, we will present a cell that is reconfigurable for reflector arrays as an application of the concept of adjustable phase reflective surfaces.

10.7.1. RPRA with rotational symmetry and switched parasitics

The structure is said to have rotational symmetry if the same load is presented to the fed antenna, whatever the configuration of the switched parasitics. Sequential rotation of the radiation pattern with a constant input impedance results from this.

On this basis, a circular array of monopoles has been developed for WLAN applications [SCH 04]. The feeding circuit is applied to the central monopole. Sectorial beam switching results from the rotational symmetry associated with the possibility that the monopole loads in the circle may be switched (Figure 10.21).

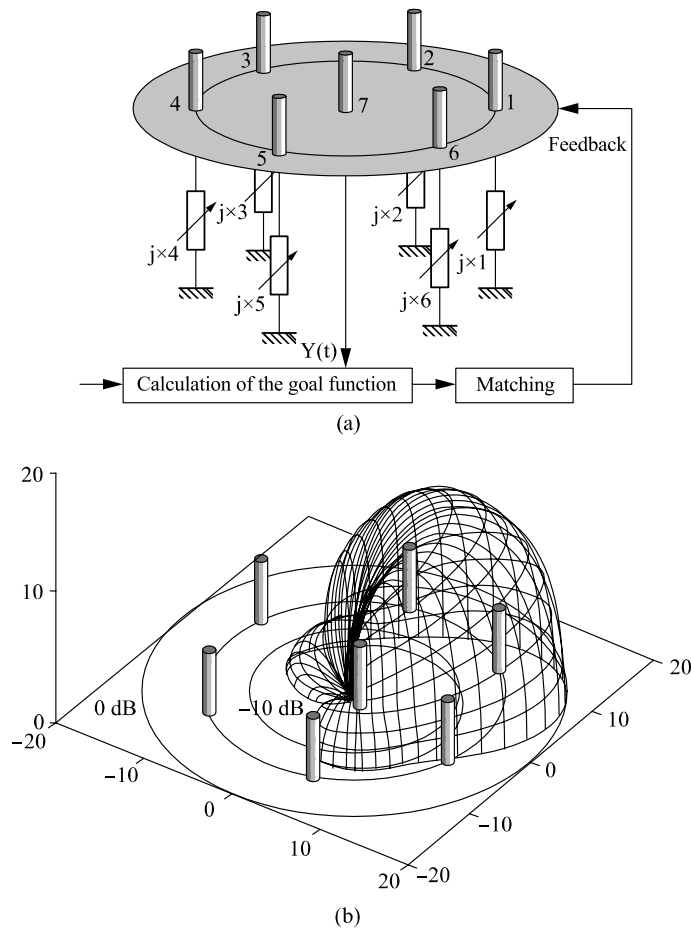


Figure 10.21. Circular array of monopoles coupled to tunable or switchable loads. (a) Architecture, and (b) principle of sectorial switching. Three directive and three reflective monopoles

The idea is to commute the monopole load from an inductive value to a capacitive one in order to make the monopole either directive or reflective, with only the central monopole being fed. The length of the monopoles, the element spacing in the array, and the value of the loads are calculated with the help of the Numerical Electromagnetics Code (NEC) simulator and a genetic optimization algorithm.

Based on this principle, a product, which has been proposed at 58 GHz [LEG 04a], uses metallized via-holes in a Teflon glass substrate of low permittivity ($\epsilon_r = 2.2$, $\tan\delta = 0.002$, $h = 0.8$ mm). Loads are produced by means of coplanar stubs, the extremities of which curl up at the base of the monopoles (Figure 10.22).

A passive prototype has been produced with half of the stubs being short-circuited (loads are therefore capacitive), and the other half being left open (loads are therefore inductive). Typical radiation patterns obtained are presented in Figure 10.22c.

In the active version, a diode connected to an extremity of the stub enables us to switch the load between the inductive and capacitive states.

A final example presented in Figure 10.23 is based on sectorial printed elements with a central Z-antenna [DON 07].

Another variant based on miniature antennas [FAS 00] is presented in Figure 10.24. The non-fed antennas become the parasitic elements of the fed antenna. Within this architecture, there is no central element and two of the symmetric elements are fed, while the others are loaded with pure reactance ($+j36\Omega$). The performances in terms of bandwidth are remarkable: $BW = 40\%$ ($VSWR < 2$) with an azimuthal beamwidth at -3 dB of 75° and an elevational beamwidth of 50° for a directivity of 7.7 dBi. Sequential beam rotation is obtained by switching the input of the monopoles between load and feed.

10.7.2. RPRA with parasitic elements loaded using switched reactance

An antenna with parasitic elements is made of a single-fed radiating element and multiple parasitic elements strongly coupled to it. The Yagi-Uda antenna is an example of this type [YAG 28]. Sensible use of coupling enables us to adjust the radiation pattern and to increase the directivity in a given direction compared to the directivity of a single radiating element.

In a reconfigurable version, the parasitic elements are loaded using switched reactance. In this section, we present the RPRA analysis method as well as an example using three coupled patches.

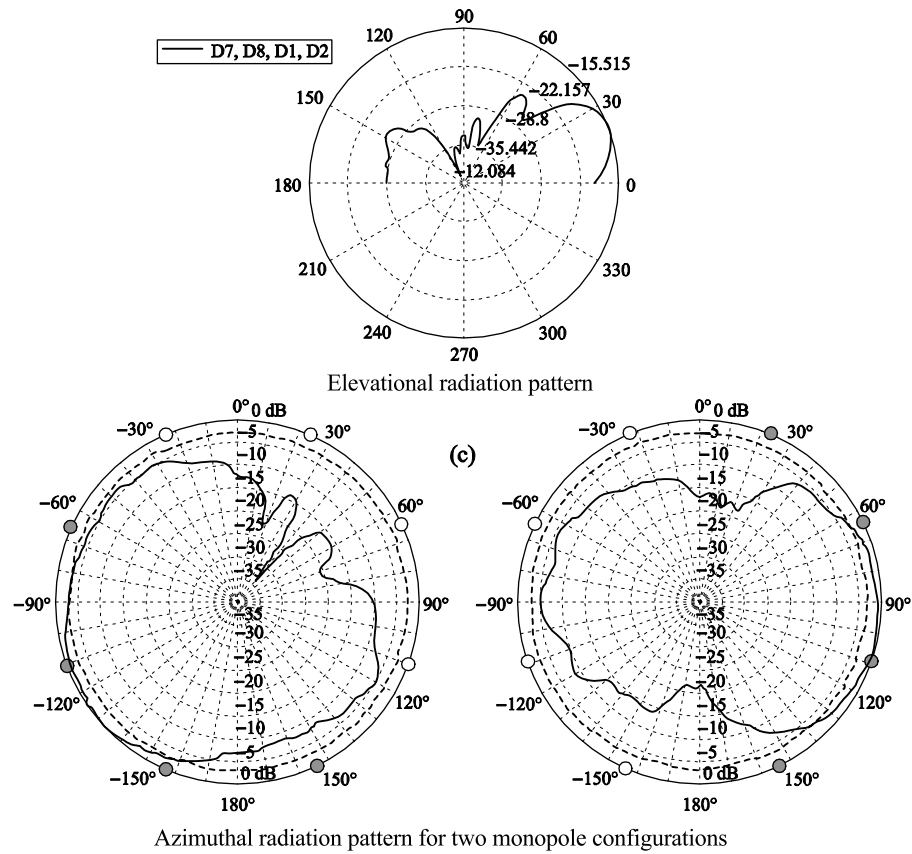
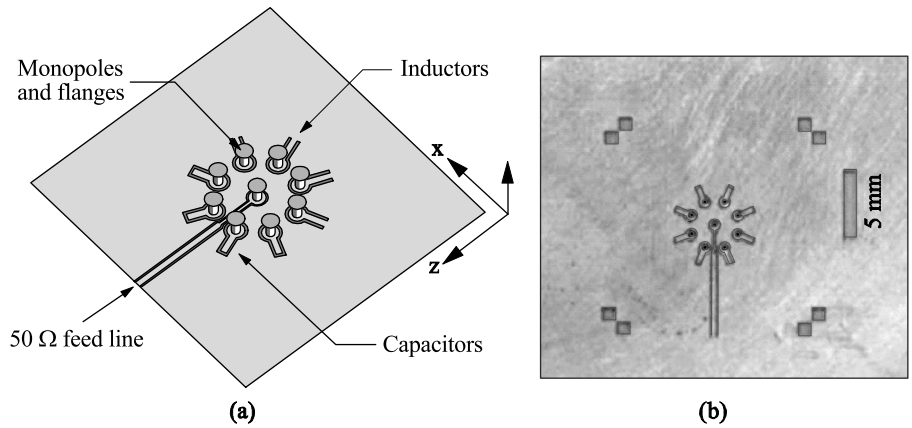


Figure 10.22. Circular array with coplanar loads [LEG 04a]:
 (a) principle, (b) production, and (c) radiation patterns

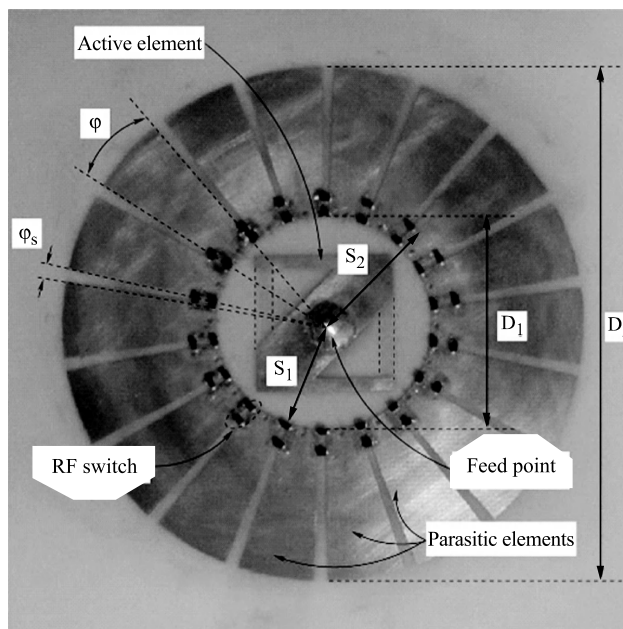


Figure 10.23. Array [DON 07]

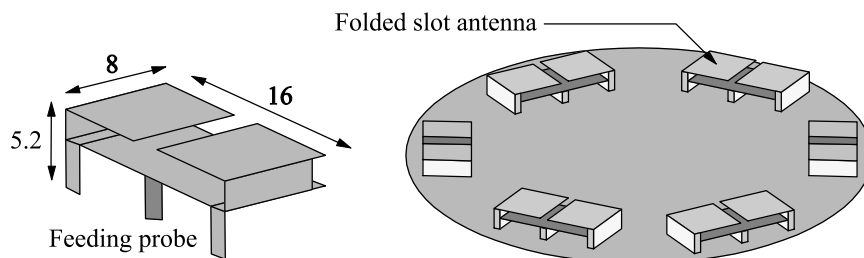


Figure 10.24. Basic folded slot antenna and array principle

10.7.2.1. Field radiated by an array of coupled antennas – active radiation pattern

Let us consider a system of n radiating elements, represented in Figure 10.25. When coupling takes place, the characteristics of each element of the array (matching and radiation) are modified by the presence of other elements.

In order to take the effects of coupling into account, [POZ 94] proposes the use of the notion of an active radiation pattern. The active radiation pattern of the

element of index i is denoted as $E_i(\theta, \varphi)$. It is defined from the conditions illustrated in Figure 10.25b, i.e. when only the i element is fed, the others being matched.

In this context, the $E_i(\theta, \varphi)$ field depends not only on the characteristics of radiation particular to the i element, but also on the effects generated, if coupling exists, from the presence of other array elements.

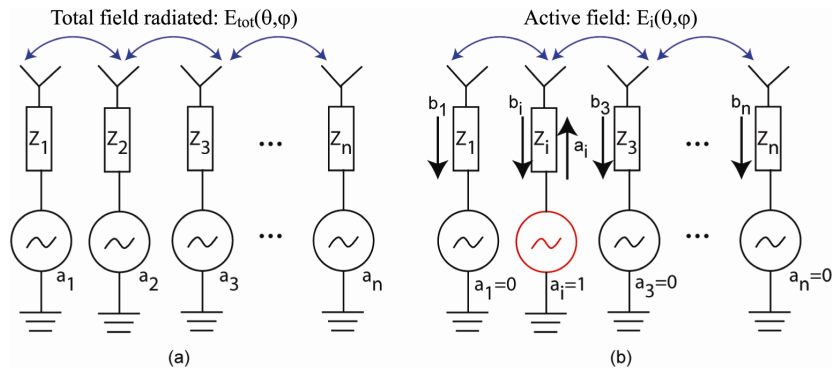


Figure 10.25. Array of n coupled antennas: (a) principle; (b) active field of the i element

The total field radiated by the array is given by the following formula:

$$\vec{E}_{tot}(\theta, \varphi) = \sum_{i=1}^n a_i \vec{E}_i(\theta, \varphi) \quad [10.1]$$

which is the direct application of the principle of superposition, by including all of the $E_i(\theta, \varphi)$ contributions. The notion of active radiation pattern will be used for the sizing of structures with parasitic elements.

10.7.2.2. Example of a central element fed and coupled to two non-fed and loaded symmetric parasitic elements

A modeling procedure utilizing simulated [S] parameters and active radiation patterns is being developed. This procedure can be implemented for any size of parasitic array. The example of a three-element array is considered here. The structure presented in Figure 10.26 comprises a central element surrounded by two parasitic elements connected to loads Z_2 and Z_3 .

Our objective is to define the reflection coefficient Γ_1 at the input of the fed element and the total field radiated by the structure for all values of the pair of loads (Z_2, Z_3). In order to do this, we model the array in the form of a flow graph (Figure 10.26b).

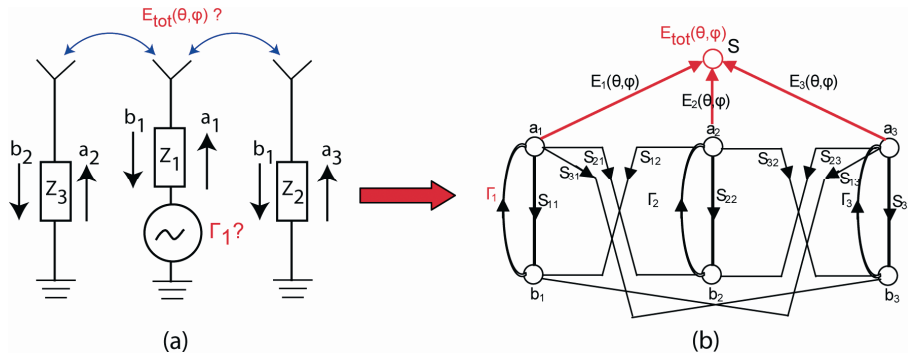


Figure 10.26. Antenna with two parasitic elements. (a) Structure, (b) modeling procedure in the form of a flow graph

For our structure, this circuit includes seven nodes. Six nodes represent the input or output RF power at the different ports. The final node represents the free space (denoted S) that receives the RF power issued from the three antennas. The parameters of the model are the matrix [S], the active radiation patterns $E_i(\theta, \phi)$, and the reflection coefficients Γ_i . The [S] parameters translate the coupling between the antennas. The reflection coefficients Γ_2 and Γ_3 are linked to the values of loads at ports 2 and 3, respectively. The active radiation pattern of each element is the radiation generated by including the influence of the surrounding array. In order to establish the analytical expressions for Γ_1 and $E_{tot}(\theta, \phi)$, it is necessary for us to calculate the following transfer functions [PET 06]:

$$\Gamma_1 = \frac{b_1}{a_1} \quad \text{and} \quad E_{tot}(\theta, \phi) = \frac{S}{a_1} \quad [10.2]$$

By utilizing the procedure established by Mason and Zimmermann [MAS 60] and by considering the symmetric system ($S_{ij} = S_{ji}$), we obtain:

$$\frac{b_1}{a_1} = \frac{\left[\begin{array}{l} S_{11} \left[1 - (S_{22}\Gamma_2 + S_{33}\Gamma_3 + \Gamma_2(S_{23})^2\Gamma_3) + (S_{22}\Gamma_2 S_{33}\Gamma_3) \right] + \\ ((S_{12})^2\Gamma_2) \left[1 - (S_{33}\Gamma_3) \right] + \\ ((S_{13})^2\Gamma_3) \left[1 - (S_{22}\Gamma_2) \right] + \\ 2 * S_{12}\Gamma_2 S_{23}\Gamma_3 S_{13} \end{array} \right]}{1 - (S_{22}\Gamma_2 + S_{33}\Gamma_3 + \Gamma_2(S_{23})^2\Gamma_3) + (S_{22}\Gamma_2 S_{33}\Gamma_3)} \quad [10.3]$$

$$\frac{S}{a_1} = \frac{\begin{bmatrix} E_1[1 - (S_{22}\Gamma_2 + S_{33}\Gamma_3 + \Gamma_2 S_{32}\Gamma_3 S_{23}) + (S_{22}\Gamma_2 S_{33}\Gamma_3)] + \\ E_2[(S_{21}\Gamma_2)[1 - (S_{33}\Gamma_3)] + (S_{31}\Gamma_3 S_{23}\Gamma_2)] \\ E_3[(S_{31}\Gamma_3)[1 - (S_{22}\Gamma_2)] + (S_{21}\Gamma_2 S_{32}\Gamma_3)] \end{bmatrix}}{\begin{bmatrix} 1 - S_{11}\Gamma_1[\Gamma_2(S_{23})^2\Gamma_3 + S_{33}\Gamma_3 + S_{22}\Gamma_2 - S_{22}\Gamma_2 S_{33}\Gamma_3] \\ + S_{22}\Gamma_2 S_{33}\Gamma_3 - (S_{12})^2\Gamma_2\Gamma_1 - (S_{13})^2\Gamma_3\Gamma_1 \\ - S_{13}\Gamma_3 S_{23}\Gamma_2 S_{12}\Gamma_1 - S_{21}\Gamma_2 S_{23}\Gamma_3 S_{13}\Gamma_1 \\ - S_{22}\Gamma_2 - S_{33}\Gamma_3 - \Gamma_2(S_{23})^2\Gamma_3 \\ + S_{22}\Gamma_2(S_{13})^2\Gamma_3\Gamma_1 + S_{33}\Gamma_3(S_{12})^2\Gamma_2\Gamma_1 \end{bmatrix}} \quad [10.4]$$

By analyzing these expressions, we note that all the terms are factors of at least one of the reflection coefficients Γ_2 or Γ_3 , apart from the terms S_{11} for the reflection coefficient and E_1 for the total field radiated. If we consider null values of Γ_2 and Γ_3 , we rediscover the S_{11} parameter for Γ_1 and the E_1 parameter for $E_{\text{tot}}(\theta, \varphi)$.

The manual determination of the analytical expressions rapidly becomes difficult for an array including a more significant number of elements. It is necessary to code an algorithm, using Matlab for instance, to translate Mason's rules.

The analytical expressions use the [S] parameters and active radiation patterns provided from electromagnetic simulators. The advantage of analytical formulation is that it enables a rapid optimization of loads connected to parasitic elements from a single electromagnetic simulation, once the dimensions of the structure have been fixed [POU 08]. The complete set of radiation patterns can then be rigorously determined, without resorting to new simulations.

Finally, reactance will be the only impedance worth selecting, a resistive part of the impedance necessarily leading to a drop in efficiency of the antenna. In practice, it is impossible to completely cancel resistances linked to losses in the stubs and the components. A previous study has indicated that the effect of these losses, if they are reasonable, is negligible when considering pattern shape. As taking them into account complicates the optimization procedure and the calculation time, they have not been included in the analysis.

10.7.2.3. Optimization procedures

The problem of antenna optimization can be formulated as follows: "What are the optimum geometry and load distribution that enable a given radiation direction and a given minimum level of matching?". This problem is complicated by the necessity for a discrete number of beam directions.

Once the antenna geometry is fixed, the only optimization parameters are the values of impedance loading each parasitic element. Hence, the values of the [S]

parameters follow on from the geometry of the three antennas, which is frozen. Coupling must be significant enough for the parasitic elements to influence the radiation pattern, but low enough in order to avoid sensitive mismatching for one or more of the beam directions.

Furthermore, scanning must take place with a common matching band while preserving, for each beam direction, good pattern stability. This pattern stability is evaluated by studying the frequency variation and angular position of the principal lobe.

For example, we consider an antenna composed of three coupled patches, represented diagrammatically in Figure 10.27. This is a MEMS structure, operating at 30 GHz [POU 07]. The distance between the edges of two adjacent patches is fixed at $0.27\lambda_0$ (2,700 μm). This distance leads to a coupling $S_{12} = -13$ dB. For each beam direction between -40° and $+40^\circ$ in steps of 10° , we determine the value of gain for a continuum of load couples (Z_2, Z_3). The couple selected for each direction is the one leading to a maximum gain value; for example, $Z_2 = -j29\Omega$ and $Z_3 = +j23\Omega$ for $\theta = 20^\circ$.

Assuming that the criterion for a good antenna matching is $S_{11} < -10$ dB, the choice of load reactances above respects the matching criterion. If the matching criterion is not verified, a new couple of loads is selected which may lead to a lower gain value, but which respects the matching criterion. This optimization procedure is carried out using a Matlab least-squares method.

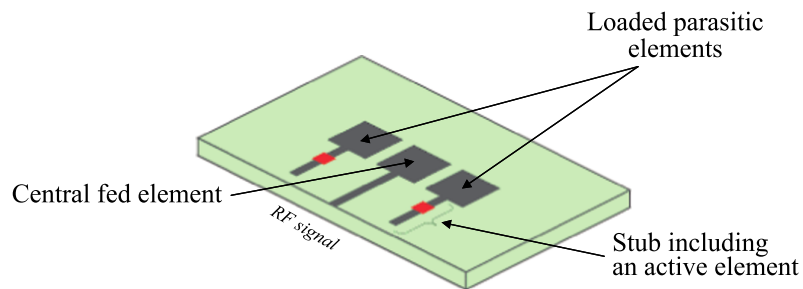


Figure 10.27. Schematic representation of a three-patch RPRA (one fed and two parasitic)

The corresponding radiation patterns are represented in Figure 10.28. We note a growing directivity when the beam angle increases. In Figure 10.29, the change in matching is given as a function of the value of loads for the central operating frequency. In all cases, we see that $S_{11} < -10$ dB.

The change in frequency in Figure 10.30 indicates a common $BW_{-10\text{ dB}}$ of 3.5% (about 1 GHz from 29.6 to 30.6 GHz), fixed by the configuration that presents the maximum level of scanning.

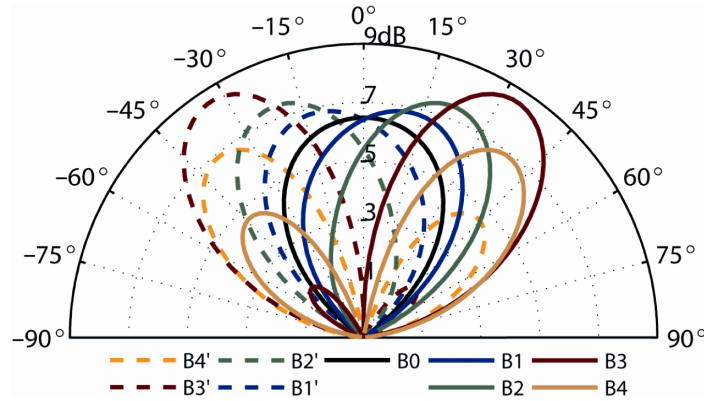


Figure 10.28. Nine radiation patterns switched for each pair (Z_2, Z_3) . $B4' = -40^\circ$, $B3' = -30^\circ$, $B2' = -20^\circ$, $B1' = -10^\circ$, $B0 = 0^\circ$, $B1 = 10^\circ$, $B2 = 20^\circ$, $B3 = 30^\circ$, and $B4 = 40^\circ$

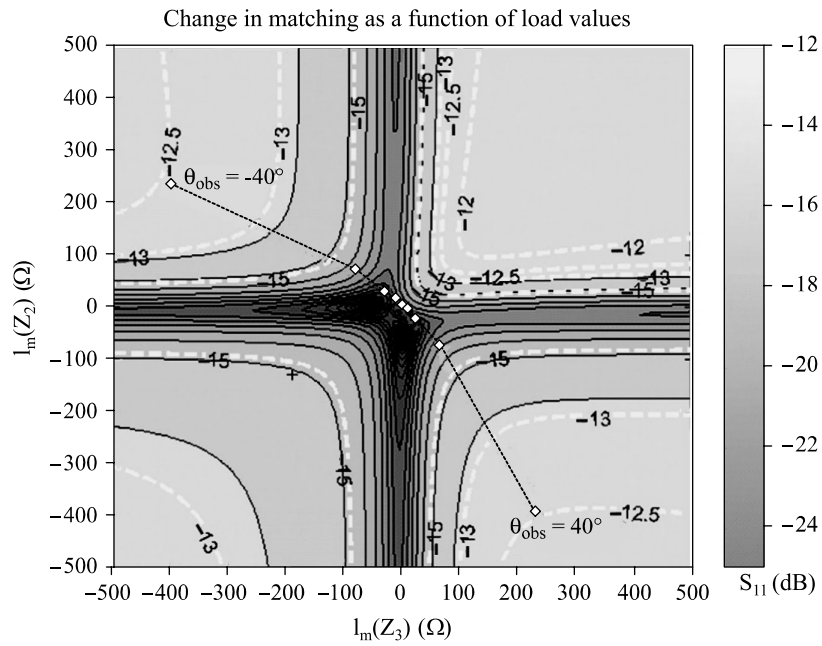


Figure 10.29. Values of matching for each pair (Z_2, Z_3) . The crosses represent pairs corresponding to the nine beam directions

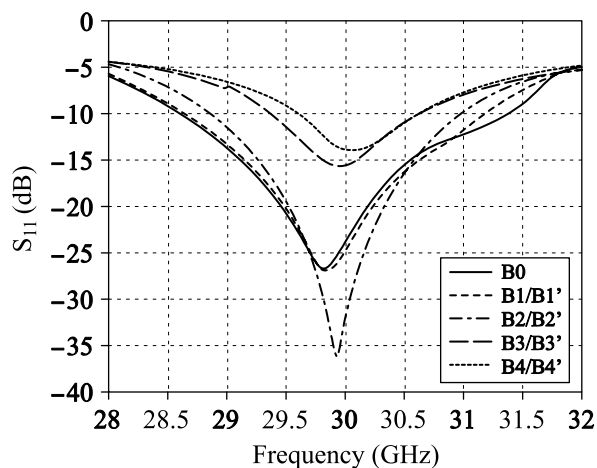


Figure 10.30. Frequency change in matching for each beam direction

The frequency changes in the gain and the angular value of the maximum gain are represented in Figures 10.31a and b, respectively. We observe that the gain drops appreciably for significant scanning angles (from 8.4 to 5.8 dB for B3 and from 7.0 to 5.0 dB for B4). The scanning angle, on the other hand, varies hardly at all. From this we deduce that, in general, this type of antenna undergoes a widening of its pattern at the edge of the band when pattern scanning is significant. Note that beyond about 40° , there are no pairs of loads that enable the synthesis of patterns with a satisfactory level of matching.

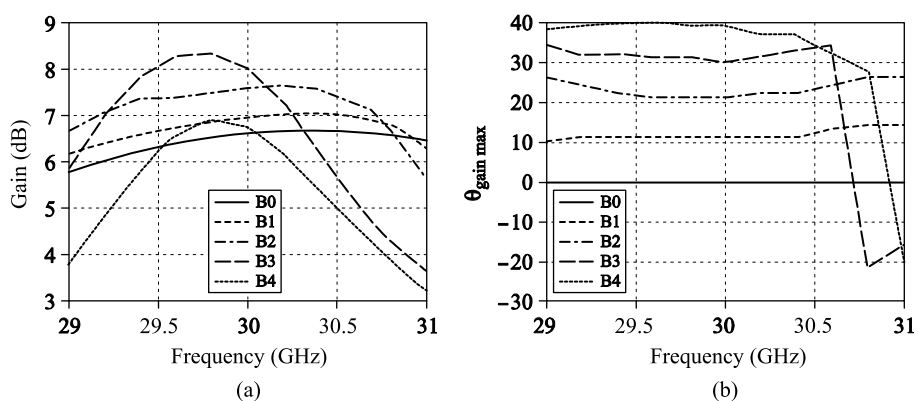


Figure 10.31. Frequency change (a) in gain in the direction of observation and (b) in the angular value of maximum gain

An example of an RPRA antenna, based on the preceding design procedure, is shown in Figure 10.32. The structure is produced over glass (thickness $625\ \mu\text{m}$, $\epsilon_r = 3.8$). The nine pairs of loads (Z_2, Z_3) are synthesized with the aid of stubs, each loaded using three MEMS. Each stub is produced using coplanar technology in order to facilitate the integration of the capacitive MEMS. Lines of high-resistivity polysilicon are used to bias the MEMS. Stub length is regulated by adjusting the number of active MEMS. The total width of the structure is $8.1\ \text{mm}$, the width of a patch is $1.9\ \text{mm}$, and the length of a MEMS is $570\ \mu\text{m}$.

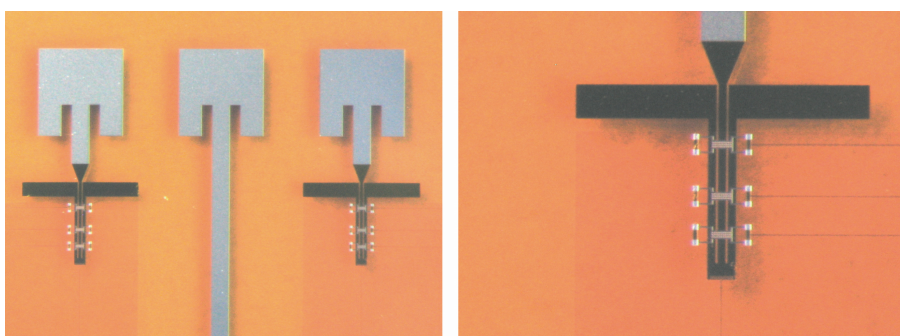


Figure 10.32. RPRA with two parasitic elements, loaded using stubs switched using capacitive MEMS [POU 07]

10.7.3. Unit cell of reflective array based on a patch of slots [CAD 05]

The reconfigurable element represented in Figure 10.33 is the unit cell of a reflect array constructed over alumina for Ku-band applications. It is based on a patch into which two parallel slots have been cut.

Five MEMS are produced in each slot during manufacture. The reflective array is illuminated by a plane wave with normal incidence. The wave reflected by the unit cell is phased with a phase set using one of the 2^{10} combinations of possible states for the MEMS (Figure 10.34). While correctly regulating the phase reflected by each cell in the reflective array, we finally reach scanning which is electronically controlled (Figure 10.35).

Propagation losses are limited since the concept does not make use of transmission lines to transport energy unlike classical phased arrays. Biasing is supplied to 10 electrodes by 10 high resistivity lines. The ground DC is applied via two other high resistivity lines to the metallic bands of the patch.

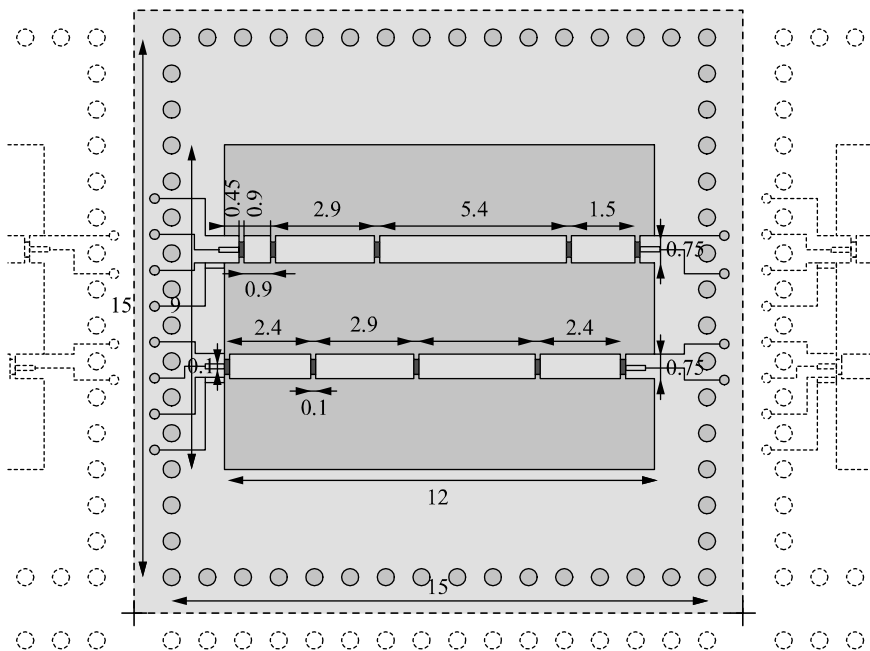


Figure 10.33. Basic cell of a reflect array at 14 GHz [CAD 05]

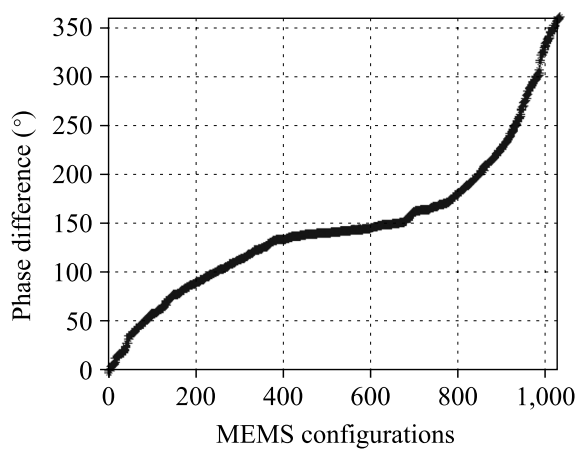


Figure 10.34. Observed phase distribution for $N=1,024$ combinations of MEMS states [CAD 05]

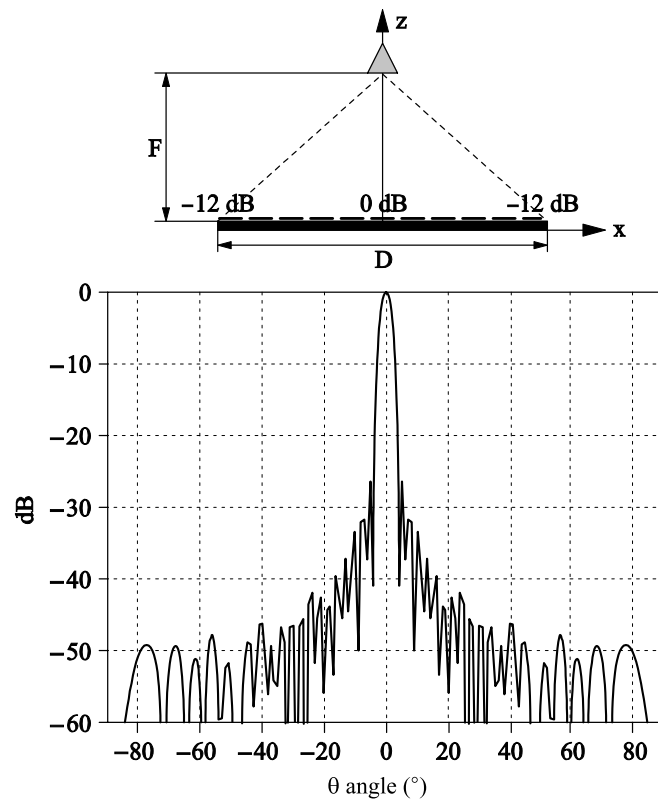


Figure 10.35. Radiation patterns for a circularly reflective array of 1,436 elements with $F/D=0.8$ at 14 GHz. Apodization of -12 dB on the edges with a horn antenna as the primary source [SAL 09]

Chapter 11

Introduction to Antenna Diversity

11.1. Benefits of antenna diversity

Modern telecommunication systems need to offer ever-improving performances in terms of coverage, reception quality, data rate, etc. Research has suggested some innovative techniques that jointly exploit multiple antennas for the transmission and/or reception of information. These multiantenna techniques offer some excellent perspectives on optimizing wireless communications, and in recent years we have seen an explosion in the number of antennas in use in wireless devices. Domestic Wi-Fi networks or even portable television receivers are widespread examples of systems that exploit antenna diversity. Some examples of these are shown in Figure 11.1.

The space available for antennas is more and more limited, as the trend is for terminals that are compact, thin, and light. Nowadays, antenna designers have to devise miniaturized multiantenna systems, while limiting interference between the concerned antennas. This chapter forms an introduction to the issues in antenna diversity. It presents the primary concepts and useful tools for optimizing multiantenna systems. First, we will discuss signal degradations due to the multipath propagation channel. We will present the principles of the multiple reception antennas that compensate these effects. Then we will see how the performance of

multiple antennas can be measured against criteria based on the radioelectrical characteristics. Finally, we will show how these criteria can be used in order to optimize multiantenna systems.



Figure 11.1. *Examples of applications exploiting antenna diversity*

11.1.1. *Effects of multipath propagation*

The establishment of wireless communications in built-up environments, such as urban areas or the insides of buildings, is a complex technological challenge. Buildings, furniture, vehicles, and even people are many of the obstacles that electromagnetic waves rebound against or are diffracted against (see illustrations in Figure 11.2). These interactions strongly disturb the properties of the waves in terms of polarization or in terms of direction of propagation, and, as these disturbances can vary from one environment to another, the properties of an antenna cannot be optimized to compensate for these effects completely. Furthermore, these propagation mechanisms generate a multitude of wave paths between transmitters and receivers. The most critical effect occurs when the waves arising from different trajectories are combined in a destructive manner by a phase opposition. We then observe fading of the received signal. Figure 11.3 illustrates the fluctuations in the received signal power γ , due to interference in multipath propagation. While the fadings in the received signal are very much localized in time and space, they are however frequently observed and can be very deep.

It is very difficult to faithfully model wave propagation mechanisms within these complex environments. However, we are able to construct a model for the behavior of the received signal from a number of simplified hypotheses regarding the conditions at the reception antenna. For example, we assume that the multiple incoming waves are statistically uniformly spread around the antenna and that each one has its own uniform phase distribution [JAK 74]. We show that in this

circumstance, the amplitude of the received signal follows a Rayleigh function with a cumulative distribution function (CDF) which is expressed as:

$$\text{Rayleigh function: } P(\gamma \leq \gamma_0) = 1 - e^{-\frac{\gamma_0}{\Gamma}} \quad [11.1]$$

γ is the instantaneous power of the signal received by the antenna, Γ the average received power, and γ_0 the level of reference power which is used for the CDF. In Figure 11.3, we can trace the CDF from a Rayleigh function with an average power $\Gamma = 0$ dBm. Reading this curve enables us to calculate the probability that the received power γ is less than the reference power γ_0 . We thus find that in 10% of cases the level of the modeled received signal is 10 dB below the average level and in 1% of cases it is 20 dB below. It is often useful to interpret the CDF in another way: in 90% of cases the guaranteed level is 10 dB below the average level, which guarantees that in 99% of cases it is 20 dB below. This corresponds to the modelization of destructive interference of multiple trajectories within an environment. The comparison between the theoretical Rayleigh function and the CDF of real signals shows that the Rayleigh statistic is faithful to the effects of a multipath channel (see Figure 11.3).

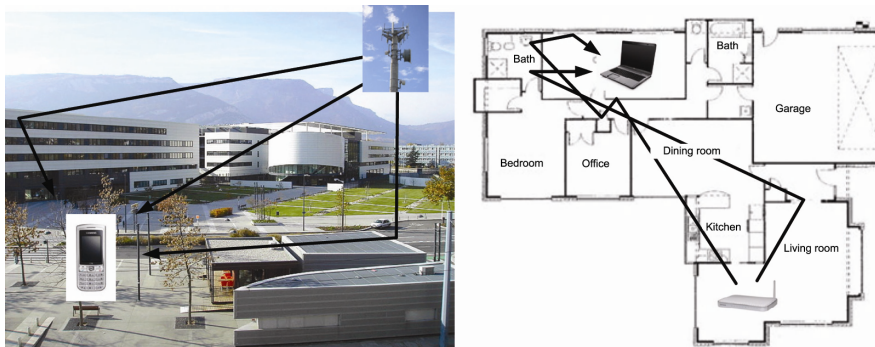


Figure 11.2. *Multipath propagation channel*

11.1.2. Principles of antenna diversity

Multipath propagation leads to deep fades in received signals, but these degradations are very localized in time and space. In order to mitigate these effects, it is possible to simultaneously use several signals received independently; each signal is subjected to degradations that are linked to the propagation, but, as each receives these independently, then the risk of seeing degradations in all signals at

the same time is slim. Thus, the transmitted information is always available from one of the received signals.

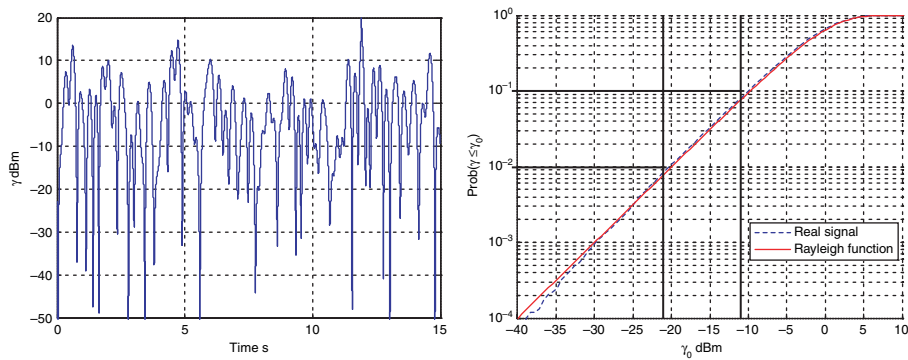


Figure 11.3. Fluctuations in received signal due to multipath propagation, cumulative distribution function (CDF)

There are several techniques for receiving several signals independently. Time and frequency diversities consist of multiple signal transmissions at different moments or in different frequency bands [JAK 74]. Since the properties of the propagation channel are different from one moment to the next, or from one frequency to the next, then the received signals are independent. These techniques require a specific transmission scheme and, since the signal is being sent at multiple times or in multiple frequency bands, they do not improve the spectral efficiency of the communication.

Another technique consists of using multiple antennas in order to receive multiple signals; this is called antenna diversity [VAU 87]. Each antenna receives a replica of the transmitted signal; it is not necessary to adapt the information transmission method. With antenna diversity, spectral efficiency is not degraded, as no additional temporal or frequential resource is necessary. The subject of this chapter is the optimization of antennas for the reception of independent signals, but we will initially present the expected benefits arising from ideal antenna diversity.

A receiver using antenna diversity brings together a multiantenna system and a receiver signal combining block (see Figure 11.4) [JAK 74]. There are several combination strategies for received signals:

- *Selection*: this consists of detecting and selecting the strongest of the signals received by the antennas. This technique requires the signals to be received together, but does not require too many resources for calculation.

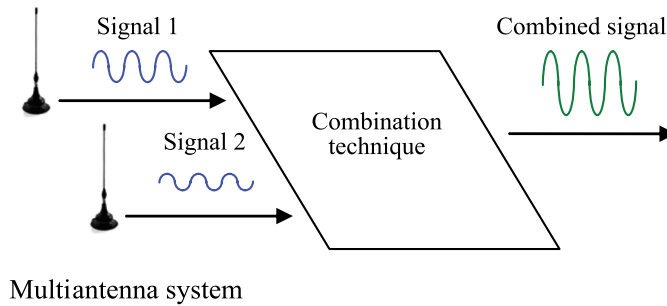


Figure 11.4. Outline of the principles of antenna diversity

With multiple antenna selection, the probability that the power γ , available from the combiner output, is less than the reference power γ_0 corresponds to the probability that the N signals entering the combiner inputs are simultaneously less than the reference power γ_0 . The CDF of the power available for the receiver device is then:

selection:

$$P(\gamma \leq \gamma_0) = (1 - e^{-\frac{\gamma_0}{\Gamma}})^N \quad [11.2]$$

where Γ is the average power of each of the N -received signals.

– *Optimum combiner*: this combination technique consists of a summation of signals received after cophasing. If the signal summation is weighted proportionally to the instantaneous powers of each of the signals, then this technique produces the best possible usage of antenna diversity; we refer to the optimum combiner. This technique clearly uses more in terms of material and calculation resources.

The total power of the recombined signal is the sum of the individual powers initially available for each antenna. The CDF of the available power on exiting the receiver can therefore be expressed as [JAK 74]:

optimum combiner:

$$P(\gamma \leq \gamma_0) = 1 - e^{-\frac{\gamma_0}{\Gamma}} \sum_{k=1}^N \frac{\left(\frac{\gamma_0}{\Gamma}\right)^{k-1}}{(k-1)!} \quad [11.3]$$

In Figure 11.5, we can trace the CDF of the signals obtained with the diversity of two and three antennas. The selection and optimum combiner techniques can be compared with a simple receiver using a single antenna. Antenna diversity strongly reduces the effects of signal fading. With two antennas, the level of guaranteed power in 99% of cases (i.e. with a reference probability of 10^{-2}) is -10 dB relative to the average level, compared with -20 dB for a single antenna, a gain of 10 dB. With an optimum combiner, the guaranteed level changes to -8 dB for two antennas, a gain of 12 dB. This difference in the levels of guaranteed power is called the diversity gain [VAU 87]. Note that the diversity gain depends on the reference probability under consideration, as well as that of the single antenna taken as a reference.

Diversity gain is more important for an increasing number of antennas, but the improvement resulting from the introduction of an additional antenna reduces with the number of antennas.

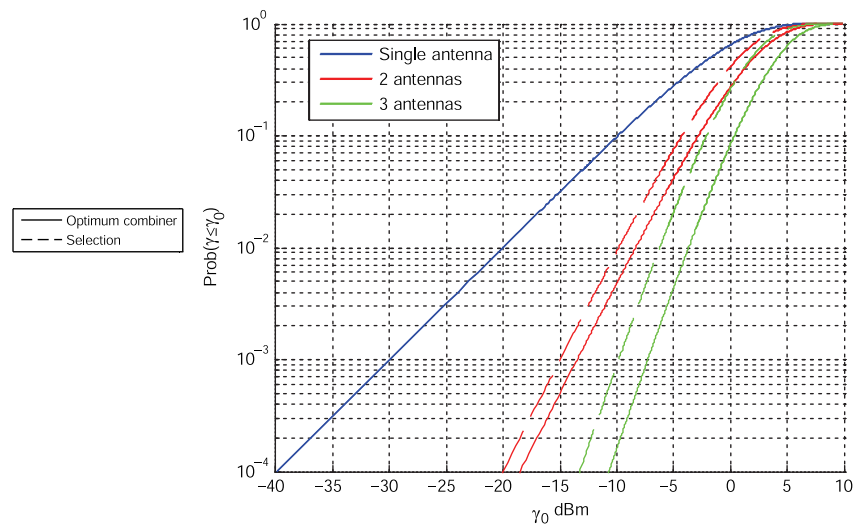


Figure 11.5. Gain of antenna diversity seen from the CDF of the received signal

There are other combination techniques, such as antenna commutation, that consist of switching one antenna with another when the received power is insufficient. In this case it is not necessary to continually connect the N received signals, but simply the selected antenna signal. Commutation enables a further reduction in the complexity of the receiver front-end; however, performance is limited [VAU 03].

Issues linked to the material and software implementations of signal recombination techniques will not be covered in any further detail in this chapter.

11.1.3. Non-ideal antenna diversity

Effective diversity gain can be restricted by faults in the balance and independence of signals received by the antennas.

11.1.3.1. Unbalanced signals

If the N signals received by the antennas present different average powers Γ_k , then the weakest signals will only partially compensate for degradations in the strongest ones; we know that the diversity is less effective in this case.

For a selection, the CDF of the recombined signal is calculated by estimating the probability that all N antennas simultaneously receive power that is less than the reference power γ_0 , and we therefore obtain [STE 66]:

selection:

$$P(\gamma \leq \gamma_0) = \prod_{k=1}^N 1 - e^{-\frac{\gamma_0}{\Gamma_k}} \quad [11.4]$$

For an optimum combiner, the calculation of the CDF of the recombined signal is not so straightforward, but if it is restricted to the low power range $\gamma_0 \ll \Gamma$, we obtain by simplification [BAR 63]:

optimum combiner:

$$P(\gamma \leq \gamma_0) \approx \frac{1}{\prod_{k=1}^N \Gamma_k} \frac{\gamma_0^N}{N!} \quad [11.5]$$

In Figure 11.6, we show the effects of an imbalance of average signal power for diversity of two antennas. Diversity gain is reduced by about 1.5 dB with an imbalance of 3 dB and about 5 dB with an imbalance of 10 dB (reference probability 10^{-2}). The diversity gain is reduced with the imbalance of signals. However, it would take an extreme imbalance in order to lose all benefits from antenna diversity.

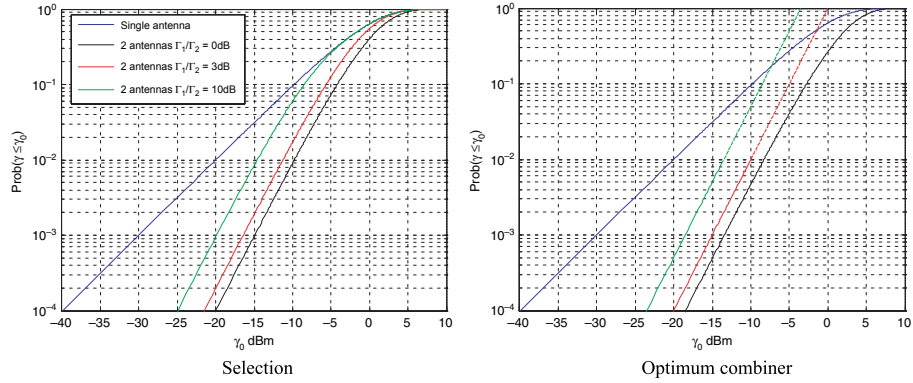


Figure 11.6. Degradations due to signal imbalance

11.1.3.2. Correlated signals

We now make the hypothesis that signals received by antennas are not completely independent. The correlation coefficient ρ is a dimensionless indicator measuring the quality of the linear relationship linking two random variables. If there is a linear relationship between two random signals s_1 and s_2 , then $\rho = \pm 1$, but if there is no linear relationship within any subset between the random variables s_1 and s_2 , then $\rho = 0$.

For the study of the mechanics of antenna diversity, it is not strictly the behavior of the signals from voltage s_k which is of interest, but rather the behavior of the envelopes of signals from power $\gamma_k \propto |s_k|^2$. Indeed, we are not only interested in the correlation coefficient of the signals ρ , but especially in the correlation coefficient of the signal envelopes ρ_e :

signal correlation:

$$\rho = \frac{\langle s_1 s_2^* \rangle}{\sqrt{\langle s_1 \rangle^2 \langle s_2 \rangle^2}} \tag{11.6}$$

envelope correlation:

$$\rho_e = \frac{\langle |s_1|^2 \cdot |s_2|^2 \rangle}{\sqrt{\langle |s_1|^2 \rangle^2 \langle |s_2|^2 \rangle^2}} = \frac{\langle \gamma_1 \cdot \gamma_2 \rangle}{\sqrt{\langle \gamma_1 \rangle^2 \langle \gamma_2 \rangle^2}} \tag{11.7}$$

In the specific case in which the signals s_k follow a Rayleigh function, the correlation coefficient of the signal envelopes can be estimated from the correlation coefficient of the signals, using [VAU 03]:

$$\rho_e \approx |\rho|^2 \quad [11.8]$$

We note that in this case the envelope correlation coefficient ρ_e remains positive. These two signals are completely correlated if $\rho_e = 1$, and they are independent if $\rho_e = 0$. The calculations that follow are based on diversity of two antennas. The signals are partially correlated, $\rho_e \neq 0$, and have different average power Γ_1 and Γ_2 . For a selection and an optimum combiner, the CDF values of the combined signal are expressed [STE 66, JAK 74]:

selection:

$$P(\gamma \leq \gamma_0) \approx \frac{\gamma_0^2}{\Gamma_1 \Gamma_2 (1 - \rho_e)} \quad [11.9]$$

optimum combiner:

$$P(\gamma \leq \gamma_0) \approx \frac{\gamma_0^2}{2\Gamma_1 \Gamma_2 (1 - \rho_e)} \quad [11.10]$$

These calculations are only valid for low values of power $\gamma_0 \ll \Gamma$.

Figure 11.7 shows the degradations from diversity gain linked solely to the correlation of received signals, i.e. with balanced signals $\Gamma_1 = \Gamma_2$. We see two levels of high correlation, 75% and 90%, that cause a reduction in diversity gain of 3 and 6 dB, respectively (reference probability 10^{-2}). Even if the diversity gain remains positive for correlated signals, we need to make every effort to optimize signal independence in order to maximize the benefits from antenna diversity.

Nevertheless, it is necessary to concurrently optimize the balance and independence of the antennas. Through development restricted around low values of power $\gamma_0 \ll \Gamma$, we are able to combine expressions [11.9] and [11.10], which were obtained by taking defects into account, with expressions [11.2] and [11.3], which correspond to the ideal case. We therefore obtain an equivalent average power Γ_{equ} which is useful as a figure-of-merit:

$$\Gamma_{equ} = \sqrt{\Gamma_1 \Gamma_2 (1 - \rho_e)} \quad [11.11]$$

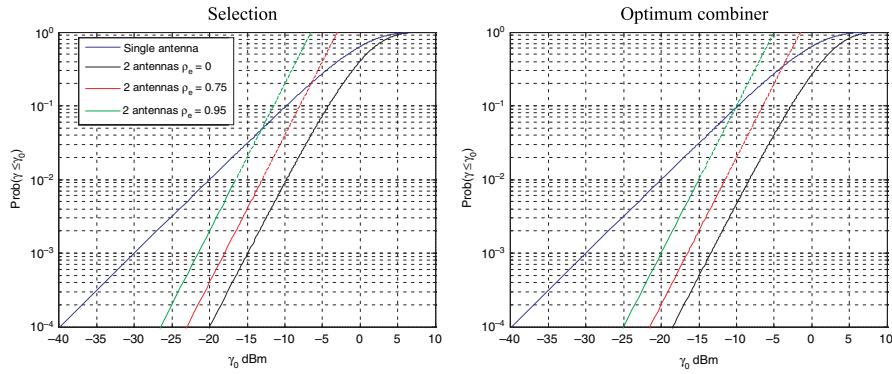


Figure 11.7. Degradations due to signal dependence

11.2. Performance of multiantenna systems

We have seen that multiantenna techniques present the best performance when received signals are balanced and independent; so how do we optimize antennas in order to achieve these favorable conditions?

In this section, we present methods that enable us to evaluate the performance of antenna diversity. These criteria enable us to compare and/or optimize multiantenna systems.

11.2.1. Antenna balance

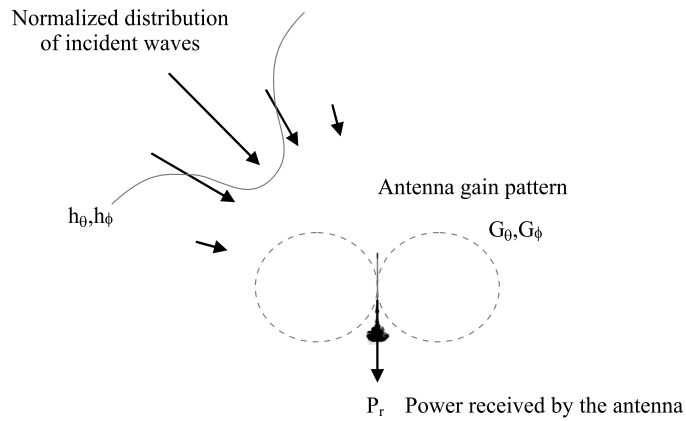


Figure 11.8. Mean effective gain of an antenna in its environment

The mean effective gain G_e of an antenna in its environment is defined as the ratio of the average power received by the antenna P_r to the total average power available within the environment of the antenna P_{tot} [TAG 90, FUJ 01]:

$$G_e = \frac{P_r}{P_{tot}} \quad [11.12]$$

The mean effective gain G_e takes into account the properties of both the environment and the antenna, as illustrated in Figure 11.8.

In order to calculate G_e , we first need to make note of the polarization properties of the incident waves. P_θ is the total power available with a vertical polarization, while P_ϕ refers to the total power with a horizontal polarization. The ratio of the orthogonal polarizations is denoted as XPR and is defined by:

$$XPR = \frac{P_\theta}{P_\phi} \quad [11.13]$$

The XPR depends both on the propagation mechanisms that change the polarization properties and on the polarization properties of the transmitter antenna. Where the transmitter antenna has a linear polarization, XPR has a value in an exterior urban environment of between ± 4 and ± 9 dB [LEE 72]. It is closer to being balanced, $XPR = 0$ dB, in buildings or when the two polarizations are jointly generated at the transmission.

As shown in Figure 11.8, the angular distribution of electrical incident waves around the antenna is also of interest to us. For this, we introduce two distinct functions of normalized distribution for the vertical and horizontal polarizations $h_\theta(\theta, \phi)$ and $h_\phi(\theta, \phi)$, where the azimuth angle ϕ and elevation angle θ describe the incidence direction. A classic model can be seen in a uniform function for the azimuthal distribution and a Gaussian function for the elevational distribution [TAG 90]. We therefore obtain:

$$h(\theta, \phi) = A \cdot e^{-\frac{(\theta - \theta_0)^2}{2\sigma_\theta^2}} \quad [11.14]$$

where θ_0 is the principal incoming direction in elevation of the incident waves and σ_θ the elevational angular spread.

The normalization of the angular distribution functions of incident waves occurs as a result of:

$$\iint_{\Sigma} h^2 d\Omega = 1 \quad [11.15]$$

where $d\Omega$ is the solid angle element and Σ the whole space around the antenna.

The calculation of the mean effective gain G_e can be seen as the integral of antenna gain in all directions over the incident energy distribution in the space and the polarizations [TAG 90, FUJ 01]:

$$G_e = \iint_{\Sigma} \left(\frac{XPR}{1 + XPR} \cdot G_{\theta} \cdot h_{\theta}^2 + \frac{1}{1 + XPR} \cdot G_{\phi} \cdot h_{\phi}^2 \right) d\Omega \quad [11.16]$$

where G_{θ} is the antenna gain over the vertical polarization and G_{ϕ} the gain over the horizontal polarization.

The mean effective gain G_e depends both on the antenna and its environment. Note that it also depends on the orientation of the antenna in its environment.

In order to optimize the balance of signals issued from a multiantenna diversity system, we will be able to evaluate and compare the different mean effective gains G_e of the antennas.

We note that in the specific case in which the incident wave distribution is uniform around the antenna $h(\theta, \phi) = \text{const}$ and the polarizations are balanced $XPR = 0$ dB, the mean effective gain G_e of the antenna is half of its radiation efficiency η :

$$G_e = \frac{\eta}{2} \quad [11.17]$$

11.2.2. Antenna independence

The independence of received signals is measured using the correlation coefficient ρ defined in equation [11.6], for which the module is null when the signals are effectively independent. There are different methods for evaluating the correlation coefficient ρ as a function of the radioelectrical characteristics of the antennas.

11.2.2.1. Utilization of far-field radiation patterns

The voltage V at the terminals of an open circuit antenna is obtained by the integral of all incident waves projected over the radiation pattern of the antenna [VAU 03]:

$$V = K \iint_{\Sigma} \mathbf{E} \cdot \mathbf{s} \cdot d\Omega \quad [11.18]$$

where \mathbf{E} is the complex vector describing the far-field electrical pattern, \mathbf{s} the vector describing the instantaneous distribution of incident waves around the antenna, K a dimensionless constant, and Σ the whole space.

The far-field electrical pattern of the antenna and the distribution of electrical incident field are broken down according to the vertical and horizontal components of polarization:

$$\mathbf{E} = E_{\theta} \cdot \mathbf{e}_{\theta} + E_{\phi} \cdot \mathbf{e}_{\phi} \quad [11.19]$$

$$\mathbf{s} = s_{\theta} \cdot \mathbf{e}_{\theta} + s_{\phi} \cdot \mathbf{e}_{\phi} \quad [11.20]$$

where E_{θ} and E_{ϕ} are complex numbers, and \mathbf{e}_{θ} and \mathbf{e}_{ϕ} the orthogonal unit vectors defining the vertical and horizontal components of polarization of the electrical field.

The correlation coefficient ρ of the voltage signals for two antennas can be calculated by introducing expression [11.18] into equation [11.6] [VAU 87].

We note that antenna patterns must be expressed in the same base with the same phase center; the incident wave distribution is the same for the two antennas. We then obtain:

$$\langle V_1 \cdot V_2^* \rangle = K_1 \cdot K_2 \cdot \left\langle \iint_{\Sigma} \iint_{\Sigma} \begin{aligned} & E_{\theta_1}(\Omega_1) \cdot E_{\theta_2}^*(\Omega_2) \cdot s_{\theta}(\Omega_1) \cdot s_{\theta}^*(\Omega_2) \\ & + E_{\theta_1}(\Omega_1) \cdot E_{\phi_2}^*(\Omega_2) \cdot s_{\theta}(\Omega_1) \cdot s_{\phi}^*(\Omega_2) \\ & + E_{\phi_1}(\Omega_1) \cdot E_{\theta_2}^*(\Omega_2) \cdot s_{\phi}(\Omega_1) \cdot s_{\theta}^*(\Omega_2) \\ & + E_{\phi_1}(\Omega_1) \cdot E_{\phi_2}^*(\Omega_2) \cdot s_{\phi}(\Omega_1) \cdot s_{\phi}^*(\Omega_2) \end{aligned} d\Omega_1 d\Omega_2 \right\rangle \quad [11.21]$$

Inverting the integral and the expectation and assuming that *the orthogonal polarizations of the incident waves are independent* [VAU 87], the expression becomes:

$$\langle s_\theta \cdot s_\theta^* \rangle = \langle s_\theta \cdot s_\theta^* \rangle = 0 \quad [11.22]$$

$$\langle V_1 \cdot V_2^* \rangle = K_1 \cdot K_2 \cdot \iint_{\Sigma} \iint_{\Sigma} \left(E_{\theta_1}(\Omega_1) \cdot E_{\theta_2}^*(\Omega_2) \cdot \langle s_\theta(\Omega_1) \cdot s_\theta^*(\Omega_2) \rangle + E_{\phi_1}(\Omega_1) \cdot E_{\phi_2}^*(\Omega_2) \cdot \langle s_\phi(\Omega_1) \cdot s_\phi^*(\Omega_2) \rangle \right) d\Omega_1 d\Omega_2 \quad [11.23]$$

We assume that each polarization of the incident waves is spatially decorrelated [VAU 87]:

$$\langle s_\theta(\Omega_1) \cdot s_\theta^*(\Omega_2) \rangle = 0 \text{ and } \langle s_\phi(\Omega_1) \cdot s_\phi^*(\Omega_2) \rangle = 0 \text{ if } \Omega_1 \neq \Omega_2 \quad [11.24]$$

$$\langle V_1 \cdot V_2^* \rangle = K_1 \cdot K_2 \cdot \iint_{\Sigma} \left(E_{\theta_1} \cdot E_{\theta_2}^* \cdot \langle |s_\theta|^2 \rangle + E_{\phi_1} \cdot E_{\phi_2}^* \cdot \langle |s_\phi|^2 \rangle \right) d\Omega \quad [11.25]$$

Only the distribution of the incident waves is not deterministic. We can introduce the incident wave distribution functions discussed in section 11.2.1:

$$\langle |s_\theta|^2 \rangle = \frac{XPR}{1 + XPR} h_\theta^2 \quad \langle |s_\phi|^2 \rangle = \frac{1}{1 + XPR} h_\phi^2 \quad [11.26]$$

The calculations for $\langle V_1 \cdot V_1^* \rangle$ and $\langle V_2 \cdot V_2^* \rangle$ are similar.

Developing the calculation gives an expression for the correlation coefficient ρ of voltage signals for two antennas as a function of their radiation pattern and their incident wave distribution [VAU 87, FUJ 01]:

$$\begin{aligned} \rho_{12} &= \frac{R_{12}}{\sigma_1 \sigma_2} \\ R_{12} &= \iint_{\Sigma} \left(\frac{XPR}{1 + XPR} E_{\theta_1} \cdot E_{\theta_2}^* \cdot |h_\theta|^2 + \frac{1}{1 + XPR} E_{\phi_1} \cdot E_{\phi_2}^* \cdot |h_\phi|^2 \right) d\Omega \\ \sigma_1^2 &= \iint_{\Sigma} \left(\frac{XPR}{1 + XPR} |E_{\theta_1}|^2 \cdot |h_\theta|^2 + \frac{1}{1 + XPR} |E_{\phi_1}|^2 \cdot |h_\phi|^2 \right) d\Omega \\ \sigma_2^2 &= \iint_{\Sigma} \left(\frac{XPR}{1 + XPR} |E_{\theta_2}|^2 \cdot |h_\theta|^2 + \frac{1}{1 + XPR} |E_{\phi_2}|^2 \cdot |h_\phi|^2 \right) d\Omega \end{aligned} \quad [11.27]$$

Thus, the correlation coefficient of received signals can be calculated from the properties of the antennas and their environment. The calculation is, however, reliant on the following hypotheses:

- the vertical and horizontal polarizations of the environment are independent;
- the incident waves are spatially decorrelated.

Given that they originate from the same transmitter, the incident waves cannot be completely independent of each other. However, if the propagation channel is sufficiently rich in obstacles, we could consider that multiple paths are high enough in number and complex enough for the hypotheses stated above to be reasonable.

This condition enables us to optimize and compare multiantenna systems. However, it requires the complete three-dimensional characterization of the properties of antenna radiation in terms of amplitude and phase, as well as the two components of polarization.

This type of measurement requires a specific experimental base in an anechoic chamber, but other more practical methods have been proposed.

11.2.2.2. Utilization of S-parameters

The interactions between multiple antennas brought together can be analyzed by the transfers of power between them. Figure 11.9 illustrates input and output waves, a_i and b_i , respectively, at the ports of a system of N antennas. a_i and b_i are two complex numbers that are normalized relative to a voltage ($|a_i|^2$ and $|b_i|^2$ are themselves relative to a power).

The matrix S is used to describe the reflection mechanisms at the antenna ports and the coupling mechanism between antennas. The coefficients of the matrix S , which are known as S-parameters, are expressed as:

$$S_{ij} = \frac{b_i}{a_j} \quad [11.28]$$

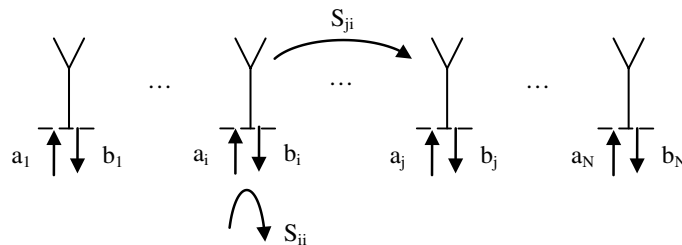


Figure 11.9. S-parameters of a system of N antennas

The S_{ii} parameters are reflection coefficients and the S_{ij} are coupling coefficients. Matrix S is linked to a reference impedance that is classically 50Ω for microwave systems.

We can simplify the situation by assuming an environment in which the incident wave distribution is uniform around the antenna $h(\theta, \phi) = \text{const}$ and the polarizations are balanced $XPR = 0$ dB. Equation [11.27] therefore becomes:

$$\rho_{ij} = \frac{\iint_{\Sigma} \mathbf{E}_i \cdot \mathbf{E}_j^* d\Omega}{\sqrt{\iint_{\Sigma} |\mathbf{E}_i|^2 d\Omega \cdot \iint_{\Sigma} |\mathbf{E}_j|^2 d\Omega}} \quad [11.29]$$

The electrical field \mathbf{E}_i , which is radiated in a direction given by the multiantenna system when only port i is excited, is linked to the input wave a_i by [BLA 03]:

$$\mathbf{E}_i = \sqrt{Z_v} \cdot \sqrt{\frac{D_{\max}}{4\pi}} \cdot \mathbf{F}_i \cdot \frac{e^{-jkr}}{r} \cdot a_i \quad [11.30]$$

where Z_v is the impedance of the vacuum, D_{\max} the maximum directivity, \mathbf{F}_i the normalized far-field electrical field pattern, k the wave number, and r the distance between the antenna and the observation point.

The Hermitian product of the electric fields \mathbf{E}_i , \mathbf{E}_j , induced by the excitation of ports i and j , respectively, gives:

$$\mathbf{E}_i \cdot \mathbf{E}_j^* = Z_v \cdot \frac{\sqrt{D_{\max_i} \cdot D_{\max_j}}}{4\pi} \cdot \mathbf{F}_i \cdot \mathbf{F}_j^* \cdot \frac{1}{r^2} \cdot a_i \cdot a_j^* \quad [11.31]$$

The Hermitian product of the radiation associated with two ports of the multiantenna system is the integral over all directions of the space. We can simplify the written form of this expression:

$$\iint_{\Sigma} \mathbf{E}_i \cdot \mathbf{E}_j^* d\Omega = Z_v \cdot C_{ij} \cdot a_i \cdot a_j^* \quad [11.32]$$

$$C_{ij} = \frac{\sqrt{D_{\max_i} \cdot D_{\max_j}}}{4\pi} \cdot \iint_{\Sigma} \mathbf{F}_i \cdot \mathbf{F}_j^* d\Omega \quad [11.33]$$

Thus, the correlation coefficient of the received signals for antennas i and j defined in equation [11.29] can be written as a function of the coefficients C_{ij} :

$$\rho_{ij} = \frac{C_{ij}}{\sqrt{C_{ii} \cdot C_{jj}}} \quad [11.34]$$

On the other hand, the total power P radiated in the free space by the two antennas is calculated by integrating the radiation patterns \mathbf{E}_i of the antennas:

$$\begin{aligned} P &= \frac{1}{Z_v} \iint_{\Sigma} \left(\sum_{i=1}^N \mathbf{E}_i \right) \cdot \left(\sum_{i=1}^N \mathbf{E}_i \right)^* d\Omega \\ &= \frac{1}{Z_v} \sum_{i=1}^N \sum_{j=1}^N \iint_{\Sigma} \mathbf{E}_i \cdot \mathbf{E}_j^* d\Omega \end{aligned} \quad [11.35]$$

Using equation [11.32], we obtain:

$$\begin{aligned} P &= \sum_{i=1}^N \sum_{j=1}^N C_{ij} \cdot a_i \cdot a_j^* \\ &= \mathbf{a}^H \cdot \mathbf{C} \cdot \mathbf{a} \end{aligned} \quad [11.36]$$

where \mathbf{a}^H denotes complex conjugate.

The total power radiated is also obtained as a result of energy at the ports of the multiantenna system. However, this assumes that the antennas are perfectly efficient and thus that *the whole of the power presented to the ports of the antenna is radiated or reflected*:

$$\begin{aligned} P &= \sum_{k=1}^N a_k a_k^* - \sum_{k=1}^N b_k b_k^* \\ &= \mathbf{a}^H \mathbf{a} - \mathbf{b}^H \mathbf{b} \\ &= \mathbf{a}^H (\mathbf{I} - \mathbf{S}\mathbf{S}^H) \mathbf{a} \end{aligned} \quad [11.37]$$

Identification of the expressions for the total power radiated, which is obtained in equations [11.36] and [11.37], gives:

$$\mathbf{I} - \mathbf{S}\mathbf{S}^H = \mathbf{C} \quad [11.38]$$

For a two-antenna system, we therefore obtain an expression for the correlation coefficient of the antenna signals as a function of the S-parameters [BLA 03]:

$$\rho = \frac{S_{11}^* S_{12} + S_{21}^* S_{22}}{\sqrt{(1 - (|S_{11}|^2 + |S_{21}|^2))(1 - (|S_{22}|^2 + |S_{12}|^2))}} \quad [11.39]$$

This method is simple to implement experimentally since it does not require a radiation characterization of the multiantenna system, but simply a measurement of the S matrix using a vector network analyzer. We should not forget here that we have made the hypothesis that the antennas are lossless. For miniaturized

multiantenna systems, the precision of the method is reduced if the radiation efficiency is degraded [HAL 05].

11.3. Multiantenna systems

To conclude this chapter, we provide two examples of multiantenna systems: space diversity, which can be simply achieved if we have sufficient space, and a colocalized multiantenna system solution, which offers better opportunities for miniaturization and integration of antennas.

11.3.1. *Space diversity*

Space diversity is the concurrent use of multiple antennas spatially separated from each other. It can easily be implemented using commercial antennas for television reception onto laptop computers, for example, as shown in Figure 11.10. The distance between the antennas induces a path difference Δ and therefore a phase difference between the received signals for each incident wave: the interference between each of the multiple trajectories will then behave differently for each antenna.



Figure 11.10. *Space diversity for mobile television reception*

If the antennas are identical and are oriented the same within their environment, a balance of received signals is immediately achieved. To ensure signal independence, there must be sufficient distance between the antennas.

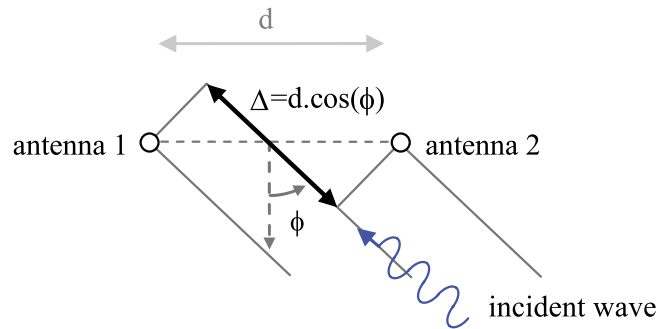


Figure 11.11. Path difference between two separate antennas

Let us take a simple example of a system where two antennas are separated by a distance d . As illustrated in Figure 11.11, we assume that the incident waves are reduced in the horizontal plane, that the antennas are omnidirectional in the horizontal plane and we consider that the incident wave polarization is the same as that of the antennas. In this case, the correlation ρ of a space diversity can be expressed [CLA 68] as:

$$\rho = \int_0^{2\pi} e^{i2\pi \frac{d}{\lambda} \cos \phi} h(\phi) \cdot d\phi \quad [11.40]$$

where λ is the wavelength in air at operating frequency and $h(\phi)$ the incident wave distribution function in the horizontal plane. The correlation coefficient of the envelopes ρ_e of a space diversity is traced to Figure 11.12 for a uniform incident wave distribution and for a Gaussian distribution similar to equation [11.14] with a restricted angular spread ($\phi_0 = 0^\circ$, $\sigma_\phi = 35^\circ$).

For a uniform distribution, we see that signal independence is satisfactory even for distances close to a quarter-wavelength.

Where the incident waves are concentrated into a restricted angular spread, the distance between antennas must be increased in order to achieve received signals independence.

This simple model does not take into account the effects of mutual coupling between antennas, in particular distortions in the radiation pattern when the antennas are close. For a more detailed evaluation of space diversity, we will need to return to the methods introduced in section 11.2, using the characteristics of antennas measured in the presence of other antennas.

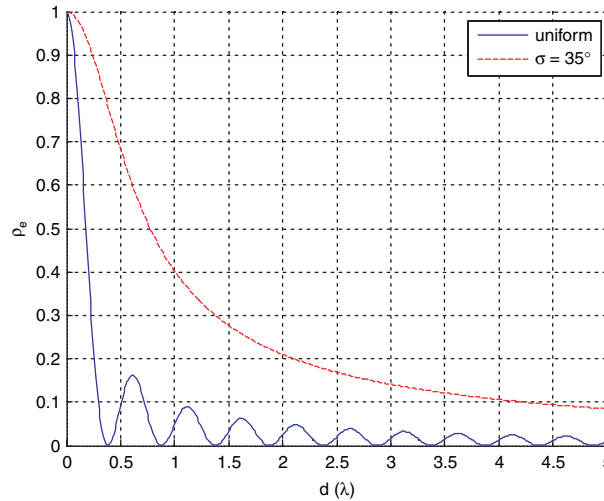


Figure 11.12. Envelope correlation coefficient linked to space diversity

11.3.2. Compact multiantenna system

Space diversity does not always apply to the terminal, since it requires a sufficient distance between the antennas.

We therefore need to establish diversity from the radiation properties by varying radiation direction, radiation pattern shapes, and/or polarization differences between antennas.

Combining antennas of the same type forces us to establish diversity according to the position of relative orientation of the antennas. The use of different antennas enables us to have independent, colocalized antennas. Antenna diversity is thus established in a single volume with size equivalent to that of the single antenna [RUD 07].

Figure 11.13 illustrates electrical fields established at the core of two antenna geometries: the PIFA (planar inverted F antenna) and a slot antenna at the edge of the ground plane, which is commonly known as a *notch* antenna.

When the notch antenna is positioned under the PIFA antenna, it remains independent as the established electrical fields in the two structures are orthogonal. The PIFA and notch antenna are quarter-wave resonators, commonly used for terminal integration.

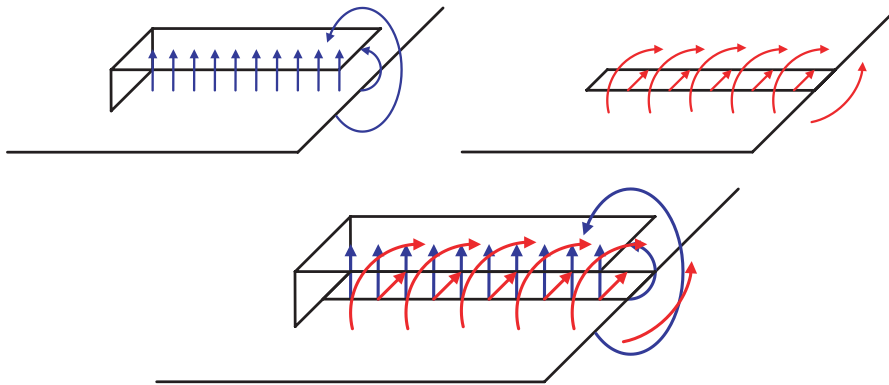


Figure 11.13. *Heterogeneous combination of antennas in a single volume PIFA and notch antennas*

Thus, the combination of a PIFA and a notch antenna enables antenna diversity to be established in the initial volume of the PIFA antenna. The demonstration prototype shown in Figure 11.14 was produced using a printed circuit with dimensions compatible with integration into a $10\text{ cm} \times 5\text{ cm}$ terminal. The compact multiantenna system, comprising one PIFA antenna and one notch antenna, is mounted on the upper part of the printed circuit.

The reflection coefficients S_{11} and S_{22} show that the combined antennas are matched over a common frequency band about 2.5 GHz. The coupling coefficient S_{21} remains very low over this same common band, in spite of the colocalization of the radiating structures. This good isolation provides evidence of the independence of the two combined antennas.

Figure 11.15 shows the radiation patterns for the compact multiantenna system. The duality of the two combined antennas is visible from the radiation properties, since the pattern of one antenna related to a component of polarization is similar to the pattern of the other related to the orthogonal component of polarization. The multiantenna system therefore makes use of a polarization diversity, as, in a given direction, each antenna radiates with a polarization which is orthogonal to that of the other. However, in a monopolarized environment, the multiantenna system makes use of pattern diversity, since the principal directions of radiation between one antenna and the other are at 90° . Thus, the use of dual antennas enables a diversity that is adapted to different types of environment [RUD 07].

The correlation coefficient is calculated by the two methods explained using equations [11.27] and [11.39], assuming a uniform spatial incident wave distribution

$h(\theta, \phi) = \text{const}$ and balancing of the orthogonal components of polarization $XPR = 0$ dB. The results are shown in Figure 11.16. Independence of the antennas is confirmed by a correlation coefficient ρ_e , which remains low; we note, however, some significant differences between the two methods, which are linked to the associated hypotheses discussed in section 11.2.2.

The radiation efficiencies η of the combined antennas are shown in Figure 11.17. The notch antenna presents a slightly lower radiation efficiency than that of the PIFA antenna as a result of losses from the substrate of the printed circuit; however, antenna balance is sufficiently established in order for satisfying diversity gain to be achieved.

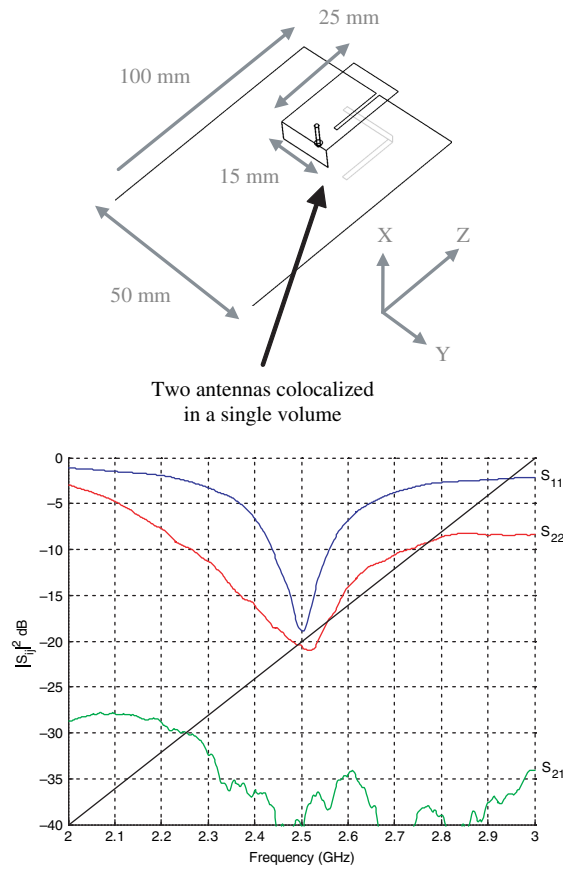


Figure 11.14. Prototype of compact multiantenna system *S*-parameters

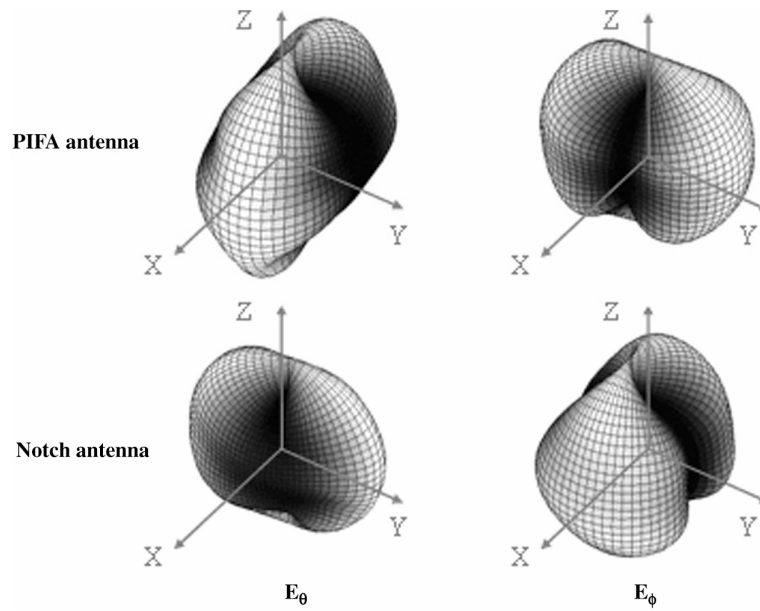


Figure 11.15. Radiation patterns of compact multiantenna systems (2.5 GHz). E_θ is the vertical component of polarization and E_ϕ is the horizontal component (coordinate system given in Figure 11.14)

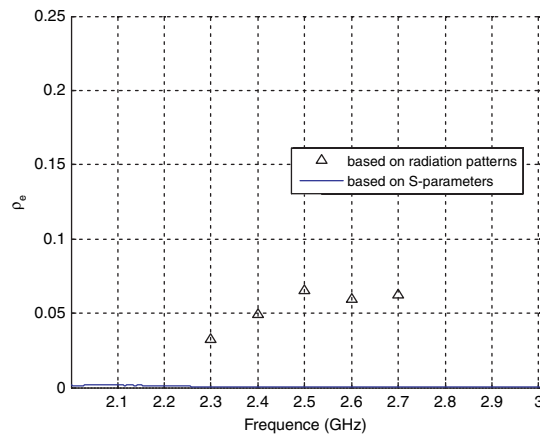


Figure 11.16. Correlation coefficient of the compact multiantenna system: calculations based on radiation patterns and S-parameters

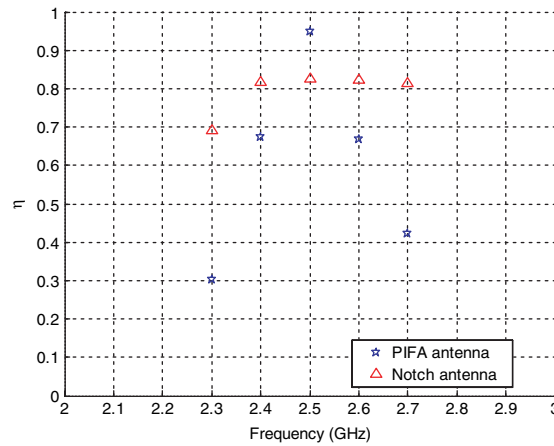


Figure 11.17. Total efficiency of the compact multiantenna system

11.4. Conclusion and looking toward MIMO

Antenna diversity enables us to mitigate degradations due to wave propagation in environments in which there are multiple paths. In this chapter, we have presented the analytical theoretical tools for evaluating antenna diversity performance in the ideal case of independent and balanced signals, as well as in the less ideal case in which signal independence and balance are degraded.

These theoretical developments rely on signals that follow a Rayleigh statistic based on the effects arising from multipath propagation. However, this type of theoretical analysis needs to be supported by numerical simulation, or better still by experimentation, in cases where the desired application and/or the environments are specific. Subsequently, we have presented analytical methods enabling more precise evaluation of the impact of the characteristics of antennas on diversity performance. The link established between the characteristics of antennas and signals from diversity requires us to make hypotheses about the environment or even on the nature of antennas.

These methods enable efficient comparison of multiantenna systems or even enable an optimization process to be followed. However, again, for specific applications or environments, experimental evaluation *in situ* enables the definitive validation of multiantenna system performance. One advantageous alternative to field measurement is the radiation test bench, known as over-the-air (OTA) testing, in which the multipath environment is synthesized in an anechoic chamber (see the example in Figure 11.18). This type of test bench enables testing of multiantenna systems under specific conditions of propagation without having

to leave the laboratory, as well as enabling the same experiences to be repeated as many times as necessary [RUD 10].

Finally, we have illustrated this chapter by presenting two types of multiantenna systems. Space diversity can be easily achieved by using simple, readily available antennas. The heterogeneous combination of antennas enables a diversity between two antennas to be established within a volume restricted to one single antenna. In order to increase system performance, we can easily picture the association of several of these compact multiantenna systems, thus combining space diversity and radiation in order to achieve a set of $2 \times N$ independent antennas.

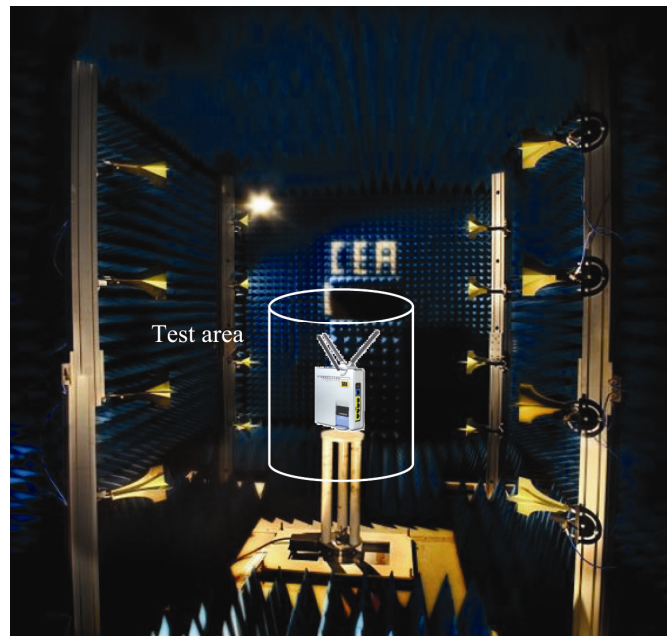


Figure 11.18. OTA test bench in anechoic chamber, multipath environments are synthesized by a multitude of antenna sources distributed around the test area

Modern telecommunication systems require even more significant data rates. The generalization of techniques relating to multiple transmission and reception antennas offers excellent perspectives on how to achieve these levels of performance.

This type of telecommunication system architecture, which is known as *multiple input multiple output* (MIMO), is illustrated in Figure 11.19. The joint utilization of multiple independent transmission and reception antennas enables us to send

multiple signals in parallel within a propagation channel and to extract them independently by means of concurrent signal treatments during transmission and reception.

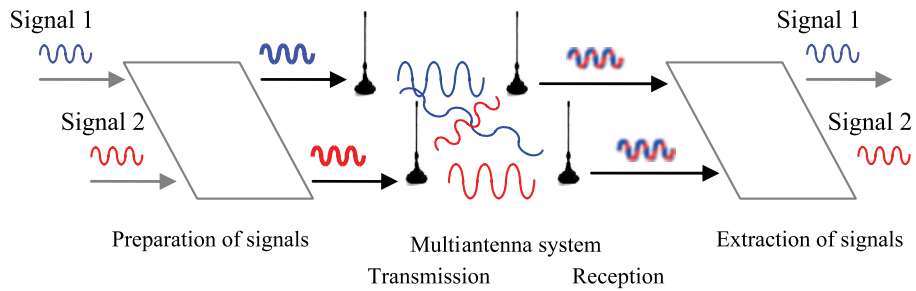


Figure 11.19. Outline of the principle of MIMO architecture

The subject of *MIMO* systems is generally a wider topic than that covered by this chapter since analysis of these should be extended at the points of transmission and reception. In *MIMO* cases, the mechanisms for propagation within the environment cannot be simply analyzed [JEN 04]. However, the tools presented in this chapter can be implemented in order to establish effective antenna diversity at both transmission and reception. This approach makes sense for a number of situations in which wireless *MIMO* systems are deployed.

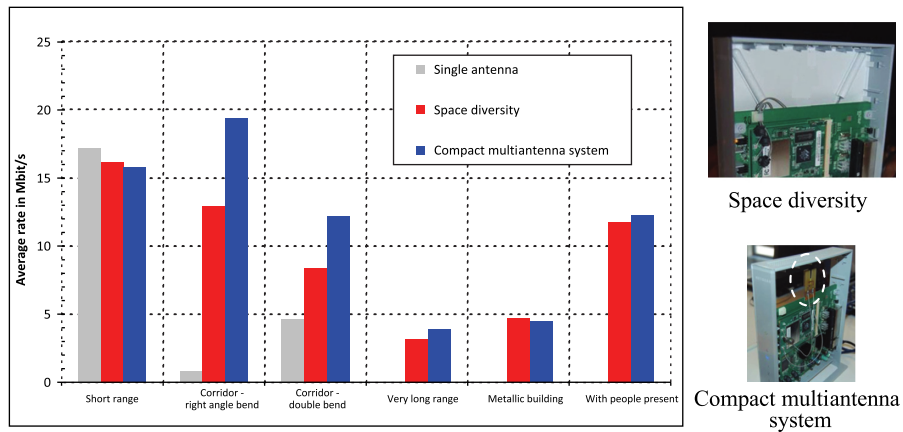


Figure 11.20. Performance of a Wi-Fi MIMO (2.4 GHz) transmission: comparison between space diversity and compact multiantenna system

Thus, the potential of compact multiantenna systems, which can be seen as the combination of a *PIFA* antenna and a notch antenna, can be extended to *Wi-Fi MIMO* systems. This has been verified using a series of tests conducted in different buildings at the Polytech'Nantes engineering school. The results presented in Figure 11.20 show the improvements in data rate obtained using *MIMO* techniques; they also show that compact multiantenna systems present performances equivalent to a space diversity produced with two dipoles inclined at 45° and 15 cm apart.

Bibliography

- [AGR 98] AGRAWALL N.-P., KUMAR G., RAY K.-P., “Wide-band planar monopole antennas”, *IEEE Trans. Antennas Propag.*, vol. 46, no. 2, 1998.
- [AIS 04] AISSAT H., CIRIO L., GRZESKOWIAK M., LAHEURTE J.-M., PICON O., “Circularly polarised planar antenna excited by coplanar waveguide feed line”, *Electron Lett.*, vol. 40, pp. 402–403, 2004.
- [ALO 94] ALONI E., KASNER R., “Analysis of a dual circularly polarized microstrip antenna fed by crossed slots”, *IEEE Trans. Antennas Propag.*, vol. 42, no. 8, 1994.
- [ARL 74] ARLON T., ROBERT A., GREENOUGH K., WALLEMBERG F., MENDELOVICZ M., LUMJIAK A.-C., “The quadrifilar helix antenna”, *IEEE Trans. Antennas Propag.*, vol. 22, no. 2, 1974.
- [BAL 89] BALANIS C.-A., *Advanced Engineering Electromagnetics*, Wiley, New York, 1989.
- [BAL 05] BALANIS C.-A., *Antenna Theory, Analysis & Design*, Wiley, New York, 2005.
- [BAR 63] BARROW B.-B., “Diversity combination of fading signals with unequal mean strengths”, *IEEE Trans Commun Syst*, vol. 11, no. 1, 1963.
- [BEG 00] BEGAUD X., POEY P., DANIEL J.-P., DUBOST G., “Design of wideband dual polarized slot antennas”, *AP2000 Millenium Conference on Antennas and Propagation*, Davos, Switzerland, April 2000.
- [BEG 10] BEGAUD X., *Ultra Wide Band Antennas*, ISTE Ltd., London and John Wiley & Sons, New York, USA, 2010.
- [BEG 96] BEGAUD X., *Analyse d’antennes et de réseaux d’antennes large bande et bipolarisation par une méthode d’éléments finis de surface*, Thesis, University of Rennes 1, 1996.
- [BIB 10] BRITO D.-B., BEGAUD X., D’ASSUNCAO A.-G., FERNADES H.-C.-C., “Ultra wideband monopole antenna with split ring resonator for notching frequencies”, *Proceedings of the 4th European Conference on Antennas and Propagation (EuCAP)*, Barcelona, Spain, pp. 1–5, 12–16 April 2010.

- [BLA 03] BLANCH S., ROMEU J., CORBELLA I., “Exact representation of antenna system diversity performance from input parameter description”, *Electron Lett.*, vol. 39, no. 9, pp. 705–707, May 2003.
- [BOT 00] BOTI M., DUSSOPT L., LAHEURTE J.-M., “A circularly polarised antenna with switchable polarisation sense”, *Electron Lett.*, vol. 36, pp. 1518–1519, 2000.
- [BRO 52] BROWN G.-H., WOODWARD O.-M., “Experimentally determined radiation characteristics of conical and triangular antennas”, *RCA Review*, vol. 13, pp. 425–452, December 1952.
- [BRO 99] BROWN A.-D., VOLAKIS J.-L., KEMPEL L.-C., BOTROS Y., “Patch antennas on ferromagnetic substrates”, *IEEE Trans. Antennas Propag.*, vol. 41, no. 1, pp. 26–32, January 1999.
- [CAD 05] CADORET D., LAISNE A., GILLARD R., LE COQ L., LEGAY H., “Design and measurement of new reflectarray antenna using microstrip patches loaded with slot”, *Electron Lett.*, vol. 41, pp. 623–624, 26 May 2005.
- [CAR 81] CARVER K.-R., MINK J.-W., “Microstrip antenna technology”, *IEEE Trans. Antennas Propag.*, vol. 29, no. 1, pp. 2–24, January 1981.
- [CHE 00a] CHEN Z.-N., CHIA Y.-W.-M., “Impedance characteristics of trapezoidal planar monopole antennas”, *Microw. Opt. Technol. Lett.*, vol. 27, no. 2, October 2000.
- [CHE 00b] CHEN Z.-N., “Impedance characteristics of planar bow-tie like monopole antennas”, *Electron Lett.*, vol. 36, no. 13, pp. 1100–1101, June 2000.
- [CHE 03] CHEN Z.-N., “Experiments on input impedance of titled planar monopole antenna”, *Microw. Opt. Technol. Lett.*, vol. 26, no. 3, August 2003.
- [CHE 06] CHEN Z.-N., CHIA M.-Y., *Broadband Planar Antennas*, Wiley, Hoboken, New York, 2006.
- [CHO 06] CHO Y.-J., CHOI D.-H., LEE S.-K., PARK S.-O., “A miniature UWB planar monopole antenna with 5-GHz band-rejection filter and the time-domain characteristics”, *IEEE Trans. Antennas Propag.*, vol. 54, no. 5, pp. 1453–1460, May 2006.
- [CHU 48] CHU L.-J., “Physical limitations of omni-directional antennas”, *J. Appl. Phys.*, vol. 19, pp. 1163–1175, December 1948.
- [CLA 68] CLARKE R.-H., “A statistical theory of mobile-radio reception”, *Bell. Syst. Tech. J.*, vol. 47, pp. 957–1000, August 1968.
- [COL 66] COLLIN R.-E., *Foundations for Microwave Engineering*, McGraw-Hill, New York, 1966.
- [COM 97] COMBES P., *Micro-Ondes – Tome 2, Circuits Passifs, Propagation, Antennes, Cours et Exercices*, Dunod, Paris, 1997.
- [DEC 02] DECROZE C., Etude et optimisation d’un nouveau type d’antenne coplanaire: application à des liaisons de proximité et utilisation pour des dispositifs multifonctions et large bande, PhD Thesis, University of Limoges, 2002.

- [DEJ 05] DE JEAN G., BAIRAVASUBRAMANIAN R., THOMPSON D., PONCHAK G.-E., TENTZERIS M.-M., PAPAPOLYMEROU J., “Liquid crystal polymer (LCP): a new organic material for the development of multilayer dual-frequency/dual-polarization flexible antenna arrays”, *IEEE Antennas Wirel. Propag. Lett.*, vol. 4, pp. 22–26, 2005.
- [DIN 95] DING X., JACOB A.-F., “Novel broadband slot antenna with low cross-polarization”, *Annual Report*, Institut für Hochfrequenztechnik, TU Braunschweig, 1995.
- [DON 07] DONELLI M., AZARO R., FIMOIGNARI L., MASSA A., “A planar electronically reconfigurable Wi-Fi band antenna based on a parasitic microstrip structure”, *IEEE Antennas Wirel. Propag. Lett.*, vol. 6, pp. 623–626, 2007.
- [DRE 05] DREINA E., Optimisation d’un système d’antennes miniatures multicapteurs pour terminal mobile 4G dans une perspective de radio logicielle, Masters Thesis, Grenoble, 2005.
- [DUH 87] DUHAMEL R.H., Dual polarized sinuous antennas, U.S. Patent 4,658,262, 14 April 1987.
- [DUS 01] DUSSOPT L., TOUTAIN Y., COUPEZ J.-P., LAHEURTE J.-M., “Circularly polarised microstrip arrays built on a polymethacrylate imid foam”, *Electron. Lett.*, vol. 36, pp. 1758–1759, 2000.
- [DYS 59] DYSON J.-D., “The equiangular spiral antenna”, *IRE Trans. Antennas Propag.*, vol. 7, no. 2, pp. 181–187, April 1959.
- [ERD 07] ERDIL E., TOPALLI K., UNLU M., CIVI O.-A., AKIN T., “Frequency tunable microstrip patch antenna using RF MEMS technology”, *IEEE Trans. Antennas Propag.*, vol. 55, no. 4, pp. 1193–1196, April 2007.
- [FAN 05] FAN Y., RAHMAT-SAMII Y., “Patch antennas with switchable slots (PASS) in wireless communications: concepts, designs, and applications”, *IEEE Antennas Propag. Mag.*, vol. 47, no. 2, pp. 13–29, April 2005.
- [FAS 00] FASSETTA S., SIBILLE A., “Switched angular diversity BSSA array antenna for WLAN”, *Electron Lett.*, vol. 36, pp. 702–703, 2000.
- [FOR 04] FORTINO N., KOSSIAVAS G., DAUVIGNAC J.-Y., STARAJ R., “Novel antennas for ultra wideband communications”, *Microw. Opt. Technol. Lett.*, vol. 41, no. 3, pp. 166–169, May 2004.
- [FOR 06] FORTINO N., Conception et caractérisation d’antennes imprimées pour systèmes Ultra Large Bande impulsionnels, Thesis, University of Nice-Sophia Antipolis, 2006.
- [FUJ 01] FUJIMOTO K., JAMES J.-R., *Mobile Antenna Systems Handbook*, 2nd ed., Artech House Publishers, London, 2001.
- [GAR 02] GARDIOL F., *Traité d’Electricité, T3 “Electromagnétisme”*, Presses Polytechniques Romandes et Universitaires, Lausanne, 2002.
- [GEY 03] GEYI W., “Physical limitations of antenna”, *IEEE Trans. Antennas Propag.*, vol. 51, no. 8, pp. 2116–2123, August 2003.

- [GIA 96] GIAUFFRET L., LAHEURTE J.-M., “Theoretical and experimental characterization of CPW-fed microstrip antennas”, *IEEE Proceedings on Microwaves, Antennas and Propagation, Part H*, pp. 13–17, February 1996.
- [GIB 79] GIBSON P.-J., “The Vivaldi aerial”, *Proceedings of the 9th European Microwave Conference*, pp. 103–105, Boca Raton, USA, 1979.
- [GOD 02] GODARA L.-C., *Handbook of Antennas in Wireless Communications*, CRC Press, 2002.
- [GRA 02] GRANT P.-D., MANSOUR R.R., DENHOFF M.W., “A comparison between RF MEMS switches and semiconductor switches”, *Canadian J. Elect. Comput. Eng.*, vol. 27, no. 1, January 2002.
- [GUI 98] GUILLANTON E., DAUVIGNAC J.-Y., PICHOT C.-H., CASHMAN J., “A new design tapered slot antenna for ultra-wide band application”, *Microw. Opt. Technol. Lett.*, vol. 19, no. 4, pp. 286–289, 1998.
- [HAL 87] HALL P.-S., “Probe compensation in thick micro strip patches”, *Electron Lett.*, vol. 23, no. 11, pp. 606–607, 21 May 1987.
- [HAL 89] HALL P.-S., DAHELE J.-S., JAMES J.-R., “Design principles of sequentially fed, wide bandwidth, circularly polarised microstrip antennas”, *IEEE Proceedings on Microwaves, Antennas and Propagation, Part H*, vol. 136, no. 5, pp. 381–389, October 1989.
- [HAL 05] HALLBJÖRNER P., “The significance of radiation efficiencies when using S-parameters to calculate the received signal correlation from two antennas”, *IEEE Antennas Propag. Lett.*, vol. 4, pp. 97–99, June 2005.
- [HAM 93] HAMMOUD M., POEY P., COLOMBEL F., “Matching the input impedance of a Broadband Disc Monopole”, *Electron Lett.*, vol. 29, no. 4, pp. 406–407, 18 February 1993.
- [HAR 61] HARRINGTON R.-C., *Time-Harmonic Electromagnetic Fields*, McGraw-Hill, New York, USA, 1961.
- [HIR 92] HIRASAWA K., HANEISHI M., *Analysis, Design, and Measurement of Small and Low-Profile Antennas*, Artech House, London, 1992.
- [HUY 95] HUYNH T., LEE K.-F., “Single-layer single-patch wideband microstrip antenna”, *Electron Lett.*, vol. 31, no. 16, pp. 1310–1312, 3 August 1995.
- [JAK 74] JAKES W.-C., *Microwave Mobile Communications*, Wiley-IEEE Press, New York, USA, 1994. (1st ed., Wiley, New York, 1974)
- [JAM 89] JAMES J.-R., HALL P.-S., “Handbook of micro strip antennas”, *IEE Electromagnetic Wave Series*, Peter Peregrinus Ltd., London, vol. 1–2, no. 28, 1989.
- [JAM 88] JAMES J.-R., HALL P.-S., *Handbook of Microstrip Antennas*, Peter Peregrinus Ltd., Institution of Engineering & Technology, London, 1 June 1988.
- [JEC 02] JECKO B., TORRES F., VILLEMAUD G., Omnidirectional resonant antenna, International Patent no. WO 02/91877, 12-9-2002.

- [JEN 04] JENSEN M.-A., WALLACE J.-W., “A review of antennas and propagation for MIMO wireless communications”, *IEEE Trans. Antennas Propag.*, vol. 52, no. 11, pp. 2810–2824, November 2004.
- [JOH 93] JOHNSON R.-C., *Antenna Engineering Handbook*, 3rd ed., McGraw-Hill, New York, USA, 1993.
- [KER 01] KERKHOFF A., ROGERS R., LING H., “The use of the genetic algorithm approach in the design of ultra-wideband antennas”, *IEEE Radio and Wireless Conference (RAWCON)*, Boston, USA, August 2001.
- [KIL 69] KILGUS C.-C., “Resonant quadrafilar helix”, *IEEE Trans. Antennas Propag.*, vol. 17, pp. 349–351, May 1969.
- [KOS 99] KOSSEL M., BENEDICKTER H., BÄCHTOLD W., KUNG R., HANSEN J., “An active tagging system using circular-polarization modulation”, *IEEE Trans. Microw. Theory Tech.*, vol. 47, pp. 2242–2248, 1999.
- [KRA 12] KRAUS J.-D., MARHEFKA R.-J., *Antennas for All Applications*, 3rd ed., McGraw-Hill Science/Engineering/Math, New York, USA, 12 November 2001.
- [LAH 01] LAHEURTE J.-M., “A switchable CPW-fed slot antenna for multifrequency operation”, *Electron Lett.*, vol. 37, pp. 1498–1500, 2001.
- [LAH 02] LAHEURTE J.-M., TOSI H., DUBARD J.-L., “Microstrip antennas controlled by pin diodes: influence of the bias current on the antenna efficiency”, *Microw. Opt. Technol. Lett.*, vol. 33, no. 1, pp. 44–47, 5 April 2002.
- [LEE 72] LEE W.-C.-Y., YEH Y.-S., “Polarization diversity system for mobile radio”, *IEEE Trans. Commun. Syst.*, vol. 20, no. 5, pp. 912–923, October 1972.
- [LEG 04a] LE GARREC L., Etude et conception en bande millimétrique d’antennes reconfigurables basées sur la technologie des MEMS, IETR, Thesis, IETR, November 2004.
- [LEG 04b] LE GARREC L., HIMDI M., SAULEAU R., MAZENQ L., GRENIER K., PLANA R., “CPW-fed slot microstrip MEMS-based reconfigurable arrays”, *Antennas and Propagation Society International Symposium, 2004. IEEE*, vol. 2, pp. 1835–1838, June 2004.
- [LEP 05] LEPAGE A.-C., Analyse et optimisation d’antennes tridimensionnelles: applications à la conception d’antennes compactes intégrées dans un système de communication ultra large bande, PhD Thesis, ENST, 27 June 2005.
- [LEP 08] LEPAGE A.-C., BEGAUD X., LE RAY G., SHARAIHA A., “UWB directive triangular patch antenna”, *Int. J. Antennas Propag.*, vol. 2008.
- [LEW 74] LEWIS L.-R., FASSET M., HUNT J., “A broadband stripline array element”, *IEEE Symposium on Antennas Propagation*, Atlanta, USA, pp. 335–337, 1974.
- [LOV 06] LOVAT G., BURGHIGNOLI P., CELOZZI S., “A tunable ferroelectric antenna for fixed-frequency scanning applications”, *IEEE Antennas Wirel. Propag. Lett.*, vol. 5, pp. 353–356, December 2006.

- [LUX 07] LUXEY C., STARAJ R., KOSSIAVAS G., PAPIERNIK A., *Antennes imprimées: Techniques et domaines d'applications*, Techniques de l'ingénieur, Electronique, vol. E5, no. E3311, 2007.
- [MAS 60] MASON S.-J., ZIMMERMANN H.-J., *Electronic Circuits, Signal and System*, Wiley, New York, 1960.
- [MCL 96] MCLEAN J.S., "A re-examination of the fundamental limits on the radiation Q of electrically small antennas", *IEEE Trans. Antennas Propag.*, vol. 44, no. 5, pp. 672–676, May 1996.
- [MOS 89] MOSIG J.R., ITOH T., *Numerical Techniques for Microwave and Millimeter Wave Passive Structures*, Wiley, New York, pp. 133–214, 1989.
- [MOT 86] MOTT T., *Polarisation in Antennas and Radar*, Wiley, New York, 1986.
- [PAN 04] PANAI A P., LUXEY C., JACQUEMOD G., STARAJ R., KOSSIAVAS G., DUSSOPT L., VACHERAND F., BILLARD C., "MEMS-based reconfigurable antennas", *IEEE International Symposium on Industrial Electronics*, vol. 1, pp. 175–179, 4–7 May 2004.
- [PET 06] PETIT L., DUSSOPT L., LAHEURTE J.-M. "MEMS-switched parasitic-antenna array for radiation pattern diversity", *IEEE Trans. Antennas Propag.*, vol. 54, no. 9, pp. 2624–2631, September 2006.
- [PEY 05] PEYROT-SOLIS M.-A., GALVAN-TEJADA G.-M., JARDON-ARGUILAR H., "State of the art in ultra-wideband antennas", *2nd International Conference on Electrical and Electronics Engineering*, pp. 101–105, 7–9 September 2005.
- [PIO 02] PIOCH S., ADELLAN N., LAHEURTE J.-M., BLONDY P., POTHIER A., "Integration of MEMS in frequency-tunable cavity-backed slot antennas", *JINA 2002*, Nice, France, November 2002.
- [POU 07] POUSSOT B., LAHEURTE J.-M., PICON O., KANNAPPAN K., LISSORGUES G., "MEMS-based reconfigurable antenna for Ka band applications", *Mo4.4.5, Antennas and Propagation (EuCAP)*, Edinburgh, UK, 11–16 November 2007.
- [POU 08] POUSSOT B., LAHEURTE J.-M., CIRIO L., PICON O., DELCROIX D., DUSSOPT L., "Diversity measurements of a reconfigurable antenna with switched polarizations and patterns", *IEEE Trans. Antennas Propag.*, vol. 56, no. 1, pp. 31–38, January 2008.
- [POW 04] POWEL J., CHANDRAKASAN A.-P., "Spiral slot patch antenna and circular discmonopole for ultra wideband communication", *IEEE International Symposium on Antennas and Propagation*, August 2004.
- [POZ 85] POZAR D.-M., "A microstrip antenna aperture coupled to a microstrip line", *Electron Lett*, vol. 21, pp. 49–50, January 1985.
- [POZ 94] POZAR D.-M., "The active element pattern", *IEEE Trans. Antennas Propag.*, vol. 42, no. 8, pp. 1176–1178, August 1994.
- [RIC 81] RICHARDS W., LO Y., HARRISON D., "An improved theory for microstrip antennas and applications", *IEEE Trans. Antennas Propag.*, vol. 29, no. 1, pp. 38–46, January 1981.

- [ROB 05] ROBLIN C.-H., SIBILLE A., BORIES S., “Semi-directional small antenna design for UWB multimedia terminals”, *ANTEM*, Saint Malo, France, 15–17 June 2005.
- [RUD 10] RUDANT L., D’ERRICO R., “Wideband over-the-air test-bed reproducing channel delay dispersion characteristics”, *3rd European Conference on Antennas and Propagation (EuCAP)*, Barcelona, Spain, April 2010.
- [RUD 07] RUDANT L., DELAVEAUD C., “Heterogeneous combination for compact integrated diversity multi-antenna system”, *2nd European Conference on Antennas and Propagation (EuCAP)*, Edinburgh, UK, November 2007.
- [RUM 57] RUMSEY V.-H., “Frequency Independent Antennas”, *IRE National Convention Record*, vol. 5, part. 1, pp. 114–118, 1957.
- [SAB 83] SABBAN A., “A new broadband stacked two-layer microstrip antenna”, *Antennas and Propagation Society International Symposium*, vol. 21, pp. 63–66, May 1983.
- [SAL 09] SALTI H., FOURN E., GILLARD R., LEGAY H., AUBERT H., “MEMS breakdown effects on the radiation of a MEMS based reconfigurable reflectarray”, *European Conference on Antennas and Propagation*, Berlin, Germany, 23–27 May 2009.
- [SAR 08] SARRAZIN J., MAHE, Y., AVRILLON S., TOUTAIN S., “Investigation on cavity/slot antennas for diversity and MIMO systems: the example of a three-port antenna”, *IEEE Antennas Wirel. Propag. Lett.*, vol. 7, pp. 414–417, 2008.
- [SCH 03] SCHANTZ H.-G., “Introduction to ultra-wideband antennas”, *IEEE UWBST Conference*, 2003.
- [SCH 04] SCHLUB R.-W., Practical realization of switched and adaptive parasitic monopole radiating structures, Thesis, Griffith University, 2004.
- [SHA 49] SHANNON C.-E., “A mathematical theory of communication”, *Bell Syst. Tech. J.*, vol. 27, pp. 379–423/623–656, July/October 1948.
- [SHA 93] SHARAIHA A., TERRET C., “Analysis of quadrifilar resonant printed helical antenna for mobile communications”, *IEEE Proceedings on Microwaves, Antennas and Propagation, Part H*, vol. 140, no. 4, pp. 269–273, August 1993.
- [STE 66] SCHWARTZ M., BENNETT W.-R., STEIN S., *Communication Systems and Techniques*, IEEE Press, Classical reissue, 1996 (1st ed., McGraw-Hill, 1966).
- [STU 97] STUTZMANN W.-L., THIELE G.-A., *Antenna Theory and Design*, 2nd ed., Wiley, New York, 1997.
- [SU 04] SU S.-W., WONG K.-L., TANG C.-L., “Ultra-wideband square planar monopole antenna for IEEE 802.16a operation in the 2-11-GHz band”, *Microw. Opt. Technol. Lett.*, vol. 42, no. 6, pp. 463–466, September 2004.
- [TAG 90] TAGA T., “Analysis for mean effective gain of mobile antennas in land mobile radio environments”, *IEEE Trans. Veh. Technol.*, vol. 39, no. 2, pp. 117–131, May 1990.
- [TAR 93] TARGONSKI S.-D., POZAR D.-M., “Design of wideband circularly aperture-coupled microstrip antennas”, *IEEE Trans. Antennas Propag.*, vol. 41, no. 2, pp. 214–220, 1993.

- [TER 71] TERRET C., Antennes indépendantes de la fréquence de type conique équiangulaire multimodes à brins épais, Thesis, University of Rennes, July 1971.
- [TES 85] TESHIGORI T., TANAKA M., CHUJO W., “Wideband circularly polarised array antenna with sequential rotations and phase shifts of elements”, *Proceedings on International Symposium on Antennas and Propagation*, 1985.
- [TUR 99] TURKI Y., STARAJ R., “Self-adjusting microstrip antenna”, *Electron Lett.*, vol. 35, no. 2, pp. 106–107, 21 January 1999.
- [UNL 06] UNLU M., TOPALLI K., ATASOY H.-I., TEMOCIN E.-U., ISTANBULLUOGLU I., BAYRAKTA O., “A reconfigurable RF MEMS triple stub impedance matching network”, *European Microwave Conference 2006*, Manchester, UK, pp. 1370–1373, 2006.
- [VAN 08] VAN BEZOOIJEN A., DE JONGH M.-A., CHANLO C., RUIJS L., VAN STRATEN F., MAHMOUDI R., VAN ROERMUND A., “A GSM/EDGE/WCDMA adaptive series-LC matching network using RF-MEMS switches”, *IEEE J. Solid-State Circuits*, vol. 43, no. 10, pp. 2259–2268, October 2008.
- [VAU 87] VAUGHAN R.-G., ANDERSEN J.-B., “Antenna diversity in mobile communications”, *IEEE Trans Veh Technol*, vol. 36, no. 4, pp. 147–172, November 1987.
- [VAU 03] VAUGHAN R., ANDERSEN J.-B., “Channels, propagation and antennas for mobile communications”, *IEEE Electromagnetic Waves Series*, vol. 50, 2003.
- [VIL 02] VILLEMAUD G., Etude d’antennes ruban tridimensionnelles compactes pour liaison de proximité: application à des systèmes de télémétrie et de localisation de téléphones cellulaires, PhD Thesis, University of Limoges, 2002.
- [WHA 06] WHATLEY R., ZHOU Z., MELDE K., “Reconfigurable RF impedance tuner for match control in broadband wireless devices”, *IEEE Trans. Antennas Propag.*, vol. 54, no. 2, pp. 470–478, February 2006.
- [WHE 47] WHEELER H.-A., “Fundamental limitations of small antennas”, *Proceedings of the IRE*, vol. 35, pp. 1479–1484, December 1947.
- [WOO 80] WOOD C., “Improved bandwidth of microstrip antennas using parasitic elements”, *IEE Proceedings on Microwaves, Optics and Antennas, Part H*, vol. 127, no. 4, pp. 231–234, August 1980.
- [YAG 28] YAGI H., “Beam transmission of ultra short waves”, *Proceedings of the IRE*, vol. 16, pp. 715–741, June 1928.
- [ZHE 91] ZHENG J.-X., CHANG D.-C., “End-correction network of a coaxial probe for microstrip patch antennas”, *IEEE Trans. Antennas Propag.*, vol. 39, no. 1, pp. 115–118, January 1991.

List of Authors

Xavier BEGAUD
Laboratoire LTCI
Institut TELECOM - TELECOM ParisTech
France

Marjorie GRZESKOWIAK
Laboratoire ESYCOM
University Paris-Est Marne La Vallée
France

Jean-Marc LAHEURTE
Laboratoire ESYCOM
University Paris-Est Marne La Vallée
France

Benoît POUSSOT
Laboratoire ESYCOM
University Paris-Est Marne La Vallée
France

Stéphane PROTAT
Laboratoire ESYCOM
University Paris-Est Marne La Vallée
France

Lionel RUDANT
CEA-Leti
MINATEC Campus
Grenoble
France

Guillaume VILLEMAUD
Laboratoire CITI
INSA Lyon
France

Index

A

antenna, 1-4, 6-9, 11, 15-19, 22, 23, 25, 30, 31, 35, 36, 39, 40, 47-53, 55, 57, 59, 60, 62-64, 66, 67, 69-71, 73, 74, 76-83, 85, 89, 92, 93, 96, 98, 108-111, 114, 116-120, 122, 123, 125-141, 143-149, 151-156, 158-167, 169-172, 174, 180-182, 184, 185, 187-190, 192, 193, 195, 198, 199, 202, 205-208, 210, 214-217, 219-222, 224-229, 231, 234
biconical, 134
fractal, 166
helical, 154
ILA, 154
miniature, 143
monofilar helix, 113
patch, 70
PIFA, 2, 159, 185, 225
reconfigurable, 169, 180, 187, 190
sinuous, 129-132
spiral, 128
wire, 148
wire-patch, 164
applications, 237, 238
area, 3, 51, 76, 140, 164

B

balance
 antennas, 214
bandwidth, 67, 138
boundaries, 27
boundary conditions, 30

C

cavity model, 25
circuit, 16, 17, 23, 55, 57, 173
 equivalent, 16, 17, 23, 57, 61
comparison, 5, 31
component, 26, 27, 35, 41, 48, 49, 52, 70, 81, 92, 94, 95, 115, 157, 225, 227
connector, 23, 122-124, 161, 163
correlation coefficient, 224, 227
coupling, 5, 19, 30, 69-71, 73-76, 78-81, 83-87, 96, 101, 106, 107, 122, 123, 153, 155, 156, 158, 161, 165, 166, 171, 180, 191, 195, 196, 199, 219, 220, 223, 225
 direct, 71

D

density, 49, 51, 64

diodes
 PIN, 177
 dipole, 2, 148
 distribution, 198, 206-208
 diverse, 132
 diversity, 166, 167, 170, 180, 185,
 187, 205-214, 216, 222-226,
 228-231
 antenna, 211
 space, 222

E

energy, 7, 8, 27, 51, 55, 56, 59,
 60, 62, 63, 65, 68, 69, 73, 74,
 76, 78, 108, 145, 174, 202,
 216, 221
 equation, 28, 37, 55, 92, 101, 127,
 217, 220
 excitation, 73, 74, 85
 dual, 98
 single, 96

F, G, H, I

factor, 4, 8, 11, 12, 19, 62-64, 66,
 103, 107, 126, 140, 145, 146,
 150, 151, 155, 156, 161, 165
 quality, 62, 163
 figure, 179
 merit, 213
 function, 207, 213, 215
 Rayleigh, 207
 gain, 106, 112, 113, 117, 118, 210
 mean effective, 214
 HFSS, 108, 109, 116, 120
 impedance
 input, 20, 33

L

law, 172
 Ampere, 55
 Faraday, 55

line, 2, 7, 8, 10, 11, 15-18, 21, 23,
 25, 53, 57, 62, 63, 69, 70, 74, 76,
 78-81, 84-87, 96, 99, 102-104,
 108, 119, 125, 128, 134, 138,
 140, 170, 172, 173, 178, 179,
 181-183, 189
 link, 8
 LTCC, 8, 10, 11, 71

M, N, O

MEMS, 170, 174, 178, 179, 182,
 183, 185, 187, 188, 199, 202, 203,
 235-240
 micromilling, 10
 MIMO, 143, 186, 228-231, 237,
 239
 mode, 27, 29, 30, 34-37, 41, 48, 49,
 58-61, 63, 68, 69, 107, 108,
 114-120, 145-153, 155, 157, 161,
 162, 165, 166, 181, 184, 190
 model, 15, 25, 151, 175
 notch, 224-226, 231
 optimum combiner, 212

P

patch, 20, 96, 157, 158, 165, 187,
 234, 235, 238
 quarter-wave, 157, 158
 rectangular, 188
 pattern
 radiation, 190, 195
 permittivity, 16, 163
 effective, 16
 plane, 1, 17, 25-27, 31, 35, 36, 39,
 40, 42, 44-48, 59, 64, 71, 74-76,
 80, 83, 85, 94, 95, 99-101, 104,
 105, 108, 111, 113, 115, 117, 118,
 122, 123, 126, 131, 135, 137-141,
 149, 151-153, 156-164, 181, 184,
 189, 223, 224
 E, 44
 H, 45

polarization, 48, 91, 111, 238
 circular, 91, 107
 linear, 90, 92
 power, 13, 18, 25, 34, 35, 48-50, 56,
 57, 62, 64, 66, 68, 95, 96, 98, 99,
 118, 132, 161, 173, 176, 197, 207,
 209-213, 215, 219, 221
 radiated, 66
 probe, 34, 69-74, 123-125, 184, 190

R

range, 132
 ratio, 49, 52, 62, 63, 79, 82, 83,
 89-96, 103-106, 111, 115, 117,
 118, 120, 121, 127, 137, 155, 160,
 178, 185, 189, 215
 axial, 92, 112, 117, 119, 189
 reconfiguration, 4, 169, 170, 173,
 174, 184, 186, 188, 190
 polarization, 188
 relation, 131
 relationship, 51
 relative, 21, 36, 49, 60, 62, 76, 80,
 81, 83, 85, 101, 103, 108, 111, 114,
 145, 146, 148, 151, 154-156, 159,
 190, 210

resistance, 22, 57, 63, 64, 79, 136,
 144, 147, 154, 171, 175, 176
 resonant loop, 149
 RFID, 3, 6, 89, 144, 173

S

sensor, 33
 sequential rotation, 95, 99, 102, 104,
 106, 192
 slot, 42, 43, 45, 50, 51, 60, 69, 70,
 74-76, 78-86, 110, 123, 125, 126,
 128, 134, 140, 150, 151, 165, 166,
 181-185, 188-190, 195, 202, 224
 radiating, 183
 Smith chart, 82
 SPDT, 172, 178
 stub, 240
 surface, 5-7, 10, 12, 13, 26, 27,
 29, 35, 37, 40, 41, 47, 55, 64, 67,
 68, 94, 107, 126, 144, 148, 155,
 191, 233

T, W

transmission line model, 15
 walls, 26, 28, 40, 183